




Universitat Autònoma de Barcelona

ADVERTIMENT. L'accés als continguts d'aquesta tesi queda condicionat a l'acceptació de les condicions d'ús establertes per la següent llicència Creative Commons:  http://cat.creativecommons.org/?page_id=184

ADVERTENCIA. El acceso a los contenidos de esta tesis queda condicionado a la aceptación de las condiciones de uso establecidas por la siguiente licencia Creative Commons:  <http://es.creativecommons.org/blog/licencias/>

WARNING. The access to the contents of this doctoral thesis it is limited to the acceptance of the use conditions set by the following Creative Commons license:  <https://creativecommons.org/licenses/?lang=en>



Universitat Autònoma de Barcelona

**Nanoengineering Composites Made of Metal- and Covalent-
Organic Frameworks and Inorganic Nanoparticles Using
Encapsulation Techniques**

Amirali Yazdi

Doctorate Thesis

Thesis Directors:

Prof. Dr. Daniel MasPOCH

Prof. Dr. Víctor F. PUNTES

Dr. Inhar IMAZ

Thesis Tutor:

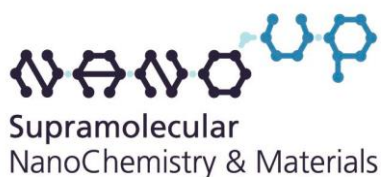
Dr. Jordi HERNANDO

Catalan Institute of Nanoscience and Nanotechnology (ICN2)

Chemistry Department-Science Faculty

Universidad Autònoma de Barcelona

2018



**Inorganic
Nanoparticles
Group**
Catalan Institute of Nanotechnology



Memoria presentada per aspirar al Grau de Doctor per Amirali Yazdi.

Vist i plau

Prof. Dr. Daniel Maspoch

Supramolecular Nanochemistry and Materials Group.

Institut Català de Nanociència i Nanotecnologia (ICN2)

Prof. Dr. Víctor F. Puntes

Inorganic Nanoparticles Group.

Institut Català de Nanociència i Nanotecnologia (ICN2)

Dr. Inhar Imaz

Supramolecular Nanochemistry and Materials Group.

Institut Català de Nanociència i Nanotecnologia (ICN2)

Dr. Jordi Hernando

Departament de Química

Universidad Autònoma de Barcelona

Bellaterra, 19 de octubre de 2018



The present PhD Thesis has been carried out at the Supramolecular NanoChemistry and Materials Group and at the Inorganic Nanoparticles Group of the Catalan Institute of Nanoscience and Nanotechnology (ICN2) following the doctoral program in Materials Science of Autonomous University of Barcelona (UAB). According to the decision of the PhD Commission, this PhD Thesis is presented as a compendium of publications.

All publications are listed below in the order of their appearance in the Thesis:

Publication 1. “The influence of the MOF shell thickness on the catalytic performance of composites made of inorganic (hollow) nanoparticles encapsulated into MOFs.” A. Yazdi, F. Mercoci, N. G. Bastus, I. Imaz, V. Puentes, D. Maspoch. *Catal. Sci. Technol.* 6, 8388-8391, (2016)

Publication 2. “Core-shell Au/CeO₂ nanoparticles supported in UiO-66 beads exhibiting full CO conversion at 100 °C.” A. Yazdi, A. Abo Markeb, L. Garzon-Tovar, J. Patarroyo, J. Moral-Vico, A. Alonso, A. Sanchez, N. G. Bastus, I. Imaz, X. Font, V. Puentes, D. Maspoch. *J. Mater. Chem. A* 5, 13966-13970, (2017)

Publication 3. “Confining Functional Nanoparticles into Colloidal Imine-Based COF Spheres by a Sequential Encapsulation-Crystallization Method.” D. Rodriguez-San-Miguel, A. Yazdi, V. Guillerm, J. Perez-Carvajal, V. Puentes, D. Maspoch, F. Zamora. *Chem. Eur. J.* 23, 8623-8627, (2017).

Additional Publications:

Publication 4. “Application of metal and metal oxide nanoparticles@MOFs”. P. Falcaro, R. Ricco, A. Yazdi, I. Imaz, S. Furukawa, D. Maspoch, R. Ameloot, J. Evans, C. Doonan. *Coord. Chem. Rev.* 307, Part 2, 237-254, (2016).

Publication 5. “Synthesis, culture medium stability, and in vitro and in vivo zebrafish embryo toxicity of metal-organic framework nanoparticles.” A. Ruyra, A. Yazdi, J. Espin, A. Carne-Sanchez, N. Roher, J. Lorenzo, I. Imaz, D. Maspoch. *Chem. Eur. J.* 21, 2508-2518, (2015).

Publication 6. “Continuous One-Step Synthesis of Porous M-XF₆-Based Metal-Organic and Hydrogen-Bonded Frameworks.” V. Guillerm, L. Garzón-Tovar, A. Yazdi, I. Imaz, J. Juanhuix, D. Maspoch, *Chem. Eur. J.* 23, 6829-6835, (2017).

Publication 7. “Sequential Deconstruction–Reconstruction of Metal-Organic Frameworks: An Alternative Strategy for Synthesizing (Multi)-Layered ZIF Composites. C. Avci, A. Yazdi, M. Tarrés, E. Bernoud, N. G. Bastús, V. Puentes, I. Imaz, X. Ribas, Daniel Maspoch. *ACS Appl. Mater. Interfaces*, 10, 23952–23960, (2018).

Table of Contents

Table of Contents.....	1
Abstract.....	3
Acknowledgments	7
Chapter 1 - General Introduction.....	8
1.1 Inorganic Nanoparticles	10
1.2 Application of Inorganic Nanoparticles.....	11
1.3 Inorganic Nanoparticles Supports.....	13
1.4 Metal-Organic Frameworks	19
1.5 Covalent-Organic Frameworks.....	25
1.6 Composites Made of Inorganic Nanoparticles and Metal- and Covalent-Organic Frameworks	30
1.7 MOF@iNPs for Gas Storage and Separation.....	42
1.8 MOF@iNPs for Sequestration.....	50
1.9 MOF@ and COF@iNPs for Catalysis	55
1.10 References	68
Chapter 2 - Objectives.....	83
Chapter 3 - The Influence of the MOF Shell Thickness on the Catalytic Performance of Composites Made of Inorganic (Hollow) Nanoparticles Encapsulated into MOFs.....	85
Chapter 4 - Core-shell Au/CeO ₂ Nanoparticles Supported in UiO-66 Beads Exhibiting Full CO Conversion at 100° C.....	119
Chapter 5 - Confining Functional Nanoparticles into Colloidal Imine-Based COF Spheres by a Sequential Encapsulation–Crystallization Method	139
Conclusion.....	177
Appendix	181

Abstract

The present PhD Thesis has been dedicated to the design and synthesis of a new type of composites of metal-organic frameworks (MOFs) or covalent-organic frameworks (COFs) with inorganic nanoparticles (iNPs) and the use of these composites for heterogeneous catalysis.

In the first chapter, we introduce the family of composites made by supporting iNPs on/in different materials, focusing on those constructed with MOFs and COFs. Then, the general objectives of the Thesis are described in Chapter 2.

Chapter 3 shows the results in “The influence of the MOF shell thickness on the catalytic performance of composites made of inorganic (hollow) nanoparticles encapsulated into MOFs”, *Catalysis Science & Technology* (2016). Herein, we report the encapsulation of hollow Pt or Pd nanoparticles (NPs) into ZIF-8, making a series of composites in which the ZIF-8 shell thickness has been systematically varied. By using these composites as catalysts for the reduction of 4-nitrophenol and Eosin Y, we show that the MOF shell thickness plays a key role in the catalytic performance of this class of composites.

In Chapter 4, hybrid core-shell Au/CeO₂ NPs dispersed in UiO-66 shaped into microspherical beads are created using the spray-drying continuous-flow method. The combined catalytic properties of nanocrystalline CeO₂ and Au in a single particle and the support and protective function of porous UiO-66 beads make the resulting composites show good performances as catalysts for CO oxidation ($T_{50} = 72\text{ °C}$; $T_{100} = 100\text{ °C}$) and recyclability. The results are included in the manuscript entitled “Core-shell Au/CeO₂ nanoparticles supported in UiO-66 beads exhibiting full CO conversion at 100 °C”, *Journal of Materials Chemistry A* (2017).

Finally, in Chapter 5, we demonstrated a two-step method that enables imparting new functionalities to COFs by nanoparticle confinement. The direct reaction between 1,3,5-tris(4-aminophenyl)benzene and 1,3,5-benzenetricarbaldehyde in the presence of a variety of metallic/metal-oxide nanoparticles resulted in the embedding of the nanoparticles in amorphous and nonporous imine-linked polymer organic spheres. Post-treatment reactions of these polymers with acetic acid under reflux led to crystalline and porous imine-based COF-

hybrid spheres. Interestingly, porous imine-based COF-hybrids with Au and Pd NPs were found to be catalytically active. These results have been reported in the publication entitled “Confining Functional Nanoparticles into Colloidal Imine-Based COF Spheres by a Sequential Encapsulation-Crystallization Method”. *Chemistry a European Journal* (2017).

Resum

La presente tesis doctoral se ha enfocado en el diseño y la síntesis de un nuevo tipo de materiales compuestos basados en metal-organic frameworks (MOFs) o covalent-organic frameworks (COFs) y nanopartículas inorgánicas y el uso de estos materiales compuestos para la catálisis heterogénea.

En el primer capítulo se introduce la familia de materiales compuestos dispersos en/sobre diferentes materiales haciendo especial énfasis en aquellos construidos con MOFs y COFs. En el capítulo 2 se presentan los objetivos generales de la tesis doctoral.

En el capítulo 3 se muestran los resultados del artículo “The influence of the MOF shell thickness on the catalytic performance of composites made of inorganic (hollow) nanoparticles encapsulated into MOFs” publicado en 2016 en la revista *Catalysis Science & Technology*. En el mismo se reporta la encapsulación de nanopartículas huecas de Platino y Paladio en el ZIF-8 formando así una serie de materiales compuestos en los cuales el espesor de la cáscara de ZIF-8 era modulada de manera sistemática.

En el capítulo 4, nanopartículas híbridas de tipo núcleo-coraza de Au/CeO₂ dispersadas en microesferas de UiO-66 han sintetizados usando el método de atomización por secado con flujo continuo. Las propiedades catalíticas combinadas en una única partícula de los nanocristales de CeO₂ y Au y la capacidad protectora de las microesferas porosas de UiO-66 hacen que estos materiales compuestos muestren resultados interesantes como catalizadores para la reacción de reducción de monóxido de Carbono. (T₅₀ = 72 °C; T₁₀₀ = 100 °C) con alta reusabilidad. Los resultados obtenidos han sido incluidos en el artículo. “Core-shell Au/CeO₂ nanoparticles supported in UiO-66 beads exhibiting full CO conversion at 100 °C” publicado en la revista *Journal of Materials Chemistry A* en 2017.

Finalmente, en el capítulo 5, hemos demostrado que usando un método en dos pasos se pueden funcionalizar COFs confinando en ellos nanopartículas. La reacción directa entre el 1,3,5-tris(4-aminofenil)benceno y el 1,3,5-benzenetricarbaldehído en presencia de una variedad de nanopartículas metálicas o de óxidos de metal resulta en la encapsulación de estas nanopartículas en un polímero amorfo de iminas-enlazadas con forma de esfera. El Post-tratamiento de estas esferas con ácido acético en reflujo conduce a la obtención de esferas cristalinas de COFs basados en iminas. Además materiales compuestos basados en COF y nanopartículas de Au y Pd han demostrado ser catalíticamente activas. Estos resultados han sido publicados en el artículo “Confining Functional

Nanoparticles into Colloidal Imine-Based COF Spheres by a Sequential Encapsulation-Crystallization Method” publicado en la revista Chemistry a European Journal en 2017.

Acknowledgments

First and foremost, I want to thank all of my advisors Prof. Daniel Maspoch, Prof Victor Puentes, Dr. Inhar Imaz, and Dr. Neus Bastús. It has been an honor to be their PhD student. They have taught me, both consciously and unconsciously, how good experimental chemistry is done. I appreciate all their contributions of time, ideas, and funding to make my PhD experience productive and stimulating.

Besides my advisors, I would like to thank all of my labmates in Nanoup and Inorganic Nanoparticles Group, specially Dr. Vincent Guillerm, Dr. Javier Perez, Luis Carlos Garzon and Civan Avci for their insightful comments and encouragement, which incensed me to widen my research from various perspectives. Working beside them was an honour for me.

My thanks also go to Institut Catala de Nanociencia i Nanotecnologia (ICN2), which gave me this opportunity to use all of their facilities during my PhD, specially Dr. Belen Ballesteros and Marcos Rosado in Electron Microscopy Division.

Last but not the least, I would like to thank my friends and family; my parents, my sister and all of my friends for supporting me spiritually and economically throughout writing this thesis and my life in general.

Chapter 1 - General Introduction

1.1 Inorganic Nanoparticles

Inorganic nanoparticles (iNPs) have been attracting increasing attention in the past decades. Since their discovery, the approach to utilize them in different applications has changed due to their unique physical and chemical properties compared to the bulk size of the same materials. Nanomaterials are classified with their dimension.[1] They are addressed as “nano” when their size is in 1-100 nm range. This difference of size between the nanoparticle and bulk materials has a tremendous effect on the properties of the material; inorganic nanomaterials are in the size range of molecules, but with a higher electron density[2] and bulk metals have delocalization of the electron clouds, which is a phenomenon that is not seen in nanosized metals. Thus, electrical, thermal and in general most of the physical and chemical properties of the bulk materials are not exhibited in the nanoparticle counterparts.

On the contrary, when the surface of the iNPs interacts with other materials, the interaction leads to a change in the electric field. This change can be measured as a signal called Surface Plasmon Resonance (SPR) (Fig. 1).[3] The changes in the cloud density of the iNPs are a direct consequence of their interaction with the support. They are dependent on the size, shape, and defects of the iNPs.[4] [5] The importance of this phenomenon makes it very crucial to choose the right type of support for iNPs in different applications since the contribution of the support can enormously affect the activity of iNPs. All these exceptional properties have made it so that nanoparticles have an exponentially increasing presence in different areas.

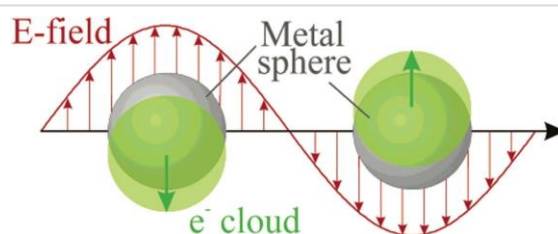
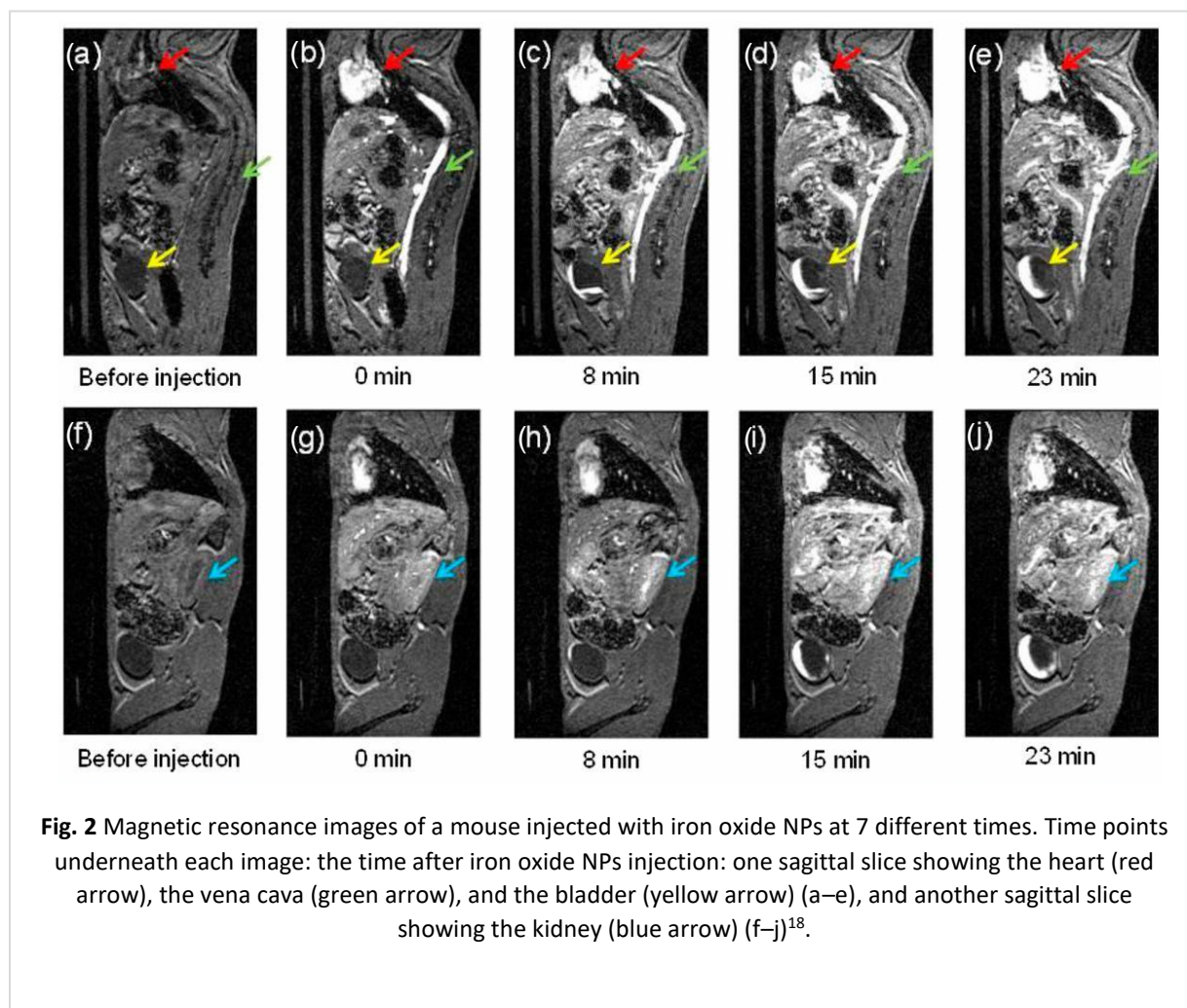


Fig. 1 Electronic cloud oscillation of metal NPs when an external electric field is applied³.

1.2 Application of Inorganic Nanoparticles

The unique electronic and optical properties and the high surface-to-volume ratios of nanoparticles lead to advanced and diverse applications, ranging from electrooptic devices[6, 7], and chemical sensing[8] to magnetic recording[9]. iNPs have also shown other applications in different fields, including energy conversion and storage, chemical manufacturing, and environmental technology[10-13].

In addition, iNPs have a wide range of application in the field of biomedicine. By using iNPs as a drug carrier, they can have potential applications in drug targeting[14], improving the release and bioavailability of drugs[15] and reducing the secondary effects of drugs[16].



iNPs have been used for biomedical imaging as well. Inorganic nanoparticle-based biomedical imaging probes have been studied extensively as a potential alternative to conventional molecular imaging probes[17]. Not only they can provide a better imaging performance but they can also offer a greater versatility of multimodal, stimuli-responsive, and targeted imaging (Fig. 2)[18-22].

Also, iNPs have a key role in assisting the development of smart sensors and detection agents. Their high surface to volume ratio and unique optical properties facilitates the development of highly sensitive analytical inorganic nanoparticle-based bio-sensing tools. Smartly fabricated gold NPs can be used as probes for selective detection of toxic contaminants and metal pollutants[23]. Optical properties of gold NPs arise due to a distinctive phenomenon termed as SPR. Any change/alteration in the size, shape or geometry of particles alters the local electron confinement which is thereby reflected in the SPR absorption maxima and color of colloidal solution[24]. For example, adsorption of metal ions in wastewater by gold NPs changes the SPR of the nanoparticles allowing to detect heavy metal pollutant with an accuracy of 1-10 ppb. Heavy metal pollutant such as As, Hg, Cu, Pb, Cr, and Cd have been detected with similar technique[25-29]. Besides detection, different types of iNPs such as TiO₂, zero valent iron, iron oxides and CeO₂[30-33] have been introduced for the removal of heavy metals from water/wastewater. These iNPs have exceptional adsorption properties, and they are cost-effective adsorbents.

Among all the applications above of iNPs, heterogeneous catalysis has undergone explosive growth during the past decade[34, 35]. Since heterogeneous catalysis is a surface phenomenon, the activity of a metal catalyst is generally proportional to the surface area of the active phase, which depends on the particle size. Smaller particles have a higher proportion of their atoms at the surface, while larger particles have a smaller proportion. For this reason, iNPs have specific and outstanding properties of a catalyst, such as selectivity, activity, durability, tenability, recoverability and other unique properties compared to bulk catalysts. Especially, noble transition metals NPs such as Pd, Au, Pt, Ru and Ag, have been extensively exploited in catalysis, and a large variety of organic transformations such as carbon-carbon coupling[36, 37], oxidation[38, 39], hydrogenation[40, 41], biocatalysis[42, 43], photocatalysis[44-46], biofuel generation[47, 48] and many more have been achieved using iNPs based on these metals[49, 50] as catalyst. However, there are still some major

barriers to the widespread use of iNPs as a heterogeneous catalyst. Firstly, they can suffer a deactivation process called sintering. When two particles collide with sufficient energy, they will coalesce with one another, reducing their surface area, and consequently their surface free energy. This reduces the number of active sites at which reactions can occur, which results in a loss of catalytic activity. For example, supported Pd NPs on MgO and ZrO₂ showed turn over frequencies (TOFs) of 464.68 and 309.8 M.M⁻¹.min⁻¹ representatively for *p*-nitrophenol reduction. These values are much higher compared to the unsupported Pd NPs (TOF= 2.7 x 10⁻³ M.M⁻¹.min⁻¹). Seth et al. investigations suggested that support-induced modification in the electronic nature of the particles and aggregation prevention were responsible for the enhanced performances of the supported Pd NPs[51]. The second limitation of using iNPs is that they are difficult to recover. Because of their small sizes, they cannot be collected by ordinary filtration methods, as they pass through the pores of most common filtration devices. Furthermore, they cannot be collected by centrifugation because of their low sedimentation rates.[52]

1.3 Inorganic Nanoparticles Supports

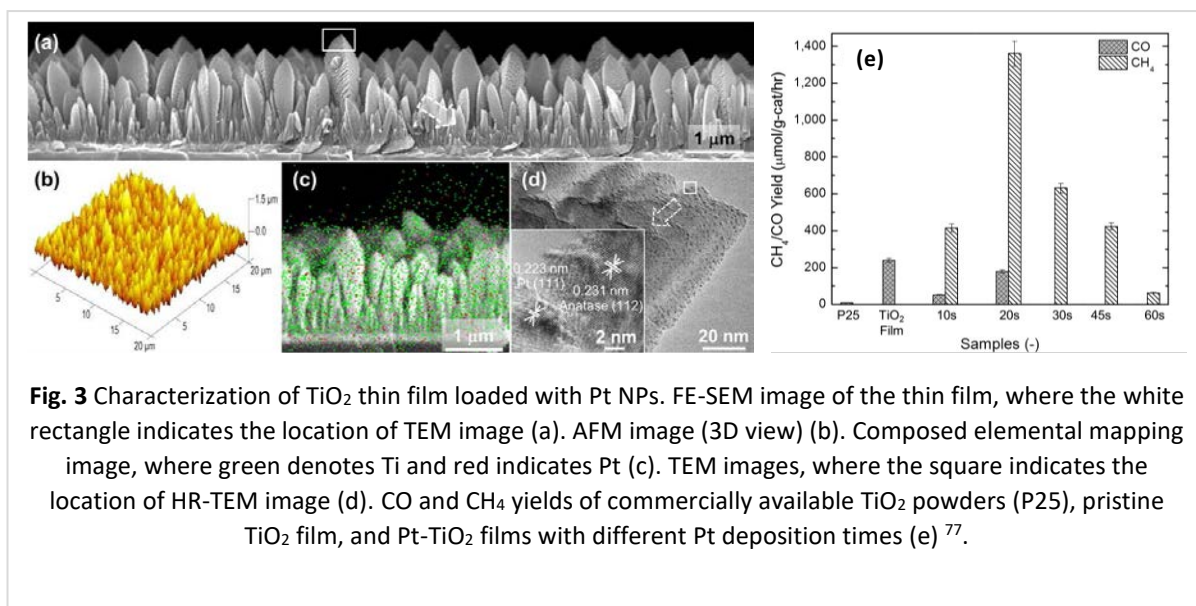
The argument of interest between using iNPs mainly for catalysis and other applications and the barriers to using them alone has prompted the synthesis and investigation of diverse highly functionalized iNPs supported on various materials. Support materials can influence a catalysis reaction in many aspects. In some cases, interactions between iNPs and support materials inhibit chemisorption of reactant species, resulting in compromising the catalytic activity. However, metal–support interactions can also promote catalytic activity, and the support material even takes a major part in catalytic reactions[53].

iNPs support materials can be categorized into metal oxides[51, 54, 55], graphene[56-58], activated carbon[59, 60], zeolite[61], mesoporous silica[62], MOFs[63] and COFs[64]. The role of the support can be different in every system for different applications. The role of metal oxide as non-porous support for iNPs can exceed from avoiding aggregation and sintering of the nanoparticles in the application media. In most cases, they can have a direct impact on the nature of the property of the composite, and they can act as an active support, either by enhancing the activity of the iNPs by orders of magnitude or adding whole new

functionality to the systems. For example, using CeO₂ as a support for metal NPs like gold for CO oxidation, enhances the catalytic activity of the iNPs drastically, because of the oxidation exchange and storage capacity of ceria[65, 54, 66]. These properties of ceria are due to its redox behavior achieved by the easy and reversible transformation of Ce⁴⁺ cations into Ce³⁺ cations, which depends on the oxygen vacancies especially on the surface of the material[67]. Different systems such as Au supported on TiO₂ and iron oxides can also reduce the oxidation temperature drastically but with a different mechanism[68-71].

Additional functionality such as photoactivity can be introduced by using materials such as TiO₂ and ZnO as a support for iNPs[72-75]. Among the photocatalysts, TiO₂ and ZnO, which are a cheap, nontoxic, and abundant semiconductor and resistant to photo-corrosion, have been most widely used in photocatalysis, photodegrading organic pollutants in a variety of environmental applications[76]. However, there are some drawbacks to use TiO₂ as a photocatalyst, its large band gap and high recombination of photogenerated charge carriers can decrease the photoactivity[77]. By pairing TiO₂ with noble metal NPs such as Pd, Pt, Au, Ag or even Cu, we can reduce the recombination of photogenerated charge carriers and improve the charge separation, which can result in higher photocatalytic activity of TiO₂-supported noble metal NPs and also, in some cases, tune the selectivity towards more desirable products[78]. As an example, in the work of Biswas et al., they demonstrated that Pt supported on TiO₂ thin film had a higher photoreduction efficiency of CO₂ with a selective formation of CH₄ compare to TiO₂ thin film alone (Fig. 3)[77].

On the other hand, ZnO has a higher electron mobility (115–155 cm² V⁻¹ s⁻¹) than TiO₂ by orders of magnitude and large exciton binding energy (60 meV) at room temperature. For this reason, it has been regarded as a promising material in a broad range of high technology applications, for example, photodetector[79], solar cell[80], and photocatalyst[81]. With a similar behavior to TiO₂, coupling ZnO with noble metal NPs can enhance the photoactivity. Pern and co-workers were able to improve the methanol oxidation activity of ZnO nanorods by incorporating Pt NPs. Irradiation of UV light on ZnO@Pt enhanced the chronoamperometric response by 62%, which demonstrates a synergistic effect of photo-oxidation of methanol on ZnO and electro-oxidation of methanol on Pt NPs.[75]



Furthermore, metal oxides support can also add other functionality such as magnetic properties to iNPs. Magnetite is a well-known material, also known as ferrite, and can be used as versatile support for functionalization of iNPs. One of the main barriers that were mentioned before for using iNPs in heterogeneous catalysis was the difficulty in recovering the catalyst from the reaction media and recyclability. Fe₃O₄ is used as a support for important catalytically active metal NPs such as Pd, Pt, Cu, Ni, Co, Ir, etc. to obtain stable and magnetically recyclable heterogeneous catalysts[82-85]. For example, the Pd-based catalyst is well known for the production of H₂O₂ from electro-generated H₂ and O₂[86]. By loading Pd NPs on the magnetic Fe₃O₄ particles, H₂O₂ and Fe²⁺ could simultaneously be produced in an electrolytic cell and the catalyst can be recycled magnetically up to 10 cycles maintaining the catalytic activity[84]. Other types of metal oxides such as ZrO₂, Al₂O₃, MnO and MgO, etc. have been used as a support for iNPs for various catalysis reactions but mostly focus enhancing the activity and/or preventing the iNPs from aggregation[87-89].

Even though non-porous supports such as metal oxides can provide a tremendous improvement in the activity of iNPs and adding multiple functionalities to the system, they are still some drawbacks in using a non-porous support in certain applications. Different localization of iNPs is very difficult on non-porous materials because mainly the localization of the iNPs is on the surface and this can also lead to a low loading of the iNPs. Incorporating iNPs into porous support can overcome these problems and allow a high loading of multiple

types of iNPs with a desirable localization[62]. Microporous/mesoporous cavities and channels of zeolites frameworks and silica have been used for decades for the encapsulation of cations, complexes and metals[90, 91]. In the particular case of metals, nanoparticles are usually formed after post-synthesis modifications such as ion-exchange or wetness impregnation[92-94]. Tough encapsulation can provide strict control of the nanoparticle size as well as a limitation of aggregation at high temperature; encapsulated nanoparticles are often hardly accessible due to diffusion limitations of reactants in sub-nanometric micropores[95-97]. The main advantage of zeolite and silica compared to amorphous porous materials is their ordered porosity, because of their crystallinity and also in some cases, it is possible to have micro and mesopores in these types of materials[98-100]. Lee and co-workers did one of the pioneer examples of using multiple porosity sizes. They reported the fabrication of spatially orthogonal bifunctional porous catalysts, through the stepwise template removal and chemical functionalization of an interconnected silica framework to obtain macroporous–mesoporous architecture with Pd and Pt embedded in different regions (Fig. 4). This different configuration of NPs in micro and mesopores allowed control over the reaction sequence in catalytic cascades for oxidation of cinnamyl alcohol to cinnamic acid[62].

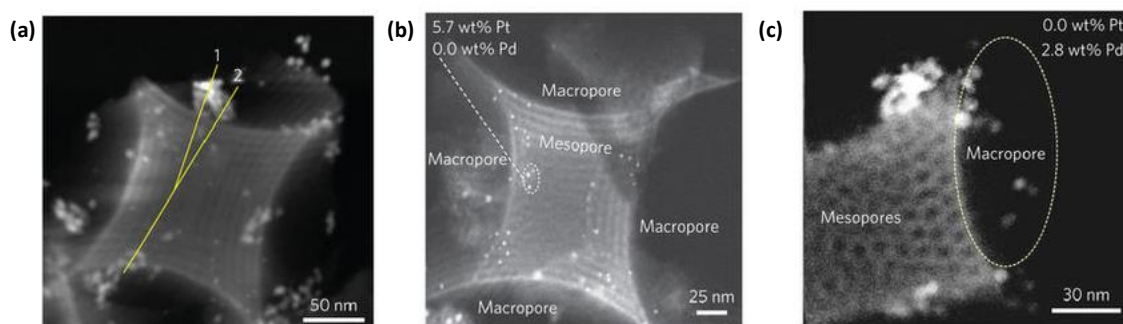
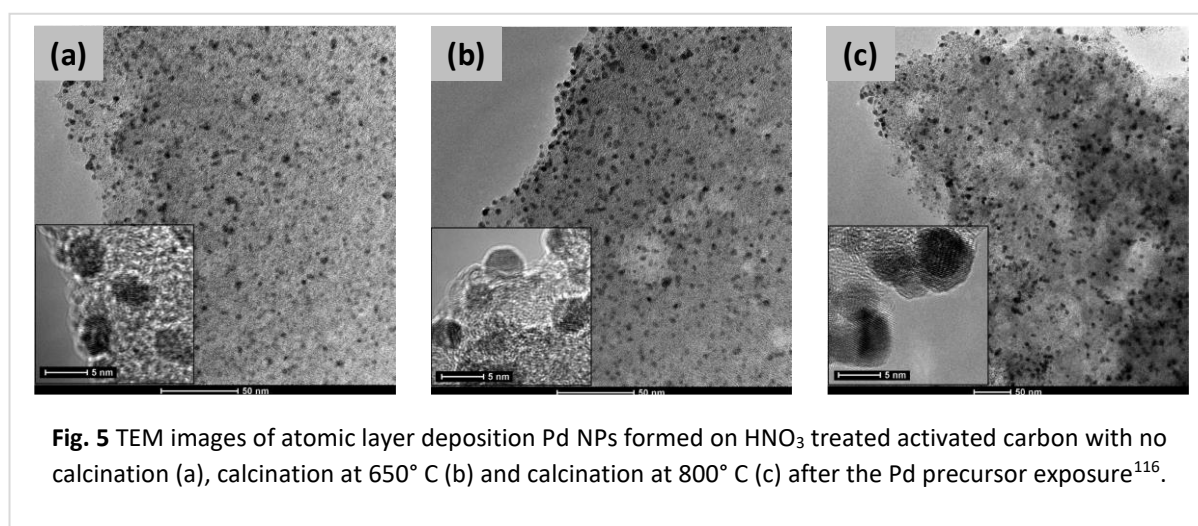


Fig. 4 High angle annular dark field scanning transmission electron microscopy (HAADF-STEM) of NPs distributed across a section of the mesoporous silica framework surrounded by macropores (a). Elemental mapping of mesopores (macropores) showing exclusive Pt (Pd) functionalization (b and c) ⁶².

Activated carbon is a porous, high surface-area adsorptive material with a largely amorphous structure. It has been used as a support for iNPs from the very early stages. The combination of activated carbon and various types of iNPs has received considerable interest in areas related to environment, energy, and sensing,[101-103] especially for practical

applications in gas adsorption/separation, fuel and energy storage, fuel cells, dye-sensitized solar cells (DSSCs), electrochemical sensors, chemical/biological sensing of toxic metal ions and catalysis[104-114]. Activated carbon has many advantages as catalyst support for iNPs. It has flexible surface chemistry and the chemical inertness of activated carbon makes it possible to use for both acidic and basic environments. Besides, it is cheap to produce and easy to obtain. However, one of the interesting advantages of activated carbon as catalyst support is that its surface chemical states can be easily modified[115]. For example, the surface functional groups are important for anchoring or stabilizing the metal precursor when using atomic layer deposition (ALD) method to produce activated carbon@iNP composites. The chemical state of the carbon surface could be an important factor determining the loading, density, distribution, and size of the catalyst particles and it can be tuned by calcination temperature and acid treatments (Fig. 5) [116].



Another type of material that can be categorized in the porous support, based on the structure of it, is graphene[117]. Graphene is one of the most exciting and advanced carbon nanomaterials nowadays, which consist of the carbon atoms arranged in hexagons network and form a 2-dimensional single sheet[118]. Due to its excellent electrical and thermal conductivity, mechanical strength and high surface area, graphene is considered to be an ideal, two-dimensional support for iNPs[119-122]. Dependent on the type of the embedded NPs, the graphene@iNP composites have been applied in a broad range of areas, such as Surface-Enhanced Raman Scattering (SERS)[123, 124], catalysis[125-127], and electrochemical sensing[128, 129]. Also, graphene has recently been shown to be

permeable to thermal protons[130]. Geim and co-workers reported that proton transport through graphene@Pt composites strongly enhanced by illuminating them with visible light. They found a photoresponsivity of $\sim 104 \text{ A W}^{-1}$, which translated into a gain of ~ 104 protons per photon with response times in the microsecond range. This observation was interesting for applications such as fuel cells, hydrogen isotope separation, light-induced water splitting, photocatalysis and novel photodetectors[131]. In catalytic applications, reduced graphene oxide has been numerously used as a catalyst support because of its low-cost and large-scale production enabled by the chemical exfoliation processes[132-134]. However, other graphene architectures like three-dimensional graphene monolith which demonstrated by the chemical vapor deposition, exhibit enhanced property in some catalytic reactions, especially when used as an electrocatalyst support. Pt NPs of 3 nm size fabricated on 3D graphene monolith exhibits a much enhanced electrocatalytic performance toward methanol oxidation compared with both reduced graphene oxide@Pt and commercial Pt/C catalysts. This enhancement is due to the structural advantage of the monodispersed ultrafine Pt NPs and the 3D graphene with interconnected conductive network (Fig. 6)[135].

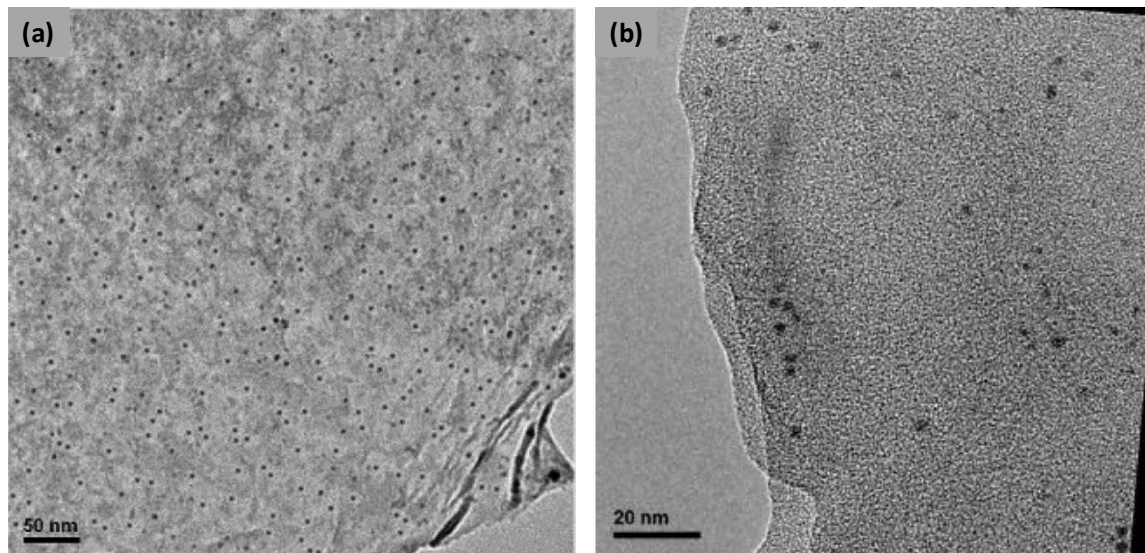
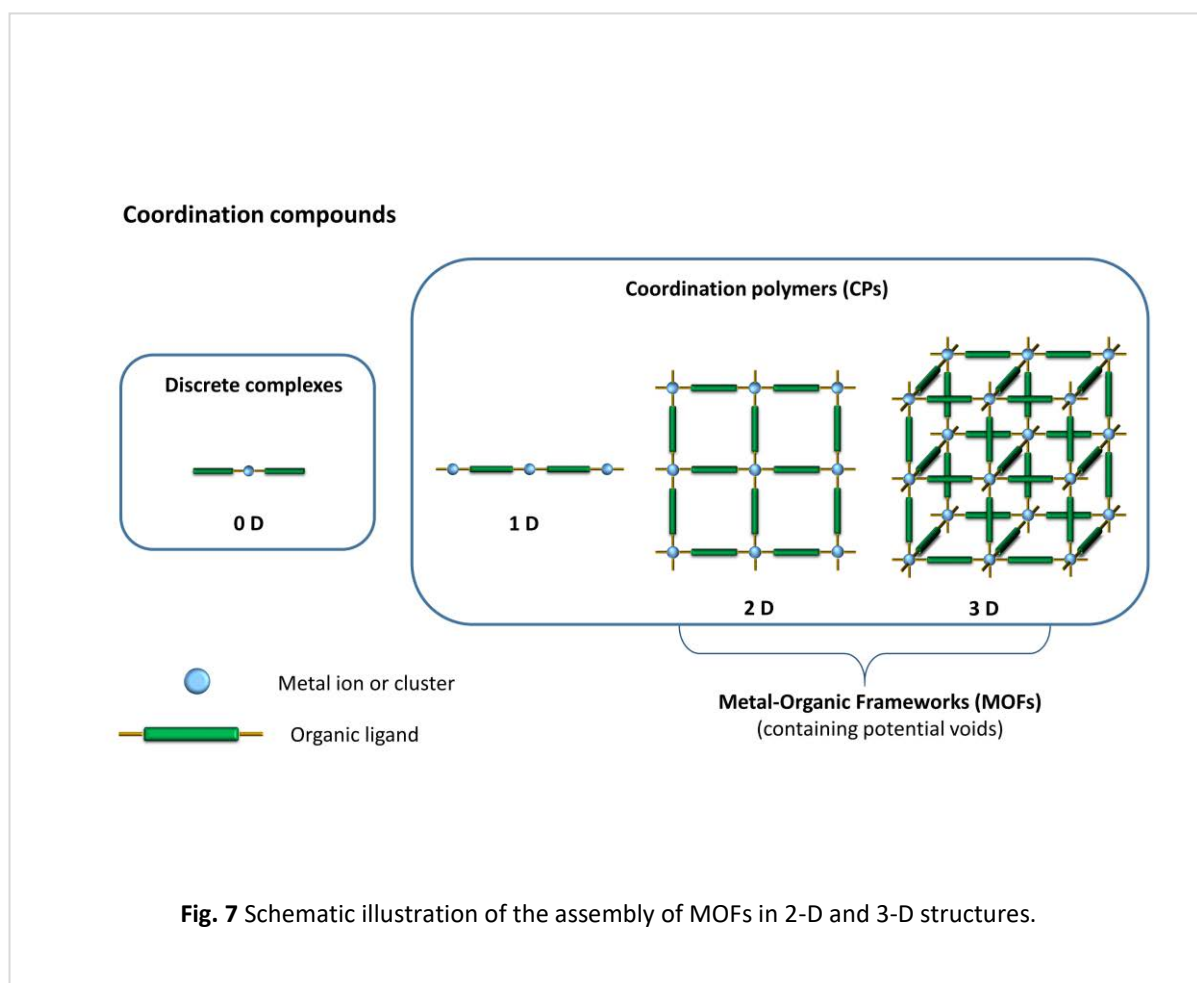


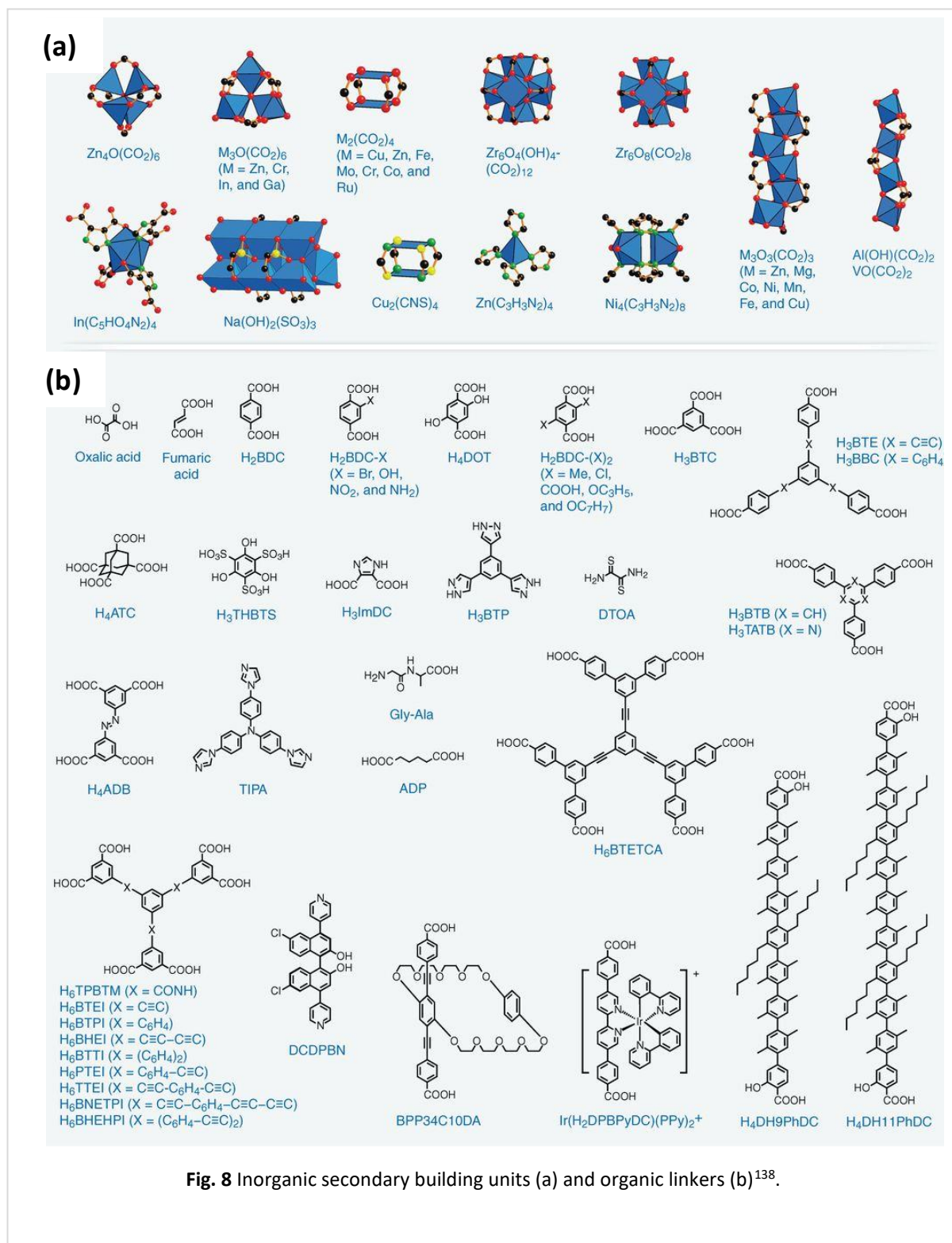
Fig. 6 TEM images of a Pt on 3D-graphene composite (a) and Pt on 2D-graphene composites (b)¹³⁵.

1.4 Metal-Organic Frameworks

Metal-organic frameworks (MOFs) can be defined as hybrid inorganic-organic compounds extended in two- or three dimensions (2-D or 3-D) through coordination bonds (Fig. 7). Essentially, they are polymer structures which are constructed by joining metal-containing units [secondary building units (SBUs)] with organic ligands, building infinite arrays to create open crystalline frameworks with permanent porosity[136, 137].

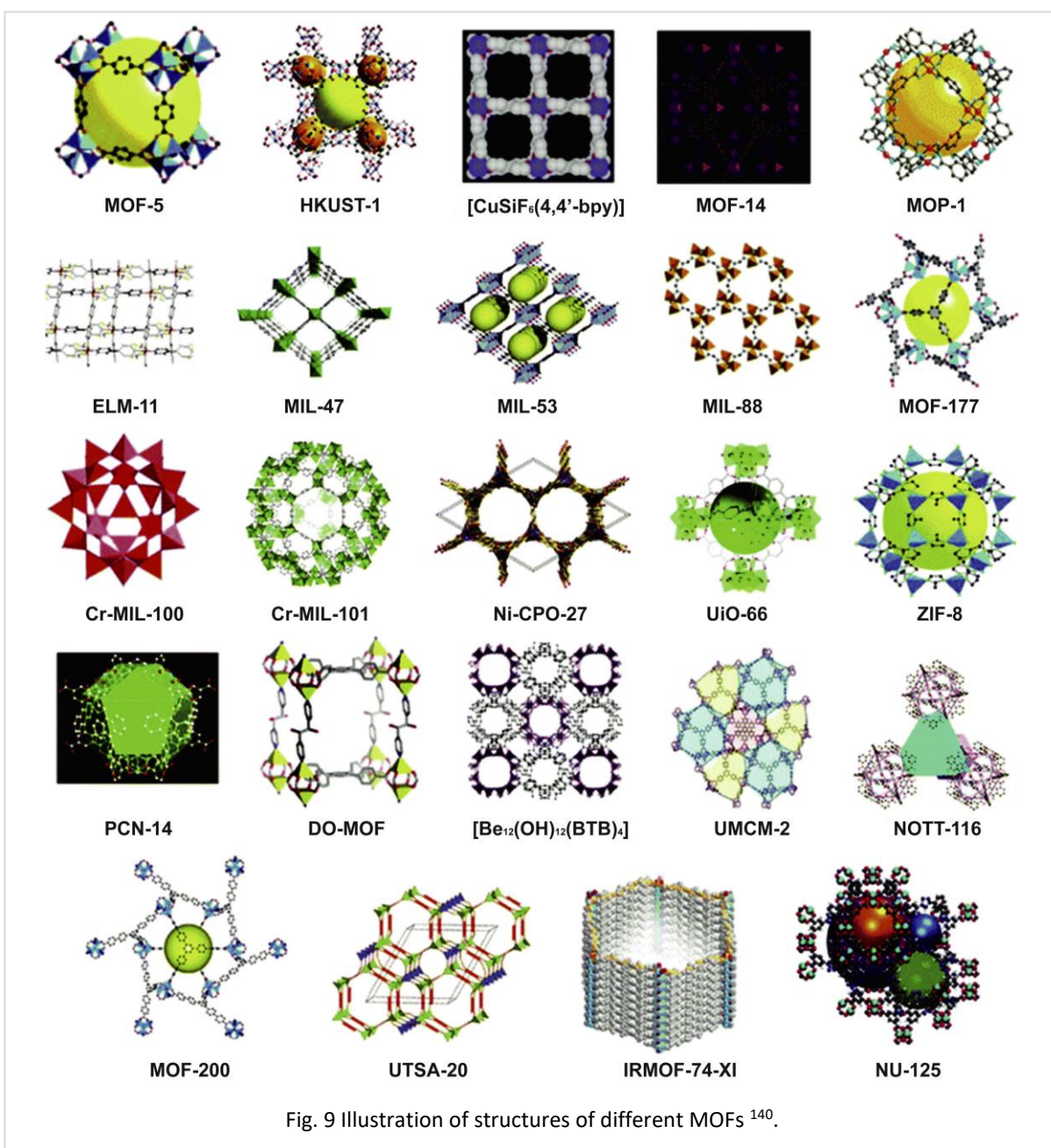


The final structure of MOFs depends on: (i) the geometric coordination of the metal ions, which can vary between 2 to 10 depending on the type of the metal (transition or rare earth metals), which leads to the geometry of the metal-containing SBUs (Fig. 8a); and (ii) the geometry and the binding modes of the organic ligands (Fig. 8b). Additionally, other



interaction forces such as hydrogen bonds, van der Waals interactions and π - π stacking influence the MOF structure[138].

This variation of the SBUs and organic linkers enables flexible structure design in MOFs, in which well-defined pore size, surface areas and functionalities can be constructed by selecting different building blocks. There are various preparation methods to produce MOFs, such as slow diffusion, hydro(solvo)thermal, microwave-assisted heating, electrochemical, mechanochemical, ultrasonic and, more recently, spray-drying [139, 140]. To date, there are more than 20000 reported structures of MOFs [141]. Some examples of the most studied MOF structures are illustrated in Figure 9.[140]



The presence of organic and inorganic SBUs in the structures of MOFs as well as their high surface area, tunable pore size with functionality and the ability to host guest molecules within their cavities allow their potential application in several fields. For instance, the extremely high pore volumes and surface areas of MOFs make them very promising candidate materials for high-pressure gas storage[142]. The high-pressure gravimetric gas storage capacities are proportional to their pore volumes or surface areas[143]; this means that the larger the porosity, the larger the gravimetric gas uptake by MOF materials under high pressure. Significant progress that has been made in synthesizing new types of MOFs allowed scientist to design MOFs with surface areas exceeding $7000 \text{ m}^2 \text{ g}^{-1}$ [144, 145] (Fig. 10). Furthermore, using MOFs in membranes and incorporation of functional sites within porous MOFs are a promising strategies to enhance their gas separation capacities[146, 147]. To date, significant efforts have been devoted to the design, synthesis and modification of MOFs to increase their adsorption capabilities for gases. However, it is the advent of MOFs with higher water stability that inspired scientists to use MOFs for water adsorption applications, including water harvesting, humidity control and adsorption heat pumps and chillers[148].

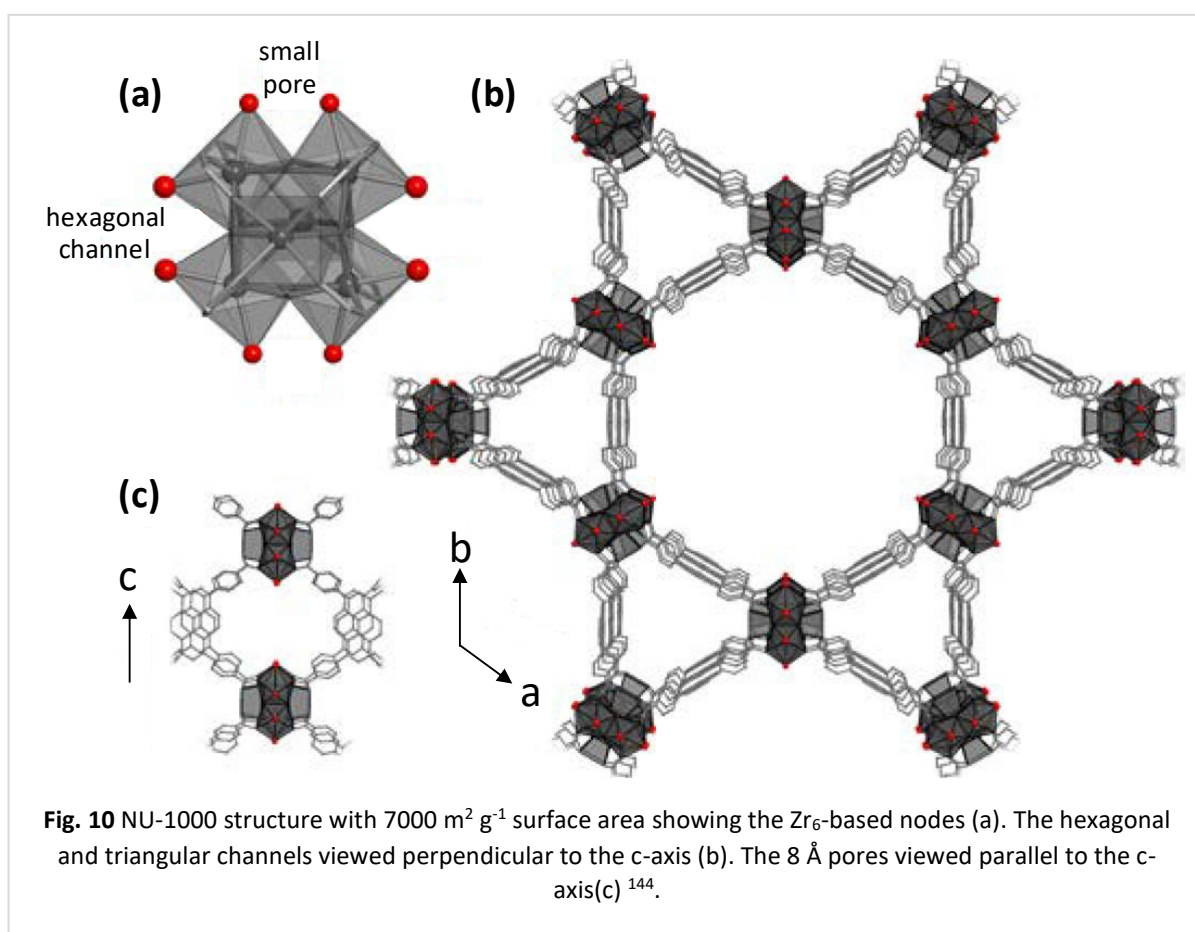


Fig. 10 NU-1000 structure with $7000 \text{ m}^2 \text{ g}^{-1}$ surface area showing the Zr₆-based nodes (a). The hexagonal and triangular channels viewed perpendicular to the c-axis (b). The 8 Å pores viewed parallel to the c-axis(c) ¹⁴⁴.

Furthermore, the extraordinary skeleton structure of MOFs provides many possibilities for the incorporation of diverse basic functionalities. MOFs can incorporate different types of basic sites into both metal nodes and organic ligands, leading to the fabrication of a range of base catalysts with special characteristics[149]. By nature, metal nodes of MOFs can have catalytic activity[150]. The functionality of the organic part can be introduced by direct synthesis[151] or post-synthetic modification[152]. MOFs can also exhibit different degrees of luminescent enhancement in response to interactions between inserted guest molecules and the framework. This unique feature opens a possibility to potential applications in chemical sensing[153]. Other noteworthy features include the high surface area of MOFs that concentrates analytes to a high level, enhancing the detection. Additionally, their tunable pore sizes, flexible porosity and specific functional sites make them excellent sensors[154]. Therefore, MOFs have been used for detection of different gases[155-157], alcohols[158, 159], toxic chemicals[160] and explosive compounds[161].

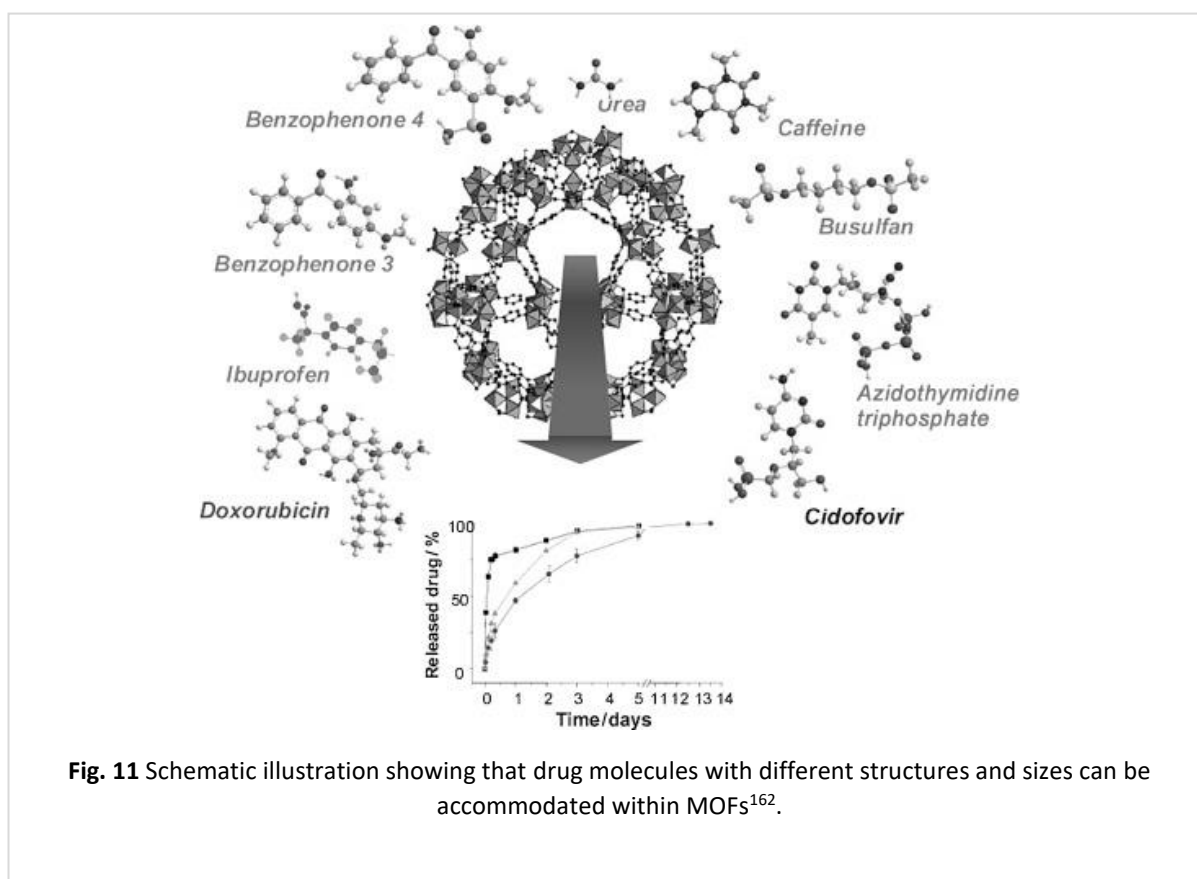


Fig. 11 Schematic illustration showing that drug molecules with different structures and sizes can be accommodated within MOFs¹⁶².

There are also several key properties that make MOFs excellent candidates for using them as a drug carrier. Firstly, their multiple pathways to incorporate the drug molecules into the framework, which allow a range of drug molecules with different structures and sizes to

be accommodated within MOFs (Fig. 11)[162-164]. And, secondly the adjustable interaction between the guest molecule and the organic linker or the metal nodes, which efficiently entrap drugs with high payloads[165]. This integration of drug molecules and MOFs have shown a promising application to treat diseases[166-168]. MOFs have also shown several other applications in various fields, such as toxic gas removal[169], magnetism (which depends on the spatial coordination of the metallic center and organic linkers)[170], potential materials in Li-based batteries[171] and as contrast agents. Indeed, using heavy metals with high relaxivity values as the metal center of the MOFs presents an opportunity to utilize them as magnetic resonance imaging contrast agents[172].

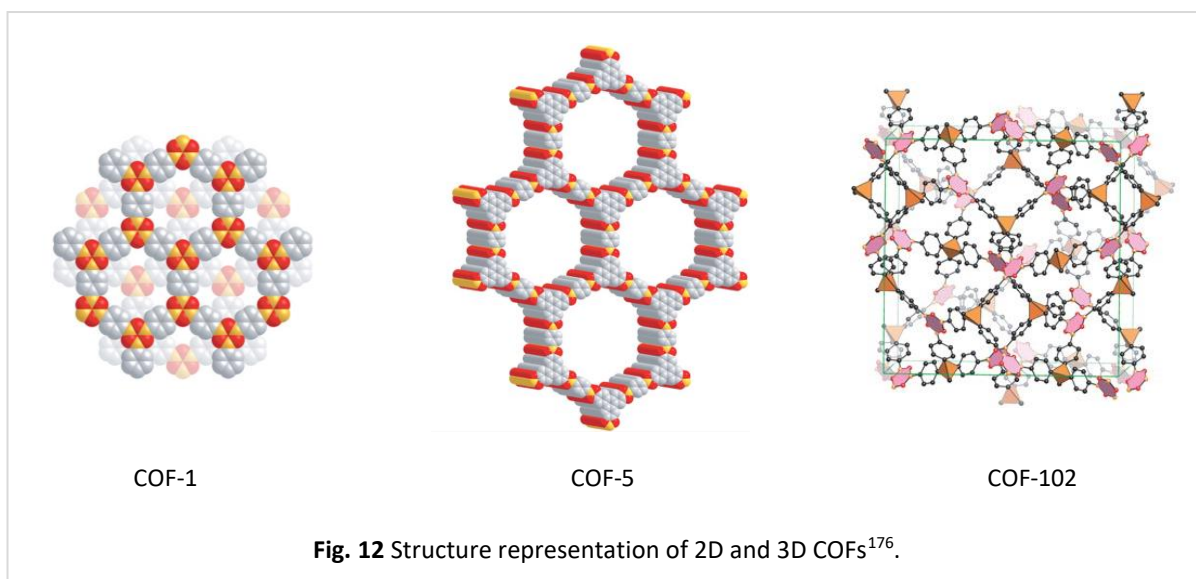
By reviewing all the properties above and applications of MOFs, we can consider them as an eligible candidate for acting as a support for iNPs. MOFs can have both advantages of porous and non-porous support materials, as mentioned. Similar to metal oxide supports, MOFs can introduce new functionalities such as, magnetic properties[173], luminescent[174] and photoactivity[175]; due to their diverse structures that consist of various metal and organic building blocks. Furthermore, compared with the traditional porous materials, MOFs exhibit many special properties such as, a typically adjustable structure, larger surface areas (which allow a higher loading of iNPs and their highly ordered porous structure) and functional pore space, which enables the localization of iNPs within different pore sizes. Finally, the multiple pathways to incorporate the drug molecules into the framework can also be used for incorporating iNPs with different sizes, natures and shapes.

1.5 Covalent-Organic Frameworks

Yaghi and co-workers proposed reticular chemistry principles that deduced covalent chemistry and further developed the 2D or 3D crystalline porous organic polymers, the so-called covalent-organic frameworks (COFs)[176], replacing the SBUs to purely organic molecular units. The formation of COFs is based on covalent bonds between the organic building blocks, and similar to their MOFs counterparts, the most characteristic properties of COFs are their large surface area, tunable pore size and structure and tailored functionality. In comparison with MOFs and other crystalline porous materials (e.g. zeolites and mesoporous silica), the COF materials have the advantages of low density and versatile covalent-combination of building units[177].

However, due to the irreversible nature of the covalent bond, the more favorable type of materials obtained by linkage of organic building units is amorphous materials. Thus, it is highly likely that the reversible formation of covalent bonds is of great importance in synthesizing the crystalline COFs, as well as the thermodynamic control of synthetic conditions; in which have to enable the reversible bond formation. To date, there are six known reversible linkage types that can form crystalline COFs, including: (i) B–O (boroxine, boronate ester, borosilicate, and spiroborate); (ii) C=N (imine, hydrazone, squaraine, and azine); (iii) C=NAr (triazine, phenazine and oxazole); (iv) C–N (β -ketonimine, imide, and amide); (v) C=C (alkene); and (vi) B=N (borazine).

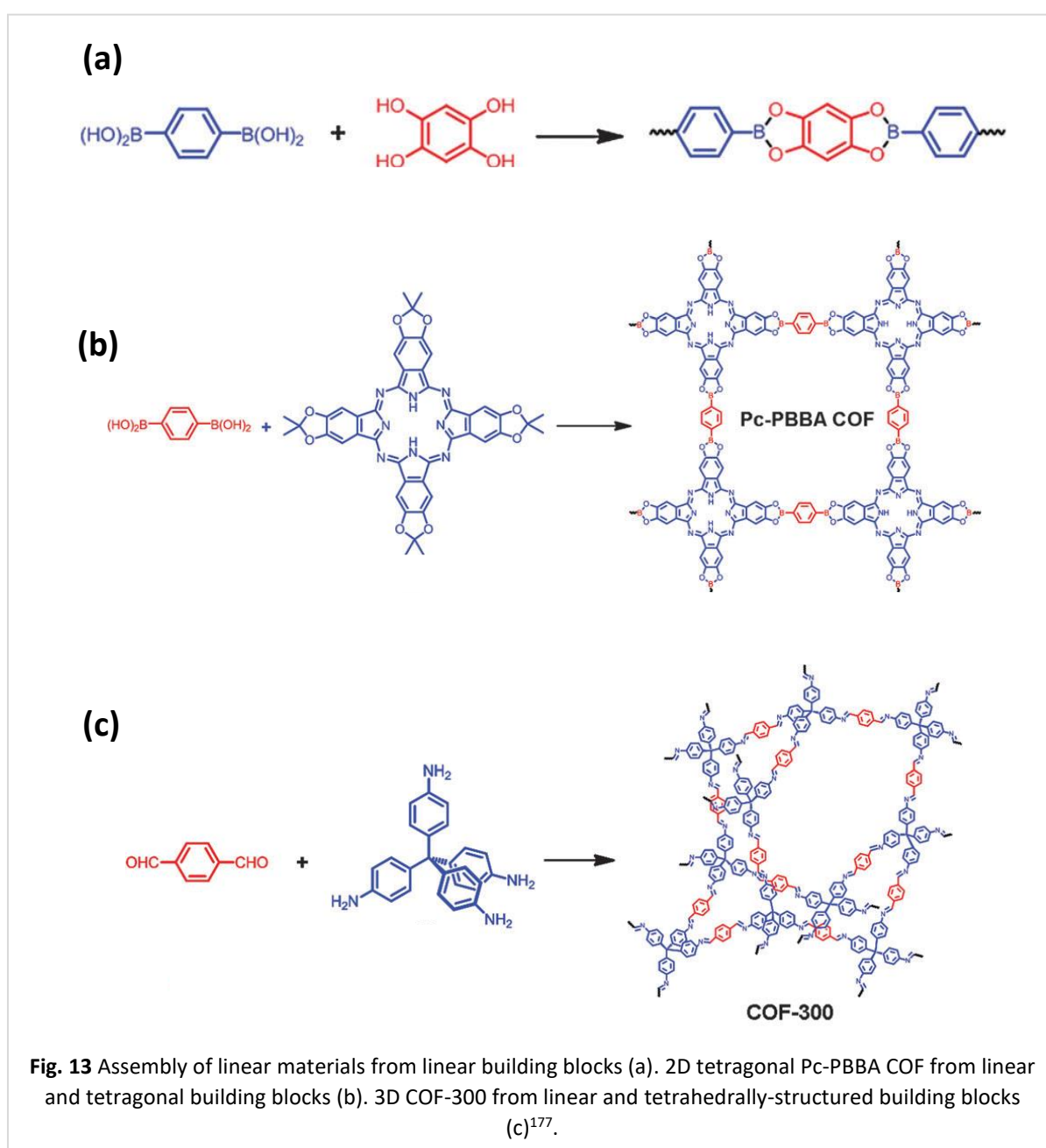
The first 2D COFs were synthesized by condensation of benzene-1,4-diboronic acid (BDDBA), resulting in hexagonal pores with a surface area of $711 \text{ m}^2 \text{ g}^{-1}$ (COF-1) and by dehydration reaction of BDDBA acid and 2,3,6,7,10,11-hexahydroxytriphenylene (HHTP), giving a hexagonal array of 1D mesopores with a higher surface area of $1590 \text{ m}^2 \text{ g}^{-1}$ [176]. The first 3D COFs appeared in the work of Yaghi and co-workers, who synthesized crystalline solids by condensation reactions of tetrahedral tetra(4-dihydroxyborylphenyl) methane or tetra(4-dihydroxyborylphenyl)silane and by co-condensation of HHTP (COF-102 and COF-103). Their apparent surface areas calculated from the BET model were 3472 and $4210 \text{ m}^2 \text{ g}^{-1}$ for COF-102 and COF-103, respectively [178] (Fig. 12).

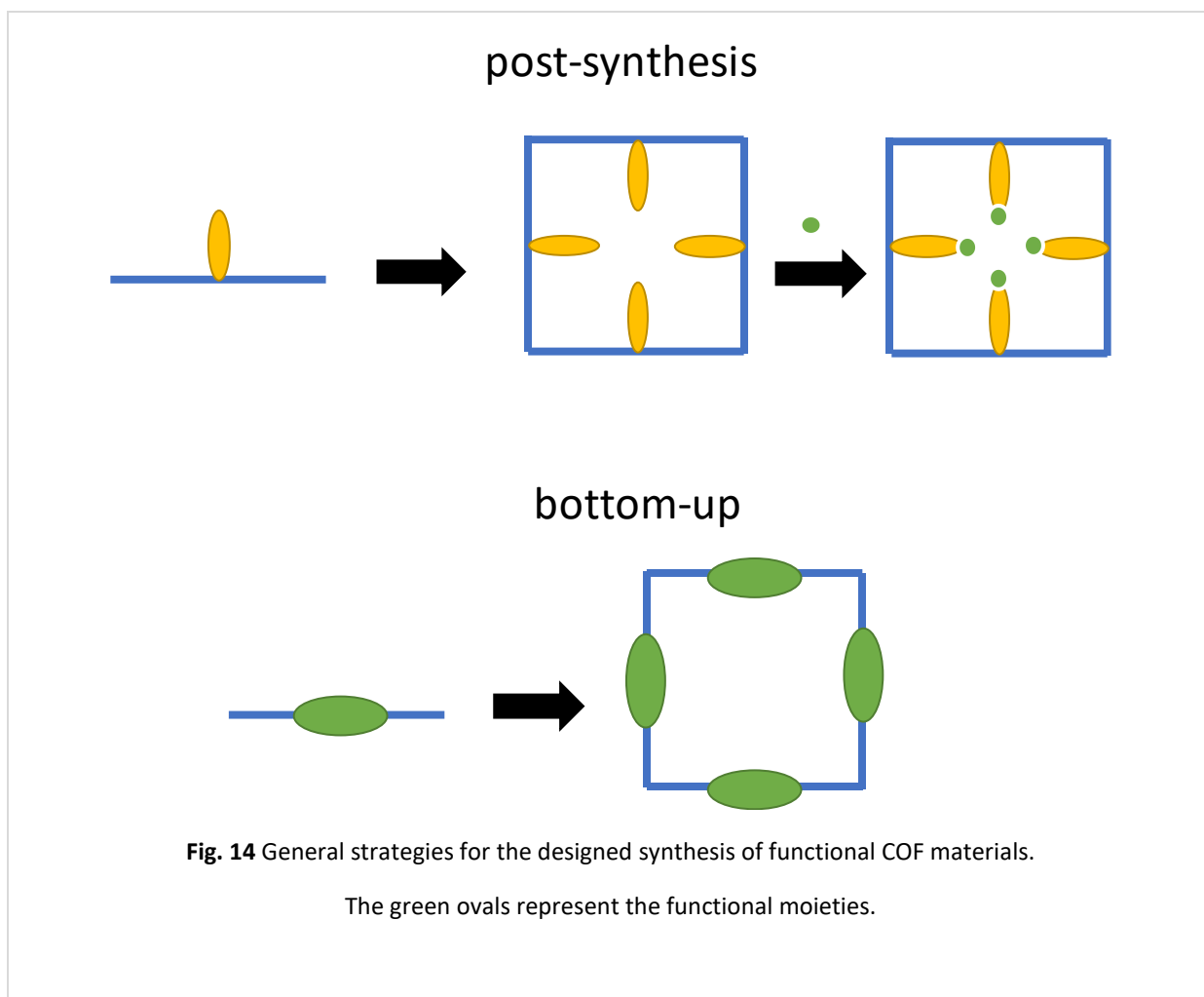


Similar to MOFs, there are some basic concerns to design COFs. The first concern is the issue of porosity. In the traditional porous materials such as zeolites and mesoporous silica, the template extraction from the as-synthesized materials was providing the porous structures[179]. In the case of COFs, the approach is to use rigid building blocks such as rigid monomers[180, 181]. The length of the molecule can control the pore size of COFs, while the shape of the building blocks determines the topology. The most common rigid linking groups for construction of COFs are boroxines[176], triazines[182], imines[183], or hydrazones[184]. Another concern is the structural regularity, which this issue is not guaranteed by only using the rigid building blocks to obtain porosity. The shape and the angle of the building blocks have to be taken into account for a reversible covalent bond in order to allow the formation of a crystalline COF. For instance, when a linear building block is subject to a reaction with another linear building block, the resulted material also has to be linear[185]. However, when a linear building block reacts to those with angles, 2D COF structures are favorable [186]. Correspondingly, to obtain a 3D COF structure, the linear building blocks have to react with a tetrahedrally-structured monomer[183] (Fig. 13).

The remaining concern in the construction of COFs is functionality. There are two main strategies to add functionality to porous and crystalline COFs. Firstly, the most common approach is a post-synthetic modification, which adds the functional groups to COFs via coordinative incorporation or chemical transformation (Fig. 14). As an example, Kim and co-

workers developed a continuous synthesis and post-synthetic modification method to form β -ketoenamine-linked COFs by confining organic building units into moving microdroplets. Using this approach, they were able to modify NO_2 - to NH_2 -substituted COFs serially[187]. The more sophisticated and difficult approach is the bottom-up strategy, in which functional moieties have to be directly included in the designed building block before the COF synthesis. For example, the DAAQ-TFP-COF with 2,6-diamioanthraquinone edges is redox active and is capable of capacitive energy storage in sulfuric acid solution (1 M) with a capacitance of $40 \pm 9 \text{ F g}^{-1}$ after 5,000 cycles[188].





As mentioned above, selecting a rigid and suitable building block is the first crucial step designing COFs. A subsequent, and also vital issue is finding a synthetic fitting condition. There are several methods to synthesize COFs. The most common method is solvothermal which the first family of COFs was synthesized by [176]. Other methods such as ionothermal [182], microwave [189], microfluidic [190], mechanochemical [191] and continuous-flow synthesis [192] are also being used to produce COFs. More recently, a method that combines the spray-drying technique with a dynamic covalent chemistry process to synthesize a two-dimensional COF superstructure, assembled from two trigonal building blocks, 1,3,5-benzenetricarbaldehyde (BTCA) and 1,3,5-tris-(4-aminophenyl)benzene (TAPB), has been reported (Fig. 15). This method also enables the incorporation of functional iNPs into hollow imine-based COF superstructures during [193].

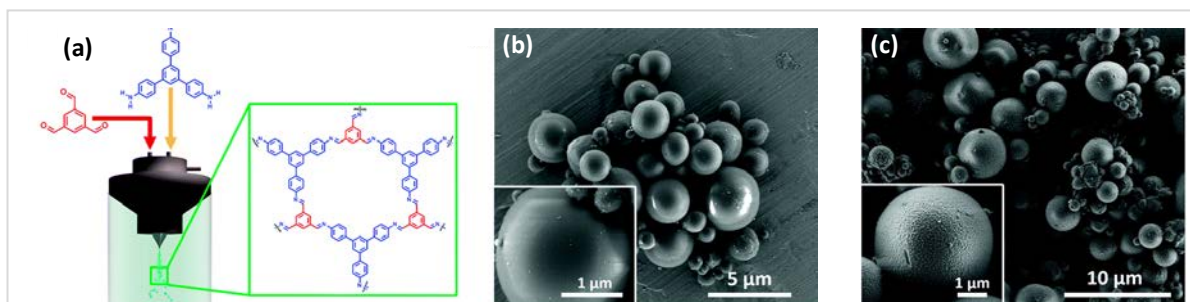
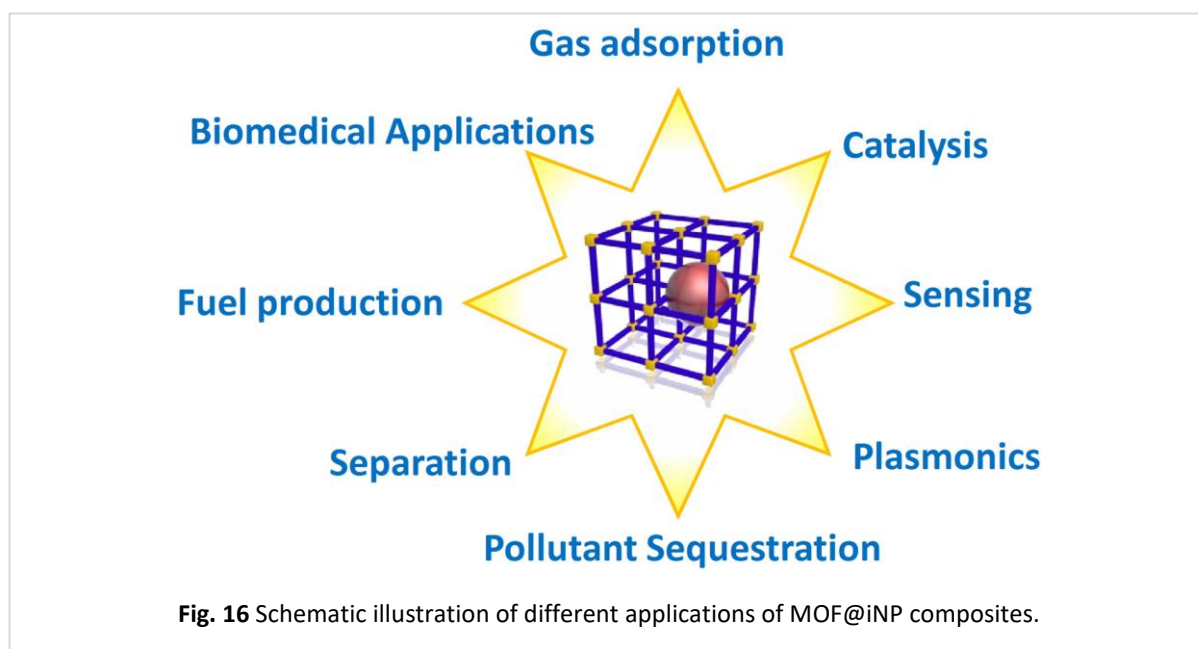


Fig. 15 Schematic representation of the spray drying synthesis of COF-TAPB-BTCA (a). FESEM images of amorphous COF-TAPB-BTCA spheres (b) and COF-TAPB-BTCA superstructures (c).¹⁹³

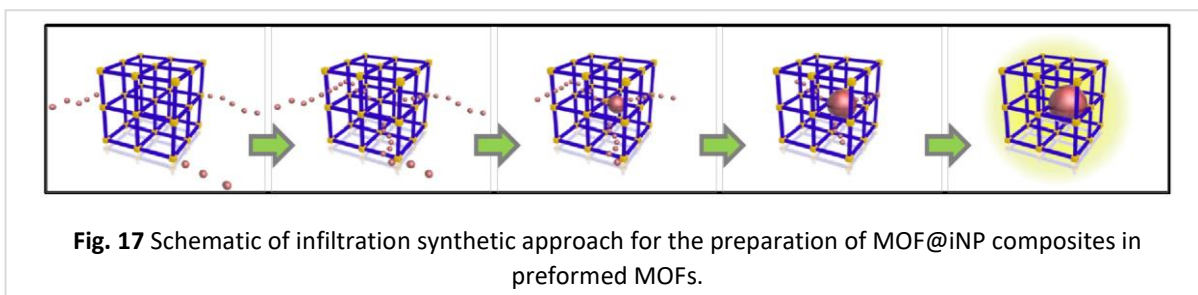
COFs, due to their similar characteristics to their counterparts MOFs (which are high regular porosity and tunable structure), can be used in akin applications such as gas sorption and storage with the advantage of lower density[177]. They demonstrated a high uptake of gases such as hydrogen[194], methane[195], carbon dioxide[196]. Also, boron-containing COFs, such as COF-10, has shown an exceptionally high ammonia uptake in comparison to other porous materials[197]. Their high chemical and thermal stability, alongside their tunable functionality aforementioned, allow them to be used in different applications including catalysis (e.g. boroxine and imine based 3D COFs consisting of both acidic and basic sites, can act as excellent bifunctional cascade catalysts[198]), sensors (bottom-up integrated COF-LZU8 with functionalized thioether group was used for selective detection and facile removal of mercury (II)[199]) and optoelectronics[200]. The primary advantages of COFs in comparison to MOFs are their low density and higher chemical stability. These characteristics make them also a viable candidate to be used as a support for iNPs for certain catalysis applications in aqueous and acidic media[201].

1.6 Composites Made of Inorganic Nanoparticles and Metal- and Covalent-Organic Frameworks

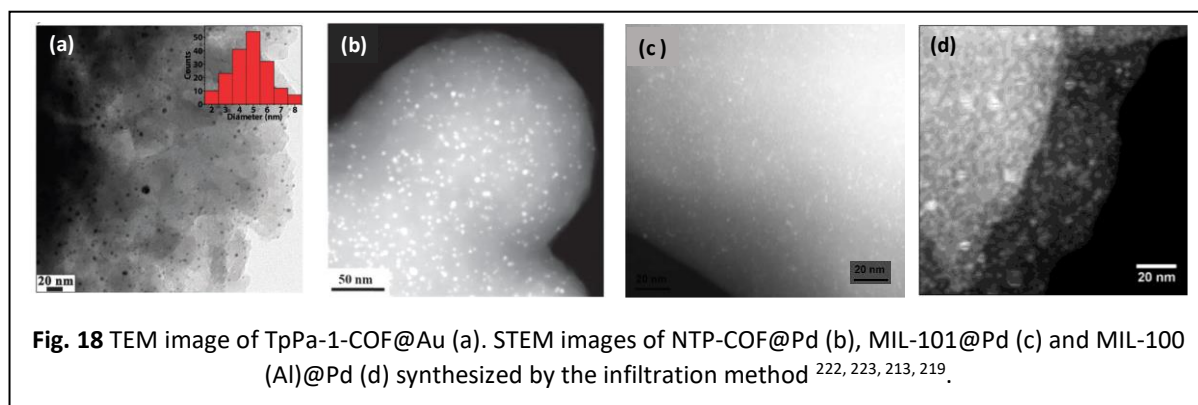
The unique features of MOFs and COFs have led researchers to explore combining them with other functional materials to form novel composites with advanced properties.[202] Indeed, ceramics, metal NPs, polymers and biomolecules have been combined with MOFs to establish new materials that have demonstrated unprecedented performance in the areas of catalysis[203], molecular separations [204], sensing [205], plasmonics[206], gas storage[207], controlled guest release[208, 209], and protection of biomacromolecules[210, 211]. The most widely studied of these composite systems are based on integrating iNPs with MOFs, a combination that creates materials with enhanced performance characteristics in the areas of gas adsorption, catalysis, sensing, microelectronics, sequestration, delivery and biomedical applications, fuel production and separation (Fig. 16). More recently, COFs have been paired with iNPs for applications such as catalysis and remediation[212, 213]. The versatility of the synthetic approaches for metal oxide (ceramic) and metallic nanomaterials can also be attributed to this combination.



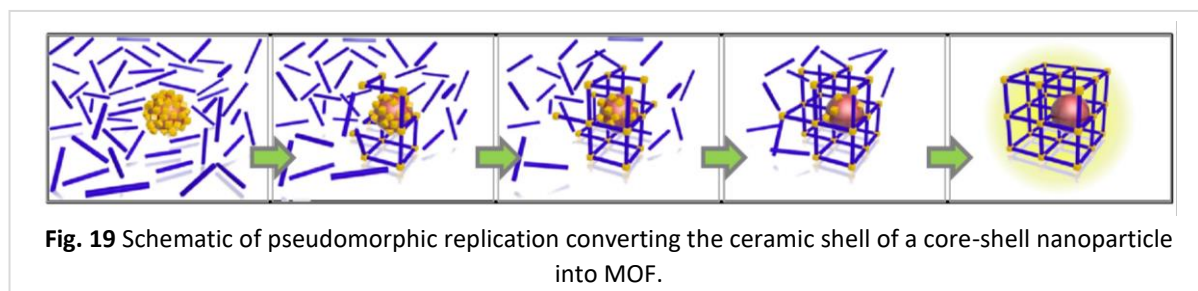
There are different synthetic approaches for the preparation of MOFs or COFs@iNPs composites. The first method that was reported to construct these type of composites is the infiltration method. Metallic and metal oxide NPs can be prepared by infiltrating the precursors in the pre-formed porous MOF or COF crystals, either via the vapour or liquid phase[214, 215]. Particle formation is subsequently triggered within the MOF or COF by the application of heat[216, 217], reducing agents[218, 219] or radiation[220, 221] (Fig. 17).



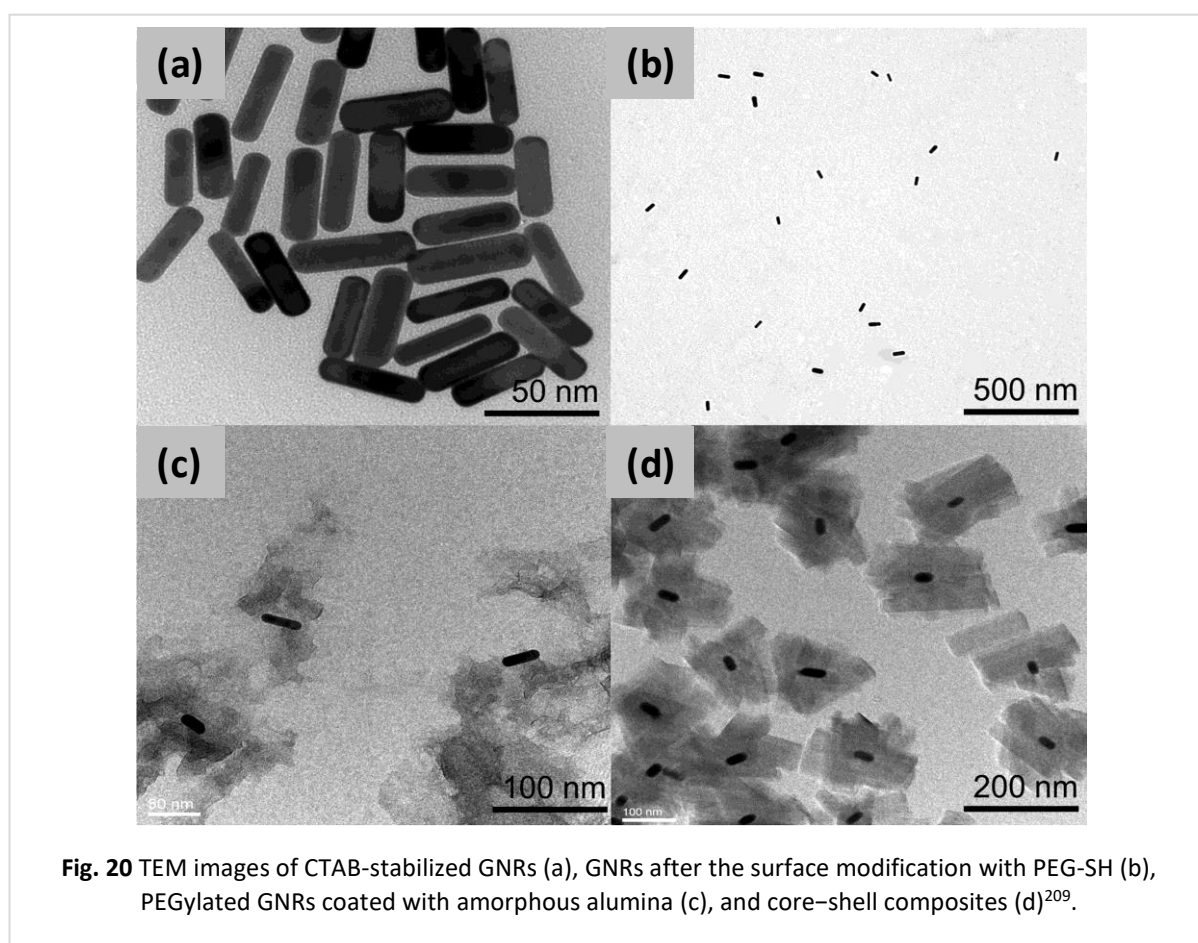
Fischer et al. reported the first example of making MOF@iNPs applying the infiltration method. Notably, their work demonstrated that Cu, Pd and Au precursors were infiltrated into activated MOF-5 via chemical vapour deposition and then reduced by H₂ at different temperatures[222]. Another example by Zhou and co-workers was the confining of Pd NPs (<3 nm) in the cages of MIL-101 via infiltration of Pd precursor solution in MOF and reduced in a 10% H₂/Ar flow at 493°K for two hours (Fig. 18). The composite was employed as a catalyst for the domino synthesis of indole in water. With a similar approach, Pd precursor was deposited into MIL-100 (Al) by a chemical-wetting method but instead reduced by NaBH₄[219]. Infiltration was also the first method to pair iNPs into COFs, iNPs such as Pd, Ni₃N and Au, which were embedded into COFs using this process (Fig. 18) [223, 224, 213].



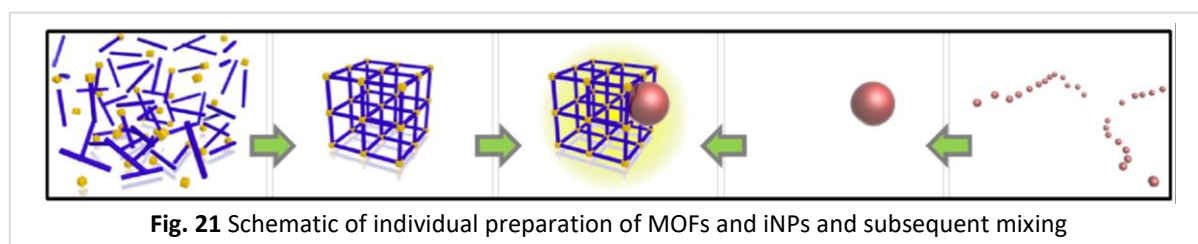
However, the main limitation of this method is that it is significantly challenging to precisely control the location, composition, structure, and morphology of incorporated guests.



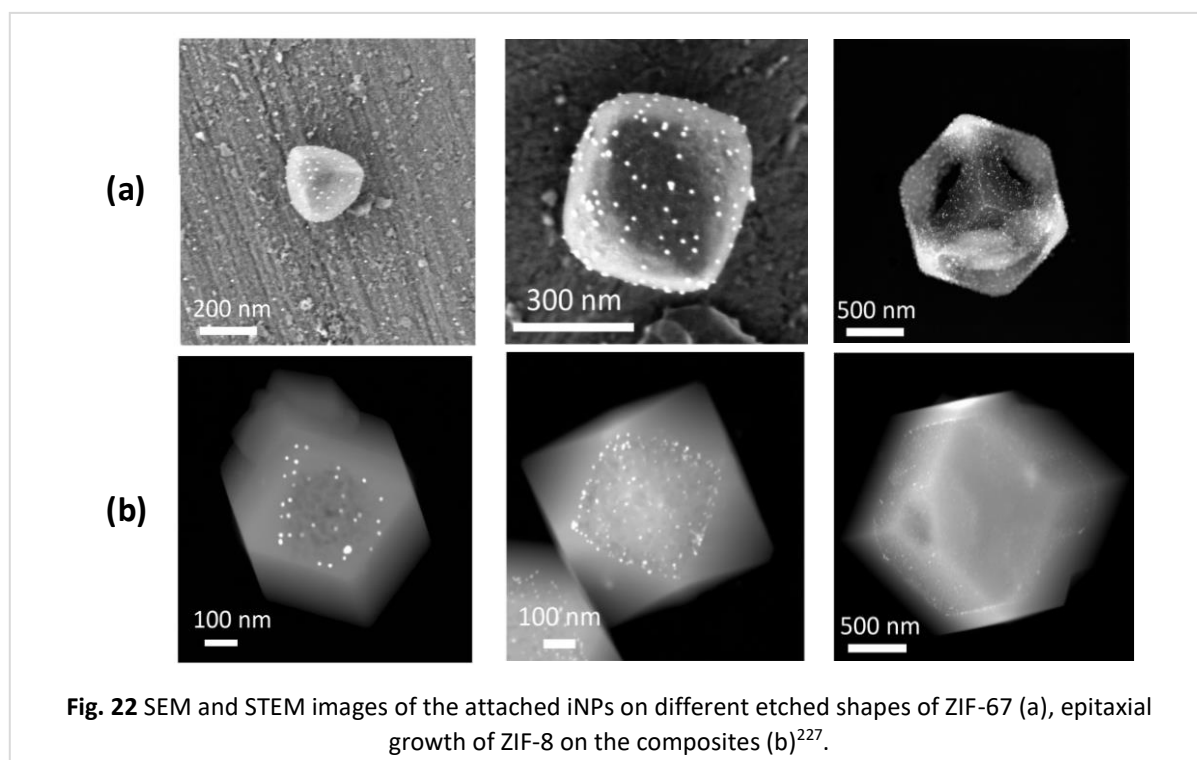
A conceptually different, emerging approach termed pseudomorphic replication relies on the preparation of core-shell inorganic particles, where the core is the ‘functional’ nanoparticles, and the shell is a feedstock material for the inorganic node of the MOF (Fig. 19). Under judiciously controlled conditions, the shell reacts rapidly with the organic precursor ligands to grow the MOF network around the core nanoparticles.[225] For example, gold nanorods (GNRs) were coated with amorphous alumina in a suspension of nanoparticles. Then, the formation of core-shell composites was performed in the microwave reactor, which converted the surface of the GNRs into Al-based MOF (Fig. 20).[209]



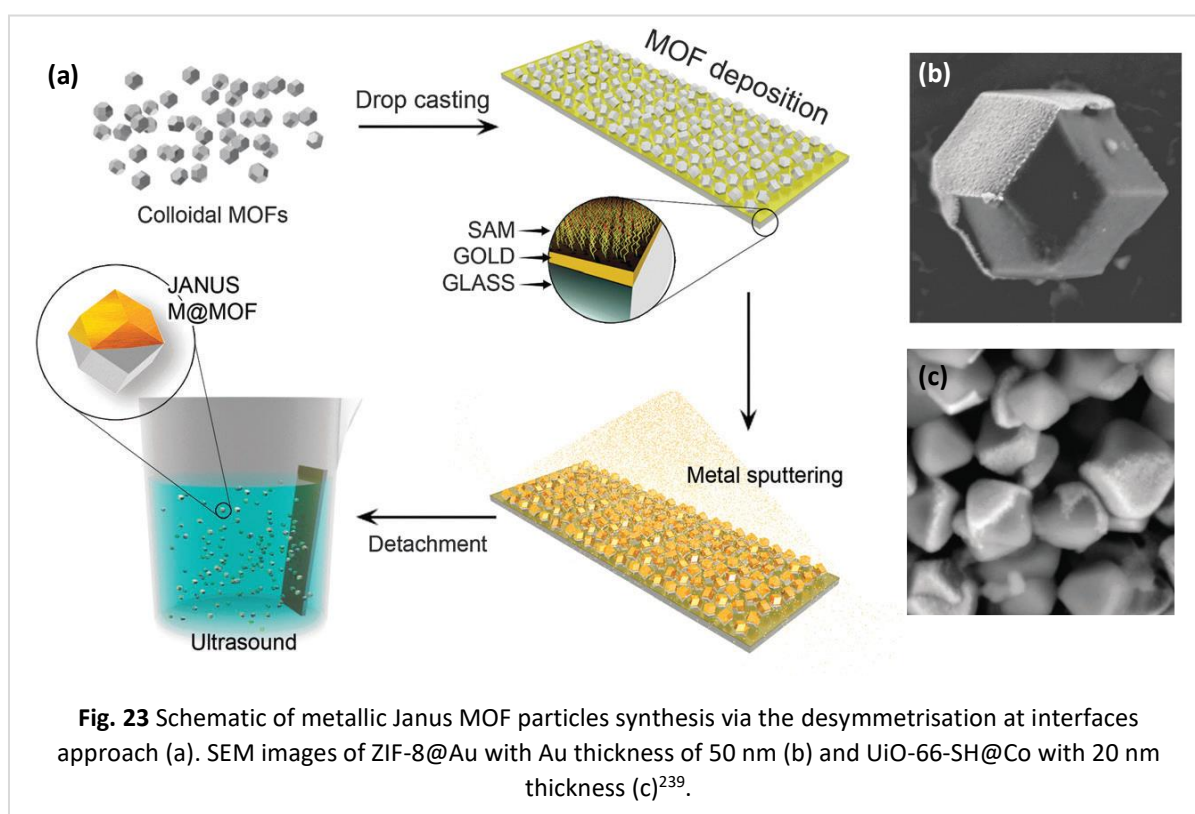
Another strategy is to combine pre-formed MOFs and nanoparticles to form clusters of the two components. The direct interaction between iNPs and the surface of MOFs or COFs is the key factor to help accommodation of iNPs (Fig. 21). The main advantage of using this



method is that both compounds can be synthesized into desirable size, morphology and composition individually and then the attachment can take place without affecting any characteristics of both materials. A pioneering example of this method is the attachment of various PVP (polyvinylpyrrolidone)-capped types of iNPs with different shape and size such as Au (4, 9 and 22 nm), cubic Pd, icosahedra Pd and Cu/Pd on the surface of cubic, tetrahedra and hollow micro box etched ZIF-67 and truncated rhombic dodecahedral ZIF-8. This attachment, coupled with the ZIF-on-ZIF growth, affords layered ZIF-on-iNP-on-ZIF composites. This latter process was repeated to construct (multi)-layered composites composed of several types of iNPs. In these composites, the different iNPs were well separated by a nanometric layer of ZIF-8 that could be as small as 20 nm (Fig. 22)[226].



In a similar study, CTAB (cetyl trimethylammonium bromide)-capped Au and Ag NPs were attached on the surface of the rhombic dodecahedron and cubic ZIF-8, subsequently another layer of ZIF-8 was epitaxially grown. The thickness of ZIF-8 layer could be controlled by varying the initial amount of core suspension, or the amount of CTAB added during the second reaction process[227]. Additionally, Ayala et al. developed a new approach for attachment of functional metals based on direct evaporation of metals such as Au, Co and Pt on the surface of colloidal ZIF-8, UiO-66 or UiO-66-SH that were pre-immobilized onto planar gold surfaces (Fig. 23)[228]. There are numerous examples of this kind of iNPs attachment on the surface of the MOFs in the literature; for instance, cases where iNPs such as Pd, Pt and Fe₃O₄ were attached to the outer surfaces of MIL-101[229, 230].



Alternatively, because the mild synthetic conditions typically used to synthesize MOFs and COFs do not affect the chemical composition, structure, and morphology of most metal or metal oxide NPs, a ‘one-pot’ approach can be applied which generally involves two steps. Firstly, the functional iNPs are synthesized individually and often stabilized by capping agents or surfactants such as PVP or CTAB. Subsequently, the pre-synthesized iNPs are added into a

synthetic solution containing MOF or COF precursors to assemble them. The nanoscale objects do not occupy the pore space of the MOF and COF, but conversely, are surrounded by grown materials[231, 203]. In the resulting composite, MOF and COF encapsulate the functional nanoparticles with different shapes and compositions (Fig. 24).

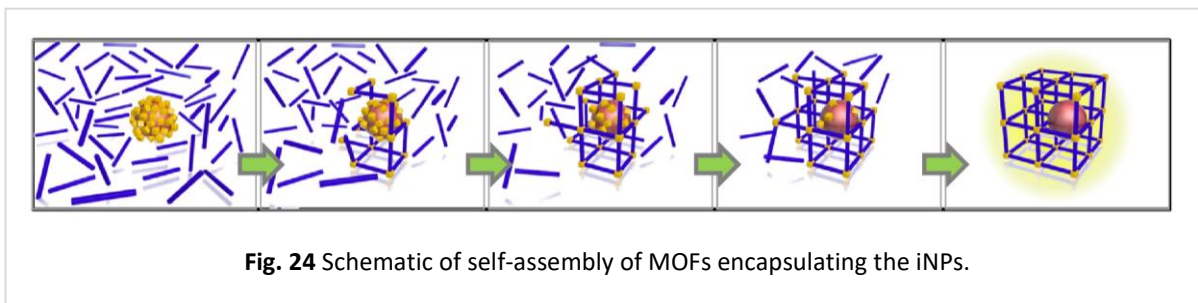


Fig. 24 Schematic of self-assembly of MOFs encapsulating the iNPs.

The most common methodology that has been reported to produce composites with this strategy is solvo/hydrothermal strategy. The first example of this method was reported by Hou and co-workers, in which, through surface modification with surfactant PVP, nanoparticles (Au, Ag, Fe₃O₄, CdTe, NaYF₄ and β-FeOOH) of various sizes, shapes and compositions were encapsulated in a well-dispersed fashion in ZIF-8 crystals, themselves formed by assembling identical amount of zinc ions with imidazolate ligands in methanol at room temperature. Additionally, this method enabled the incorporation of multiple

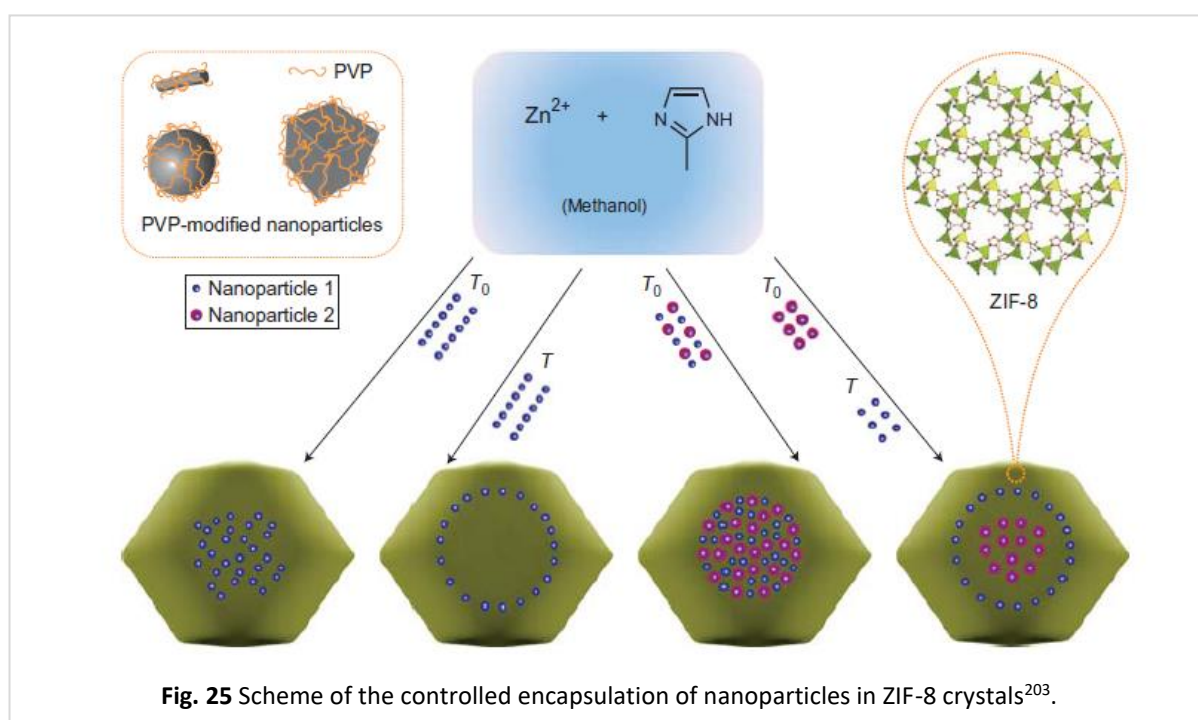
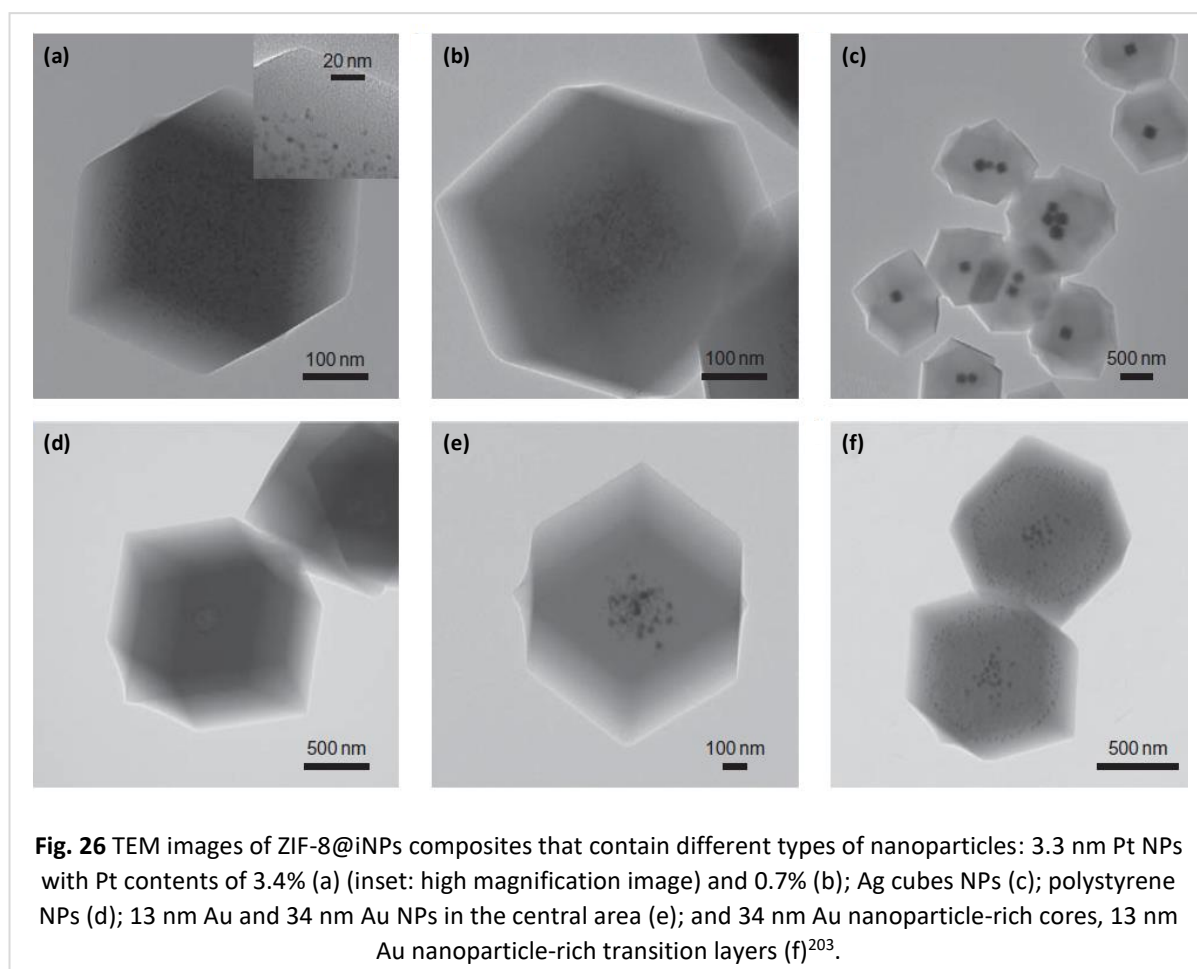


Fig. 25 Scheme of the controlled encapsulation of nanoparticles in ZIF-8 crystals²⁰³.

nanoparticles with controllable spatial distribution by tuning the addition time of iNPs during the MOF synthesis [203](Fig. 25 and 26).



Another alternative strategy to control the positions of the encapsulated iNPs inside the ZIF-8 crystals is by adjusting the PVP concentration in the growth solution. The size of the Au NP core becomes larger as the PVP concentration increases, but the MOF crystal size stays constant (Fig 27a)[232]. In order to change the crystal size of ZIF-8, the methanolic concentration of 2-methyl-imidazole and Zn^{2+} has to be modified in the encapsulation process[233]. Furthermore, iNPs can individually be encased into a single crystal of ZIF-8 with the assistance of self-assembling CTAB molecules or modifying the synthesis conditions, such as time, temperature and the concentration of the precursors[234, 235] (Fig. 27b,c).

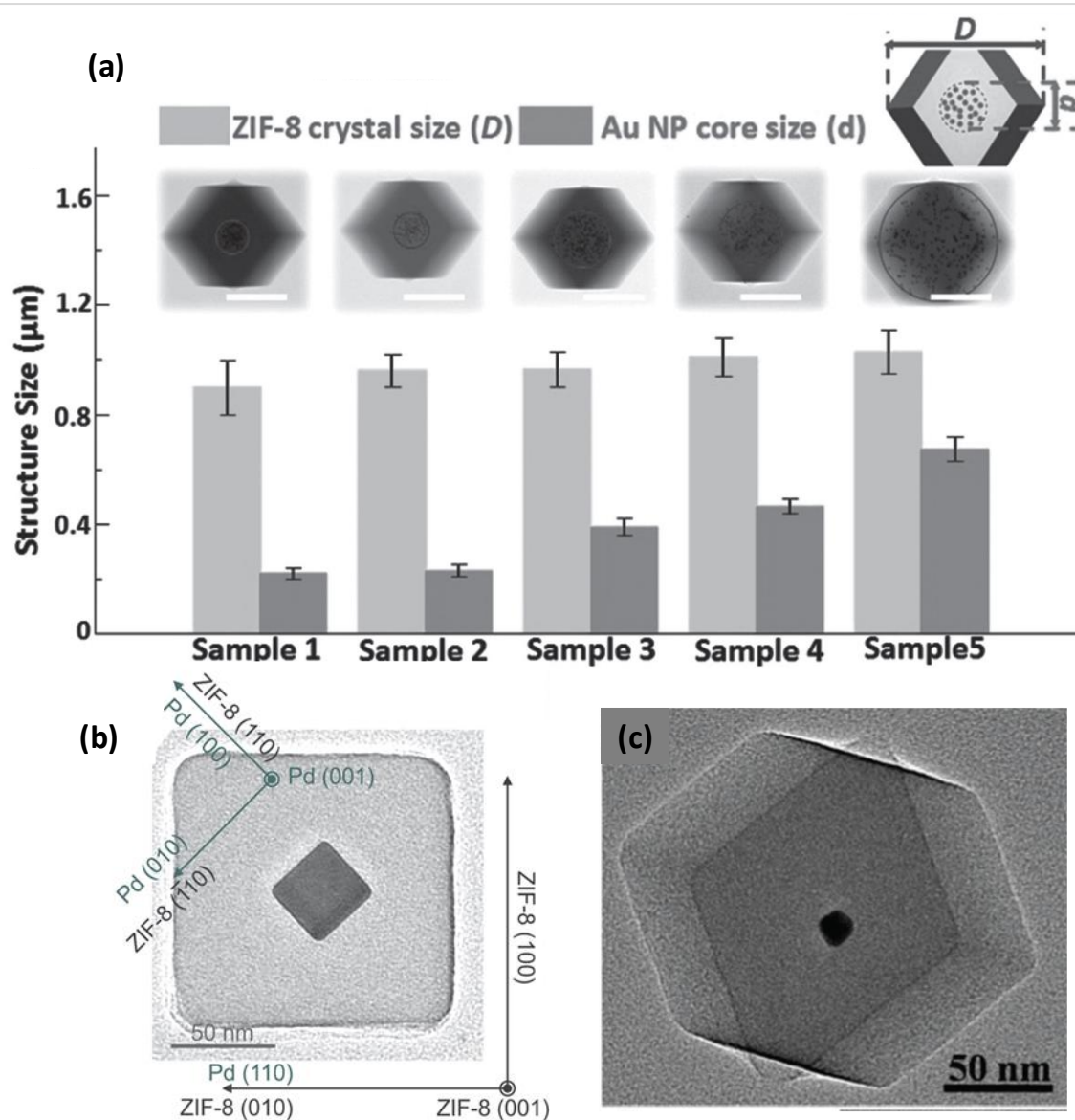
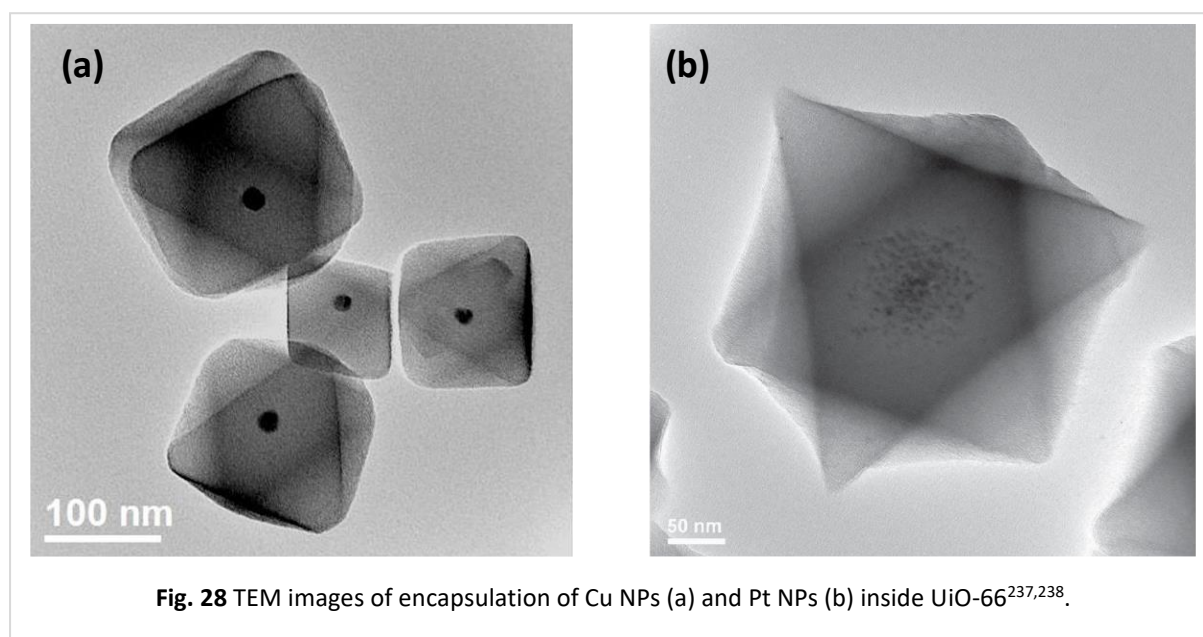


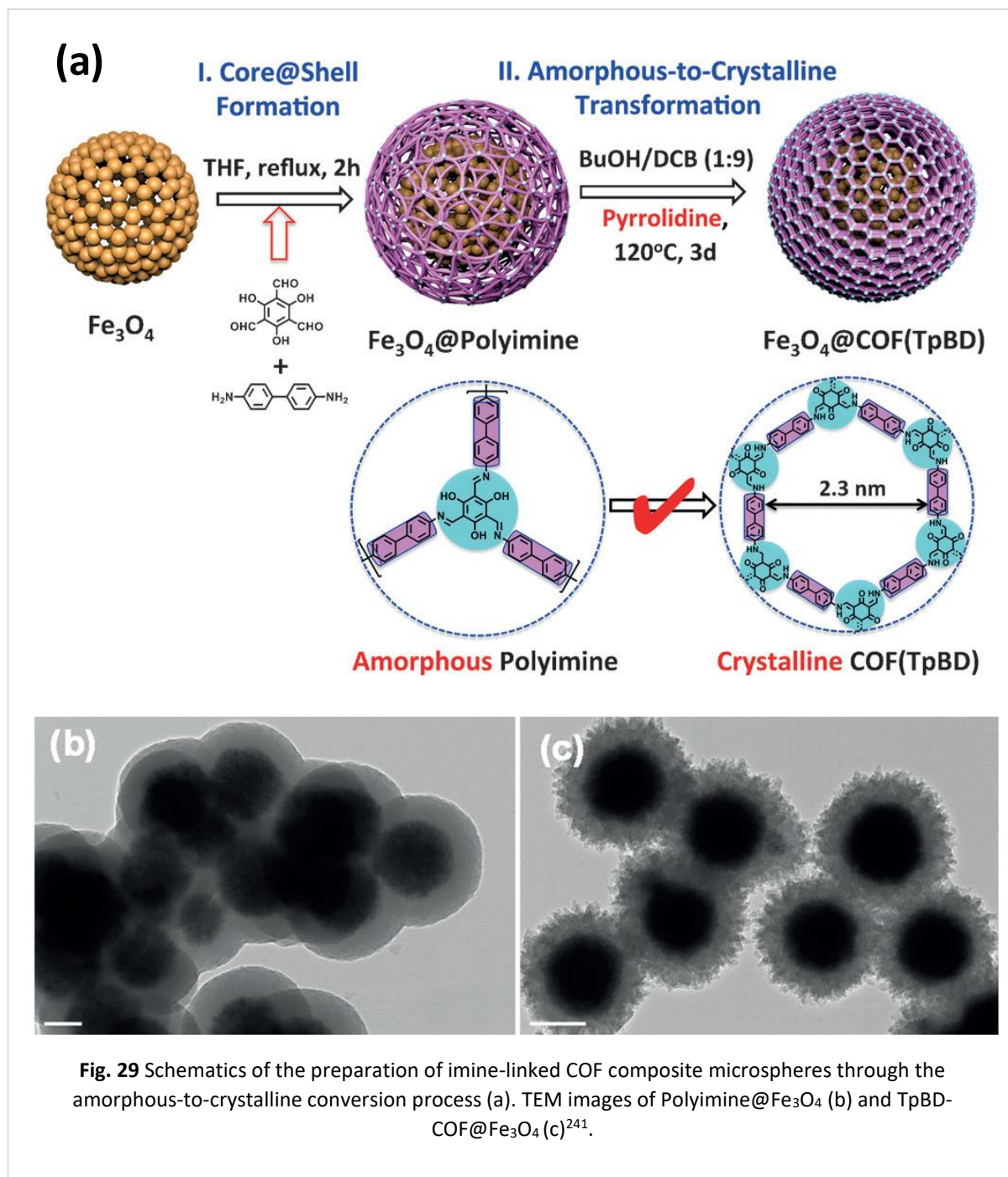
Fig. 27 The distribution of the Au NPs in ZIF-8 can be tuned by the PVP concentration. The PVP concentration in the growth solutions were adjusted to 10^{-5} (sample 1), 5×10^{-4} (sample 2), 2×10^{-3} (sample 3), 10^{-3} (sample 4), and 2×10^{-2} (sample 5) wt% (a)²³³. TEM images of individual cubic Pd NP encapsulated in cubic ZIF-8 (b)²³⁵ and individual Au NP encapsulated in ZIF-8 (c)²³⁶.

This method was further developed using a hydrothermal synthetic approach to incorporate iNPs into MOFs with carboxylic acid-based ligands such as UiO-66, NH_3 -UiO-66, and NH_3 -MIL-53[236] (Fig. 28). At first, the encapsulation of iNPs inside these types of MOFs was limited to Pd and Pt NPs, due to the grating synthetic conditions. In the case of UiO-66, a common Zr source to produce this MOF are ZrCl_4 and $\text{ZrOCl}_2 \cdot 8\text{H}_2\text{O}$, which are highly acidic.

By dissolving it in an organic solvent such as dimethylformamide (DMF) at the high temperatures (120-180°C) (that are required to synthesize UiO-66), makes it unbearable for NPs such as Au, Ag and Cu to survive these encapsulation conditions. Thus, an alternative synthetic condition was developed by using other Zr sources like $Zr(OPr^n)_4$. Somorjai et al. were able to encapsulate Cu NPs into UiO-66 network applying this method[237] (Fig 28).

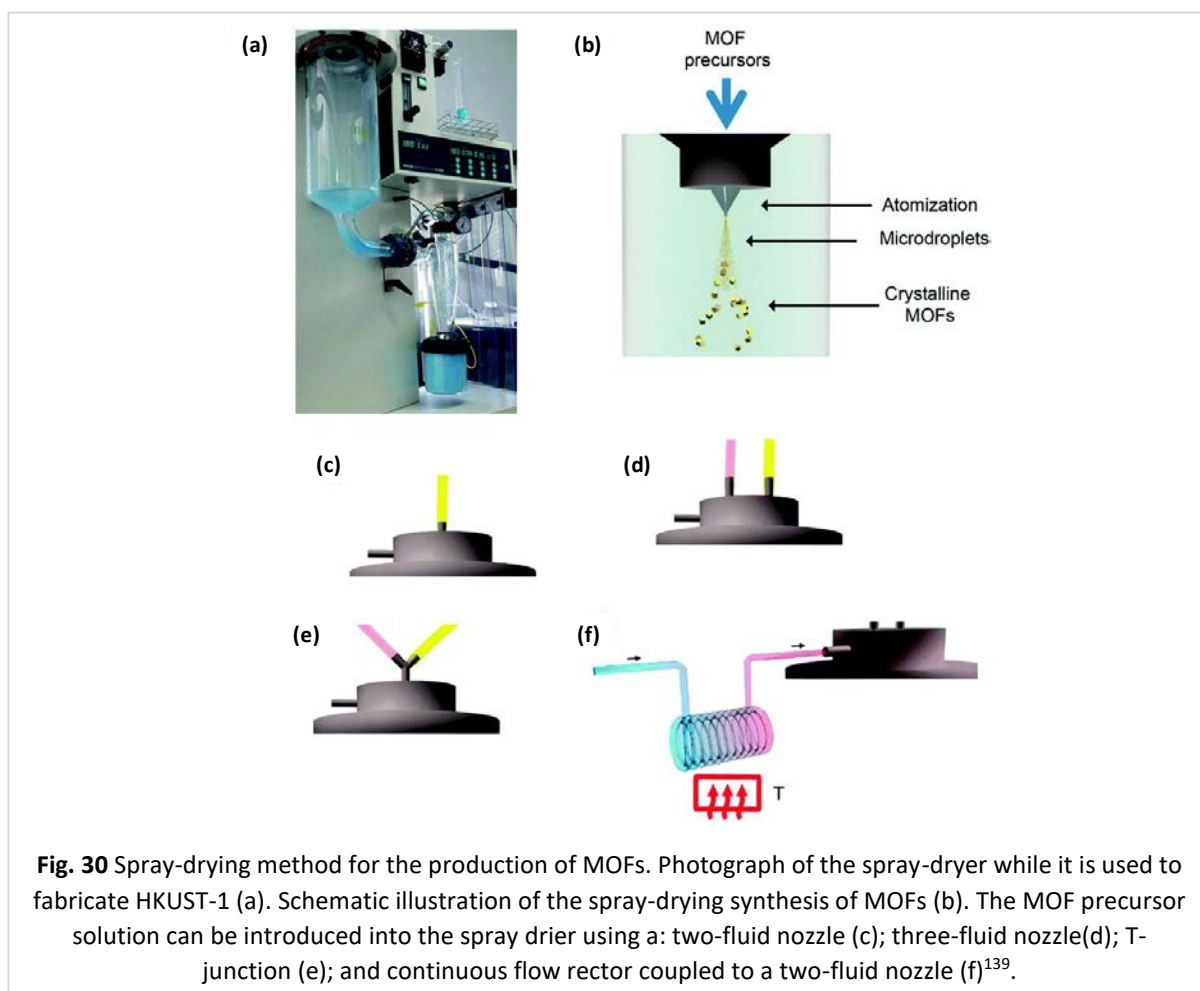


Pairing iNPs with this encapsulation method can be extended from MOFs, to other types of material such as COFs; where they can heterogeneously nucleate and grow around the outer surfaces of some nanosized objects and form a core-shell structure. Nanomaterials such as carbon nanotube[238], ZnO nanorods[239] and Fe_3O_4 [212] were incorporated into different types of COFs. The incorporation of the merits of COFs and magnetic NPs to construct a novel class of nanocomposites with both enhanced functionality and magnetic separability is of significant interest. Wang et al. presented an approach to encapsulate Fe_3O_4 clusters into an amorphous organic polyimine network. This shell was created through the template-controlled precipitation polymerization of benzidine (BD) and 1,3,5-triformylphloroglucinol (Tp) by the Schiff-base reaction. Consequently, the organic polyimine shell was transformed into imine-linked COFs under the certain thermodynamic condition to form a core-shell magnetic TpBD-COF@ Fe_3O_4 (Fig. 29)[240]. It was with a similar approach that, smaller nanoparticles such as Au and Pd were encapsulated in 2D crystalline COF[241].



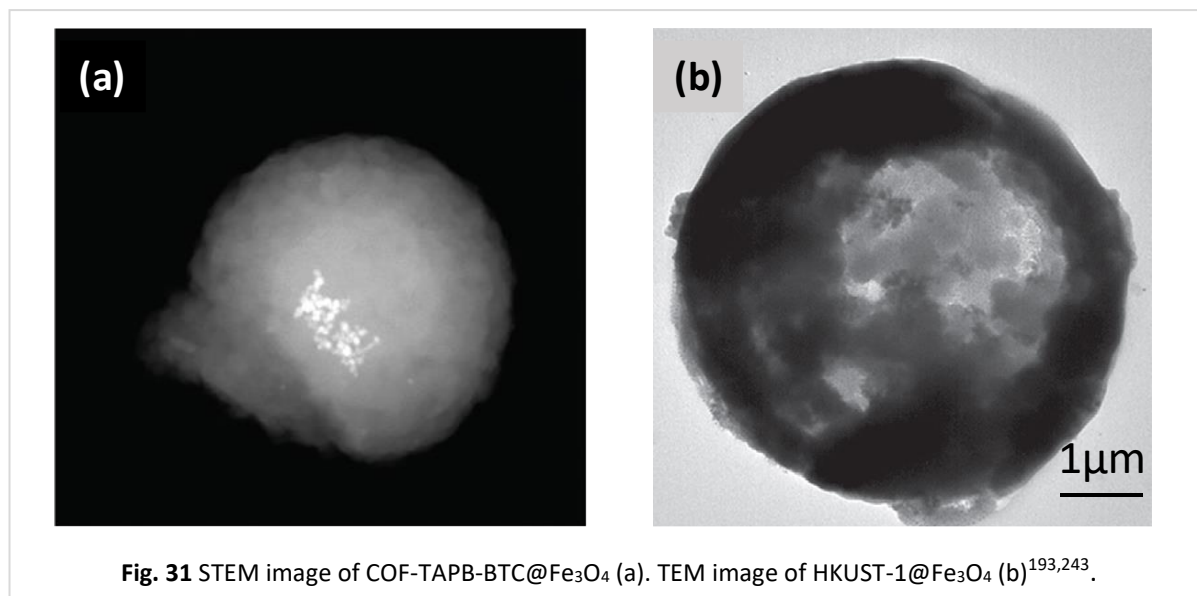
The fundamental limitation of the solvo/hydrothermal method for encapsulation of iNPs in MOFs are time and energy consumption. Its application for large scale composite production is not feasible, as MOF synthesis relies on the nucleation at a reactor vessel surface. Up-scaling the reactor vessel significantly decreases the surface-to-volume ratio and consequently, reduces the efficiency of the reaction. One of the principal objectives of this PhD Thesis is to develop a new method that allows the simultaneous synthesis and shaping of MOF, while encapsulating the pre-synthesized NPs in a fast and continuous one-step

process. In 2013, a spray-drying technique was developed that can be exploited as a general method for the continuous synthesis and self-assembly of MOFs. Initially, this methodology facilitated the scale-up of production levels up to kilograms for HKUST-1 and related paddle-wheel Cu(II)-based MOFs[242]. The key step in this process is based on the fast drying of atomized microdroplets of a solution that contains the MOF precursors (Fig 30). Thus, the process initiates with the atomization of a solution of the MOF precursors into a spray of microdroplets. This step is accomplished by simultaneously injecting one or more solutions and evaporating the solvent by heated gas; in order to induce the MOF precursors to react, forming MOF nanoparticles which accumulate and merge into spherical MOF superstructures/beads[139]. An additional method for introducing the MOF precursors inside the spray drier instrument is to use multi-fluid nozzles, to independently atomize the solutions containing the MOF precursors which allowed to produce ZIF-8 and M-XF6 based MOFs such as SIFSIX family[243].



Finally, this method was extended by introducing a continuous-flow reactor at the entrance of the spray dryer, enabling the production of MOFs assembled from high-nuclearity second-building units such as UiO family[244].

The spray-dryer method is a low-cost, rapid and scalable continuous way to produce MOFs[139] in comparison to the solvo/hydrothermal encapsulation method, which has a very low time yield (reaction times are in the range of 12-48 hours with unsatisfactory yield). In addition, this can be a preferred technique to produce composites made of MOFs or COFs and iNPs. For instance, magnetic Fe_3O_4 NPs were encapsulated into hollow superstructures of HKUST-1[242] and COF-TAPB-BTC[193] via this methodology (Fig. 31).



1.7 MOF@iNPs for Gas Storage and Separation

MOFs have been thoroughly investigated for their application to the storage and separation of number of gases, including hydrogen, carbon dioxide, and methane.[245-247] To improve the relatively weak physisorption forces, researchers have applied their efforts to tuning pore sizes, modifying pore chemistry and generating coordinatively unsaturated metal sites.[248, 215] In addition, combining iNPs with MOFs has shown promise in increasing the interactions with adsorbates that typically have extremely weak interactions with the pore surfaces such as hydrogen and noble gases. Here we demonstrate examples where the introduction of nanoparticles into MOFs has been successfully employed to enhance gas adsorption and separation (Fig. 32).

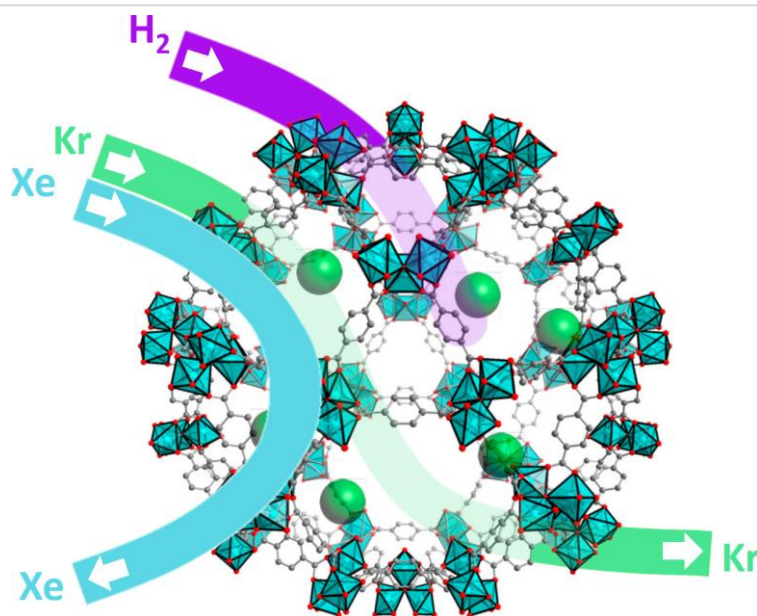


Fig. 32 Schematic illustration of MOFs@iNPs for gas adsorption (H₂) and gas separation (Kr and Xe).

Alternative energy sources are in high demand, given the topical concerns of climate change, energy security and pollution. One such alternative is hydrogen gas, as it can be produced from domestic resources and powering fuel cells and, in turn, zero-emission energy generators[249]. Despite the advantages of hydrogen as a fuel source, there are concerns over safe storage methods at high pressures, primarily for automotive applications. Some strategies mitigate this issue; by storing hydrogen within porous frameworks. Most porous

materials store hydrogen by way of weak van der Waals interactions[250]. However, transition metals can adsorb hydrogen via a metallic bonding and dissociation processes, described conceptually in Figure 33a. The combination of high surface areas and enhanced adsorption enthalpy to a metal surface suggests that MOF@iNP composites are promising materials for hydrogen storage.

An early example of MOF@iNP composites for hydrogen storage was reported by Yang and Li, who demonstrated that a physical mixture of MOF and Pt supported active carbon significantly enhances hydrogen uptake capacity at room temperature[251]. Remarkably, the increase in adsorption did not follow the weighted average of MOF and Pt/C. The observed enhancement was attributed to the so-called ‘hydrogen spillover’ effect (Fig. 33b), where hydrogen molecules dissociate at the metal cluster, then move to the carbon support and subsequently to the organic components of the MOF[252]. This effect has been demonstrated in some MOF@iNP composites [253-257].

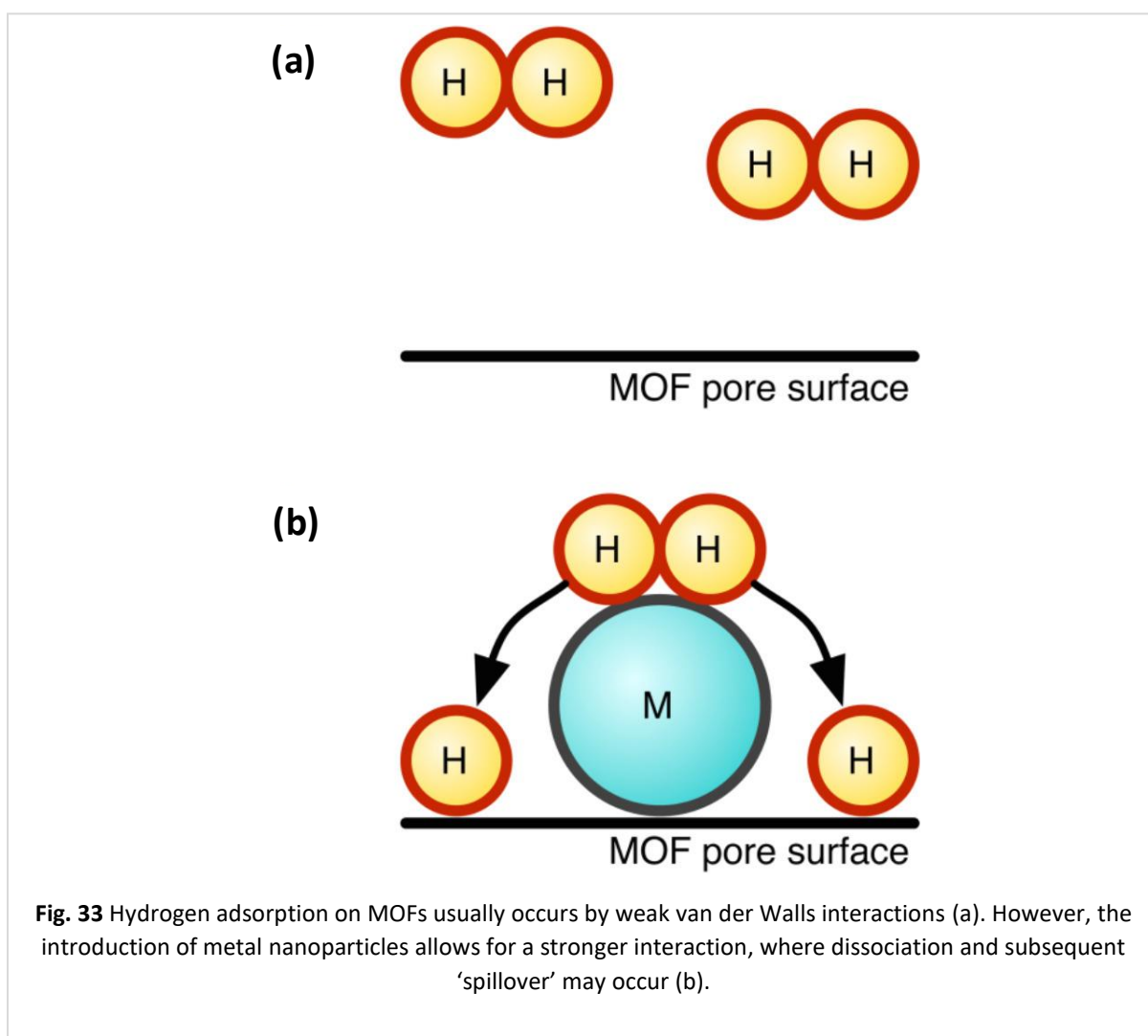


Fig. 33 Hydrogen adsorption on MOFs usually occurs by weak van der Waals interactions (a). However, the introduction of metal nanoparticles allows for a stronger interaction, where dissociation and subsequent ‘spillover’ may occur (b).

After this study, other works focused on more structurally well-defined MOF@iNPs has also shown auspicious results. For instance, Pd NPs loaded in MOF-5 (1 wt% loading) and SNU-3 (3 wt% loading) demonstrated increased hydrogen adsorption at low pressure and temperature[258, 259]. SNU-3@Pd also showed an increase in hydrogen uptake at room temperature and high pressure compared to SNU-3. However, calculated isosteric heats of adsorption indicated that the SNU-3@Pd possessed a lower enthalpy of adsorption for H₂. This result highlights that the mechanism of action in these materials is still not fully understood comprehensively. Materials with significantly higher Pd content have been described by Latrouche and co-workers, who were able to produce MIL-100(Al) embedded with 10 wt% metallic Pd [219]. These high loadings actuated a decrease in surface area and pore volume, as indicated by nitrogen adsorption experiments. This could be anticipated due to the pore volume consumed by Pd NPs. Consistent with the lower pore volume of these

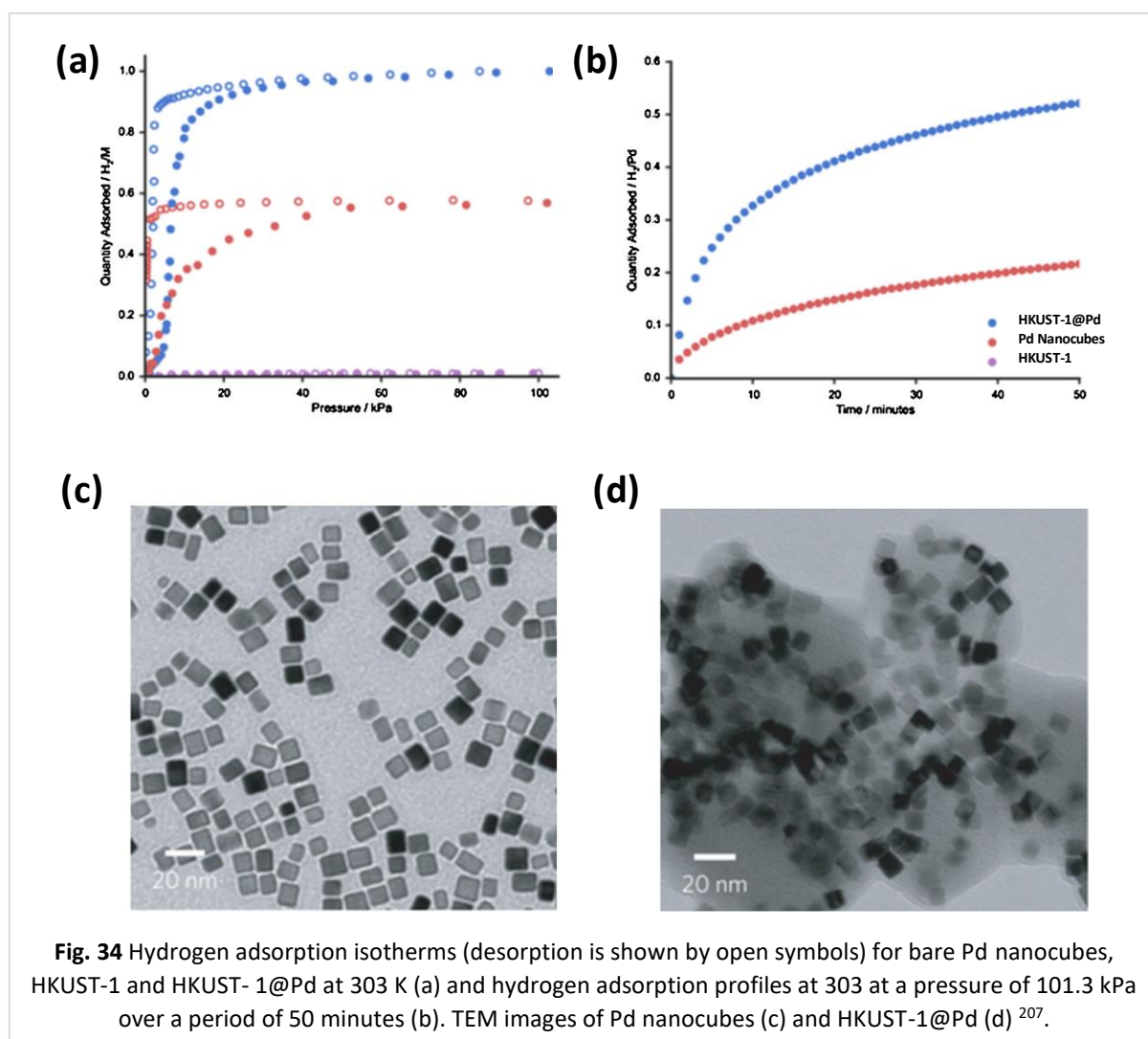
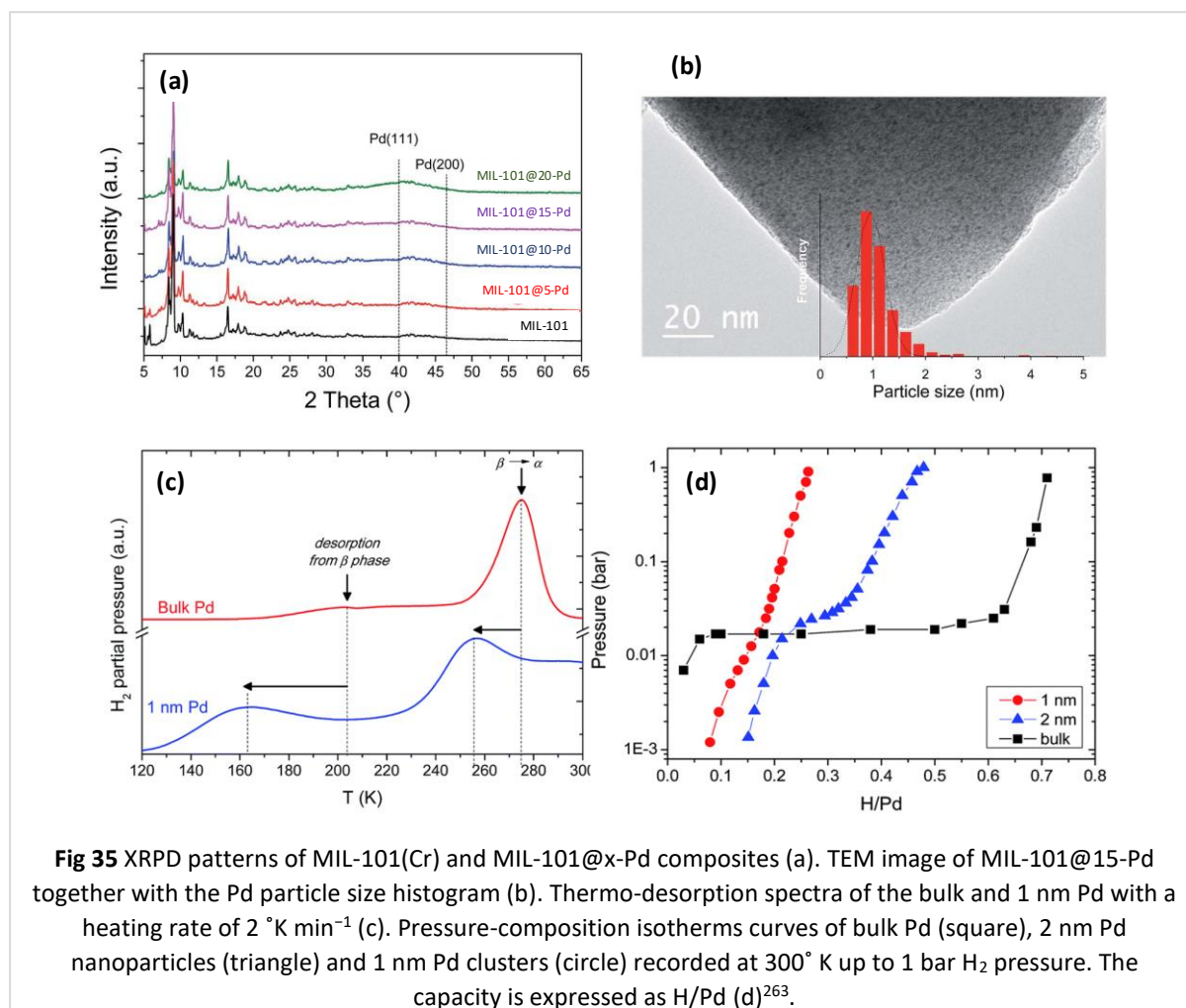


Fig. 34 Hydrogen adsorption isotherms (desorption is shown by open symbols) for bare Pd nanocubes, HKUST-1 and HKUST- 1@Pd at 303 K (a) and hydrogen adsorption profiles at 303 at a pressure of 101.3 kPa over a period of 50 minutes (b). TEM images of Pd nanocubes (c) and HKUST-1@Pd (d) ²⁰⁷.

samples, the 77 K hydrogen capacity of the MIL-100(Al)@Pd samples were less than that of the bare framework. However, the hydrogen uptake capacity at room temperature was significantly improved; 0.35 wt% at room temperature and 4 MPa. These values are approximately double that of MIL-100(Al). Characterization by X-ray diffraction revealed that the high capacity at room temperature is partially explained by the formation of Pd hydride that occurs readily at room temperature. Kitagawa and co-workers have significantly improved hydrogen storage capacity of Pd NPs by employing a MOF coating [207]. Here, samples of Pd nanocrystals were successfully covered in the HKUST-1, leading to a drastic increase in the storage capacity and kinetics of hydrogen adsorption compared to the base Pd nanocubes (Fig. 34). Notably, at elevated temperatures, HKUST-1 shows no appreciable hydrogen adsorption. Further investigations using X-ray photoelectron spectroscopy (XPS) suggested the enhanced hydrogen storage capacity in the composite material is a result of electron transfer from Pd nanocrystals to the HKUST-1 coating. This approach is widely applicable to other MOF@iNP systems and may provide a general method to enhance the reactivity of metal NPs.

Additionally, Pd NPs of 5-9 nm were dispersed in ZIF-8 by infiltration method. The results showed that the hydrogen uptake capacity of ZIF-8@Pd was 30% higher than the pure ZIF-8 at room temperature, and only 3% of this uptake was due to the formation of PdH_{0.18} and the excess, to a cooperative spillover effect.[260] More recently, Huaming Yang and co-workers synthesized a series of Zn and Al MOFs and hybridized them with natural halloysite nanotube (HNTs), and consequently, MOFs were transformed into carbon by carbonization calcination. The hydrogen adsorption capacity of MOF@HNT composites were 0.23 and 0.24 wt% for Zn and Al-based MOF respectively, while those of carbonized product were 0.24 and 0.27wt% at room temperature. Moreover, the hydrogen storage capacity of carbonized Al-MOF@HNT was promoted by incorporating Pd NPs with impregnation method to 0.32 wt% at room temperature. Dissociation was assumed to take place on Pd with spillover effect over to the structure of HNTs, MOF, and carbon products[261]. In a similar experiment, C. Zlotea et al. studied the interaction of 1 nm Pd clusters with hydrogen. Pd clusters showed an unprecedented modification of the hydrogen adsorption/desorption properties compared to bulk and nanoparticles of 2-3 nm. Pd clusters were confined into Cr-MIL-101 by double solvent impregnation method with different loading of 5-20 wt%. These clusters did not form

a hydride phase at room temperature and atmospheric pressure, in contrast with bulk Pd. However, they adsorb hydrogen in the form of solid solutions under these conditions. At lower a temperature, they formed a hydride phase, and the desorption of the clusters had lower activation energy compare to bulk Pd (Fig. 35)[262].



Pt NPs are known to afford powerful interactions with hydrogen. For example, Pt black can absorb and desorb hydrogen at room temperature. However, hydrogen cannot be desorbed from Pt black at room temperature under evacuation [250]. Inspired by the results of Yang and Li's bridged Pt/C and MOF materials[251], Senker et al. were able to synthesize samples of ultra-high surface area MOF-177 loaded with 43 wt% Pt NPs [263]. The resulting composite was reported to adsorb 2.5 wt% of hydrogen at room temperature at 144 bar. This produced to a storage capacity of 62.5 g_{H₂}.L⁻¹, which is close to that of liquid hydrogen at 70 g_{H₂}.L⁻¹. Unfortunately, subsequent cycles showed decreasing capacity which can be explained by passivation of the Pt surface by stable Pt-H moieties.

Overall, research into hydrogen adsorption in these materials highlights the advantages

of combining the strong adsorption potential of metallic NPs and high surface areas of MOFs. However, to progress these findings, more work is required on elucidating the mechanism of action for hydrogen adsorption; specially concerning the observed hydrogen spillover effect[252]. A better understanding of these systems will facilitate the hypothesis-driven design of novel composites for H₂ storage.

In addition, MOFs have attracted considerable interest in the last two decades in CO₂ adsorption, due to their high porosity[147]. CO₂ is a primary anthropogenic greenhouse gas and the foremost perpetrator in global climate change[264]. Thus, it is crucial to develop an efficient technique to rebalance the CO₂ distribution to reduce the greenhouse effect on global warming. One of the most efficient technology for CO₂ capture is physical adsorption. Recently, this unique property of MOFs has been enhanced by combining them with INPs. Kuen-Song Li et al. modified Ni-MOF-74 and Co-MOF-74 with Pd-loaded activated carbon and evaluated the CO₂ adsorption capacity. Pristine Ni-MOF-74 and Co-MOF-74 adsorbed 11.06 and 10.28 mmol.g⁻¹, respectively, at room temperature and 32 bar. Subsequently, these values were enhanced after Pd doping to 12.24 and 11.42 mmol.g⁻¹, and the composites were able to utterly separate CO₂ from the mixture of CO₂/N₂[265]. Furthermore, El-Shall and co-workers developed a practical and straightforward approach based on microwave irradiation for the incorporation of Pd nanoparticle catalyst within Ce-MOF. The Pd/Ce-MOF was capable of CO oxidation at a relatively low temperature (96° C), and also the composite showed an efficient uptake of the product (CO₂ gas) at 0 °C[266].

Gas separation is one of the most critical and challenging steps for industrial processes, and there are significant advances in using MOFs for this application[267]. However, the separation of noble gases such as Kr and Xe remains a challenging process. Molecular separation of Kr and Xe is essential as reprocessing nuclear fuel requires the removal of radioactive Kr from Xe in the off-gas [268]. Currently, separation of these gases is achieved by cryogenic distillation. This process is extremely energy intense, owing to the low boiling points of Kr and Xe at -153 °C and -108 °C, respectively. Similar to hydrogen, noble gases interact very weakly with the surfaces of porous materials. This has motivated researchers to use metallic NPs as a strategy towards enhancing uptake capacity. Goose and co-workers reported that Ag clusters in X- and Y-type zeolites instigated to a higher uptake of Xe, when compared to the original sodium ion containing zeolites, and was dependent on Ag

loading[269]. Subsequently, Thallpapally et al. were able to produce Ag NPs in Ni-MOF-74 with up to 6.59 wt% Ag [270]. The Xe and Kr adsorption of these materials showed the Xe capacity at 1 bar and room temperature was increased by 15.6% when compared to the bare framework (Fig. 36). Importantly, the introduction of Ag NPs to Ni-MOF-74 did not significantly increase the Kr capacity, as it is less polarizable than Xe. Accordingly, the adsorption selectivity (calculated from the pure gas isotherms and a 50:50 mixture) was double that of the achieved benchmark activated carbon. These encouraging results suggest that MOF@iNP composites should be further investigated for their potential application to noble gas separations.

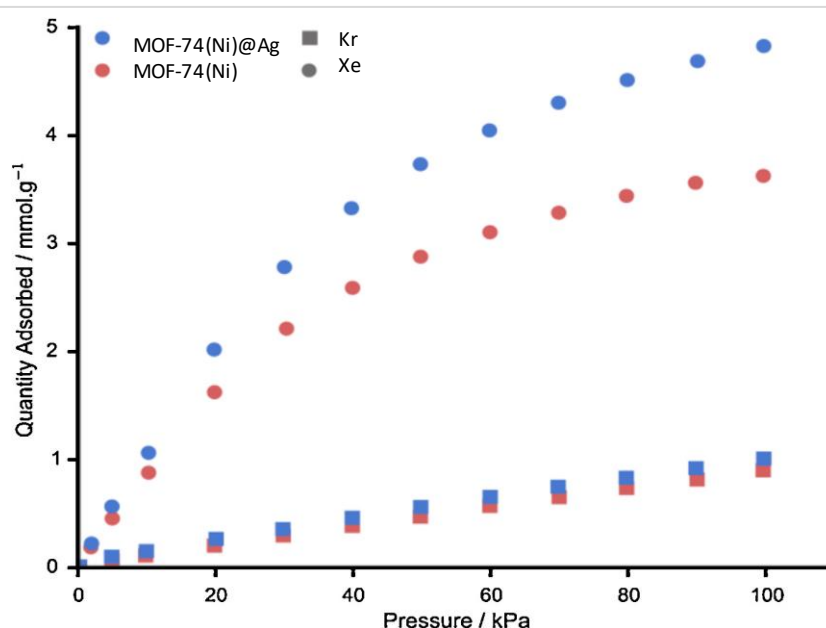
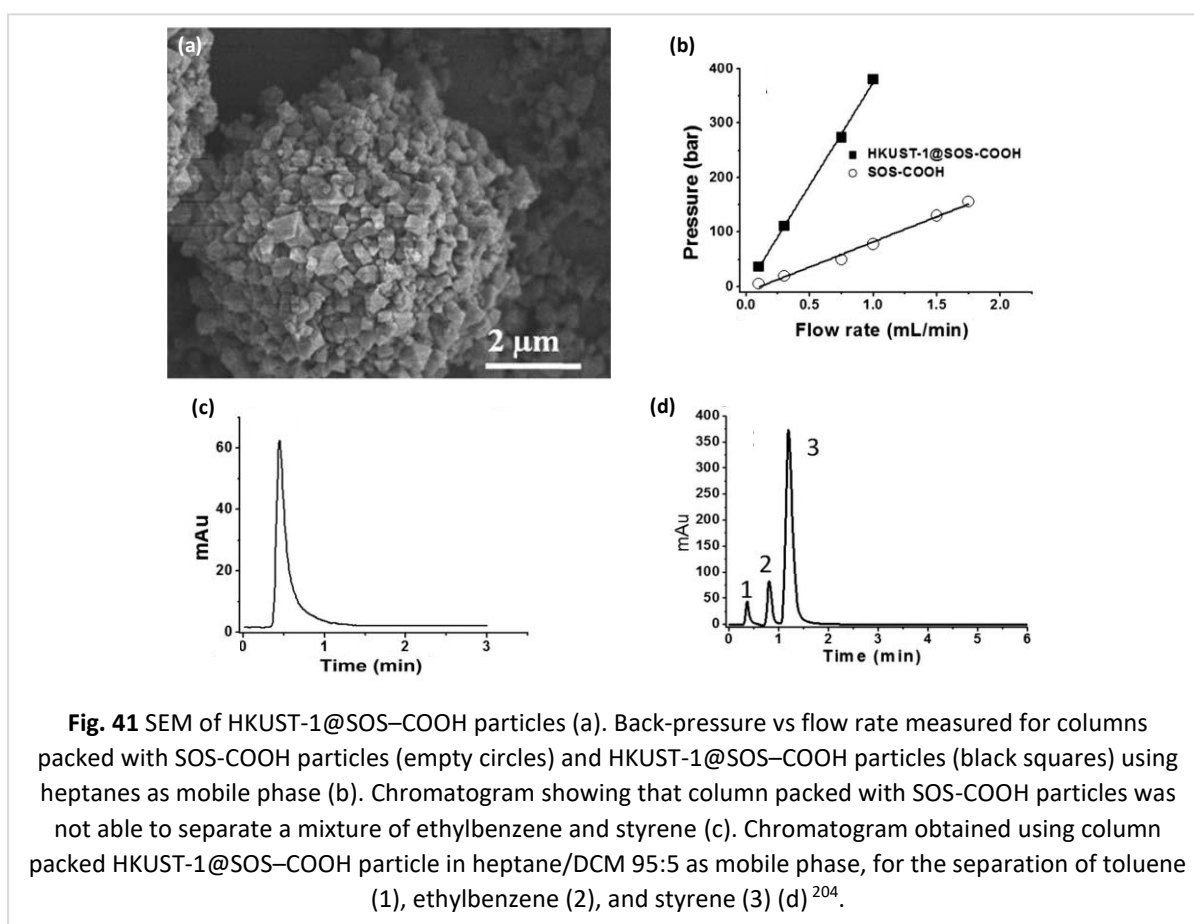


Fig. 36 Xe and Kr isotherms for bare MOF-74(Ni) and a sample of MOF-74(Ni)@Ag loaded with 1.47 wt% Ag²⁷¹.

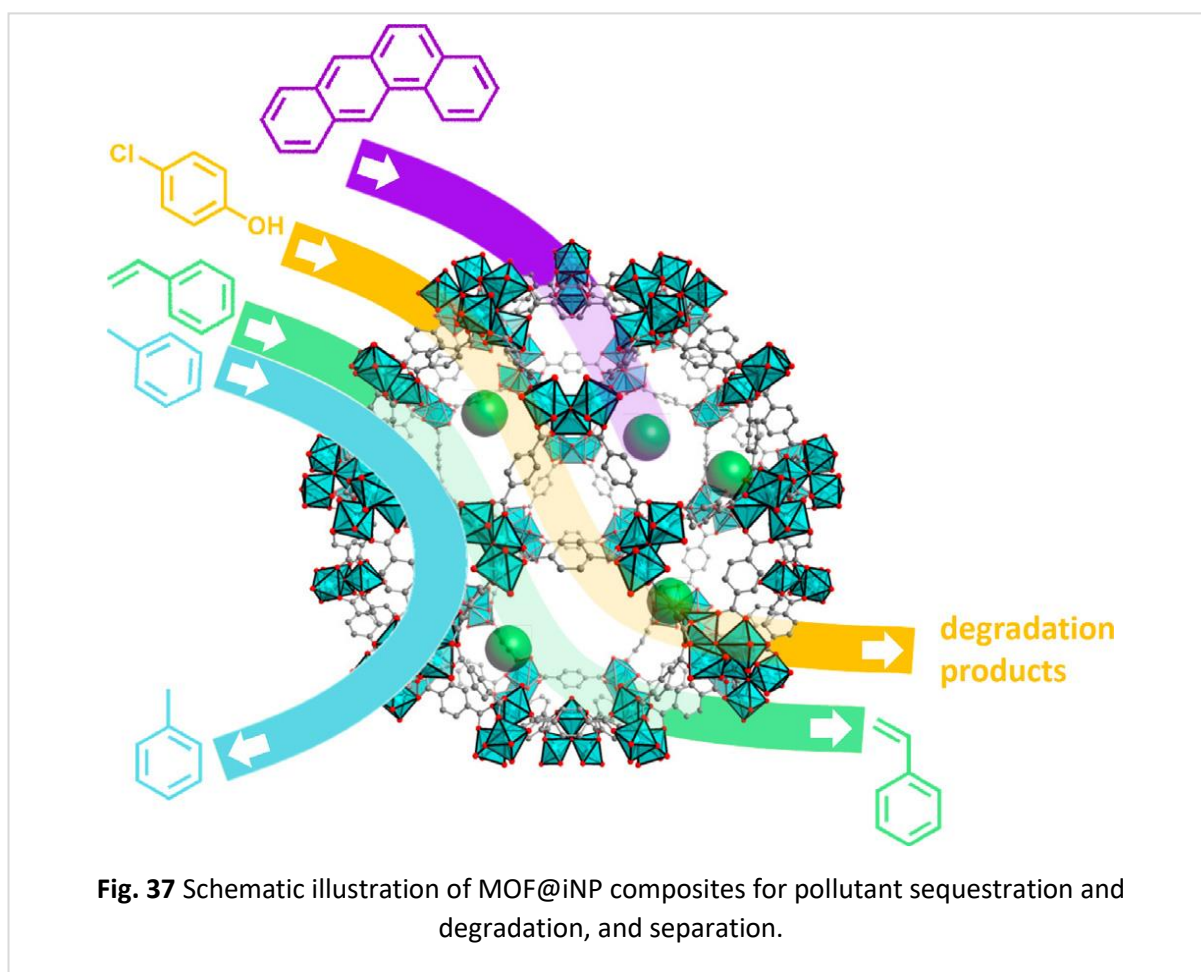
Furthermore, due to their crystalline structure and high porosity, MOFs have recently emerged as candidates for analytical and chromatographic separations[271]. Separation by adsorption is more energy-efficient than distillation, but to date, limited examples with acceptable selectivity have been reported[272]. Silica is the most common stationary phase used in normal phase chromatography and therefore, a natural step forward is to combine silica and MOFs to achieve better performances. Bradshaw's group[204] introduced a sphere-on-sphere (SOS) technique to immobilize small engineered 200 nm silica nanospheres on 5.5 μm silica microspheres. The SOS system with carboxylic groups acted as a scaffold for the

subsequent growth of HKUST-1 crystals, and the obtained HKUST-1@SOS-COOH composite (Fig. 41ab) was packed with high-performance liquid chromatography (HPLC) column. The results indicated that the composite was able to separate a mixture of toluene, ethylbenzene and styrene using heptanes/dichloromethane 95:5, whereas the neat SOS-COOH showed no separation properties (Fig 41cd). Moreover, the same composite was used, after dichloromethane or toluene pre-conditioning for 24 h, to successfully separate xylene isomers using heptane as the mobile phase. Silvestre et al. used layer-by-layer epitaxy to grow HKUST-1 on magnetic silica nanocubes, producing a magnetic framework composite with high surface area ($1150 \text{ m}^2 \text{ g}^{-1}$) after 200 coating cycles[273]. The obtained material was used for HPLC chromatography, showing an appreciable, although incomplete separation of toluene and pyridine. In both cases, the presence of MOFs was found important to enhance, and in some case achieve optimal separation performance.



1.8 MOF@iNPs for Sequestration

The high and tunable porosity of MOFs eases the penetration, accumulation, and separation of various species, not only from gas but also from the liquid phase. Nanoparticles embedded inside MOF structures can impart additional functionalities. For instance, enabling the recollection using a magnetic field of the MOF used as a sorbent for pollutants, using the photocatalytic properties for their degradation, or acting support that facilitates the separation of organic compounds (Fig. 37).



MOFs have shown great potential for the removal of carcinogenic polycyclic aromatic hydrocarbons (PAHs), heavy metals, pesticides, dyes, radionuclides, and other toxic chemicals[274-282]. Introducing additional functionality via magnetic NPs can be achieved by synthesizing magnetic framework composites (MFCs)[283]. There are two main advantages provided by the magnetic particles. Firstly, they facilitate positioning the porous material

using an external magnetic force. This can be applied to simple magnetic recovery in a batch reactor to more precise localization in microfluidic devices. Secondly, magnetic NPs afford a magneto-thermal effect when exposed to an alternate magnetic field which can be exploited to release guests from the pores of the MFCs [284]. We note that the surface area of the MFCs are lower compared to the parent MOF due to the gravimetric contribution of the particles that, under optimized conditions, lies in the range of 3–5 wt% (e.g., 4% using Co NPs[285]). The use of MFCs for the sequestration of polycyclic aromatic hydrocarbons (PAHs) has been reported by Doherty et al. [286] and Huo and Yan[287] in 2012. Yan demonstrated that silica coated magnetic iron oxide and MIL-101(Cr) could be mixed and used for the efficient recovery (81–96%) of six different PAHs from water, whereas Doherty et al. showed that cobalt and nickel ferrites superparamagnetic nanofibers directly embedded into MOF-5 crystals afforded a 1.3 mmol g^{-1} uptake of benz[a]anthracene (Fig. 38a)[286]. Similarly, Carne et al. showed that spherical magnetic framework made of HKUST-1 and iron oxide NPs was used for capturing dibenzothiophene (DBT) from iso-octane with a remarkable extraction capacity of 200 g kg^{-1} (Fig. 38b)[242]. Also, Chen and co-workers[288] investigated using core-

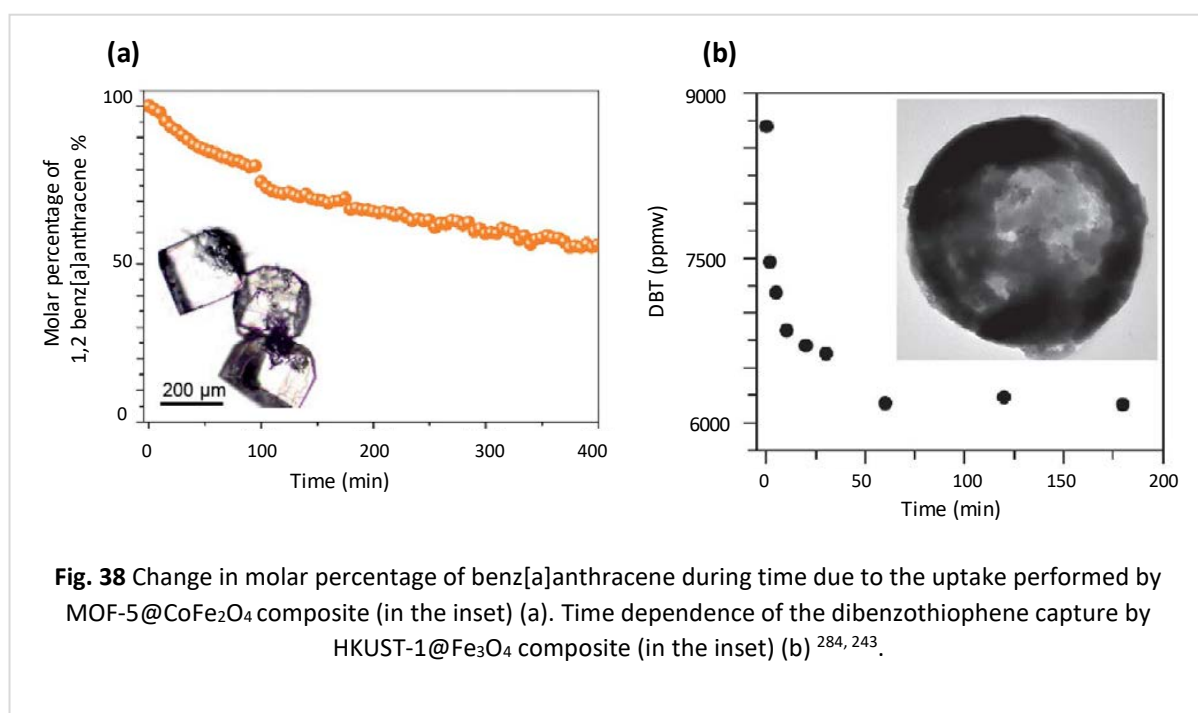


Fig. 38 Change in molar percentage of benz[a]anthracene during time due to the uptake performed by MOF-5@CoFe₂O₄ composite (in the inset) (a). Time dependence of the dibenzothiophene capture by HKUST-1@Fe₃O₄ composite (in the inset) (b) ^{284, 243}.

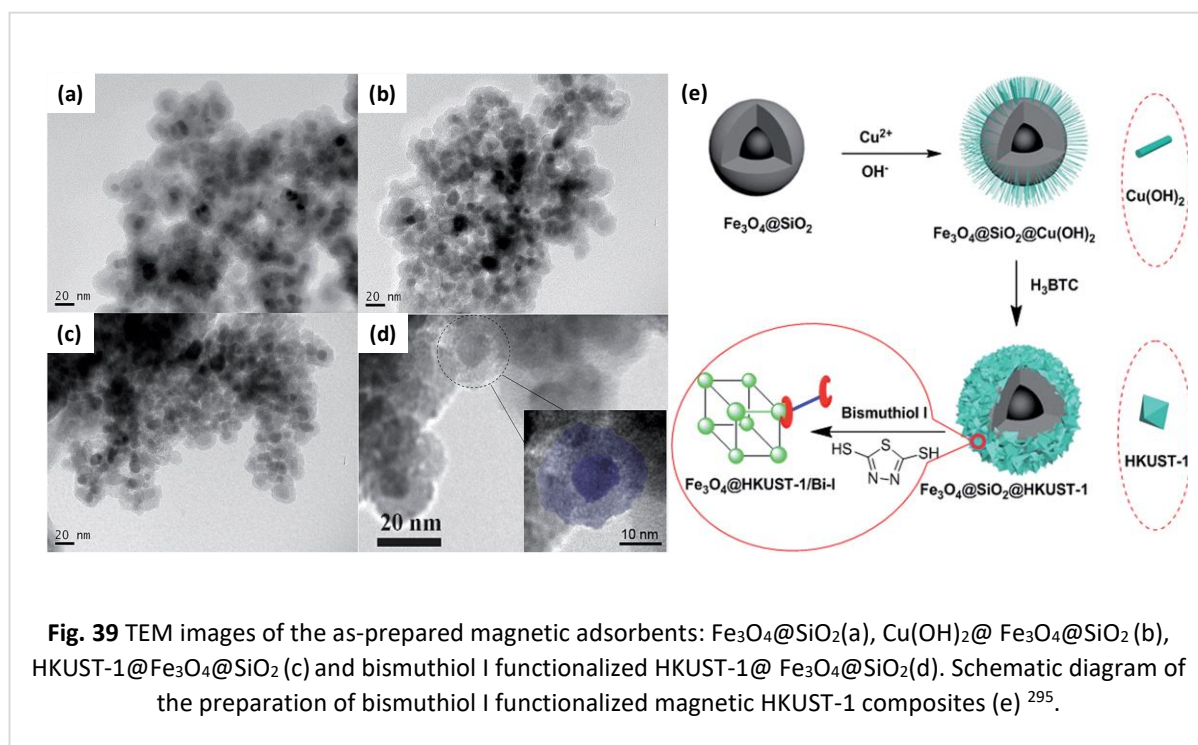
shell magnetic spheres (made with a magnetic iron oxide core and a MIL-100(Fe) MOF shell), towards the sequestration of polychlorinated biphenyls (PCBs) from the water. This MOF composite yielded excellent recovery (above 81%) of the PCB, and it was also being able to

reach a very low limit of detection (down to 1.07 ng L^{-1}), suitable for harvesting trace amounts of pollutant.

A second important application in environmental remediation is related to inorganic pollutants, such as heavy metals[289, 290]. This is due to the environmental and health issues connected with the contamination from, particularly, As, Pb, Hg, Ni, Cr, and Cd. Additionally, the efficient sequestration of certain rare heavy metals such as Ag, Au, Pd, and Pt is of interest due to their high economic value. Examples of MFCs exploited for the collection of dangerous heavy metals have been reported by Sohrabi et al.[291], Wang et al. [292], Taghizadeh et al. [293], and Hu et al.[294]. All of these studies used modified silica-coated, iron oxide NPs embedded into HKUST-1. Sohrabi explored the optimization of Cd(II) and Pb(II) ions uptake using pyridine grafted on the surface of the magnetic particles. Excellent extraction values of ca. 190 mg g^{-1} were reported. Wang et al. chose post-functionalization of HKUST-1@magnetite with dithizone as a strategy for the sequestration of Pb(II) obtaining a modest uptake of 1.67 mg g^{-1} . Based on a very similar system to Sohrabi, Taghizadeh studied the uptake of Cd(II), Pb(II), Ni(II), and Zn(II), reporting sequestration values between 98 (Ni) and 206 (Zn) mg g^{-1} . Hu and co-workers prepared a core-shell nanostructure of bismuthiol I functionalized HKUST-1@Fe₃O₄@SiO₂ through a facile coordination-based post-synthetic strategy (Fig. 39). The resulting magnetic MOF composites were attractive due to their rapid, selective and efficient removal of Hg²⁺ from environmental water samples[294].

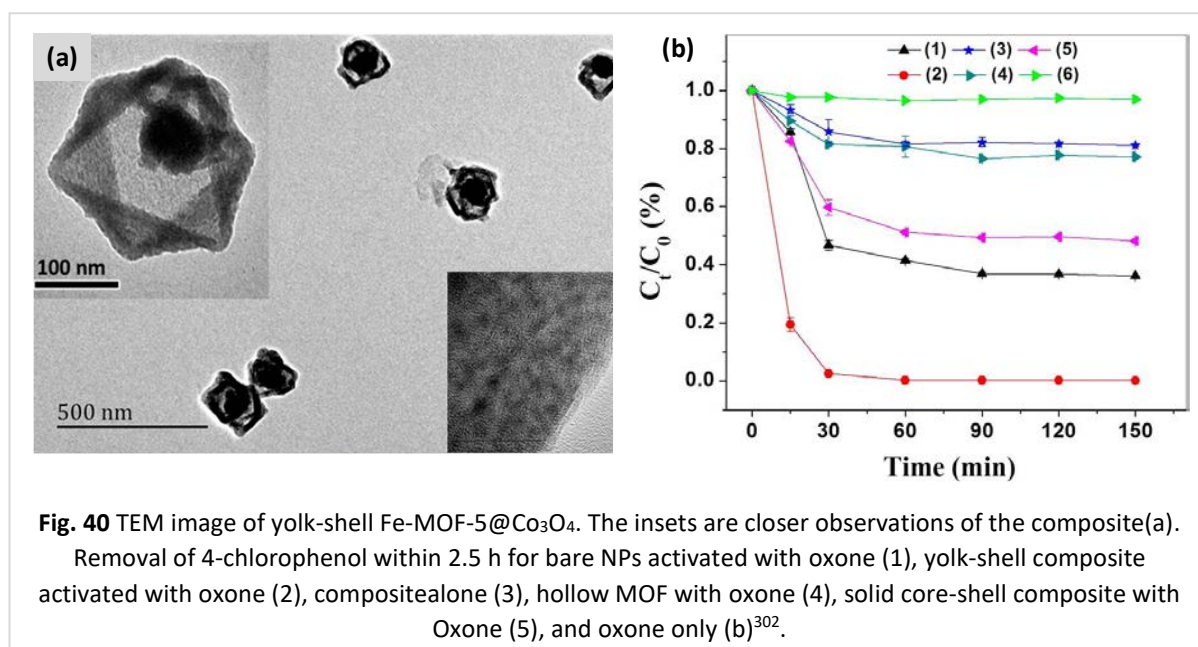
The capture of high value heavy metals by MFCs has been canvassed in the work of Falcaro et al., [295]Bagheri et al.[296] and Van Der Voort[229]. In the first case, a composite based on a MOF made of two linkers (terephthalic acid and 2-aminoterephthalic acid) and Co NPs was used to selectively harvest Ag(I) ions from a microchannel, in which the MFCs were moved from a dodecanol filled zone to a silver enriched methanol one. It was posited that sequestration of Ag(I) ions were due to the presence of the amino groups in the MOF pores. Finally, the nanocomposite was moved to a third channel filled with dodecanol for recovery. In the work of Bagheri et al., the aforementioned pyridine functionalized iron oxide magnetic particles, embedded into HKUST-1 were used to collect Pd from water with a maximum absorption capacity of 105 mg g^{-1} . Van Der Voort et al. used MIL-101(Cr) as a host for Fe₃O₄ NPs and tested this hybrid nanomaterial as an adsorbent for As(III) and As(V) species in

groundwater and surface water. The composite showed excellent adsorption capacities of 121 and 80 mg g⁻¹ for As(III) and As(V), respectively[229].



A different strategy in environmental remediation is the concomitant removal and degradation of pollutants, particularly concerning noxious organic agents. In this case, the high uptake capacity afforded by the MOF and the potential of the embedded nanoparticles to decompose pollutant molecules are utilised. In 2013, Shen et al. proposed a pioneering study that described the simultaneous uptake and degradation of toxic species, such as hexavalent chromium and model dyes, using UiO-66-NH₂@Pd[297]. In this composite, small Pd NPs (3–6 nm) were homogeneously generated within the pores of a preformed amino functionalized UiO-66. Under a 420 nm visible light irradiation, this system was able to photocatalytically reduce the carcinogenic Cr(VI) to Cr(III) within 90 min at a pH range of 1–5, demonstrating superior performance when compared with bare UiO-66-NH₂ and N-doped titania. More interestingly, the same system was investigated toward the complete degradation of methyl orange (MO) and methylene blue (MB). Here, the measured conversion was modest when using either the dye (5% for MO and 38% for MB) or the Cr(VI) alone. However, this conversion drastically enhanced when the dye was added to the reaction system: Cr(VI) reduction increased from initial 70% to 79% in the presence of MO, and from 70% to nearly 100% in the presence of MB, demonstrating a beneficial synergistic effect.

Among the different active materials with degradation capabilities, titania particles are extensively used as efficient photocatalytic nanomaterials, especially for self-cleaning surfaces [298, 299]. For such purpose, Hu and co-workers studied the MIL-101(Cr)@TiO₂ composite, which was prepared by post-infiltration of different amounts of *tert*-butyl titanate into the MOF cavities[300]. The resulting titania was then converted to the more photocatalytically active anatase phase by thermal treatment. The composite demonstrated higher adsorption of formaldehyde than the titania alone, due to the high surface area of MIL-101(Cr). Additionally, the titania was able to degrade the pollutant using a 100 W lamp at 365 nm. The composite with 14.5 wt% TiO₂ was found to be the most efficient with ca. 80% of product destroyed within 200 min. Furthermore, the same material was successfully used for the degradation of *o*-xylene with analogous results.



A recent example of one-pot uptake and degradation carried out by a MOF@iNP composite was reported by Cai's group[301]. In this work, Fe-doped MOF-5 was prepared around pre-synthesized 60 nm Co₃O₄ NPs, using Fe(acac)₃ as the source of iron (Fig. 40a)[302]. The high porosity and open pore network of the MOF structure enabled fast molecule diffusion, thus rapidly concentrating the pollutant species (in this case, 4-chlorophenol) and exposing it to the catalytic NPs for its degradation. In this case, the degradation was mediated by potassium peroxydisulfate (oxone), which was diffused into the MOF pores. The as-prepared yolk-shell catalyst was highly active with a removal efficiency of 4-chlorophenol over 99% within 150 min even after four successive cycles (Fig. 40b).

1.9 MOF@ and COF@iNPs for Catalysis

As mentioned before, iNPs are highly attractive materials for catalysis due to their larger surface area/unit volume ratio, when compared to their bulk metal analogs that are traditionally used in industrial catalysis[303, 304]. However, in most cases, it is crucial to use a support for catalysis applications. A common strategy is to use porous materials with well-defined pore characteristics; whereby, the partition between the exterior and the interior pore structure permits the selective gating of the molecules that reach, and therefore reacts with the nanoparticles[305]. Porous materials also have the advantage of confining and protecting the nanoparticles, thus facilitating their recovery from the bulk solution and preventing particle aggregation. In this context, the regular porosity of MOFs and COFs together with the possibility to tailor their pore size, shape, and chemical functionality makes them an excellent platform to support active metal NPs for heterogeneous catalysis[306].

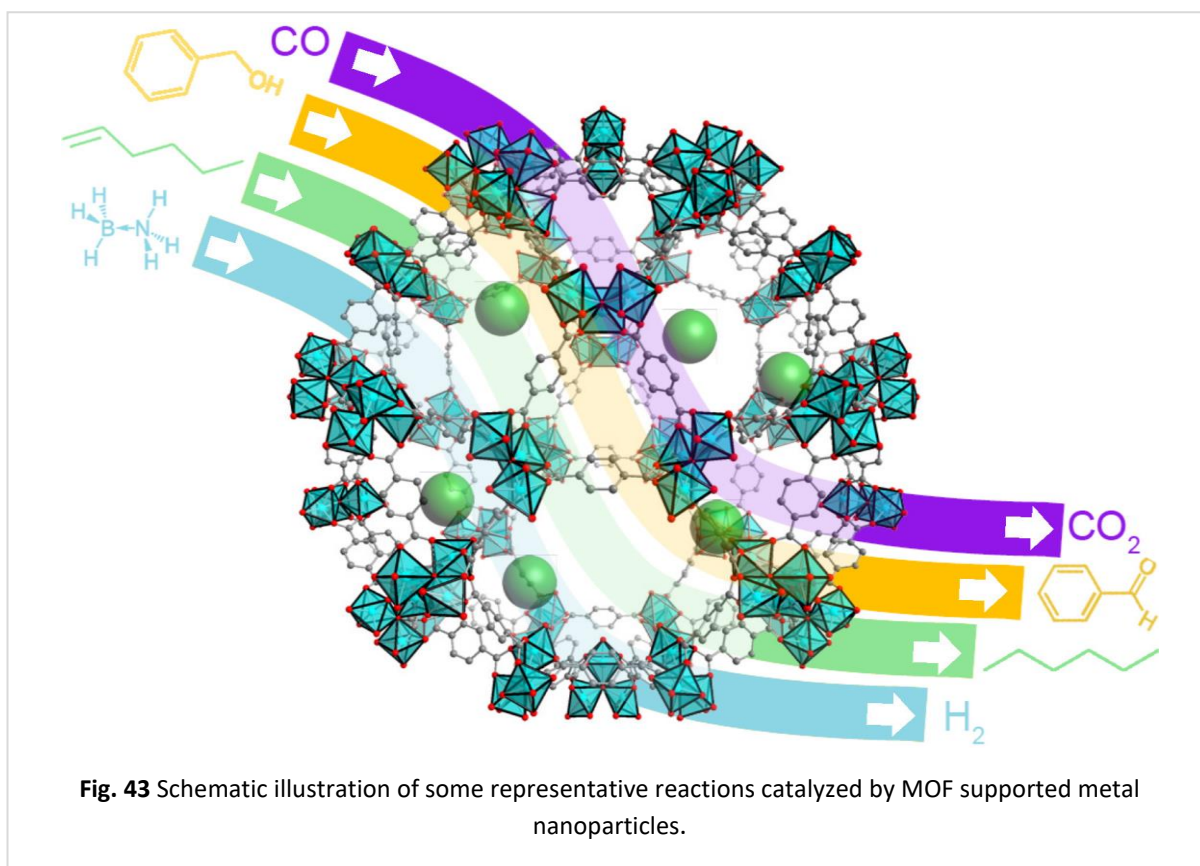


Fig. 43 Schematic illustration of some representative reactions catalyzed by MOF supported metal nanoparticles.

Table 1 summarizes some reactions already tested using MOF or COF supported iNPs as catalysts, highlighting the nature of the MOF or COF and the nanoparticle, the nanoparticle size, and the weight percentage of the nanoparticle in the MOF or COF. These studies are

largely based on oxidation, hydrogenation, C-C coupling and H₂ production reactions (Fig. 43). However, other important catalytic processes are now being investigated. For instance, complex cascade reactions involving Knoevenagel condensations and subsequent hydrogenations have been successfully catalyzed using IRMOF-3 supported Pd NPs [307].

Among the oxidation processes, oxidation of carbon monoxide to carbon dioxide has been extensively studied because of the high toxicity of carbon monoxide and its importance in fuel cell technology, where the preferential oxidation of carbon monoxide in excess of hydrogen is a key process for the production of clean fuel[308]. Overall, MOF or COF supported nanoparticles have shown good performance for carbon monoxide oxidation at elevated temperatures. For example, Xu, Hupp, and Gascón groups reported that Au and Pt NPs supported in ZIF-8, MIL-101-NH₂ (Al) and UiO-66 (Fig. 44ab) afford the total conversion of carbon monoxide to carbon dioxide at around 160–200 °C [309, 203, 310, 236]. Importantly, the reaction temperature could be reduced to 100–150 °C by incorporating Pt, Pd and Cu NPs within MIL-101 and Ce-based MOF (Fig. 44cd) and Pd NPs within MOF-5[311-313, 266]. In addition, 3.2 nm Pd NPs dispersed in triptycene-based COF converted CO to CO₂ at 160° C[223].

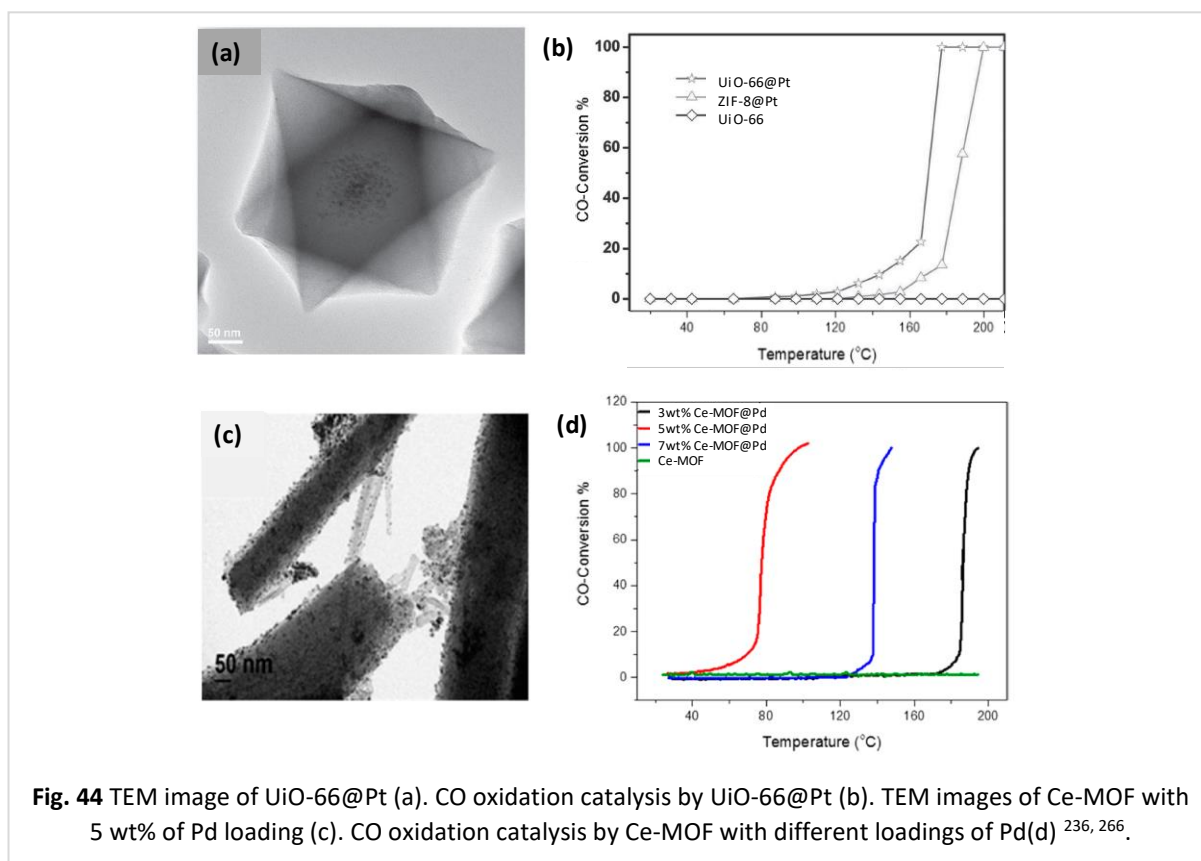


Table 1 List of MOF or COF supported iNPs catalysts by reaction and substrate.

MOF/COF composite	Nanoparticle	Weight %	Size (nm)	Conv. (%) [§]	Ref.
Oxidation					
<i>CO</i>					
ZIF-8	Pt	3.4	2.5±4.1	100	[203]
ZIF-8	Au	5	4.2±2.6	100	[309]
MIL-101-NH ₂ (Al)	PTA/Pt			100	[310]
MIL-101(Cr)	Cu/Pd	2.9	2-6	100	[312]
MIL-101(Cr)	Pt/Pd	2.9	3-9	100	[311]
MOF-5	Pd	0.19		65	[313]
MIL-101(Cr)	Pt	2/1/5	1.8±0.2	100	[314]
Ra-MOF	Pd	3.6	1.8±0.3	100	[315]
Ce-MOF	Pd	5	4.6	100	[266]
UiO-66	Pt	2	2.9	100	[236]
NPT-COF	Pd	2.2	3	100	[223]
<i>Alcohols</i>					
MOF-5	Ru	30	1.5-1.7	25	[316]
MOF-5	Au /ZnO-Au/TiO ₂ -Au	1-20	2.7-20	50/68/74	[317]
MOF-5/MIL-53(Al)	Au		1.5±0.7	99	[318]
DUT-5/UiO-66/MOF-253	Pt	0.5	1.5-2	99	[319]
UiO-67	Pd	1	3±0.5	99	[320]
MIL-101(Cr)	Au	0.5	2.3±1.1	100	[321]
ZIF-8	Au	30	3.7	81	[322]
UiO-66	Au		5-7	94	[323]
MOF-177	Pt	43	2-3		[324]
UiO-66-NH ₂	Au	1.8	2.8-3.1	94	[325]
UiO-66	Au	8		54	[326]
MIL-101(Cr)	Pd	0.35	2.5±0.5	99	[327]
<i>Cyclohexane</i>					
MIL-101(Cr)/ MIL-53(Cr)	Au	4.64/4.63	4.8±2.9	30/31	[328]
MIL-101(Cr)	Au/Pd	1	2.4±0.6	51	[329]
<i>Benzylic hydrocarbons</i>					
HKUST-1	Fe ₃ O ₄	28.78	20		[288]
HKUST-1	Cu-CuFe ₂ O ₄	5	200	100	[330]
UiO-66-NH ₂	Au	2.4	15	30	[331]

MOF/COF composite	Nanoparticle	Weight %	Size (nm)	Conv. (%) [§]	Ref.
COF-ASB	Ru	4.1	2-5	90	[332]
<i>Benzyl-amine</i>					
UiO-66	Au	5-7		53	[323]
<i>Ethylene</i>					
ZIF-8	Pt/Pd	4.95/2.70	6.2	94	[333]
Hydrogenation					
<i>Ketones</i>					
MIL-101(Cr)	Pt		1.5-2.5	97-98	[334]
MIL-101(Cr)	Pd	15	2-3.5	100	[335]
MIL-101(Cr)	Pd	42-45	1.7	100	
<i>1-Hexene</i>					
ZIF-8	Pt	0.23-0.74	2-3	95	[336]
ZIF-8	Pd	0.5	5	100	[337]
ZIF-8	Pd	8.7	17±3	100	[338]
HKUST-1/ZIF-8	Pd	0.55		83	[339]
UiO-66	Pt	2	2.9	100	[236]
<i>1-Hexyne</i>					
ZIF-8	Pt	1	2.7	100	[233]
<i>1,4-Butynediol</i>					
ZIF-8	Pd	5	4-6	98	[340]
<i>Styrene</i>					
MIL-101(Cr)	Pd	1	1.5	80-100	[341]
MOF-5	Pt	1		97	[259]
MesMOF-1	Ni	20	1.1	99	[342]
HKUST-1/ZIF-8	Pd	0.55		65	[339]
<i>Toluene</i>					
MIL-101-NH ₂ (Al)	PTA/Pt				[310]
<i>Acetylene</i>					
MIL-101(Cr)	Pd	1	1.5	80-100	[341]
<i>Nitroarenes/ Nitrobenzene</i>					
MIL-101(Cr)	Pt	1	1.5-2.5	100	[343]
MesMOF-1	Ni	20,35	1.1,1.4-1.9	100	[342]
UiO-66	Pd/Pt	5	3.4-4.2	100	[344]
<i>Phenol</i>					

MOF/COF composite	Nanoparticle	Weight %	Size (nm)	Conv. (%) [§]	Ref.
MIL-101(Cr)-MIL-53(Cr)	Pd	4.3/4.9	2.5/4.3	100	[345]
<i>Nitrophenol</i>					
ZIF-8	Au	10-15	2-3	100	[227]
ZIF-8	Au/Ag	2/2		100	[346]
MIL-100(Fe)	Au			100	[347]
UiO-66	Pt	2	2.9	100	[236]
TAPB-DMTP-COF	Au	0.2	15	100	[241]
TpPa-1-COF	Au	1.2	5±3	100	[213]
Thio-COF	Pt	34	1.7±0.2	100	
<i>Cyclohexanone / Cycloheptanone</i>					
MIL-101	Ni/Pd	18	2.5-3.5	80/100	[348]
UiO-66-S	Pt	0.4	2.5	64	[349]
<i>Octane</i>					
MIL-101(Cr)	Pt	1.2	5±0.5	100	[350]
<i>2,3,5-trimethylbenzoquinone</i>					
MIL-101(Cr)	Pd	2	2-3	100	[351]
<i>Benzene/cyclohexene</i>					
MOF-5	Ru	0.98	2	99	[352]
<i>Other olefins</i>					
HKUST-1	Au/Pt		100	25	[353]
<i>2.16. Vanilin</i>					
MIL-101(Cr)	Pd	2	1.8±0.2	45	[354]
<i>Dehalogenation of aryl chlorides</i>					
MIL-101-NH ₂ (Cr)	Pd	0.62	2.49	98	[355]
<i>α, β-unsaturated aldehyde</i>					
MIL-101(Cr)-MIL-101(Fe)	Pt	4.6	2.8	100	[230]
C-C coupling					
<i>Suzuki-Miyaura coupling</i>					
MIL-101(Cr)	Pd	1	1.9±0.7	82	[356]
MIL-53-NH ₂ (Al)	Pd	1	3.12	99	[357]
MIL-101-NH ₂ (Cr)	Pd	8	2-3	99	[358]
MCoS-1	Pd	1	2-3	97	[359]
SPCP-3/I	Pd	2.6	1.5±0.3	89	[360]
UiO-66-NH ₂	Pd	0.67	1.2	100	[361]

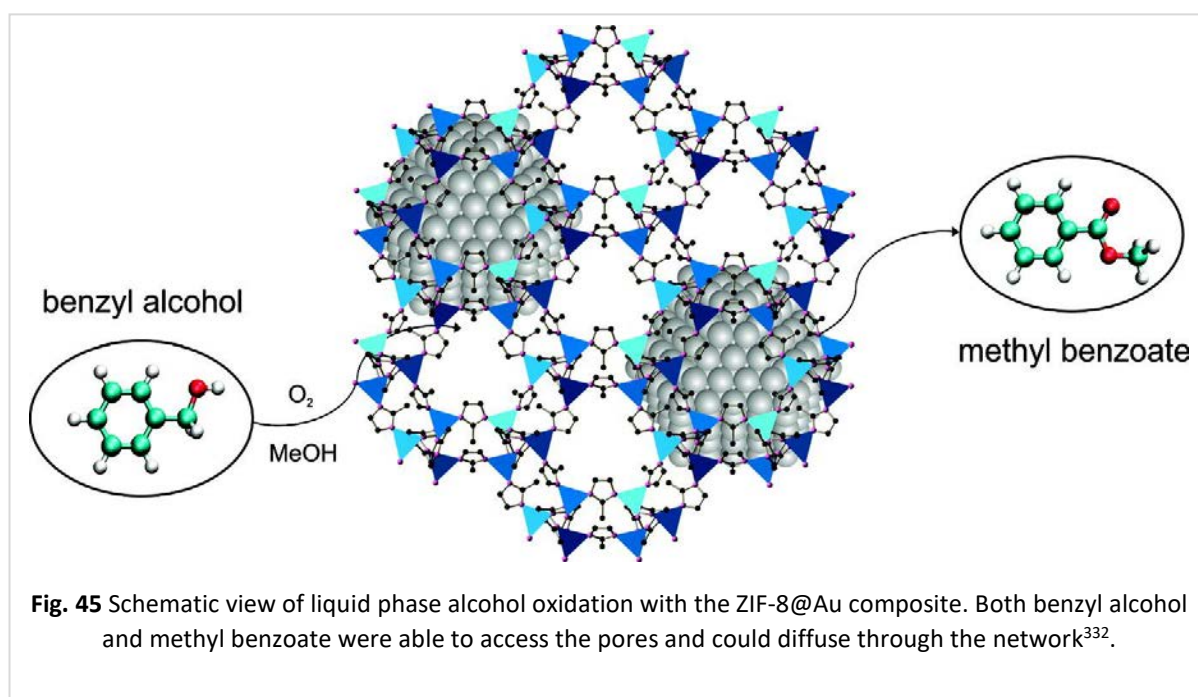
MOF/COF composite	Nanoparticle	Weight %	Size (nm)	Conv. (%) [§]	Ref.
MOF-5-NPC	Pd	10.6	2.7	100	[362]
COF-LZU1	Pd	7.1±0.5		98	[363]
Thio-COF	Pd	26	1.7±0.2	100	[364]
<i>Ullman coupling</i>					
MIL-101(Cr)	Pd	1	1.9±0.7	99	[356]
<i>Sonogashira reaction</i>					
MCoS-1	Pd	1	2-3	94	[359]
MOF-5	Pd	3	3-6	100	[365]
<i>Heck reaction</i>					
MIL-53-NH ₂ (Fe)	Pd	0.96	3.2	83	[366]
CCOF-MPC	Pd	34	2-5	100	[64]
trzn-COF	Pd	18-20	5-20	97	[367]
Hydrogen generation					
IRMOF-3	Pd	2	35	100	[307]
MIL-101(Cr)	Ni/Au		1.8±0.2	100	[368]
ZIF-8	Ni	19	2.7±0.7	100	[369]
ZIF-8	Ni/Pt	1-3	2.2±0.3	100	[370]
MIL-101-EDA(Cr)	Au/Pd	13.7/1.5	2-3	100	[371]
MIL-125-NH ₂	Pd	0.5	3.1		[372]
MIL-101-NH ₂ (Cr)	Pt	1.5	3.75±0.5		[373]
HKUST-1	Pd	0.86	4.3 ±1.1	100	[374]
Other					
<i>Hydroisomerization of n-hexane</i>					
Al-MCF-17	Pt	0.1	3	100	[375]
<i>Methylene blue degradation</i>					
ZIF-8	SnO	2	5	100	[376]
<i>Imination of nitrobenzene</i>					
UiO-66	Pt	2.3	3±0.3	73	[377]
<i>Reduction of Cr(VI)</i>					
UiO-66-NH ₂	Pd	0.93	3-6	100	[297]
MIL-101(Cr)	Pt	2	2.6	100	[378]
<i>Methanol synthesis</i>					
MOF-5	Cu/ZnO	1.4/40	1-3		[379]
UiO-66	Cu	1	18		[380]

MOF/COF composite	Nanoparticle	Weight %	Size (nm)	Conv. (%) [§]	Ref.
UiO-bpy	Cu/ZnO	6.9	0.5-2	17.4	[381]
ZIF-8	Cu/TiO ₂		25		[382]
<i>Conversion of methylcyclopentane</i>					
UiO-66	Pt	0.4	2.5	100	[383]
<i>Synthesis of arylamines</i>					
MIL-101(Cr)	Pd/Pt				[384]
<i>Aminocarbonylation</i>					
ZIF-8	Pd	1	4-9	99	[385]
MOF-5	Pd	1	3-12	92	[386]
<i>Indole synthesis</i>					
MIL-101(Cr)	Pd	3	2.6	67	[387]
<i>Phenylation of naphthalene</i>					
MOF-5	Pd	2.3	20	65	[388]
<i>Direct arylation</i>					
MIL-101(Cr)	Pd	0.5	2.6±0.5	85	[389]
<i>Synthesis of 2-substituted benzofuran derivatives</i>					
TpBpy-COF	Pd	15.2	12±4	70	[390]

[§] Maximum conversion value reached (or reported).

In addition, MOF or COF supported iNPs have been used as catalysts for aerobic alcohol oxidation reactions which are considered as key reactions in 'green' organic synthesis. These processes usually require temperatures above 100 °C (under solvent-free conditions), or the presence of a large excess of a base. The majority of these investigations employ Au and Pd NPs supported in different MOFs or COFs. Fischer and co-workers first studied the oxidation of benzyl alcohol to benzyl aldehyde using Ru and Au NPs[316], and Au/ZnO and Au/TiO₂ NPs[317] supported on MOF-5. For the Ru NPs, which could be easily converted to RuOx by oxidation with diluted O₂ gas inside MOF-5, the conversion of benzyl alcohol was low (25%). This was attributed to the structural decomposition of MOF-5 during the oxidation reaction. However, in the case of Au and hybrid Au/ZnO and Au/TiO₂ NPs, the authors observed better performance (conversion ranges of 50–70%) when a base was added to accelerate the oxidation reactions by deprotonation of the alcohol. These results were in contrast to those obtained by Ishida et al., who reported that Au NPs embedded in MOF-5

activate the oxidation reaction with base (conversion = 100%) but also without a base (conversion = ~70%) [318]. The group of Li has investigated a variety of alcohol oxidation reactions. Here, the catalytic activity of a series of composites that were made from different combinations of MOFs (DUT-5, UiO-66, MOF-253, UiO-67, and MIL-101(Cr)) and metal NPs (Pt, Pd and Au) was assessed. Overall, they showed that the confined metal NPs were highly active in these types of oxidations under base-free conditions (conversions up to 100%). The authors attributed these results to the electron donation and confinement effects offered by MOFs[320, 319, 321]. Other systems including Au NPs supported on ZIF-8 (Fig. 45) and UiO-66, Ru NPs impregnated in COF-ASB and Pt NPs supported on MOF-177 also showed an excellent catalytic activity for the conversion of alcohols to aldehydes[332, 258, 322, 323].

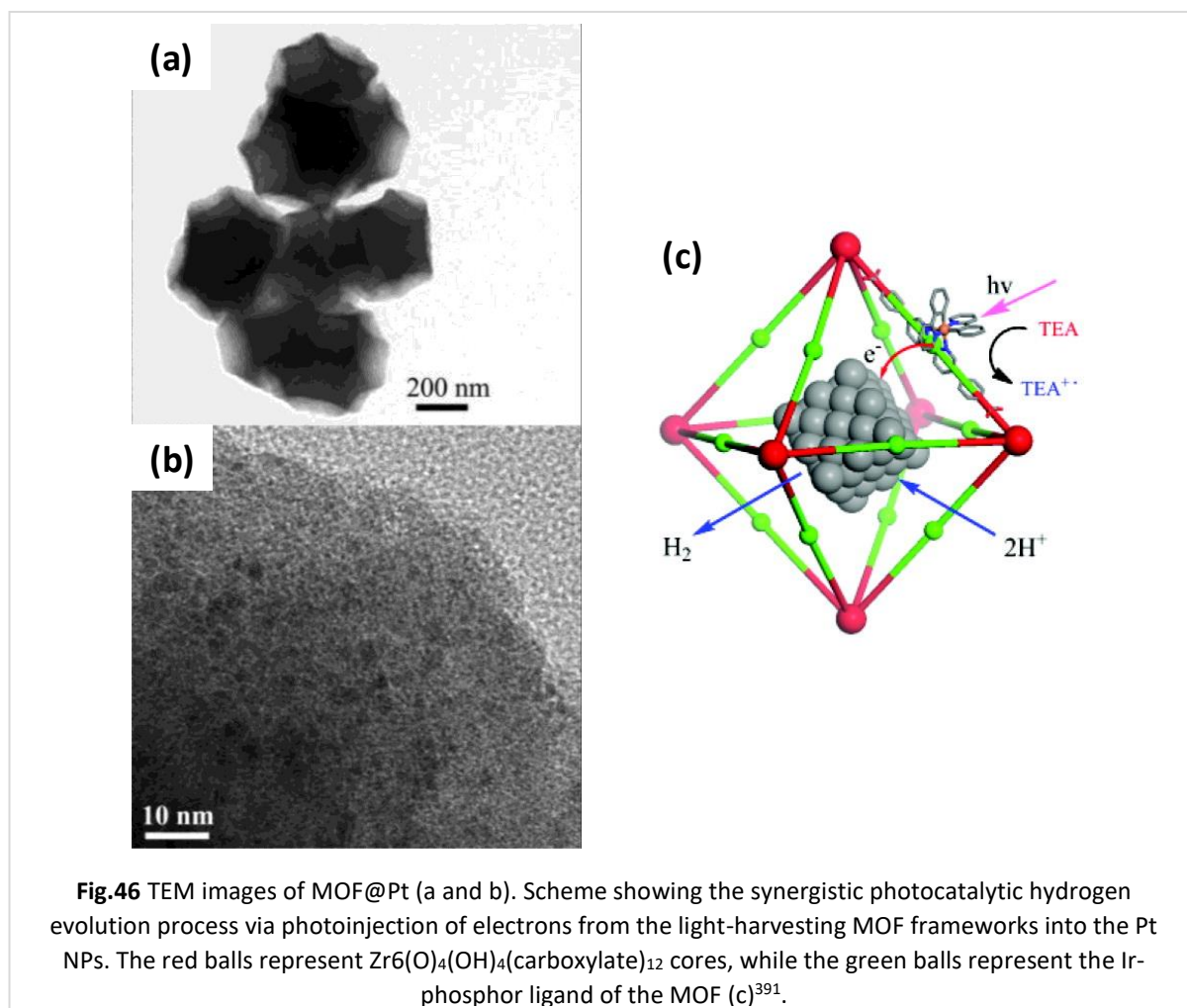


Beyond alcohols, the oxidation of hydrocarbons has been catalyzed using MOF or COF supported iNPs. Hydrocarbons have been selectively oxidized, with molecular oxygen as the oxidant, by Au, Au/Pd, Fe₃O₄, Cu-CuFe₂O₄ or Pt/Pd NPs immobilized in several MOFs including MIL-101 (Cr), MIL-53 (Cr), HKUST-1 and ZIF-8[288, 330, 333, 329, 328]. Huang et al. studied the activity of ZIF-8 supported bimetallic Pt/Pd NPs for the photoactivated oxidation-degradation of ethylene to CO₂ and H₂O[333]. This nanocomposite showed an excellent synergistic photocatalytic activity (conversion = 94%). This high activity was due to an excellent capacity of ZIF-8 to adsorb ethylene and thus, promote its photodegradation to CO₂

and H₂O. Moreover, Duan and co-workers developed a new synthetic method to encapsulate Au in UiO-66-NH₂ with small molecule-assisted heterogeneous nucleation of MOF. Subsequently, photocatalytic performance of UiO-66-NH₂@Au was tested, and the results showed an excellent performance in the oxidation of benzyl alcohol in the visible light region[331]. Also, Ru supported on COF-ASB was able to highly promote the one-pot tandem-synthesis of imine products from benzyl alcohols[332].

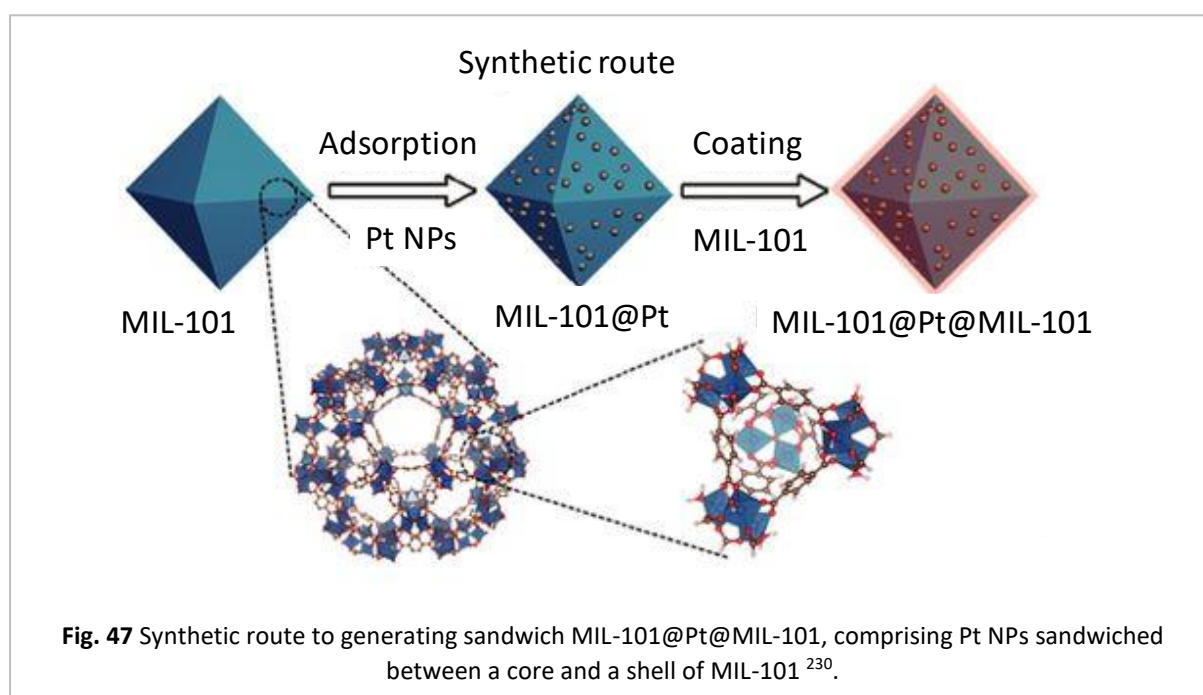
One of the biggest challenges in chemistry today is achieving energy efficient generation of H₂. With this goal in mind, Xu and co-workers evaluated the activity of Au, Ni and hybrid Au/Ni NPs in MIL-101 and of Ni NPs in ZIF-8 for the catalytic dehydrogenation of ammonia borane to generate H₂. In this case, complete dehydrogenation was observed[369, 368]. Other reactions for hydrogen production have also been evaluated. Singh and Xu successfully studied the generation of H₂ with the decomposition of hydrazine in aqueous solution using ZIF-8 supported Ni-Pt bimetallic NPs[370]. In addition, the same group and Martis et al. proved that it was possible to catalyze the dehydrogenation of formic acid using bare and amine-functionalized MIL-101-ethylenediamine supported Au-Pd bimetallic NPs[371] and amine-functionalized MIL-125 supported Pd NPs[372]. Recently, water splitting to produce H₂ using Pt NPs embedded into MIL-101-NH₂(Cr) has also been evaluated. A maximum turnover of 100 mol_{H₂}/mol_{cat}⁻¹ was achieved when the loading of Pt NPs was 0.5%[373]. Finally, the photocatalytic properties of MOFs@Pt were tested for H₂ production. Here, Lin's group initially studied the photocatalytic performance of Pt NPs embedded into two UiO frameworks functionalized with [Ir(ppy)₂(bpy)]⁺ (where ppy is 2-phenyl-pyridine, and bpy is 2,2'-bipyridine) complexes, and found high Ir-based turnover numbers [defined as $n(1/2H_2)/n(Ir)$] of 3400 and 7000. These values were achieved when irradiated under visible light (>420 nm). Under these conditions, the [Ir(ppy)₂(bpyradical^{••-})] radicals generated by triethylamine-mediated photoreduction transferred electrons to Pt NPs to reduce protons for H₂ production (Fig. 46)[391]. Additionally, Matsuoka's group found that Pt NPs photo deposited on amino-functionalized MIL-125(Ti) were able to photocatalyze the generation of H₂, reaching a total production of 33 μmol H₂ when this system was immersed in an aqueous solution containing triethanolamine at room temperature while being subjected to visible-light (>420 nm) for 9 h. In this case, the reaction proceeded through the light absorption by

the organic linker, forming the MOF followed by the electron transfer to the photocatalytically active titanium-oxo cluster. In this process, Pt NPs acted as co-catalyst[392].



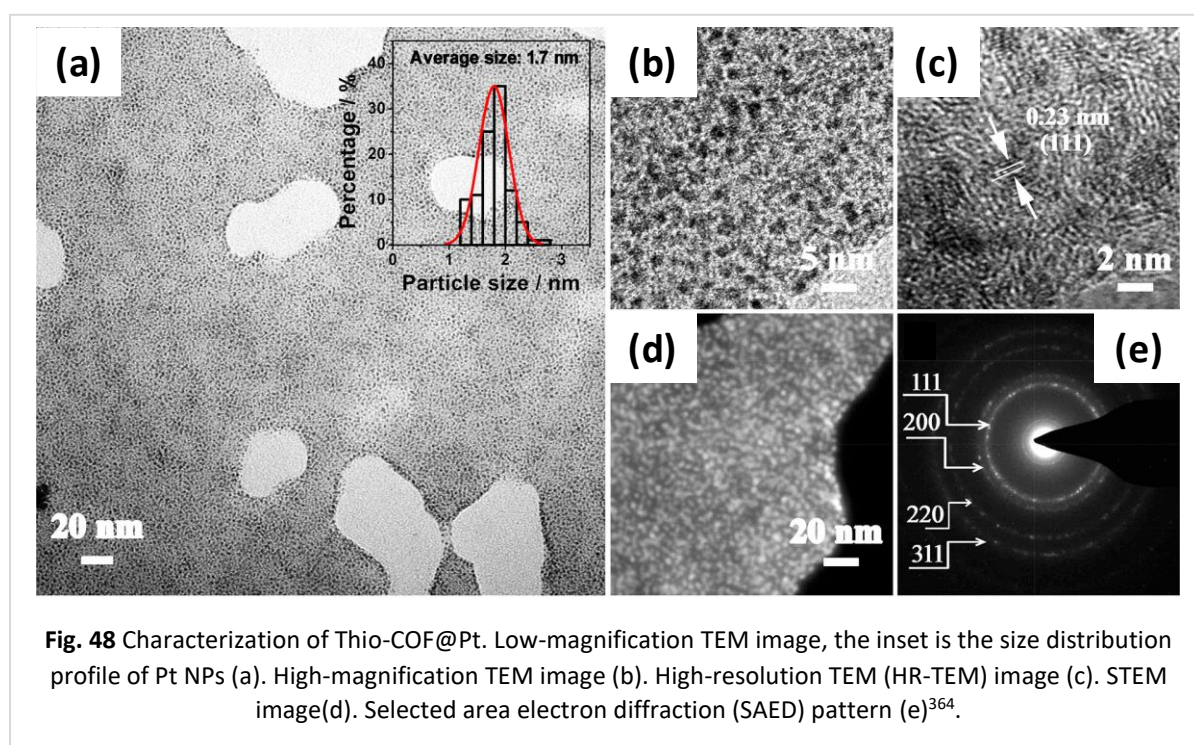
A fourth vast family of catalytic reactions studied using MOF supported iNPs as catalysts are the hydrogenation of alkenes[341, 336] alkynes[349, 341, 233], ketones[334]:[335], and aromatics[341, 259, 345], all of which are key processes in the chemical industry. As can be seen in Table 1, the most active metal NPs for these reactions are Pt and Pd, and the most promising MOF support is MIL-101, most probably due to its stability and large pore channels. Using this combination, excellent conversion rates (~100%) for the hydrogenation of ketones, aromatic molecules, alkenes, alkynes and nitro compounds have been observed [343, 341, 335, 393, 355, 350, 334, 345, 230, 351]. In addition, MIL-101 has been used as a support for Pt NPs for hydrogenation of α , β -unsaturated aldehyde. Tang and co-workers demonstrated that MOFs could serve as effective selectivity regulators for

hydrogenation, by sandwiching Pt NPs between an inner core and an outer core shell composed of Fe and Cr MIL-101. The results showed a series of catalyst that converts cinnamaldehyde into fufural, 3-methyl-2-butenal and acrolein with different selectivity based on the configuration of the layers (Fig. 47)[230]. Moreover, MOFs with smaller pore and windows size showed a better selectivity towards smaller molecules such as 1-hexane. Combination of ZIF-8 and Pd NPs showed a high selectivity and conversion rate for hydrogenation of 1-hexane[337, 339, 338].



Another series of reactions that have been catalyzed by MOF or COF supported NPs concern the C-C coupling reactions. Such transformations include Suzuki-Miyaura[362, 357-359, 361, 356], Sonogashira[365, 359], Ullmann[356], and Heck[366] reactions. Compared to other metal NPs, Pd offers undoubtedly the best conversion rates in C-C coupling, and thus, MOF@Pd composites are primarily tested for these types of catalytic reactions. An illustrative example was reported by Yuan et al., who developed a very efficient MIL-101(Cr)@Pd catalyst for water-mediated Suzuki-Miyaura and Ullmann coupling reactions. This catalyst showed high stability, low metal leaching and high activities (conversion = 100 %) over a large number of cycles[356]. Li et al. encapsulated Pd cluster smaller than 1.2 nm inside the cavity of UiO-66-NH₂ via double solvent approach combined with a photoreduction process. This catalyst showed excellent results for the scope of Suzuki coupling reactions under visible light[361]. Additionally, Pd NPs supported on various COFs showed an excellent activity for different

Heck and Suzuki coupling reactions[363, 64, 367]. Dong and co-workers, fabricated Pd NPs supported CCOF-MPC (*S*-(+)-2-methylpiperazine and cyanuric chloride based COF) via impregnation and reduction method. The composite was tested for various Henry and Heck reactions and demonstrated high yields (up to 99%) with excellent stereoselectivities (up to 97%) for these reactions under mild reaction conditions[64]. More recently, Wei and co-workers used thioether containing COF for the confined growth of ultrafine and highly dispersed Pt and Pd NPs (1.7 ± 0.2 nm) with a narrow size distribution (Fig. 48). They performed a series of Suzuki-Miyaura reactions with high yield and excellent reusability[364].



Finally, another type of reaction catalyzed by MOF@iNPs is the methanol production by hydrogenation of CO₂. Methanol is a key chemical intermediate, and numerous applications transform it into vital products and commodities that span and drive modern life[394]. Currently, in industry, methanol is produced by Cu/ZnO/Al₂O₃ from a mixture of gases such as CO, CO₂, and H₂. Recently, MOF@iNPs have been tested as catalysts that consume CO₂ and H₂ as the source for methanol production. For instance, the catalytic synthesis of methanol from CO₂ and H₂, using Cu NPs stabilized into MOF-5, was demonstrated by Fischer et al., who found a maximum $70 \mu\text{mol}_{\text{MeOH}} \text{g}^{-1}_{\text{cat}} \text{h}^{-1}$ methanol production[379]. More recently, Zr-based MOFs were tested as a support for Cu[380] and

Cu/ZnO_x[381] NPs for selective methanol synthesis. A pioneering example of this type of catalysts was reported by Somorajai et al., who encapsulated a single Cu nanoparticle within a single UiO-66 crystal. The performance of this catalyst constructs exceeded the benchmark of traditional Cu/ZnO/Al₂O₃ catalyst and gave an enhanced yield with 100% selectivity for methanol[380]. Moreover, a combination of Cu/TiO₂ and ZIF-8 in the form of a membrane demonstrated photocatalytic activity for converting CO₂ to methanol in the work of Dumeénil and co-workers[382].

1.10 References

- [1] C. Altavilla, E. Ciliberto, *Inorganic Nanoparticles : Synthesis, Applications, and Perspectives*, CRC Press, Boca Raton, FL, 2011.
- [2] P. Alivisatos, P.F. Barbara, A.W. Castleman, J. Chang, D.A. Dixon, M.L. Klein, G.L. McLendon, J.S. Miller, M.A. Ratner, P.J. Rossky, S.I. Stupp, M.E. Thompson, *Advanced Materials*, 10 (1998) 1297-1336.
- [3] A. Zanon, F. Verpoort, *Coordination Chemistry Reviews*, 353 (2017) 201-222.
- [4] K.L. Kelly, E. Coronado, L.L. Zhao, G.C. Schatz, *The Journal of Physical Chemistry B*, 107 (2003) 668-677.
- [5] T. Okamoto, I. Yamaguchi, *The Journal of Physical Chemistry B*, 107 (2003) 10321-10324.
- [6] J. Han, M.C. Freyman, E. Feigenbaum, T. Yong-Jin Han, *ACS Photonics*, 5 (2018) 1343-1350.
- [7] H.-Y. Jung, H.-J. Kim, S. Yang, Y.-G. Kang, B.-Y. Oh, H.-G. Park, D.-S. Seo, *Liquid Crystals*, 39 (2012) 789-793.
- [8] K. Saha, S.S. Agasti, C. Kim, X. Li, V.M. Rotello, *Chemical Reviews*, 112 (2012) 2739-2779.
- [9] A.R. Mohtasebzadeh, L. Ye, T.M. Crawford, *International Journal of Molecular Sciences*, 16 (2015) 19769-19779.
- [10] M.B. Gawande, P.S. Branco, K. Parghi, J.J. Shrikhande, R.K. Pandey, C.A.A. Ghumman, N. Bundaleski, O.M.N.D. Teodoro, R.V. Jayaram, *Catalysis Science & Technology*, 1 (2011) 1653-1664.
- [11] M.B. Gawande, A. Goswami, F.X. Felpin, T. Asefa, X. Huang, R. Silva, X. Zou, R. Zboril, R.S. Varma, *Chemical Reviews*, 116 (2016) 3722-3811.
- [12] S. Laurent, D. Forge, M. Port, A. Roch, C. Robic, L. Vander Elst, R.N. Muller, *Chemical Reviews*, 108 (2008) 2064-2110.
- [13] M. Liong, J. Lu, M. Kovoichich, T. Xia, S.G. Ruehm, A.E. Nel, F. Tamanoi, J.I. Zink, *ACS Nano*, 2 (2008) 889-896.
- [14] R. Singh, J.W. Lillard, *Experimental and Molecular Pathology*, 86 (2009) 215-223.
- [15] S. Modi, B.D. Anderson, *Molecular Pharmaceutics*, 10 (2013) 3076-3089.
- [16] F. Alexis, E.M. Pridgen, R. Langer, O.C. Farokhzad, Nanoparticle Technologies for Cancer Therapy, in: M. Schäfer-Korting (Ed.) *Drug Delivery*, Springer Berlin Heidelberg, Berlin, Heidelberg, 2010, pp. 55-86.
- [17] D. Kim, J. Kim, Y.I. Park, N. Lee, T. Hyeon, *ACS Central Science*, 4 (2018) 324-336.
- [18] L.K. Bogart, G. Pourroy, C.J. Murphy, V. Puentes, T. Pellegrino, D. Rosenblum, D. Peer, R. Lévy, *ACS Nano*, 8 (2014) 3107-3122.
- [19] J. Kim, P. Chhour, J. Hsu, H.I. Litt, V.A. Ferrari, R. Popovtzer, D.P. Cormode, *Bioconjugate Chemistry*, 28 (2017) 1581-1597.
- [20] S.J. Sigg, F. Santini, A. Najer, P.U. Richard, W.P. Meier, C.G. Palivan, *Chemical Communications*, 52 (2016) 9937-9940.
- [21] E.Y. Sun, L. Josephson, R. Weissleder, *Molecular Imaging*, 5 (2006) 7290.2006.00013.
- [22] H. Wei, O.T. Bruns, M.G. Kaul, E.C. Hansen, M. Barch, A. Wiśniowska, O. Chen, Y. Chen, N. Li, S. Okada, J.M. Cordero, M. Heine, C.T. Farrar, D.M. Montana, G. Adam, H. Ittrich, A. Jasanoff, P. Nielsen, M.G. Bawendi, *Proceedings of the National Academy of Sciences*, 114 (2017) 2325-2330.
- [23] E. Priyadarshini, N. Pradhan, *Sensors and Actuators B: Chemical*, 238 (2017) 888-902.

- [24] P.K. Jain, K.S. Lee, I.H. El-Sayed, M.A. El-Sayed, *The Journal of Physical Chemistry B*, 110 (2006) 7238-7248.
- [25] G.-H. Chen, W.-Y. Chen, Y.-C. Yen, C.-W. Wang, H.-T. Chang, C.-F. Chen, *Analytical Chemistry*, 86 (2014) 6843-6849.
- [26] L. Gong, B. Du, L. Pan, Q. Liu, K. Yang, W. Wang, H. Zhao, L. Wu, Y. He, *Microchimica Acta*, 184 (2017) 1185-1190.
- [27] Y.-W. Lin, C.-C. Huang, H.-T. Chang, *Analyst*, 136 (2011) 863-871.
- [28] J. Wei, L. Yang, G. Yue, J. Zhu, D. Huang, P. Zhao, *Analytical Methods*, 9 (2017) 2805-2811.
- [29] Y. Xue, H. Zhao, Z. Wu, X. Li, Y. He, Z. Yuan, *Analyst*, 136 (2011) 3725-3730.
- [30] S. Bang, G.P. Korfiatis, X. Meng, *Journal of Hazardous materials*, 121 (2005) 61-67.
- [31] K.A. Gebru, C. Das, *Chemosphere*, 191 (2018) 673-684.
- [32] M.S. Islam, W.S. Choi, B. Nam, C. Yoon, H.-J. Lee, *Chemical Engineering Journal*, 307 (2017) 208-219.
- [33] L. Li, Y. He, X. Lu, *Frontiers of Environmental Science & Engineering*, 12 (2017) 11.
- [34] D. Wang, D. Astruc, *Chemical Society Reviews*, 46 (2017) 816-854.
- [35] S. Zhang, L. Nguyen, Y. Zhu, S. Zhan, C.-K. Tsung, F. Tao, *Accounts of Chemical Research*, 46 (2013) 1731-1739.
- [36] Y. Li, E. Boone, M.A. El-Sayed, *Langmuir*, 18 (2002) 4921-4925.
- [37] M. Pérez-Lorenzo, *The Journal of Physical Chemistry Letters*, 3 (2012) 167-174.
- [38] N. Ameer, S. Bedrane, R. Bachir, A. Choukchou-Braham, *Journal of Molecular Catalysis A: Chemical*, 374-375 (2013) 1-6.
- [39] P.V. Kamat, D. Meisel, *Current Opinion in Colloid & Interface Science*, 7 (2002) 282-287.
- [40] X. Li, G. Li, W. Zang, L. Wang, X. Zhang, *Catalysis Science & Technology*, 4 (2014) 3290-3297.
- [41] B. Pawelec, R. Mariscal, R. Navarro Cerrillo, S. van Bokhorst, S. Rojas, J.L.G. Fierro, *Applied Catalysis A General*, 225 (2002) 223-237.
- [42] A.D. Dwivedi, L.Q. Ma, *Critical Reviews in Environmental Science and Technology*, 44 (2014) 1679-1739.
- [43] M.A. Miller, B. Askevold, H. Mikula, R.H. Kohler, D. Pirovich, R. Weissleder, *Nature Communications*, 8 (2017) 15906.
- [44] D. Chen, P. Cui, H. He, H. Liu, F. Ye, J. Yang, *RSC Advances*, 5 (2015) 10944-10950.
- [45] S. Peiris, J. McMurtrie, H.-Y. Zhu, *Catalysis Science & Technology*, 6 (2016) 320-338.
- [46] S. Peiris, S. Sarina, C. Han, Q. Xiao, H.-Y. Zhu, *Dalton Transactions*, 46 (2017) 10665-10672.
- [47] N.H. Khadry, M.A. Ghanem, *RSC Advances*, 4 (2014) 50114-50122.
- [48] M. Navlani-García, K. Mori, Y. Kuwahara, H. Yamashita, *NPG Asia Materials*, 10 (2018) 277-292.
- [49] D. Astruc, Transition-Metal Nanoparticles in Catalysis: From Historical Background to the State-of-the-Art, in: *Nanoparticles and Catalysis*, Wiley, 2008.
- [50] R. Narayanan, M.A. El-Sayed, *The Journal of Physical Chemistry B*, 109 (2005) 12663-12676.
- [51] J. Seth, P. Dubey, V.R. Chaudhari, B.L.V. Prasad, *New Journal of Chemistry*, 42 (2018) 402-410.
- [52] R.M. Rioux, H. Song, J.D. Hoefelmeyer, P. Yang, G.A. Somorjai, *The Journal of Physical Chemistry B*, 109 (2005) 2192-2202.
- [53] J.A. Rodriguez, S. Ma, P. Liu, J. Hrbek, J. Evans, M. Pérez, *Science*, 318 (2007) 1757-1760.
- [54] L. Soler, A. Casanovas, A. Urrich, I. Angurell, J. Llorca, *Applied Catalysis B- Environmental*, 197 (2016) 47-55.
- [55] H. Tang, Y. Su, B. Zhang, A.F. Lee, M.A. Isaacs, K. Wilson, L. Li, Y. Ren, J. Huang, M. Haruta, B. Qiao, X. Liu, C. Jin, D. Su, J. Wang, T. Zhang, *Science Advances*, 3 (2017).

- [56] S.M. Choi, M.H. Seo, H.J. Kim, W.B. Kim, *Synthetic Metals*, 161 (2011) 2405-2411.
- [57] J. Melke, B. Peter, A. Habereeder, J. Ziegler, C. Fasel, A. Nefedov, H. Sezen, C. Wöll, H. Ehrenberg, C. Roth, *ACS Applied Materials & Interfaces*, 8 (2016) 82-90.
- [58] W.-k. Suh, P. Ganesan, B. Son, H. Kim, S. Shanmugam, *International Journal of Hydrogen Energy*, 41 (2016) 12983-12994.
- [59] Y. Li, M. Ma, X. Wang, X. Wang, *Journal of Environmental Sciences*, 20 (2008) 1527-1533.
- [60] R. Wojcieszak, M. Zieliński, S. Monteverdi, M.M. Bettahar, *Journal of Colloid and Interface Science*, 299 (2006) 238-248.
- [61] L. Wang, J. Zhang, X. Yi, A. Zheng, F. Deng, C. Chen, Y. Ji, F. Liu, X. Meng, F.-S. Xiao, *ACS Catalysis*, 5 (2015) 2727-2734.
- [62] Christopher M.A. Parlett, Mark A. Isaacs, Simon K. Beaumont, Laura M. Bingham, Nicole S. Hondow, K. Wilson, Adam F. Lee, *Nature Materials*, 15 (2015) 178.
- [63] S. Li, F. Huo, *Nanoscale*, 7 (2015) 7482-7501.
- [64] H.-C. Ma, J.-L. Kan, G.-J. Chen, C.-X. Chen, Y.-B. Dong, *Chemistry of Materials*, 29 (2017) 6518-6524.
- [65] T. Montini, M. Melchionna, M. Monai, P. Fornasiero, *Chemical Reviews*, 116 (2016) 5987-6041.
- [66] L. Zhou, X. Li, Z. Yao, Z. Chen, M. Hong, R. Zhu, Y. Liang, J. Zhao, *Scientific Reports*, 6 (2016) 23900.
- [67] A. Trovarelli, *Catalysis Reviews*, 38 (1996) 439-520.
- [68] M. Du, D. Sun, H. Yang, J. Huang, X. Jing, T. Odoom-Wubah, H. Wang, L. Jia, Q. Li, *The Journal of Physical Chemistry C*, 118 (2014) 19150-19157.
- [69] A.E.R.S. Khder, S.S. Ashour, H.M. Altass, K.S. Khairou, *Journal of Environmental Chemical Engineering*, 4 (2016) 4794-4800.
- [70] Y.-G. Wang, D.C. Cantu, M.-S. Lee, J. Li, V.-A. Glezakou, R. Rousseau, *Journal of the American Chemical Society*, 138 (2016) 10467-10476.
- [71] L. Yu, Y. Liu, F. Yang, J. Evans, J.A. Rodriguez, P. Liu, *The Journal of Physical Chemistry C*, 119 (2015) 16614-16622.
- [72] N. Gogoi, G. Borah, P.K. Gogoi, T.R. Chetia, *Chemical Physics Letters*, 692 (2018) 224-231.
- [73] N. Gogurla, A.K. Sinha, S. Santra, S. Manna, S.K. Ray, *Scientific Reports*, 4 (2014) 6483.
- [74] J. Jiao, Y. Wei, Z. Zhao, W. Zhong, J. Liu, J. Li, A. Duan, G. Jiang, *Catalysis Today*, 258 (2015) 319-326.
- [75] C.-Y. Su, Y.-C. Hsueh, C.-C. Kei, C.-T. Lin, T.-P. Perng, *The Journal of Physical Chemistry C*, 117 (2013) 11610-11618.
- [76] P. Huo, Z. Lu, X. Liu, X. Gao, J. Pan, D. Wu, J. Ying, H. Li, Y. Yan, *Chemical Engineering Journal*, 198-199 (2012) 73-80.
- [77] W.-N. Wang, W.-J. An, B. Ramalingam, S. Mukherjee, D.M. Niedzwiedzki, S. Gangopadhyay, P. Biswas, *Journal of the American Chemical Society*, 134 (2012) 11276-11281.
- [78] E.A. Kozlova, T.P. Lyubina, M.A. Nasalevich, A.V. Vorontsov, A.V. Miller, V.V. Kaichev, V.N. Parmon, *Catalysis Communications*, 12 (2011) 597-601.
- [79] Y.-H. Lin, Y.-C. Hsueh, C.-C. Wang, J.-M. Wu, T.-P. Perng, H.C. Shih, *Electrochemical and Solid-State Letters*, 13 (2010) K93-K95.
- [80] R. Vittal, K.-C. Ho, *Renewable and Sustainable Energy Reviews*, 70 (2017) 920-935.
- [81] C.B. Ong, L.Y. Ng, A.W. Mohammad, *Renewable and Sustainable Energy Reviews*, 81 (2018) 536-551.
- [82] M.B. Gawande, P.S. Branco, R.S. Varma, *Chemical Society Reviews*, 42 (2013) 3371-3393.

- [83] L. León Félix, J.A.H. Coaquira, M.A.R. Martínez, G.F. Goya, J. Mantilla, M.H. Sousa, L.d.I.S. Valladares, C.H.W. Barnes, P.C. Morais, *Scientific Reports*, 7 (2017) 41732.
- [84] M. Luo, S. Yuan, M. Tong, P. Liao, W. Xie, X. Xu, *Water Research*, 48 (2014) 190-199.
- [85] Y. Tuo, G. Liu, B. Dong, J. Zhou, A. Wang, J. Wang, R. Jin, H. Lv, Z. Dou, W. Huang, *Scientific Reports*, 5 (2015) 13515.
- [86] S. Yuan, Y. Fan, Y. Zhang, M. Tong, P. Liao, *Environmental Science & Technology*, 45 (2011) 8514-8520.
- [87] K. Blick, T.D. Mitrelias, J.S.J. Hargreaves, G.J. Hutchings, R.W. Joyner, C.J. Kiely, F.E. Wagner, *Catalysis Letters*, 50 (1998) 211-218.
- [88] Z. Wang, C. Xu, H. Wang, *Catalysis Letters*, 144 (2014) 1919-1929.
- [89] X. Zhang, H. Wang, B.-Q. Xu, *The Journal of Physical Chemistry B*, 109 (2005) 9678-9683.
- [90] R. Luque, A. Mariana Balu, J. Manuel Campelo, M. Dolores Gracia, E. Losada, A. Pineda, A. Angel Romero, J. Carlos Serrano-Ruiz, *Catalytic Applications of Mesoporous Silica-Based Materials*, in: *Catalysis: Volume 24, The Royal Society of Chemistry*, 2012, pp. 253-280.
- [91] A. Taguchi, F. Schüth, *Microporous and Mesoporous Materials*, 77 (2005) 1-45.
- [92] A. Brito, F.J. García, M.C. Alvarez-Galván, M.E. Borges, C. Díaz, V.A. de la Peña O'Shea, *Catalysis Communications*, 8 (2007) 2081-2086.
- [93] R. Gupta, V. Ganesan, *Sensors and Actuators B: Chemical*, 219 (2015) 139-145.
- [94] D.K. Mishra, A.A. Dabbawala, J.-S. Hwang, *Journal of Molecular Catalysis A: Chemical*, 376 (2013) 63-70.
- [95] D. Farrusseng, A. Tuel, *New Journal of Chemistry*, 40 (2016) 3933-3949.
- [96] H. Li, Z. Zheng, M. Cao, R. Cao, *Microporous and Mesoporous Materials*, 136 (2010) 42-49.
- [97] S. Li, A. Tuel, D. Laprune, F. Meunier, D. Farrusseng, *Chemistry of Materials*, 27 (2015) 276-282.
- [98] Z.A. Allothman, *Materials*, 5 (2012) 2874-2902.
- [99] Y. Lu, G. Cao, R.P. Kale, S. Prabakar, G.P. López, C.J. Brinker, *Chemistry of Materials*, 11 (1999) 1223-1229.
- [100] B.M. Weckhuysen, J. Yu, *Chemical Society Reviews*, 44 (2015) 7022-7024.
- [101] M. Govindhan, B.-R. Adhikari, A. Chen, *RSC Advances*, 4 (2014) 63741-63760.
- [102] R. Madhu, V. Veeramani, S.-M. Chen, *Scientific Reports*, 4 (2014) 4679.
- [103] M. Sevilla, A.B. Fuertes, R. Mokaya, *Energy & Environmental Science*, 4 (2011) 1400-1410.
- [104] C. Arino, N. Serrano, J.M. Diaz-Cruz, M. Esteban, *Analytica Chimica Acta*, 990 (2017) 11-53.
- [105] J. Deng, M.M. Li, Y. Wang, *Green Chemistry*, 18 (2016) 4824-4854.
- [106] T.K. Enock, C.K. King'ondeu, A. Pogrebnoi, Y.A.C. Jande, *International Journal of Electrochemistry*, (2017).
- [107] Z. Gao, Y.Y. Zhang, N.N. Song, X.D. Li, *Materials Research Letters*, 5 (2017) 69-88.
- [108] Y.Y. Lu, X.Q. Liang, C. Niyungeko, J.J. Zhou, J.M. Xu, G.M. Tian, *Talanta*, 178 (2018) 324-338.
- [109] R. Madhu, V. Veeramani, S.M. Chen, P. Veerakumar, S.B. Liu, N. Miyamoto, *Physical Chemistry Chemical Physics*, 18 (2016) 16466-16475.
- [110] J. Molina, F. Cases, L.M. Moretto, *Analytica Chimica Acta*, 946 (2016) 9-39.
- [111] P. Veerakumar, S.M. Chen, R. Madhu, V. Veeramani, C.T. Hung, S.B. Liu, *ACS Applied Materials & Interfaces*, 7 (2015) 24810-24821.
- [112] P. Veerakumar, I.P. Muthuselvam, C.T. Hung, K.C. Lin, F.C. Chou, S.B. Liu, *ACS Sustainable Chemistry & Engineering*, 4 (2016) 6772-6782.
- [113] P. Vijayakumar, M.S. Pandian, A. Pandikumar, P. Ramasamy, *Ceramics International*, 43 (2017) 8466-8474.

- [114] L.L. Xiao, S.H. Zhou, G.Z. Hu, H.B. Xu, Y. Wang, Q.H. Yuan, *RSC Advances*, 5 (2015) 77159-77167.
- [115] J.L. Figueiredo, M.F.R. Pereira, M.M.A. Freitas, J.J.M. Órfão, *Carbon*, 37 (1999) 1379-1389.
- [116] T. Gong, L. Qin, W. Zhang, H. Wan, J. Lu, H. Feng, *The Journal of Physical Chemistry C*, 119 (2015) 11544-11556.
- [117] P. Ramos Ferrer, A. Mace, S.N. Thomas, J.-W. Jeon, *Nano Convergence*, 4 (2017) 29.
- [118] K.S. Novoselov, A.K. Geim, S.V. Morozov, D. Jiang, Y. Zhang, S.V. Dubonos, I.V. Grigorieva, A.A. Firsov, *Science*, 306 (2004) 666-669.
- [119] R.H. Baughman, A.A. Zakhidov, W.A. de Heer, *Science*, 297 (2002) 787-792.
- [120] M. Pumera, *Chemical Society Reviews*, 39 (2010) 4146-4157.
- [121] C. Tan, X. Huang, H. Zhang, *Materials Today*, 16 (2013) 29-36.
- [122] X. Yu, H. Cheng, M. Zhang, Y. Zhao, L. Qu, G. Shi, *Nature Reviews Materials*, 2 (2017) 17046.
- [123] G. Goncalves, P.A.A.P. Marques, C.M. Granadeiro, H.I.S. Nogueira, M.K. Singh, J. Grácio, *Chemistry of Materials*, 21 (2009) 4796-4802.
- [124] X. Zhou, X. Huang, X. Qi, S. Wu, C. Xue, F.Y.C. Boey, Q. Yan, P. Chen, H. Zhang, *The Journal of Physical Chemistry C*, 113 (2009) 10842-10846.
- [125] B.K. Barman, K.K. Nanda, *ACS Sustainable Chemistry & Engineering*, 6 (2018) 4037-4045.
- [126] G.M. Scheuermann, L. Rumi, P. Steurer, W. Bannwarth, R. Mülhaupt, *Journal of the American Chemical Society*, 131 (2009) 8262-8270.
- [127] Z. Wei, R. Pan, Y. Hou, Y. Yang, Y. Liu, *Scientific Reports*, 5 (2015) 15664.
- [128] S. Guo, S. Dong, E. Wang, *ACS Nano*, 4 (2010) 547-555.
- [129] Z. Wang, X. Zhou, J. Zhang, F. Boey, H. Zhang, *The Journal of Physical Chemistry C*, 113 (2009) 14071-14075.
- [130] S. Hu, M. Lozada-Hidalgo, F.C. Wang, A. Mishchenko, F. Schedin, R.R. Nair, E.W. Hill, D.W. Boukhvalov, M.I. Katsnelson, R.A.W. Dryfe, I.V. Grigorieva, H.A. Wu, A.K. Geim, *Nature*, 516 (2014) 227.
- [131] M. Lozada-Hidalgo, S. Zhang, S. Hu, V.G. Kravets, F.J. Rodriguez, A. Berdyugin, A. Grigorenko, A.K. Geim, *Nature Nanotechnology*, (2018).
- [132] S. Guo, S. Sun, *Journal of the American Chemical Society*, 134 (2012) 2492-2495.
- [133] S. Guo, D. Wen, Y. Zhai, S. Dong, E. Wang, *ACS Nano*, 4 (2010) 3959-3968.
- [134] J.-D. Qiu, G.-C. Wang, R.-P. Liang, X.-H. Xia, H.-W. Yu, *The Journal of Physical Chemistry C*, 115 (2011) 15639-15645.
- [135] H. Qiu, X. Dong, B. Sana, T. Peng, D. Paramelle, P. Chen, S. Lim, *ACS Applied Materials & Interfaces*, 5 (2013) 782-787.
- [136] S.R. Batten, N.R. Champness, X.-M. Chen, J. Garcia-Martinez, S. Kitagawa, L. Ohrstrom, M. O'Keeffe, M.P. Suh, J. Reedijk, *CrystEngComm*, 14 (2012) 3001-3004.
- [137] O.M. Yaghi, M. O'Keeffe, N.W. Ockwig, H.K. Chae, M. Eddaoudi, J. Kim, *Nature*, 423 (2003) 705.
- [138] H. Furukawa, K.E. Cordova, M. O'Keeffe, O.M. Yaghi, *Science*, 341 (2013).
- [139] M. Rubio-Martinez, C. Avci-Camur, A.W. Thornton, I. Imaz, D. MasPOCH, M.R. Hill, *Chemical Society Reviews*, 46 (2017) 3453-3480.
- [140] P. Silva, S.M.F. Vilela, J.P.C. Tome, F.A. Almeida Paz, *Chemical Society Reviews*, 44 (2015) 6774-6803.
- [141] M.H. Yap, K.L. Fow, G.Z. Chen, *Green Energy & Environment*, 2 (2017) 218-245.
- [142] B. Li, H.-M. Wen, W. Zhou, B. Chen, *The Journal of Physical Chemistry Letters*, 5 (2014) 3468-3479.

- [143] G.Q. Kong, Z.D. Han, Y. He, S. Ou, W. Zhou, T. Yildirim, R. Krishna, C. Zou, B. Chen, C.D. Wu, *Chemistry – A European Journal*, 19 (2013) 14886-14894.
- [144] O.K. Farha, I. Eryazici, N.C. Jeong, B.G. Hauser, C.E. Wilmer, A.A. Sarjeant, R.Q. Snurr, S.T. Nguyen, A.Ö. Yazaydin, J.T. Hupp, *Journal of the American Chemical Society*, 134 (2012) 15016-15021.
- [145] A.E. Platero-Prats, A.B. League, V. Bernales, J. Ye, L.C. Gallington, A. Vjunov, N.M. Schweitzer, Z. Li, J. Zheng, B.L. Mehdi, A.J. Stevens, A. Dohnalkova, M. Balasubramanian, O.K. Farha, J.T. Hupp, N.D. Browning, J.L. Fulton, D.M. Camaioni, J.A. Lercher, D.G. Truhlar, L. Gagliardi, C.J. Cramer, K.W. Chapman, *Journal of the American Chemical Society*, 139 (2017) 10410-10418.
- [146] H. Li, K. Wang, Y. Sun, C.T. Lollar, J. Li, H.-C. Zhou, *Materials Today*, 21 (2018) 108-121.
- [147] K. Sumida, D.L. Rogow, J.A. Mason, T.M. McDonald, E.D. Bloch, Z.R. Herm, T.-H. Bae, J.R. Long, *Chemical Reviews*, 112 (2012) 724-781.
- [148] H. Furukawa, F. Gandara, Y.B. Zhang, J. Jiang, W.L. Queen, M.R. Hudson, O.M. Yaghi, *Journal of the American Chemical Society*, 136 (2014) 4369-4381.
- [149] L. Zhu, X.-Q. Liu, H.-L. Jiang, L.-B. Sun, *Chemical Reviews*, 117 (2017) 8129-8176.
- [150] H. Noei, S. Amirjalayer, M. Müller, X. Zhang, R. Schmid, M. Muhler, R.A. Fischer, Y. Wang, *ChemCatChem*, 4 (2012) 755-759.
- [151] P. Valvekens, M. Vandichel, M. Waroquier, V. Van Speybroeck, D. De Vos, *Journal of Catalysis*, 317 (2014) 1-10.
- [152] S.M. Cohen, *Chemical Reviews*, 112 (2012) 970-1000.
- [153] Z. Hu, B.J. Deibert, J. Li, *Chemical Society Reviews*, 43 (2014) 5815-5840.
- [154] L.E. Kreno, K. Leong, O.K. Farha, M. Allendorf, R.P. Van Duyne, J.T. Hupp, *Chemical Reviews*, 112 (2012) 1105-1125.
- [155] K.-J. Kim, P. Lu, J.T. Culp, P.R. Ohodnicki, *ACS Sensors*, 3 (2018) 386-394.
- [156] A. Volponi, S.G.d.S. Filho, in: 2015 30th Symposium on Microelectronics Technology and Devices (SBMicro), 2015, pp. 1-4.
- [157] Z. Xie, L. Ma, K.E. deKrafft, A. Jin, W. Lin, *Journal of the American Chemical Society*, 132 (2010) 922-923.
- [158] S. Sachdeva, S.J.H. Koper, A. Sabetghadam, D. Socol, D.J. Gravesteijn, F. Kapteijn, E.J.R. Sudhölter, J. Gascon, L.C.P.M. de Smet, *ACS Applied Materials & Interfaces*, 9 (2017) 24926-24935.
- [159] W. Vandezande, K.P.F. Janssen, F. Delpont, R. Ameloot, D.E. De Vos, J. Lammertyn, M.B.J. Roeffaers, *Analytical Chemistry*, 89 (2017) 4480-4487.
- [160] J.-J. Wu, Y.-X. Ye, Y.-Y. Qiu, Z.-P. Qiao, M.-L. Cao, B.-H. Ye, *Inorganic Chemistry*, 52 (2013) 6450-6456.
- [161] S.S. Nagarkar, B. Joarder, A.K. Chaudhari, S. Mukherjee, S.K. Ghosh, *Angewandte Chemie International Edition*, 52 (2013) 2881-2885.
- [162] P. Horcajada, T. Chalati, C. Serre, B. Gillet, C. Sebrie, T. Baati, J.F. Eubank, D. Heurtaux, P. Clayette, C. Kreuz, J.-S. Chang, Y.K. Hwang, V. Marsaud, P.-N. Bories, L. Cynober, S. Gil, G. Férey, P. Couvreur, R. Gref, *Nature Materials*, 9 (2009) 172.
- [163] P. Horcajada, C. Serre, M. Vallet-Regí, M. Sebban, F. Taulelle, G. Férey, *Angewandte Chemie International Edition*, 45 (2006) 5974-5978.
- [164] A.C. McKinlay, R.E. Morris, P. Horcajada, G. Férey, R. Gref, P. Couvreur, C. Serre, *Angewandte Chemie International Edition*, 49 (2010) 6260-6266.
- [165] H. Ren, L. Zhang, J. An, T. Wang, L. Li, X. Si, L. He, X. Wu, C. Wang, Z. Su, *Chemical Communications*, 50 (2014) 1000-1002.
- [166] J. Della Rocca, D. Liu, W. Lin, *Accounts of Chemical Research*, 44 (2011) 957-968.

- [167] P. Horcajada, R. Gref, T. Baati, P.K. Allan, G. Maurin, P. Couvreur, G. Férey, R.E. Morris, C. Serre, *Chemical Reviews*, 112 (2012) 1232-1268.
- [168] J. Wang, D. Chen, B. Li, J. He, D. Duan, D. Shao, M. Nie, *Scientific Reports*, 6 (2016) 26126.
- [169] E. Barea, C. Montoro, J.A.R. Navarro, *Chemical Society Reviews*, 43 (2014) 5419-5430.
- [170] M. Kurmoo, *Chemical Society Reviews*, 38 (2009) 1353-1379.
- [171] G. Xu, P. Nie, H. Dou, B. Ding, L. Li, X. Zhang, *Materials Today*, 20 (2017) 191-209.
- [172] M.A. Chowdhury, *ChemBioEng Reviews*, 4 (2017) 225-239.
- [173] Y. Cui, B. Li, H. He, W. Zhou, B. Chen, G. Qian, *Accounts of Chemical Research*, 49 (2016) 483-493.
- [174] Y. Cui, Y. Yue, G. Qian, B. Chen, *Chemical Reviews*, 112 (2012) 1126-1162.
- [175] S. Diring, A. Carné-Sánchez, J. Zhang, S. Ikemura, C. Kim, H. Inaba, S. Kitagawa, S. Furukawa, *Chemical Science*, 8 (2017) 2381-2386.
- [176] A.P. Côté, A.I. Benin, N.W. Ockwig, M. O'Keeffe, A.J. Matzger, O.M. Yaghi, *Science*, 310 (2005) 1166-1170.
- [177] S.-Y. Ding, W. Wang, *Chemical Society Reviews*, 42 (2013) 548-568.
- [178] H.M. El-Kaderi, J.R. Hunt, J.L. Mendoza-Cortés, A.P. Côté, R.E. Taylor, M. O'Keeffe, O.M. Yaghi, *Science*, 316 (2007) 268-272.
- [179] M.E. Davis, *Nature*, 417 (2002) 813.
- [180] A.I. Cooper, *Advanced Materials*, 21 (2009) 1291-1295.
- [181] N.B. McKeown, P.M. Budd, *Chemical Society Reviews*, 35 (2006) 675-683.
- [182] P. Kuhn, M. Antonietti, A. Thomas, *Angewandte Chemie International Edition*, 47 (2008) 3450-3453.
- [183] F.J. Uribe-Romo, J.R. Hunt, H. Furukawa, C. Klöck, M. O'Keeffe, O.M. Yaghi, *Journal of the American Chemical Society*, 131 (2009) 4570-4571.
- [184] F.J. Uribe-Romo, C.J. Doonan, H. Furukawa, K. Oisaki, O.M. Yaghi, *Journal of the American Chemical Society*, 133 (2011) 11478-11481.
- [185] B.M. Rambo, J.J. Lavigne, *Chemistry of Materials*, 19 (2007) 3732-3739.
- [186] E.L. Spitler, W.R. Dichtel, *Nature Chemistry*, 2 (2010) 672.
- [187] V. Singh, S. Jang, N.K. Vishwakarma, D.-P. Kim, *NPG Asia Materials*, 10 (2018) e456.
- [188] C.R. DeBlase, K.E. Silberstein, T.-T. Truong, H.D. Abruña, W.R. Dichtel, *Journal of the American Chemical Society*, 135 (2013) 16821-16824.
- [189] H. Wei, S. Chai, N. Hu, Z. Yang, L. Wei, L. Wang, *Chemical Communications*, 51 (2015) 12178-12181.
- [190] D. Rodríguez-San-Miguel, A. Abrishamkar, J.A.R. Navarro, R. Rodríguez-Trujillo, D.B. Amabilino, R. Mas-Ballesté, F. Zamora, J. Puigmartí-Luis, *Chemical Communications*, 52 (2016) 9212-9215.
- [191] B.P. Biswal, S. Chandra, S. Kandambeth, B. Lukose, T. Heine, R. Banerjee, *Journal of the American Chemical Society*, 135 (2013) 5328-5331.
- [192] S. Karak, S. Kandambeth, B.P. Biswal, H.S. Sasmal, S. Kumar, P. Pachfule, R. Banerjee, *Journal of the American Chemical Society*, 139 (2017) 1856-1862.
- [193] L. Garzon-Tovar, C. Avci-Camur, D. Rodríguez-San-Miguel, I. Imaz, F. Zamora, D. Maspoch, *Chemical Communications*, 53 (2017) 11372-11375.
- [194] S.S. Han, H. Furukawa, O.M. Yaghi, W.A. Goddard, *Journal of the American Chemical Society*, 130 (2008) 11580-11581.
- [195] J.L. Mendoza-Cortés, T.A. Pascal, W.A. Goddard, *The Journal of Physical Chemistry A*, 115 (2011) 13852-13857.
- [196] A. Sharma, A. Malani, N.V. Medhekar, R. Babarao, *CrystEngComm*, 19 (2017) 6950-6963.

- [197] C.J. Doonan, D.J. Tranchemontagne, T.G. Glover, J.R. Hunt, O.M. Yaghi, *Nature Chemistry*, 2 (2010) 235.
- [198] H. Li, Q. Pan, Y. Ma, X. Guan, M. Xue, Q. Fang, Y. Yan, V. Valtchev, S. Qiu, *Journal of the American Chemical Society*, 138 (2016) 14783-14788.
- [199] S.-Y. Ding, M. Dong, Y.-W. Wang, Y.-T. Chen, H.-Z. Wang, C.-Y. Su, W. Wang, *Journal of the American Chemical Society*, 138 (2016) 3031-3037.
- [200] S. Wan, J. Guo, J. Kim, H. Ihee, D. Jiang, *Angewandte Chemie International Edition*, 48 (2009) 5439-5442.
- [201] N. Huang, P. Wang, D. Jiang, *Nature Reviews Materials*, 1 (2016) 16068.
- [202] Q.-L. Zhu, Q. Xu, *Chemical Society Reviews*, 43 (2014) 5468-5512.
- [203] G. Lu, S. Li, Z. Guo, O.K. Farha, B.G. Hauser, X. Qi, Y. Wang, X. Wang, S. Han, X. Liu, J.S. DuChene, H. Zhang, Q. Zhang, X. Chen, J. Ma, S.C.J. Loo, W.D. Wei, Y. Yang, J.T. Hupp, F. Huo, *Nature Chemistry*, 4 (2012) 310-316.
- [204] A. Ahmed, M. Forster, R. Clowes, D. Bradshaw, P. Myers, H. Zhang, *Journal of Materials Chemistry A*, 1 (2013) 3276-3286.
- [205] P. Falcaro, A.J. Hill, K.M. Nairn, J. Jasieniak, J.I. Mardel, T.J. Bastow, S.C. Mayo, M. Gimona, D. Gomez, H.J. Whitfield, R. Ricco, A. Patelli, B. Marmiroli, H. Amenitsch, T. Colson, L. Villanova, D. Buso, *Nature Communications*, 2 (2011).
- [206] K. Sugikawa, S. Nagata, Y. Furukawa, K. Kokado, K. Sada, *Chemistry of Materials*, 25 (2013) 2565-2570.
- [207] G. Li, H. Kobayashi, J.M. Taylor, R. Ikeda, Y. Kubota, K. Kato, M. Takata, T. Yamamoto, S. Toh, S. Matsumura, H. Kitagawa, *Nature Materials*, 13 (2014) 802-806.
- [208] R. Ameloot, F. Vermoortele, W. Vanhove, M.B.J. Roeffaers, B.F. Sels, D.E. De Vos, *Nature Chemistry*, 3 (2011) 382-387.
- [209] K. Khaletskaya, J. Reboul, M. Meilikhov, M. Nakahama, S. Diring, M. Tsujimoto, S. Isoda, F. Kim, K.-i. Kamei, R.A. Fischer, S. Kitagawa, S. Furukawa, *Journal of the American Chemical Society*, 135 (2013) 10998-11005.
- [210] K. Liang, R. Ricco, C.M. Doherty, M.J. Styles, S. Bell, N. Kirby, S. Mudie, D. Haylock, A.J. Hill, C.J. Doonan, P. Falcaro, *Nature Communications*, 6 (2015).
- [211] K. Liang, J.J. Richardson, J. Cui, F. Caruso, C.J. Doonan, P. Falcaro, *Advance Materials*, 28 (2016) 7910-7914.
- [212] C. Gao, G. Lin, Z. Lei, Q. Zheng, J. Lin, Z. Lin, *Journal of Materials Chemistry B*, 5 (2017) 7496-7503.
- [213] P. Pachfule, S. Kandambeth, D. Diaz Diaz, R. Banerjee, *Chemical Communications*, 50 (2014) 3169-3172.
- [214] H. Deng, C.J. Doonan, H. Furukawa, R.B. Ferreira, J. Towne, C.B. Knobler, B. Wang, O.M. Yaghi, *Science*, 327 (2010) 846-850.
- [215] J.D. Evans, C.J. Sumby, C.J. Doonan, *Chemical Society Reviews*, 43 (2014) 5933-5951.
- [216] S. Hermes, F. Schroder, S. Amirjalayer, R. Schmid, R.A. Fischer, *Journal of Materials Chemistry*, 16 (2006) 2464-2472.
- [217] C. Rosler, R.A. Fischer, *CrystEngComm*, 17 (2015) 199-217.
- [218] M. Saikia, D. Bhuyan, L. Saikia, *New Journal of Chemistry*, 39 (2015) 64-67.
- [219] C. Zlotea, R. Campesi, F. Cuevas, E. Leroy, P. Dibandjo, C. Volkringer, T. Loiseau, G. Ferey, M. Latroche, *Journal of the American Chemical Society*, 132 (2010) 2991-2997.

- [220] L. He, L.F. Dumeé, D. Liu, L. Velleman, F. She, C. Banos, J.B. Davies, L. Kong, *RSC Advances*, 5 (2015) 10707-10715.
- [221] R.J.T. Houk, B.W. Jacobs, F. El Gabaly, N.N. Chang, A.A. Talin, D.D. Graham, S.D. House, I.M. Robertson, M.D. Allendorf, *Nano Letters*, 9 (2009) 3413-3418.
- [222] S. Hermes, M.K. Schroter, R. Schmid, L. Khodeir, M. Muhler, A. Tissler, R.W. Fischer, R.A. Fischer, *Angewandte Chemie International Edition*, 44 (2005) 6237-6241.
- [223] Q. Liang, J. Liu, Y. Wei, Z. Zhao, M.J. MacLachlan, *Chemical Communications*, 49 (2013) 8928-8930.
- [224] S. Nandi, S.K. Singh, D. Mullangi, R. Illathvalappil, L. George, C.P. Vinod, S. Kurungot, R. Vaidhyanathan, *Advanced Energy Materials*, 6 (2016) 1601189.
- [225] J. Reboul, S. Furukawa, N. Horike, M. Tsotsalas, K. Hirai, H. Uehara, M. Kondo, N. Louvain, O. Sakata, S. Kitagawa, *Nature Materials*, 11 (2012) 717-723.
- [226] C. Avci, A. Yazdi, M. Tarrés, E. Bernoud, N.G. Bastús, V. Puentes, I. Imaz, X. Ribas, D. MasPOCH, *ACS Applied Materials & Interfaces*, 10 (2018) 23952-23960.
- [227] Z. Li, H.C. Zeng, *Chemistry of Materials*, 25 (2013) 1761-1768.
- [228] A. Ayala, C. Carbonell, I. Imaz, D. MasPOCH, *Chemical Communications*, 52 (2016) 5096-5099.
- [229] K. Folens, K. Leus, N.R. Nicomel, M. Meledina, S. Turner, G. Van Tendeloo, G.D. Laing, P. Van Der Voort, *European Journal of Inorganic Chemistry*, 2016 (2016) 4395-4401.
- [230] M. Zhao, K. Yuan, Y. Wang, G. Li, J. Guo, L. Gu, W. Hu, H. Zhao, Z. Tang, *Nature*, 539 (2016) 76-80.
- [231] C.M. Doherty, D. Buso, A.J. Hill, S. Furukawa, S. Kitagawa, P. Falcaro, *Accounts of Chemical Research*, 47 (2014) 396-405.
- [232] S. Li, F. Huo, *Small*, 10 (2014) 4371-4378.
- [233] C.J. Stephenson, J.T. Hupp, O.K. Farha, *Inorganic Chemistry Frontiers*, 2 (2015) 448-452.
- [234] L. Chen, Y. Peng, H. Wang, Z. Gu, C. Duan, *Chemical Communications*, 50 (2014) 8651-8654.
- [235] P. Hu, J. Zhuang, L.Y. Chou, H.K. Lee, X.Y. Ling, Y.C. Chuang, C.K. Tsung, *Journal of the American Chemical Society*, 136 (2014) 10561-10564.
- [236] W. Zhang, G. Lu, C. Cui, Y. Liu, S. Li, W. Yan, C. Xing, Y.R. Chi, Y. Yang, F. Huo, *Advanced Materials*, 26 (2014) 4056-4060.
- [237] B. Rungtaweeworant, J. Baek, J.R. Araujo, B.S. Archanjo, K.M. Choi, O.M. Yaghi, G.A. Somorjai, *Nano Letters*, 16 (2016) 7645-7649.
- [238] F. Xu, S. Jin, H. Zhong, D. Wu, X. Yang, X. Chen, H. Wei, R. Fu, D. Jiang, *Scientific Reports*, 5 (2015) 8225.
- [239] P. Pachfule, S. Kandmabeth, A. Mallick, R. Banerjee, *Chemical Communications*, 51 (2015) 11717-11720.
- [240] J. Tan, S. Namuangruk, W. Kong, N. Kungwan, J. Guo, C. Wang, *Angewandte Chemie International Edition*, 55 (2016) 13979-13984.
- [241] X. Shi, Y. Yao, Y. Xu, K. Liu, G. Zhu, L. Chi, G. Lu, *ACS Applied Materials & Interfaces*, 9 (2017) 7481-7488.
- [242] A. Carné-Sánchez, I. Imaz, M. Cano-Sarabia, D. MasPOCH, *Nature Chemistry*, 5 (2013) 203-211.
- [243] V. Guillermin, L. Garzón-Tovar, A. Yazdi, I. Imaz, J. Juanhuix, D. MasPOCH, *Chemistry – A European Journal*, 23 (2017) 6829-6835.
- [244] L. Garzon-Tovar, M. Cano-Sarabia, A. Carne-Sanchez, C. Carbonell, I. Imaz, D. MasPOCH, *Reaction Chemistry & Engineering*, 1 (2016) 533-539.
- [245] T. Duren, L. Sarkisov, O.M. Yaghi, R.Q. Snurr, *Langmuir*, 20 (2004) 2683-2689.

- [246] J.L.C. Rowsell, O.M. Yaghi, *Angewandte Chemie International Edition*, 44 (2005) 4670-4679.
- [247] K. Sumida, D.L. Rogow, J.A. Mason, T.M. McDonald, E.D. Bloch, Z.R. Herm, T.-H. Bae, J.R. Long, *Chemical Reviews*, 112 (2012) 724-781.
- [248] M. Eddaoudi, J. Kim, N. Rosi, D. Vodak, J. Wachter, M. O'Keeffe, O.M. Yaghi, *Science*, 295 (2002) 469-472.
- [249] J.J. Hwang, *Renewable and Sustainable Energy Reviews*, 16 (2012) 3803-3815.
- [250] M. Yamauchi, H. Kobayashi, H. Kitagawa, *Chemphyschem*, 10 (2009) 2566-2576.
- [251] Y.W. Li, R.T. Yang, *Journal of the American Chemical Society*, 128 (2006) 726-727.
- [252] R. Prins, *Chemical Reviews*, 112 (2012) 2714-2738.
- [253] Y.W. Li, R.T. Yang, *Journal of the American Chemical Society*, 128 (2006) 8136-8137.
- [254] X.M. Liu, S.-u. Rather, Q. Li, A. Lueking, Y. Zhao, J. Li, *The Journal of Physical Chemistry C*, 116 (2012) 3477-3485.
- [255] Y.-Y. Liu, J.-L. Zeng, J. Zhang, F. Xu, L.-X. Sun, *International Journal of Hydrogen Energy*, 32 (2007) 4005-4010.
- [256] N.R. Stuckert, L. Wang, R.T. Yang, *Langmuir*, 26 (2010) 11963-11971.
- [257] C.-S. Tsao, M.-S. Yu, C.-Y. Wang, P.-Y. Liao, H.-L. Chen, U.S. Jeng, Y.-R. Tzeng, T.-Y. Chung, H.-C. Wut, *Journal of the American Chemical Society*, 131 (2009) 1404-+.
- [258] Y.E. Cheon, M.P. Suh, *Angewandte Chemie International Edition*, 48 (2009) 2899-2903.
- [259] M. Sabo, A. Henschel, H. Froede, E. Klemm, S. Kaskel, *Journal of Materials Chemistry*, 17 (2007) 3827-3832.
- [260] J.A. Villajos, G. Orcajo, G. Calleja, J.A. Botas, C. Martos, *International Journal of Hydrogen Energy*, 41 (2016) 19439-19446.
- [261] J. Jin, J. Ouyang, H. Yang, *Nanoscale Research Letters*, 12 (2017) 240.
- [262] A. Malouche, G. Blanita, D. Lupu, J. Bourgon, J. Nelayah, C. Zlotea, *Journal of Materials Chemistry A*, 5 (2017) 23043-23052.
- [263] S. Proch, J. Herrmannsdoerfer, R. Kempe, C. Kern, A. Jess, L. Seyfarth, J. Senker, *Chemistry-A European Journal*, 14 (2008) 8204-8212.
- [264] T.R. Anderson, E. Hawkins, P.D. Jones, *Endeavour*, 40 (2016) 178-187.
- [265] A.K. Adhikari, K.-S. Lin, *Chemical Engineering Journal*, 284 (2016) 1348-1360.
- [266] A. Lin, A.A. Ibrahim, P. Arab, H.M. El-Kaderi, M.S. El-Shall, *ACS Applied Materials & Interfaces*, 9 (2017) 17961-17968.
- [267] Z. Kang, L. Fan, D. Sun, *Journal of Materials Chemistry A*, 5 (2017) 10073-10091.
- [268] D. Banerjee, A.J. Cairns, J. Liu, R.K. Motkuri, S.K. Nune, C.A. Fernandez, R. Krishna, D.M. Strachan, P.K. Thallapally, *Accounts of Chemical Research*, 48 (2015) 211-219.
- [269] R. Grosse, R. Burmeister, B. Boddenberg, A. Gedeon, J. Fraissard, *Journal of Physical Chemistry*, 95 (1991) 2443-2447.
- [270] J. Liu, D.M. Strachan, P.K. Thallapally, *Chemical Communications*, 50 (2014) 466-468.
- [271] Z.-Y. Gu, C.-X. Yang, N. Chang, X.-P. Yan, *Accounts of Chemical Research*, 45 (2012) 734-745.
- [272] M. Palomino, A. Cantin, A. Corma, S. Leiva, F. Rey, S. Valencia, *Chemical Communications*, (2007) 1233-1235.
- [273] M.E. Silvestre, M. Franzreb, P.G. Weidler, O. Shekhah, C. Woell, *Advanced Functional Materials*, 23 (2013) 1210-1213.
- [274] C.W. Abney, K.M.L. Taylor-Pashow, S.R. Russell, Y. Chen, R. Samantaray, J.V. Lockard, W. Lin, *Chemistry of Materials*, 26 (2014) 5231-5243.

- [275] C.O. Audu, H.G.T. Nguyen, C.-Y. Chang, M.J. Katz, L. Mao, O.K. Farha, J.T. Hupp, S.T. Nguyen, *Chemical Science*, 7 (2016) 6492-6498.
- [276] J.B. DeCoste, G.W. Peterson, *Chemical Reviews*, 114 (2014) 5695-5727.
- [277] Q.-R. Fang, D.-Q. Yuan, J. Sculley, J.-R. Li, Z.-B. Han, H.-C. Zhou, *Inorganic Chemistry*, 49 (2010) 11637-11642.
- [278] M. Majumder, P. Sheath, J.I. Mardel, T.G. Harvey, A.W. Thornton, A. Gonzago, D.F. Kennedy, I. Madsen, J.W. Taylor, D.R. Turner, M.R. Hill, *Chemistry of Materials*, 24 (2012) 4647-4652.
- [279] M. Sarker, J.Y. Song, S.H. Jung, *Journal of Hazardous materials*, 335 (2017) 162-169.
- [280] E. Tahmasebi, M.Y. Masoomi, Y. Yamini, A. Morsali, *Inorganic Chemistry*, 54 (2015) 425-433.
- [281] E. Zanchetta, L. Malfatti, R. Ricco, M.J. Styles, F. Lisi, C.J. Coghlan, C.J. Doonan, A.J. Hill, G. Brusatin, P. Falcaro, *Chemistry of Materials*, 27 (2015) 690-699.
- [282] X. Zhu, B. Li, J. Yang, Y. Li, W. Zhao, J. Shi, J. Gu, *ACS Applied Materials & Interfaces*, 7 (2015) 223-231.
- [283] R. Ricco, L. Malfatti, M. Takahashi, A.J. Hill, P. Falcaro, *Journal of Materials Chemistry A*, 1 (2013) 13033-13045.
- [284] M.R. Lohe, K. Gedrich, T. Freudenberg, E. Kockrick, T. Dellmann, S. Kaskel, *Chemical Communications*, 47 (2011) 3075-3077.
- [285] P. Falcaro, F. Normandin, M. Takahashi, P. Scopece, H. Amenitsch, S. Costacurta, C.M. Doherty, J.S. Laird, M.D.H. Lay, F. Lisi, A.J. Hill, D. Buso, *Advanced Materials*, 23 (2011) 3901.
- [286] C.M. Doherty, E. Knystautas, D. Buso, L. Villanova, K. Konstas, A.J. Hill, M. Takahashi, P. Falcaro, *Journal of Materials Chemistry*, 22 (2012) 11470-11474.
- [287] S.-H. Huo, X.-P. Yan, *Analyst*, 137 (2012) 3445-3451.
- [288] X. Chen, N. Ding, H. Zang, H. Yeung, R.-S. Zhao, C. Cheng, J. Liu, T.W.D. Chan, *Journal of Chromatography A*, 1304 (2013) 241-245.
- [289] G.W. Bryan, W.J. Langston, *Environmental Pollution*, 76 (1992) 89-131.
- [290] L. Jarup, *British Medical Bulletin*, 68 (2003) 167-182.
- [291] M.R. Sohrabi, Z. Matbouie, A.A. Asgharinezhad, A. Dehghani, *Microchimica Acta*, 180 (2013) 589-597.
- [292] Y. Wang, J. Xie, Y. Wu, H. Ge, X. Hu, *Journal of Materials Chemistry A*, 1 (2013) 8782-8789.
- [293] M. Taghizadeh, A.A. Asgharinezhad, M. Pooladi, M. Barzin, A. Abbaszadeh, A. Tadjarodi, *Microchimica Acta*, 180 (2013) 1073-1084.
- [294] L. Huang, M. He, B. Chen, B. Hu, *Journal of Materials Chemistry A*, 3 (2015) 11587-11595.
- [295] P. Falcaro, F. Lapiere, B. Marmiroli, M. Styles, Y. Zhu, M. Takahashi, A.J. Hill, C.M. Doherty, *Journal of Materials Chemistry C*, 1 (2013) 42-45.
- [296] A. Bagheri, M. Taghizadeh, M. Behbahani, A.A. Asgharinezhad, M. Salarian, A. Dehghani, H. Ebrahimzadeh, M.M. Amini, *Talanta*, 99 (2012) 132-139.
- [297] L. Shen, W. Wu, R. Liang, R. Lin, L. Wu, *Nanoscale*, 5 (2013) 9374-9382.
- [298] E.I. Cedillo-Gonzalez, R. Ricco, M. Montorsi, M. Montorsi, P. Falcaro, C. Siligardi, *Building and Environment*, 71 (2014) 7-14.
- [299] M. Pelaez, N.T. Nolan, S.C. Pillai, M.K. Seery, P. Falaras, A.G. Kontos, P.S.M. Dunlop, J.W.J. Hamilton, J.A. Byrne, K. O'Shea, M.H. Entezari, D.D. Dionysiou, *Applied Catalysis B-Environmental*, 125 (2012) 331-349.
- [300] Y. Hu, Z. Huang, L. Zhou, D. Wang, G. Li, *Journal of Separation Science*, 37 (2014) 1482-1488.
- [301] T. Zeng, X. Zhang, S. Wang, H. Niu, Y. Cai, *Environmental Science & Technology*, 49 (2015) 2350-2357.

- [302] Z. Zhang, Y. Chen, X. Xu, J. Zhang, G. Xiang, W. He, X. Wang, *Angewandte Chemie International Edition*, 53 (2014) 429-433.
- [303] J.A. Kent, *Springer, Boston, MA*, (2007).
- [304] L. Lloyd, *Springer, Boston, MA*, (2011).
- [305] D. Astruc, F. Lu, J.R. Aranzaes, *Angewandte Chemie International Edition*, 44 (2005) 7852-7872.
- [306] S. Hermes, M.K. Schroter, R. Schmid, L. Khodeir, M. Muhler, A. Tissler, R.W. Fischer, R.A. Fischer, *Angewandte Chemie International Edition*, 44 (2005) 6237-6241.
- [307] M. Zhao, K. Deng, L. He, Y. Liu, G. Li, H. Zhao, Z. Tang, *Journal of the American Chemical Society*, 136 (2014) 1738-1741.
- [308] M. Homel, T.M. Gur, J.H. Koh, A.V. Virkar, *Journal of Power Sources*, 195 (2010) 6367-6372.
- [309] H.-L. Jiang, B. Liu, T. Akita, M. Haruta, H. Sakurai, Q. Xu, *Journal of the American Chemical Society*, 131 (2009) 11302-+.
- [310] E.V. Ramos-Fernandez, C. Pieters, B. van der Linden, J. Juan-Alcaniz, P. Serra-Crespo, M.W.G.M. Verhoeven, H. Niemantsverdriet, J. Gascon, F. Kapteijn, *Journal of Catalysis*, 289 (2012) 42-52.
- [311] A. Aijaz, T. Akita, N. Tsumori, Q. Xu, *Journal of the American Chemical Society*, 135 (2013) 16356-16359.
- [312] M.S. El-Shall, V. Abdelsayed, A.E.R.S. Khder, H.M.A. Hassan, H.M. El-Kaderi, T.E. Reich, *Journal of Materials Chemistry*, 19 (2009) 7625-7631.
- [313] W. Kleist, M. Maciejewski, A. Baiker, *Thermochimica Acta*, 499 (2010) 71-78.
- [314] A. Aijaz, A. Karkamkar, Y.J. Choi, N. Tsumori, E. Roennebro, T. Autrey, H. Shioyama, Q. Xu, *Journal of the American Chemical Society*, 134 (2012) 13926-13929.
- [315] J.Y. Kim, M. Jin, K.J. Lee, J.Y. Cheon, S.H. Joo, J.M. Kim, H.R. Moon, *Nanoscale Research Letters*, 7 (2012).
- [316] F. Schröder, D. Esken, M. Cokoja, M.W.E. van den Berg, O.I. Lebedev, G. Van Tendeloo, B. Walaszek, G. Buntkowsky, H.-H. Limbach, B. Chaudret, R.A. Fischer, *Journal of the American Chemical Society*, 130 (2008) 6119-6130.
- [317] M. Müller, S. Turner, O.I. Lebedev, Y. Wang, G. van Tendeloo, R.A. Fischer, *European Journal of Inorganic Chemistry*, 2011 (2011) 1876-1887.
- [318] T. Ishida, M. Nagaoka, T. Akita, M. Haruta, *Chemistry-A European Journal*, 14 (2008) 8456-8460.
- [319] H. Liu, L. Chang, L. Chen, Y. Li, *Journal of Materials Chemistry A*, 3 (2015) 8028-8033.
- [320] L. Chen, H. Chen, R. Luque, Y. Li, *Chemical Science*, 5 (2014) 3708-3714.
- [321] H. Liu, Y. Liu, Y. Li, Z. Tang, H. Jiang, *The Journal of Physical Chemistry C*, 114 (2010) 13362-13369.
- [322] D. Esken, S. Turner, O.I. Lebedev, G. Van Tendeloo, R.A. Fischer, *Chemistry of Materials*, 22 (2010) 6393-6401.
- [323] K. Leus, P. Concepcion, M. Vandichel, M. Meledina, A. Grrirane, D. Esquivel, S. Turner, D. Poelman, M. Waroquier, V. Van Speybroeck, G. Van Tendeloo, H. Garcia, P. Van Der Voort, *RSC Advances*, 5 (2015) 22334-22342.
- [324] S. Proch, J. Herrmannsdorfer, R. Kempe, C. Kern, A. Jess, L. Seyfarth, J. Senker, *Chemistry – A European Journal*, 14 (2008) 8204-8212.
- [325] Y. Luan, Y. Qi, H. Gao, N. Zheng, G. Wang, *Journal of Materials Chemistry A*, 2 (2014) 20588-20596.
- [326] J. Zhu, P.C. Wang, M. Lu, *Applied Catalysis A General*, 477 (2014) 125-131.
- [327] G. Chen, S. Wu, H. Liu, H. Jiang, Y. Li, *Green Chemistry*, 15 (2013) 230-235.
- [328] Z. Sun, G. Li, L. Liu, H.-o. Liu, *Catalysis Communications*, 27 (2012) 200-205.
- [329] J. Long, H. Liu, S. Wu, S. Liao, Y. Li, *ACS Catalysis*, 3 (2013) 647-654.

- [330] S. Fan, W. Dong, X. Huang, H. Gao, J. Wang, Z. Jin, J. Tang, G. Wang, *ACS Catalysis*, 7 (2016) 243-249.
- [331] Z. Gu, L. Chen, B. Duan, Q. Luo, J. Liu, C. Duan, *Chemical Communications*, 52 (2016) 116-119.
- [332] G.-J. Chen, X.-B. Li, C.-C. Zhao, H.-C. Ma, J.-L. Kan, Y.-B. Xin, C.-X. Chen, Y.-B. Dong, *Inorganic Chemistry*, 57 (2018) 2678-2685.
- [333] Y. Huang, Y. Zhang, X. Chen, D. Wu, Z. Yi, R. Cao, *Chemical Communications*, 50 (2014) 10115-10117.
- [334] H. Pan, X. Li, D. Zhang, Y. Guan, P. Wu, *Journal of Molecular Catalysis A-Chemical*, 377 (2013) 108-114.
- [335] J. Hermansdoerfer, M. Friedrich, R. Kempe, *Chemistry-A European Journal*, 19 (2013) 13652-13657.
- [336] P. Wang, J. Zhao, X. Li, Y. Yang, Q. Yang, C. Li, *Chemical Communications*, 49 (2013) 3330-3332.
- [337] L. Lin, T. Zhang, H. Liu, J. Qiu, X. Zhang, *Nanoscale*, 7 (2015) 7615-7623.
- [338] Q. Yang, Q. Xu, S.H. Yu, H.L. Jiang, *Angewandte Chemie International Edition*, 55 (2016) 3685-3689.
- [339] M. Wan, X. Zhang, M. Li, B. Chen, J. Yin, H. Jin, L. Lin, C. Chen, N. Zhang, *Small*, (2017).
- [340] M. Zhang, Y. Yang, C. Li, Q. Liu, C.T. Williams, C. Liang, *Catalysis Science & Technology*, 4 (2014) 329-332.
- [341] A. Henschel, K. Gedrich, R. Kraehnert, S. Kaskel, *Chemical Communications*, (2008) 4192-4194.
- [342] T.-H. Park, A.J. Hickman, K. Koh, S. Martin, A.G. Wong-Foy, M.S. Sanford, A.J. Matzger, *Journal of the American Chemical Society*, 133 (2011) 20138-20141.
- [343] W. Du, G. Chen, R. Nie, Y. Li, Z. Hou, *Catalysis Communications*, 41 (2013) 56-59.
- [344] C. Rosler, S. Dissegna, V.L. Rechac, M. Kauer, P. Guo, S. Turner, K. Ollegott, H. Kobayashi, T. Yamamoto, D. Peeters, Y. Wang, S. Matsumura, G. Van Tendeloo, H. Kitagawa, M. Muhler, I.X.F.X. Llabres, R.A. Fischer, *Chemistry – A European Journal*, 23 (2017) 3583-3594.
- [345] D. Zhang, Y. Guan, E.J.M. Hensen, L. Chen, Y. Wang, *Catalysis Communications*, 41 (2013) 47-51.
- [346] H.-L. Jiang, T. Akita, T. Ishida, M. Haruta, Q. Xu, *Journal of the American Chemical Society*, 133 (2011) 1304-1306.
- [347] F. Ke, J. Zhu, L.G. Qiu, X. Jiang, *Chemical Communications*, 49 (2013) 1267-1269.
- [348] J. Hermansdoerfer, M. Friedrich, N. Miyajima, R.Q. Albuquerque, S. Kuemmel, R. Kempe, *Angewandte Chemie International Edition*, 51 (2012) 11473-11477.
- [349] K.M. Choi, K. Na, G.A. Somorjai, O.M. Yaghi, *Journal of the American Chemical Society*, (2015).
- [350] H. Khajavi, H.A. Stil, H.P.C.E. Kuipers, J. Gascon, F. Kapteijn, *ACS Catalysis*, 3 (2013) 2617-2626.
- [351] X. Zhao, Y. Jin, F. Zhang, Y. Zhong, W. Zhu, *Chemical Engineering Journal*, 239 (2014) 33-41.
- [352] Y. Zhao, J. Zhang, J. Song, J. Li, J. Liu, T. Wu, P. Zhang, B. Han, *Green Chemistry*, 13 (2011) 2078-2082.
- [353] Y. Liu, W. Zhang, S. Li, C. Cui, J. Wu, H. Chen, F. Huo, *Chemistry of Materials*, 26 (2014) 1119-1125.
- [354] A. Aijaz, Q.-L. Zhu, N. Tsumori, T. Akita, Q. Xu, *Chemical Communications*, 51 (2015) 2577-2580.
- [355] Y. Huang, S. Liu, Z. Lin, W. Li, X. Li, R. Cao, *Journal of Catalysis*, 292 (2012) 111-117.
- [356] B. Yuan, Y. Pan, Y. Li, B. Yin, H. Jiang, *Angewandte Chemie International Edition*, 49 (2010) 4054-4058.
- [357] Y. Huang, Z. Zheng, T. Liu, J. Lu, Z. Lin, H. Li, R. Cao, *Catalysis Communications*, 14 (2011) 27-31.
- [358] V. Pascanu, Q. Yao, A.B. Gomez, M. Gustafsson, Y. Yun, W. Wan, L. Samain, X. Zou, B. Martin-Matute, *Chemistry-A European Journal*, 19 (2013) 17483-17493.

- [359] A.S. Roy, J. Mondal, B. Banerjee, P. Mondal, A. Bhaumik, S.M. Islam, *Applied Catalysis A General*, 469 (2014) 320-327.
- [360] Y.B. Huang, Q. Wang, J. Liang, X. Wang, R. Cao, *Journal of the American Chemical Society*, 138 (2016) 10104-10107.
- [361] D.R. Sun, Z.H. Li, *The Journal of Physical Chemistry C*, 120 (2016) 19744-19750.
- [362] W.H. Dong, L. Zhang, C.H. Wang, C. Feng, N.Z. Shang, S.T. Gao, C. Wang, *RSC Advances*, 6 (2016) 37118-37123.
- [363] S.-Y. Ding, J. Gao, Q. Wang, Y. Zhang, W.-G. Song, C.-Y. Su, W. Wang, *Journal of the American Chemical Society*, 133 (2011) 19816-19822.
- [364] S. Lu, Y. Hu, S. Wan, R. McCaffrey, Y. Jin, H. Gu, W. Zhang, *Journal of the American Chemical Society*, 139 (2017) 17082-17088.
- [365] S. Gao, N. Zhao, M. Shu, S. Che, *Applied Catalysis A General*, 388 (2010) 196-201.
- [366] Y. Huang, S. Gao, T. Liu, J. Lu, X. Lin, H. Li, R. Cao, *Chempluschem*, 77 (2012) 106-112.
- [367] D. Mullangi, S. Nandi, S. Shalini, S. Sreedhala, C.P. Vinod, R. Vaidhyanathan, *Scientific Reports*, 5 (2015) 10876.
- [368] Q.-L. Zhu, J. Li, Q. Xu, *Journal of the American Chemical Society*, 135 (2013) 10210-10213.
- [369] P.-Z. Li, K. Aranishi, Q. Xu, *Chemical Communications*, 48 (2012) 3173-3175.
- [370] A.K. Singh, Q. Xu, *Chemcatchem*, 5 (2013) 3000-3004.
- [371] X. Gu, Z.-H. Lu, H.-L. Jiang, T. Akita, Q. Xu, *Journal of the American Chemical Society*, 133 (2011) 11822-11825.
- [372] M. Martis, K. Mori, K. Fujiwara, W.-S. Ahn, H. Yamashita, *The Journal of Physical Chemistry C*, 117 (2013) 22805-22810.
- [373] M. Wen, K. Mori, T. Kamegawa, H. Yamashita, *Chemical Communications*, 50 (2014) 11645-11648.
- [374] M. Gulcan, M. Zahmakiran, S. Ozkar, *Applied Catalysis B-Environmental*, 147 (2014) 394-401.
- [375] K. Sabyrov, J. Jiang, O.M. Yaghi, G.A. Somorjai, *Journal of the American Chemical Society*, (2017).
- [376] J.P. Mehta, T. Tian, Z. Zeng, G. Divitini, B.M. Connolly, P.A. Midgley, J.-C. Tan, D. Fairen-Jimenez, A.E.H. Wheatley, *Advanced Functional Materials*, (2018) 1705588.
- [377] B. Wang, W. Liu, W. Zhang, J. Liu, *Nano Research*, (2017).
- [378] M. Yadav, Q. Xu, *Chemical Communications*, 49 (2013) 3327-3329.
- [379] M. Mueller, S. Hermes, K. Kaehler, M.W.E. van den Berg, M. Muhler, R.A. Fischer, *Chemistry of Materials*, 20 (2008) 4576-4587.
- [380] B. Rungtaweivoranit, J. Baek, J.R. Araujo, B.S. Archanjo, K.M. Choi, O.M. Yaghi, G.A. Somorjai, *Nano Letters*, (2016).
- [381] B. An, J. Zhang, K. Cheng, P. Ji, C. Wang, W. Lin, *Journal of the American Chemical Society*, 139 (2017) 3834-3840.
- [382] J.W. Maina, J.A. Schutz, L. Grundy, E. Des Ligneris, Z. Yi, L. Kong, C. Pozo-Gonzalo, M. Ionescu, L.F. Dumee, *ACS Appl Mater Interfaces*, 9 (2017) 35010-35017.
- [383] K. Na, K.M. Choi, O.M. Yaghi, G.A. Somorjai, *Nano Letters*, 14 (2014) 5979-5983.
- [384] F.G. Cirujano, A. Leyva-Perez, A. Corma, F.X. Llabres i Xamena, *Chemcatchem*, 5 (2013) 538-549.
- [385] T.T. Dang, Y. Zhu, J.S.Y. Ngiam, S.C. Ghosh, A. Chen, A.M. Seayad, *ACS Catalysis*, 3 (2013) 1406-1410.
- [386] T.T. Dang, Y. Zhu, S.C. Ghosh, A. Chen, C.L.L. Chai, A.M. Seayad, *Chemical Communications*, 48 (2012) 1805-1807.
- [387] H. Li, Z. Zhu, F. Zhang, S. Xie, H. Li, P. Li, X. Zhou, *ACS Catalysis*, 1 (2011) 1604-1612.

- [388] Y.K. Park, S.B. Choi, H.J. Nam, D.-Y. Jung, H.C. Ahn, K. Choi, H. Furukawa, J. Kim, *Chemical Communications*, 46 (2010) 3086-3088.
- [389] Y. Huang, Z. Lin, R. Cao, *Chemistry-A European Journal*, 17 (2011) 12706-12712.
- [390] M. Bhadra, H.S. Sasmal, A. Basu, S.P. Midya, S. Kandambeth, P. Pachfule, E. Balaraman, R. Banerjee, *ACS Applied Materials & Interfaces*, 9 (2017) 13785-13792.
- [391] C. Wang, K.E. deKrafft, W. Lin, *Journal of the American Chemical Society*, 134 (2012) 7211-7214.
- [392] Y. Horiuchi, T. Toyao, M. Saito, K. Mochizuki, M. Iwata, H. Higashimura, M. Anpo, M. Matsuoka, *The Journal of Physical Chemistry C*, 116 (2012) 20848-20853.
- [393] J. Hermansdoerfer, R. Kempe, *Chemistry-A European Journal*, 17 (2011) 8071-8077.
- [394] A. Riaz, G. Zahedi, J.J. Klemeš, *Journal of Cleaner Production*, 57 (2013) 19-37.

Chapter 2 - Objectives

The main objective of the present PhD Thesis is to optimize and develop the encapsulation methodologies for incorporating iNPs into MOFs and COFs. The first aim of this work is to optimize a common reported synthetic encapsulation methodology; to encapsulate iNPs into MOF frameworks, and to obtain a controllable crystal and shell thickness size of the MOF after the encapsulation process. Secondly, to develop a new continuous-flow methodology to encapsulate iNPs into MOFs on a larger scale, faster and with an enhanced encapsulation efficiency, using a spray-dryer. A further aim is to develop a synthetic method to confine various iNPs into another type of porous crystalline materials such as COF in a similar form of encapsulation to MOFs. Lastly, to test all the synthesized composites for different heterogeneous catalysis (CO oxidation and 4-nitrophenol reduction). To achieve these objectives, a series of partial objectives have been defined which they are summarized in the following:

- Synthesis and full characterization of a series of composites, which vary in size, made of encapsulated hollow Pd and Pt NPs in ZIF-8. Here, we aim to control the crystal size of ZIF-8 and the shell thickness of the composites; which is the distance between the encapsulated NPs in the center of the ZIF-8 and the outer layer of ZIF-8. Finally, following the catalytic activity of the synthesized composites in various sizes and shell thicknesses with two model reactions, such as reduction of 4-nitrophenol and Eosin Y and study the effect of the shell thickness on the reduction time.
- To develop a new methodology to encapsulate iNPs into MOFs using the spray-drying method. Here, we aim to encapsulate iNPs such as Pd and core shell NPs of Au/CeO₂ with different concentrations into UiO-66 beads. One of the main objectives of this project is to be able to encapsulate the NPs with maximum efficacy and a high yield. A subsequent objective is to test the catalytic activity of the synthesized composites with CO oxidation and utilize the high activity of Au/CeO₂ NPs for this reaction, and furthermore, to test the recyclability of the UiO-66@Au/CeO₂ for this reaction.
- To design, synthesize and fully characterize the composites made of iNPs and COFs. Here, we aim to develop a new synthetic method to confine various iNPs (Au, Pd and

Fe₃O₄) into the amorphous imine-linked polymer and then apply the post-treatment crystallization condition to these hybrid polymers to obtain a porous crystalline COF with encapsulated INPs. Finally, compare the catalytic activity of the polymeric composites to the crystalline composite by the reduction of 4-nitrophenol to 4-aminophenol.

Chapter 3 - The Influence of the MOF Shell Thickness on the Catalytic Performance of Composites Made of Inorganic (Hollow) Nanoparticles Encapsulated into MOFs

Cite this: *Catal. Sci. Technol.*, 2016, 6, 8388Received 29th September 2016,
Accepted 31st October 2016

DOI: 10.1039/c6cy02071b

www.rsc.org/catalysis

Herein we report the encapsulation of hollow Pt or Pd nanoparticles into ZIF-8, making a series of composites in which the ZIF-8 shell thickness has been systematically varied. By using these composites as catalysts for the reduction of 4-nitrophenol and Eosin Y, we show that the MOF shell thickness plays a key role in the catalytic performance of this class of composites.

The combination of two or more materials forming composites is a powerful strategy to create new materials with superior (multi)functions. With this aim, inorganic nanoparticles (iNPs) have recently been incorporated in metal-organic frameworks (MOFs) to create a new class of porous composites (hereafter called MOF@iNPs) with interesting applications in sensing, catalysis, plasmonics and pollutant sequestration and degradation.^{1,2} Among these applications, their use for heterogeneous catalysis is promising. Combining iNPs and MOFs overcomes some of the intrinsic problems of iNPs when used in catalysis,³ such as their tendency to aggregate, their low recyclability, and the difficulty to recover them from the reaction media. MOFs can support and protect them, thus facilitating their recovery from the bulk solution and preventing particle aggregation. In addition, the well-defined pore characteristics of MOFs can ideally permit the selective gating of the molecules that reach, and therefore react with the iNPs.

The most common methods to produce MOF@iNP composites include infiltration of the iNP precursors and subsequent growth of the iNPs inside the MOF,⁴ attachment of the iNPs onto the surface of the MOF,⁵ and the use of iNPs as nucleation centers to grow the MOF around them, thus encapsulating the iNPs into the synthesized MOFs. First reported

The influence of the MOF shell thickness on the catalytic performance of composites made of inorganic (hollow) nanoparticles encapsulated into MOFs†

A. Yazdi,^a F. Mercoçi,^a N. G. Bastús,^a I. Imaz,^a V. Puntes^{*abc} and D. Maspoch^{*ab}

by Huo *et al.*,⁶ this latter method is very versatile to design MOF@iNPs for heterogeneous catalysis applications since it allows using and protecting iNPs with no size, shape and nature restriction as well as controlling the number and localization of these iNPs inside the MOFs. For example, analogous ZIF-8@iNP composites have been successfully synthesized with Pt and Au NPs of different sizes (*e.g.* 2.5, 2.7, 3.3 and 4.1 nm for Pt; and 13, 15 and 34 nm for Au),^{6–8} Au NPs of different shapes (spheres and cubes), and iNPs of different nature (*e.g.* Au, Pt, Fe₃O₄, CdTe, CdSe and Pd).^{6,9} Also, ZIF-8@Au composites in which the embedded Au NPs are localized at the core (even at the single particle level) or spread over the ZIF-8 crystals have been generated.^{9–11}

To date, some advances have been made in using these MOF@iNP composites for heterogeneous catalysis. For example, ZIF-8@AuNP and ZIF-8@PtNP composites have been shown to be efficient catalysts for the oxidation of CO,⁶ the reduction of 4-nitrophenol (4-NP),^{9,12} the oxidation of benzyl alcohol,¹¹ and the hydrogenation of alkynes.⁷ Thus far, however, almost no one has paid special attention to the study of which parameters play a key role in the catalytic performance of these MOF@iNP composites. Farha *et al.* noticed that an increase of the external crystal surface of the MOF leads to an increase of the yield of the hydrogenation of alkynes.⁷ Here we report on the influence of the MOF shell thickness on the catalytic performance of this class of MOF@iNP composites. We postulate that this parameter must be critical for their catalytic properties since it has a direct impact on the accessibility and diffusion of the molecules to the iNPs. In this study, we chose ZIF-8 as the MOF, and hollow Pt and Pd NPs as the iNPs. We chose ZIF-8 because it has been widely used to produce MOF@iNP composites. And we chose hollow Pt and Pd NPs because they present some advantages over their solid counterparts in terms of lighter weight, conservation of the material, reduction of cost and superior catalytic activities associated with a nanoreactor cage effect and with the highly active uncapped and rough inner surfaces. In fact, they are excellent catalysts for the two model reactions

^a Catalan Institute of Nanoscience and Nanotechnology (ICN2), CSIC and The Barcelona Institute of Science and Technology, Campus UAB, Bellaterra, 08193 Barcelona, Spain. E-mail: victor.puntes@icn2.cat, daniel.maspoch@icn2.cat

^b ICREA, Pg. Lluís Companys 23, 08010 Barcelona, Spain

^c Vall, d'Hebron Institut de Recerca (VHIR), 08035, Barcelona, Spain

† Electronic supplementary information (ESI) available. See DOI: 10.1039/c6cy02071b

selected for this study: the reduction of 4-NP and the bulkier Eosin Y (EY). Reduction of 4-NP is a common reaction since it is usually used for the remediation of 4-NP, a water pollutant with high toxicity.¹³ Reduction of dye EY is a commonly used model reaction to probe the catalytic activity of iNPs.¹⁴

This study began with the systematic synthesis of a series of ZIF-8@PtNP and ZIF-8@PdNP composites, which vary in size (hereafter defined as $c = (c_1 + c_2)/2$; Fig. 1c, Table 1, and Experimental section, ESI†). In a typical synthesis, a methanolic dispersion containing hollow Pt NPs (diameter: 27.4 ± 2.0 nm; shell: 2.8 ± 0.6 nm; Fig. 1a) or hollow Pd NPs (diameter: 35.6 ± 3.8 nm; shell: 2.4 ± 0.4 nm; Fig. 1b), which were previously synthesized by galvanic replacement using Ag NPs as sacrificial templates (Experimental section and Fig. S1–S4, ESI†),^{15,16} was first prepared at a concentration of 0.25 mM and 0.3 mM, respectively. Then, 4 mL of these dispersions was introduced into different 20 mL methanolic solutions of 2-methylimidazole (2-MiM) (2-MiM concentrations: 6.5, 25, 37.5 and 50 mM for Pt; and 6.25, 25 and 50 mM for Pd). After 2 min, 20 mL of a methanolic solution of $\text{Zn}(\text{NO}_3)_2 \cdot 6\text{H}_2\text{O}$ (of equal molarity to 2-MiM) was added to these mixtures. The final mixtures were allowed to react at room temperature without stirring for 24 h. Finally, each one of the synthesized solids was collected by centrifugation (13 200 rcf), washed 2 times with methanol and dried overnight at 60 °C.

High angle annular dark field scanning transmission electron microscopy (HAADF-STEM) demonstrated the encapsulation of both hollow Pt and Pd NPs in the inner core of the ZIF-8 crystals with average diameters c ranging from 197 ± 26 nm to 1832 ± 270 nm, depending on the concentration of 2-MiM and $\text{Zn}(\text{NO}_3)_2 \cdot 6\text{H}_2\text{O}$ used (Table 1 and Fig. 2). In addition, they clearly showed that the number of encapsulated hollow Pd and Pt NPs per ZIF-8 crystal also increases when the concentrations of 2-MiM and $\text{Zn}(\text{NO}_3)_2 \cdot 6\text{H}_2\text{O}$ increase in the reaction. Thus, to measure the average MOF shell thickness of each sample, we first measure the distance (hereafter defined as distance a) from the centre of the ZIF-8 crystal to the NP located closer to the crystal surface (Fig. 1c). Then,

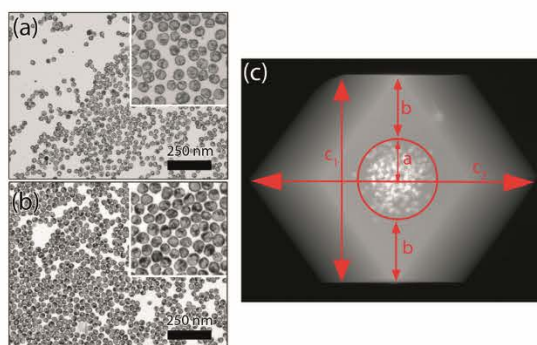


Fig. 1 HAADF-STEM images of (a) hollow Pt NPs, (b) hollow Pd NPs, and (c) a single ZIF-8@PdNP composite highlighting the dimensions shown in Table 1.

Table 1 Hollow Pt/Pd NP content and size distribution of the synthesized composites

Sample	c (nm)	b (nm)	a (nm)	NP w.t. (%)
ZIF-8@PtNP-1	284 ± 54	66 ± 42	76 ± 15	2.8
ZIF-8@PtNP-2	511 ± 87	156 ± 64	99 ± 21	1.0
ZIF-8@PtNP-3	746 ± 88	236 ± 64	137 ± 20	0.8
ZIF-8@PtNP-4	1832 ± 270	562 ± 198	354 ± 63	0.8
ZIF-8@PdNP-1	197 ± 26	55 ± 24	43 ± 11	1.8
ZIF-8@PdNP-2	453 ± 70	148 ± 50	78 ± 15	0.6
ZIF-8@PdNP-3	1689 ± 152	585 ± 135	259 ± 59	0.4

the average MOF shell thickness b of each composite was obtained from $b = c/2 - a$. In addition, the encapsulation of both hollow NPs was further confirmed by elemental mapping with energy dispersive X-ray spectrometry (EDX) on single composites, which revealed a uniform distribution of Zn atoms along the composite and the presence of Pt or Pd where the NPs are located (Fig. S5, ESI†). Finally, the percentage of Pt and Pd in each composite ($\% w_{\text{Pd/Pt}}/w_{\text{composite}}$) was measured by ICP-MS, whereas the formation of ZIF-8 in all composites was corroborated by powder X-ray diffraction (PXRD; Fig. S6, ESI†). The different parameters for all synthesized ZIF-8@PtNP and ZIF-8@PdNP composites are listed in Table 1.

To start evaluating the catalytic performance of the synthesized composites, we first studied the aqueous reduction of 4-NP to 4-aminophenol (4-AP) in the presence of NaBH_4 and of the composites. In this reaction, NaBH_4 is oxidized on the surface of the hollow NPs, provoking the reduction of 4-NP to 4-AP.¹⁷ This reduction can be simply followed by a reduction of the optical absorption at 400 nm corresponding to 4-NP.

The catalytic reactions were conducted at basic pH by mixing 0.5 mL of an aqueous solution of NaBH_4 (1.3 M) with 3.0 mL of an aqueous solution of 4-NP (0.125 mM). After 2 min, 0.2 mL of an aqueous dispersion containing ZIF-8@PtNP-1 at a Pt concentration of 2.8% w/w or ZIF-8@PdNP-1 at a Pd concentration of 1.8% w/w was injected into the reaction mixture, and the reaction was monitored every 10 min by UV-vis spectroscopy in the range of 280–460 nm (Fig. 2). It is important to highlight here that these reactions were monitored only for 30 min in the case of ZIF-8@PtNP-1 and for 40 min in the case of ZIF-8@PdNP-1 because this is the maximum time that the ZIF-8 shells of the composites remain unaltered, as was confirmed by Scanning Electron Microscopy (SEM; Fig. S8 and S14, ESI†). For longer times, etching of the external ZIF-8 shell was observed, increasing with time and finally exposing the hollow iNPs to the surface of the composites and releasing them. For both catalysts, the concentration of 4-NP at each time was determined using an extinction coefficient of $12.8 \times 10^3 \text{ M}^{-1} \text{ cm}^{-1}$ (Fig. S23, ESI†). The conversion efficiency ($4\text{-AP}/4\text{-NP}_0$) of each composite was then measured by difference.

Fig. 2 shows the evolution of the resulting UV-vis spectra. In both cases, we observed that the intensity of the absorption peak at 400 nm decreases with time while a new

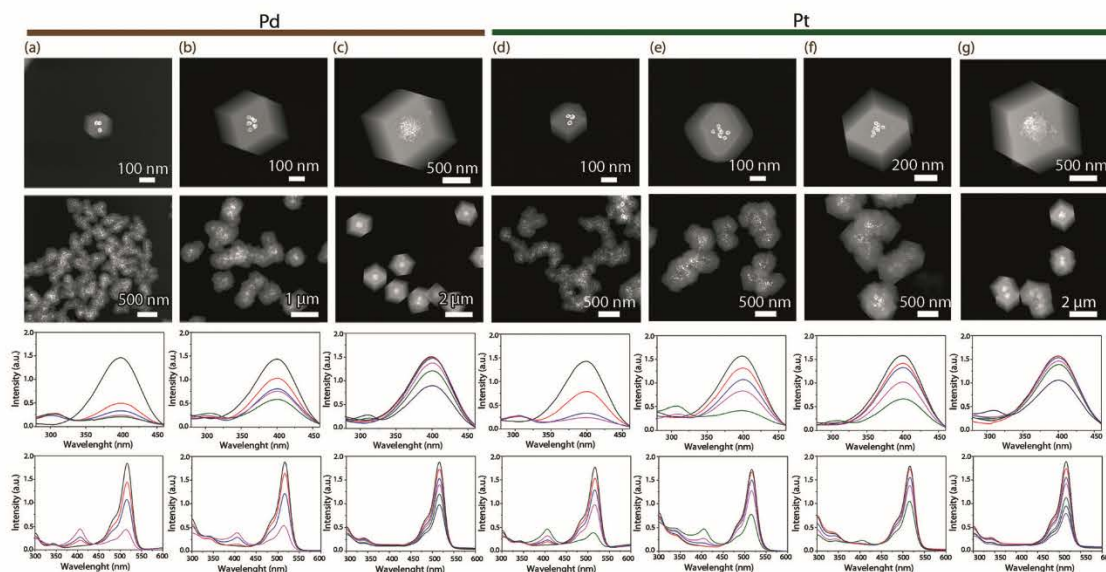


Fig. 2 HAADF-STEM images (first row: single composite; second row: general view) of (a) ZIF-8@PdNP-1, (b) ZIF-8@PdNP-2, (c) ZIF-8@PdNP-3, (d) ZIF-8@PtNP-1, (e) ZIF-8@PtNP-2, (f) ZIF-8@PtNP-3 and (g) ZIF-8@PtNP-4. Third and fourth rows show the UV-vis evolution of the 4-NP (third row) and EY^{2-} (fourth row) reduction using the corresponding composites as catalysts. In these spectra: 0 min (black); 10 min (red); 20 min (blue); 30 min (pink); 40 min (green); 50 min (navy); and 60 min (violet).

absorption peak at 305 nm characteristic of 4-AP appears after 10 min of reaction. The reduction of the peak at 400 nm also decreased with time, achieving maximum conversion efficiencies of 79% for ZIF-8@PtNP-1 and 83% for ZIF-8@PdNP-1. These results are important since they confirm that both reactants, 4-NP and $NaBH_4$, are able to cross the ZIF-8 shells, with thicknesses of 66 ± 42 nm and 55 ± 24 nm, and reach the catalytic hollow NPs.

To study if the ZIF-8 shell thickness has an effect on the catalytic performance of these composites, we then repeated the same reaction but using the composites with thicker ZIF-8 shells as catalysts. Each reaction was again run for the time that allowed the stability of the ZIF-8 shells (Fig. S8–22, ESI†). Fig. 3a and b show the evolution of the conversion efficiency for the different composites with time. A first clear observation is that, independently of the nature of the iNPs, the yield at a specific time decreases as the ZIF-8 shell thickness increases. For example, at 20 min, the conversion efficiencies were 0% for both ZIF-8@PtNP-4 and ZIF-8@PdNP-3 with thicknesses of 562 ± 198 nm and 585 ± 135 nm, respectively, 15% for ZIF-8@PtNP-3 with a thickness of 236 ± 64 nm, 30% for ZIF-8@PtNP-2 with a thickness of 156 ± 64 nm, 42% for ZIF-8@PdNP-2 with a thickness of 148 ± 50 nm, and 72% for ZIF-8@PdNP-1 and ZIF-8@PtNP-1 with thicknesses of 55 ± 24 nm and 66 ± 42 nm, respectively. Additional clear evidence from this data is that, independently of the nature of the iNPs, the time at which 4-AP starts to be formed increases as the ZIF-8 shell thickness also increases. Indeed, for the thicker composites, the formation of 4-AP was detected after 30 min of reaction.

Both observations agree well with the fact that the diffusion time of 4-NP and $NaBH_4$ molecules through the MOF shell to reach the surface of the hollow iNPs is a rate-determining step in the reduction of 4-NP when using these MOF@iNP composites. To further confirm this conclusion, we also studied the one-electron reduction of a bulkier

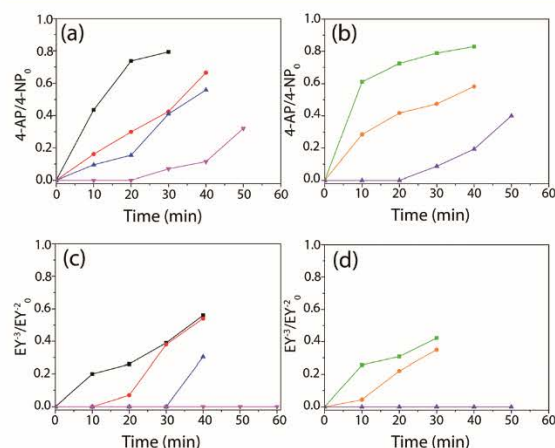


Fig. 3 (a and b) Variation of 4-AP/4-NP₀ conversion efficiency as a function of time when using (a) ZIF-8@PtNP and (b) ZIF-8@PdNP composites as catalysts. (c and d) Variation of EY^{3-}/EY^{2-} conversion efficiency as a function of time when using (c) ZIF-8@PtNP and (d) ZIF-8@PdNP composites as catalysts. Colour code: ZIF-8@PtNP-1 (black), ZIF-8@PtNP-2 (red), ZIF-8@PtNP-3 (blue), ZIF-8@PtNP-4 (pink), ZIF-8@PdNP-1 (green), ZIF-8@PdNP-2 (orange) and ZIF-8@PdNP-3 (violet).

molecule such as EY^{2-} in water and in the presence of $NaBH_4$ and the composites as catalysts. It is important to note here that, in the presence of $NaBH_4$ but not of hollow iNPs, the initial EY^{2-} species suffer a two-electron reduction forming the colourless species EY^{4-} , which can be followed by a reduction of the optical absorption at 516 nm corresponding to EY^{2-} . However, when both $NaBH_4$ and hollow NPs are present, the reduction pathway changes to a one-electron reduction forming EY^{3-} , whose formation can also be followed by not only the reduction of the peak at 516 nm but also the appearance of a new peak at 405 nm.¹⁴

Similar to the reduction of 4-NP, catalytic reactions to study the reduction of EY^{2-} were conducted by mixing 1.5 mL of an aqueous solution of EY^{2-} (4×10^{-5} M) with 0.6 mL of an aqueous dispersion containing ZIF-8@PtNP at a Pt concentration of 2.8% w/w or ZIF-8@PdNP at a Pd concentration of 1.8% w/w. Then, the volume of the resulting mixture was adjusted to 2.5 mL by the addition of 0.4 mL of deionized water. After 3 min, 0.5 mL of an aqueous solution of $NaBH_4$ (0.12 M) was injected into the reaction mixture, and the reaction was monitored every 10 min by UV-vis spectroscopy in the range of 300–600 nm (Fig. 2). For these reactions, the concentrations of EY^{2-} and EY^{3-} were determined using their previously reported extinction coefficients of 10.2×10^4 M⁻¹ cm⁻¹ and 4.5×10^4 M⁻¹ cm⁻¹,¹⁸ respectively. And the conversion efficiency (EY^{3-}/EY_0^{2-}) of each composite was measured by the ratio between the concentration of EY^{3-} at a given time and the initial concentration of EY^{2-} right after mixing all reactants.

Importantly, the general trends were very similar for both reduction reactions (Fig. 3). We found that the conversion rate EY^{3-}/EY_0^{2-} also increases as the ZIF-8 shell thickness decreases, and that the time at which EY^{3-} starts to be formed also increases as the ZIF-8 shell thickness increases. In particular, this latter trend is more evident in the formation of EY^{3-} . For example, in the case of ZIF-8@PtNP composites, the formation of EY^{3-} was detected at 10 min for a thickness of 66 ± 42 nm, at 20 min for a thickness of 156 ± 64 nm, and at 40 min for a thickness of 236 ± 64 nm. In the case of the thicker composite, we could not detect catalytic activity even after one hour of reaction. We attributed this behaviour to the bigger size of EY^{2-} in comparison with 4-NP, which makes its diffusion through the ZIF-8 shell more difficult.

In conclusion, we have determined that the MOF shell thickness is an important parameter to be considered when MOF@iNP composites are used as catalysts, as evidenced by the lower conversion efficiencies given for the composites with thicker shells at a certain time. Our findings suggest that decreasing the size (at the nanoscale) of these composites should facilitate the production of faster and more efficient catalysts. However, the smaller the composite, the lower the stability in time, which could prevent their recyclability. Nevertheless, this study clearly illustrates the importance of reporting the different size parameters (e.g. crystal size, MOF shell thickness, etc.) of MOF@iNP composites to obtain reproducible results when they are used in catalysis.

This work was supported by the Spanish MINECO (projects PN MAT2015-65354-C2-1-R and MAT2015-70725-R), the Catalan AGAUR (projects 2014-SGR-80 and 2014-SGR-612), and the ERC under the EU FP7 (ERC-Co 615954). I. I. and N. G. B. thank the MINECO for their RyC grants (RYC-2010-06530 and RYC-2012-10991). N. G. B. also acknowledges financial support by the European Commission Seventh Framework Programme (FP7) through the Marie Curie Career Integration Grant (322153-MINE). ICN2 acknowledges the support of the Spanish MINECO through the Severo Ochoa Centres of Excellence Programme, under Grant SEV-2013-0295.

Notes and references

- 1 C. R. Kim, T. Uemura and S. Kitagawa, *Chem. Soc. Rev.*, 2016, **45**, 3828–3845.
- 2 P. Falcaro, R. Ricco, A. Yazdi, I. Imaz, S. Furukawa, D. Maspocho, R. Ameloot, J. D. Evans and C. J. Doonan, *Coord. Chem. Rev.*, 2016, **307**(Part 2), 237–254.
- 3 Y. Xia, H. Yang and C. T. Campbell, *Acc. Chem. Res.*, 2013, **46**, 1671–1672.
- 4 A. Aijaz, A. Karkamkar, Y. J. Choi, N. Tsumori, E. Ronnebro, T. Autrey, H. Shioyama and Q. Xu, *J. Am. Chem. Soc.*, 2012, **134**, 13926–13929.
- 5 Z. Li and H. C. Zeng, *Chem. Mater.*, 2013, **25**, 1761–1768.
- 6 G. Lu, S. Li, Z. Guo, O. K. Farha, B. G. Hauser, X. Qi, Y. Wang, X. Wang, S. Han, X. Liu, J. S. DuChene, H. Zhang, Q. Zhang, X. Chen, J. Ma, S. C. Loo, W. D. Wei, Y. Yang, J. T. Hupp and F. Huo, *Nat. Chem.*, 2012, **4**, 310–316.
- 7 C. J. Stephenson, J. T. Hupp and O. K. Farha, *Inorg. Chem. Front.*, 2015, **2**, 448–452.
- 8 W. Zhang, Y. Liu, G. Lu, Y. Wang, S. Li, C. Cui, J. Wu, Z. Xu, D. Tian, W. Huang, J. S. DuChene, W. D. Wei, H. Chen, Y. Yang and F. Huo, *Adv. Mater.*, 2015, **27**, 2923–2929.
- 9 S. Li and F. Huo, *Small*, 2014, **10**, 4371–4378.
- 10 P. Hu, J. Zhuang, L. Y. Chou, H. K. Lee, X. Y. Ling, Y. C. Chuang and C. K. Tsung, *J. Am. Chem. Soc.*, 2014, **136**, 10561–10564.
- 11 L. Chen, Y. Peng, H. Wang, Z. Gu and C. Duan, *Chem. Commun.*, 2014, **50**, 8651–8654.
- 12 W. Zhang, G. Lu, C. Cui, Y. Liu, S. Li, W. Yan, C. Xing, Y. R. Chi, Y. Yang and F. Huo, *Adv. Mater.*, 2014, **26**, 4056–4060.
- 13 S. M. El-Sheikh, A. A. Ismail and J. F. Al-Sharab, *New J. Chem.*, 2013, **37**, 2399–2407.
- 14 G. Weng, M. A. Mahmoud and M. A. El-Sayed, *J. Phys. Chem. C*, 2012, **116**, 24171–24176.
- 15 E. Gonzalez, F. Merkoci, R. Arenal, J. Arbiol, J. Esteve, N. G. Bastus and V. Puntes, *J. Mater. Chem. A*, 2016, **4**, 200–208.
- 16 N. G. Bastús, F. Merkoçi, J. Piella and V. Puntes, *Chem. Mater.*, 2014, **26**, 2836–2846.
- 17 M. A. Mahmoud, B. Garlyyev and M. A. El-Sayed, *J. Phys. Chem. C*, 2013, **117**, 21886–21893.
- 18 J. Zhang, L. Sun and T. Yoshida, *J. Electroanal. Chem.*, 2011, **662**, 384–395.

Supplementary Information

The influence of the MOF shell thickness in the catalytic performance of composites made of inorganic (hollow) nanoparticles encapsulated into MOFs

Amirali Yazdi, Florind Merkoci, Neus Bastus, Inhar Imaz, Victor Puentes, and Daniel Maspoch

Experimental details

Materials

All reagent and solvents used were purchased from Sigma Aldrich and used without further purification.

Synthesis of hollow nanoparticles

Synthesis of silver nanoparticles (Ag NPs): Ag NPs of ~ 24 nm in diameter were prepared by scaling up the seeded-growth method previously reported by Bastús *et al.*¹ In this method, silver seeds were first obtained by filling a three-neck round-bottomed flask with 750 mL of an aqueous solution containing 5 mM sodium citrate (SC) and 0.1 mM of tannic acid (TA). This mixture was then heated up to 100 °C using a heating mantle. After boiling had started, 7.5 mL of 25 mM AgNO₃ was injected into this solution under vigorous stirring. The obtained silver seeds were then grown by cooling down the solution to 90 °C, and sequentially injecting 0.75 mL of 25 mM SC, 1.875 mL of 2.5 mM TA and 1.875 mL of 25 mM AgNO₃. This process was repeated up to four times, progressively growing the Ag NPs up to ~ 24 nm. The obtained Ag NPs were purified by centrifugation and further re-suspended in water. See Figure S1 for STEM images.

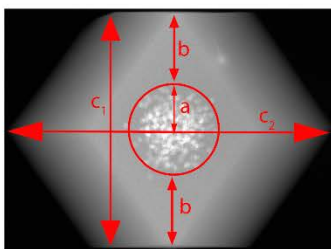
Synthesis of hollow nanoparticles: The standard protocol for the preparation of hollow nanoparticles consisted in two simple steps. First, 200 mL of the synthesized Ag NPs solution were precipitated by centrifugation, re-dispersed in 15 mL of PVP (5 mM, 275 mg/mL), and the resulting solution was left in a glass vial under soft stirring for 24 h. And second, 2.5 mL of HCl (250 mM) and 0.5 mL of 1 mM of K₂PtCl₄ or K₂PdCl₆ were simultaneously added into this solution. After this very first injection, an additional volume of 9.5 mL of the precursor was added into the vial in 19 consecutive 0.5 mL injections with a time delay of 5 min between each one. During the whole process, the solution was kept under vigorous stirring at room temperature until the reaction was completed; which can be clearly identified by a progressive change in color: from yellow (Ag NPs) to dark gray in the case of the hollow Pt NPs, and from yellow to blue/purple for the hollow Pd NPs. See Figure S2 for the schematic representation of this synthetic process.

Purification of the hollow nanoparticles: 20 min after the last precursor injection, the solution was diluted by adding 16 mL of mQ-water and 4 mL of acetone, and then centrifuged at 10,000 g for 60 min. The supernatant was then removed to discard the unreacted precursor species, and the pellet was re-dispersed in 10 mL of 5 mM PVP. After that, the solution was supersaturated with NaCl and gently stirred for 30 min to remove the insoluble AgCl (by-product of the galvanic reaction) from the hollow NP surface. The obtained hollow NPs were then precipitated and re-suspended in mQ-water three times to get rid of the excess PVP in solution. Finally, the solution was left overnight without stirring to let possible remaining AgCl to precipitate at the bottom of the vial (white pellet), which was finally discarded.

Size determination of the composites

The size of the rhombic dodecahedral MOF@iNP composites (defined as c) was calculated by the average of the distance between opposite vertices (c_2) and the distance between opposite rhombic faces (c_1). The average MOF shell thickness b of each composite was obtained from $b = c/2 - a$ ($\Delta b = \Delta c/2 + \Delta a$).

$$c = (c_1 + c_2) / 2$$



Reduction of 4-nitrophenol

The catalytic reactions were conducted by mixing 0.5 mL of an aqueous solution of NaBH_4 (1.3 M) with 3.0 mL of an aqueous solution of 4-NP (0.125 mM). After 2 min, 0.2 mL of an aqueous solution of 0.6, 1.68, 2.1 and 2.1 $\text{mg}\cdot\text{mL}^{-1}$ of ZIF-8@PtNP-1, ZIF-8@PtNP-2, ZIF-8@PtNP-3 and ZIF-8@PtNP-4, respectively, and 0.4, 1.1 and 1.76 $\text{mg}\cdot\text{mL}^{-1}$ of ZIF-8@PdNP-1, ZIF-8@PdNP-2 and ZIF-8@PdNP-3, respectively, were injected into the reaction mixture, and the reaction was followed every 10 min by UV-vis spectroscopy in the range of 280–460 nm.²

Reduction of Eosin Y

The catalytic reactions to study the reduction of EY^{2-} were conducted by mixing 1.5 mL of an aqueous solution of EY^{2-} (4×10^{-5} M) with 0.6 mL of an aqueous solution of 0.6, 1.68, 2.1 and 2.1 $\text{mg}\cdot\text{mL}^{-1}$ of ZIF-8@PtNP-1, ZIF-8@PtNP-2, ZIF-8@PtNP-3 and ZIF-8@PtNP-4, respectively, and 0.4, 1.1 and 1.76 $\text{mg}\cdot\text{mL}^{-1}$ of ZIF-8@PdNP-1, ZIF-8@PdNP-2 and ZIF-8@PdNP-3, respectively. Then, the volume of the resulting mixture was adjusted to 2.5 mL by the addition of 0.4 mL of deionized water. After 3 min, 0.5 mL of an aqueous solution of NaBH_4 (0.12 M)

was injected into the reaction mixture, and the reaction was followed every 10 min by UV-vis spectroscopy in the range of 300–600 nm.³

Characterization

Field-emission scanning electron microscopy (FESEM) images were collected on a scanning electron microscope (FEI Magellan 400L XHR) at acceleration voltage of 2.0 kV, using aluminium as support. The size of crystals was calculated from high angle annular dark field scanning transmission electron microscope (HAADF-STEM) images by averaging the diameter of at least 100 particles from images of different areas of the same samples. HAADF-STEM and TEM images and EDX composition profiles were collected on a Transmission Electron Microscopy (TEM; FEI Tecnai G2 F20) at 200 KV. X-ray powder diffraction (XRPD) measurements were performed using an X'Pert PRO MPDP analytical diffractometer. ICP-MS measurements were performed using an ICP_MS Agilent Serie 7500. UV-Vis Spectroscopy. UV-visible spectra were acquired with a Shimadzu UV-2400 spectrophotometer. Samples were placed in a cell, and spectral analysis was performed at room temperature.

References

1. N. G. Bastús, F. Merkoçi, J. Piella and V. Puntes, *Chemistry of Materials*, 2014, **26**, 2836-2846.
2. Z. Li and H. C. Zeng, *Chemistry of Materials*, 2013, **25**, 1761-1768.
3. G. Weng, M. A. Mahmoud and M. A. El-Sayed, *The Journal of Physical Chemistry C*, 2012, **116**, 24171-24176.

Figure S1. STEM images of the Ag NPs used as templates for the synthesis of the hollow Pt and Pd NPs. Inset shows the size distribution after counting more than 600 NPs.

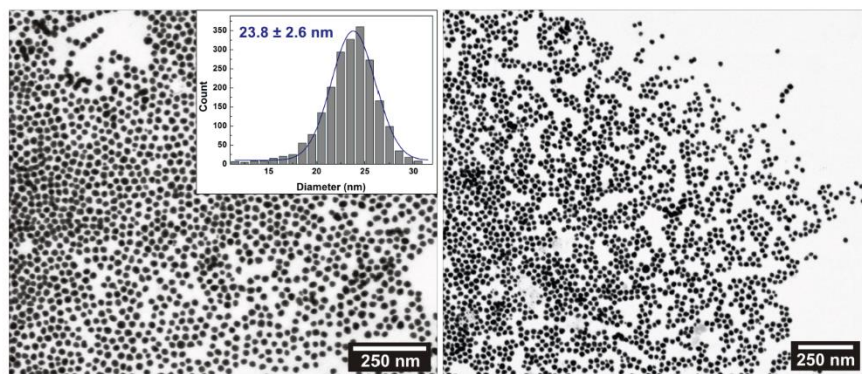


Figure S2. Schematic procedure of the synthesis of the hollow Pt and Pd NPs.

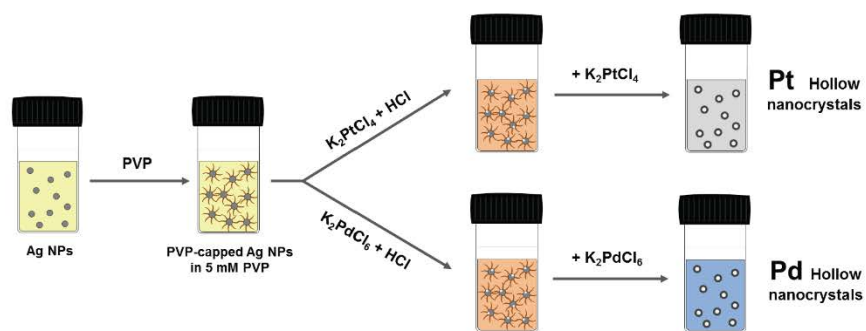


Figure S3. (a) TEM images of the synthesized hollow Pt NPs; and (b) corresponding size distribution of both diameter and shell thickness.

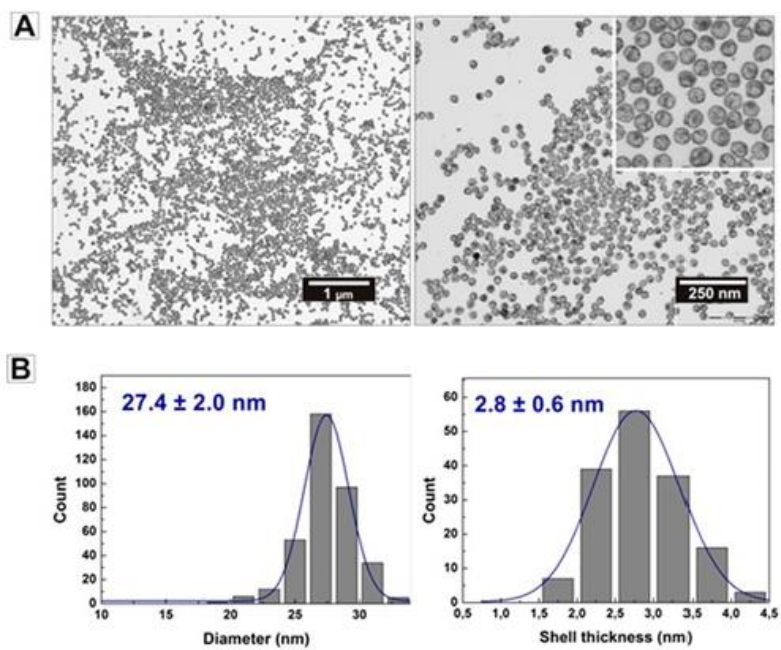


Figure S4. (a) STEM images of the synthesized hollow Pd NPs; and (b) corresponding size distribution of both diameter and shell thickness.

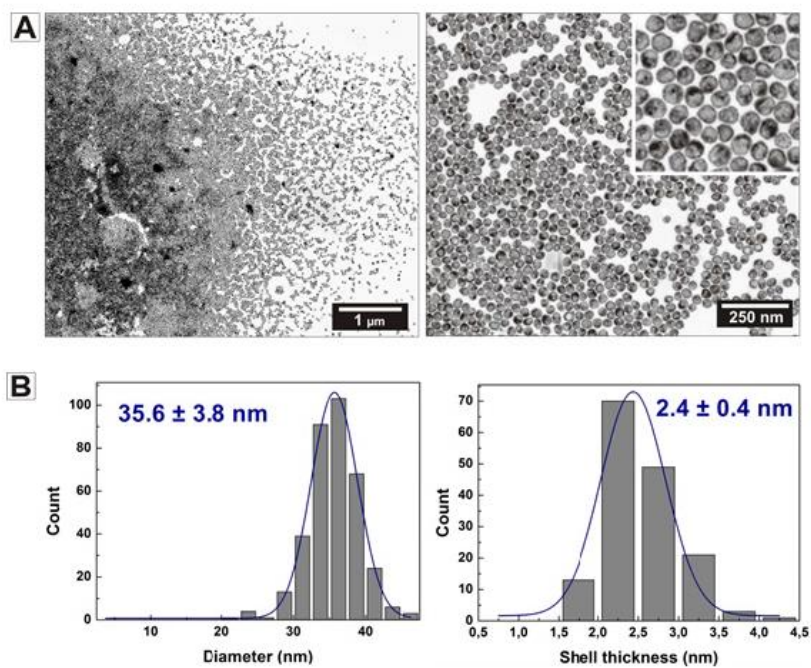


Figure S5. EDX profile of (a) ZIF-8@PtNP-3 and (b) ZIF-8@PdNP-2.

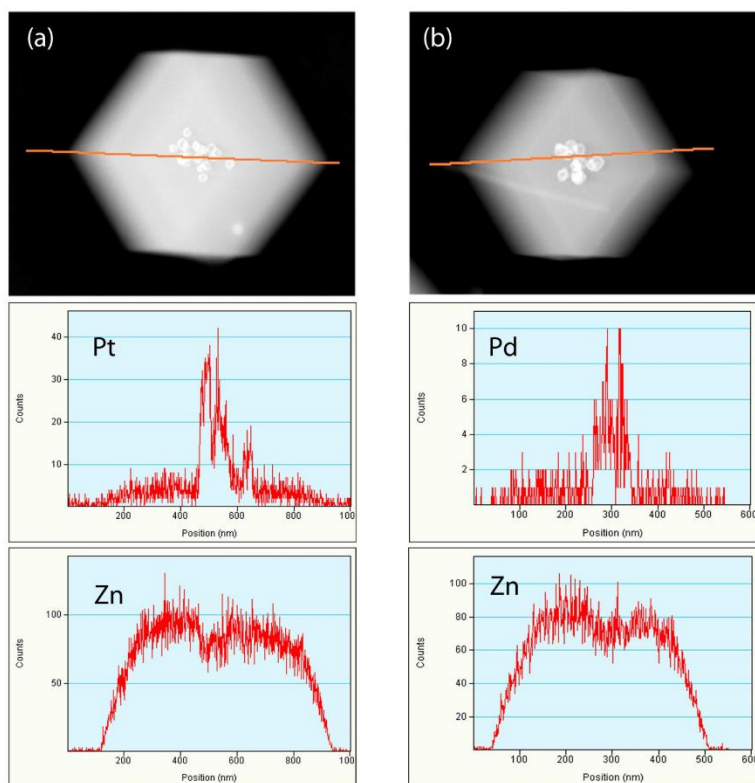


Figure S6. X-Ray Powder Diffraction (XRPD) patterns of ZIF-8@PtNP and ZIF-8@PdNP composites, as compared to the simulated pattern for the crystal structure of ZIF-8 (black).

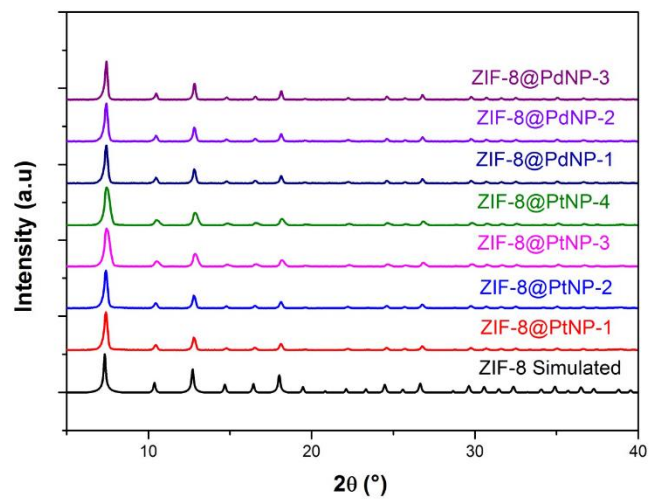


Figure S7. UV-vis spectra evolution of the EY^{2-} reduction with $NaBH_4$ in the absence of hollow iNPs as catalysts: in (a), with the presence of 3 mg of ZIF-8; and in (b), with the absence of ZIF-8. For all spectra: 0 min (black), 10 min (red), 20 min (blue), 30 min (pink), 40 min (green), and 50 min (navy). Both control experiments confirm that the reduced EY^{3-} (peak at 405 nm) is not formed in the absence of hollow iNPs.

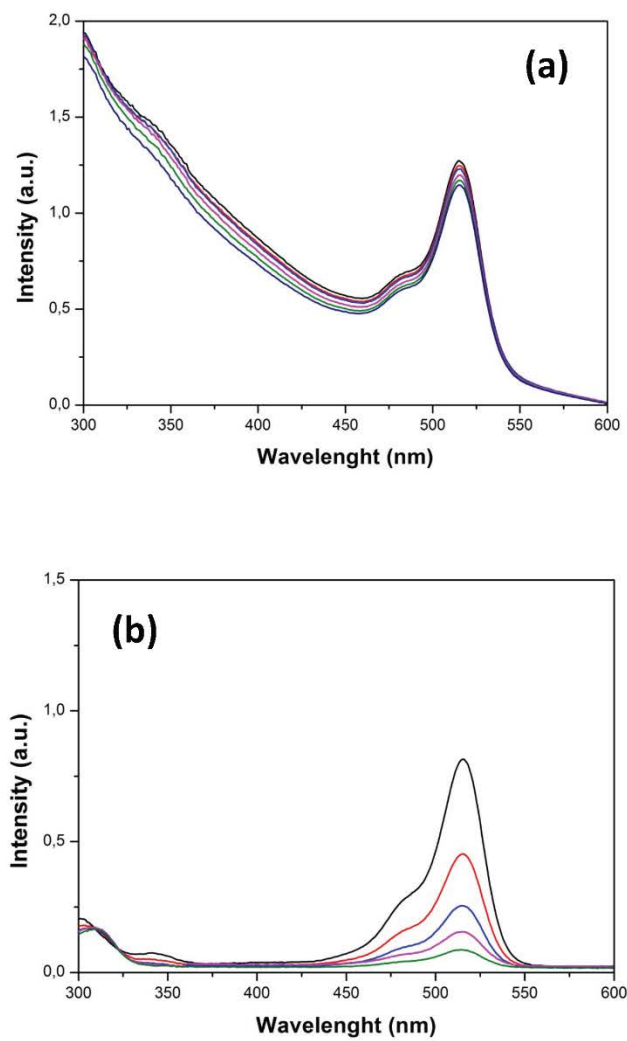


Figure S8. FESEM images of ZIF-8@PdNP-1 after (a) 10 min, (b) 20 min, (c) 30 min, (d) 40 min and (e) 50 min of 4-*NP* reduction. White arrows in (e) highlight the etching of ZIF-8. Scale bars for all images are 1 μm .

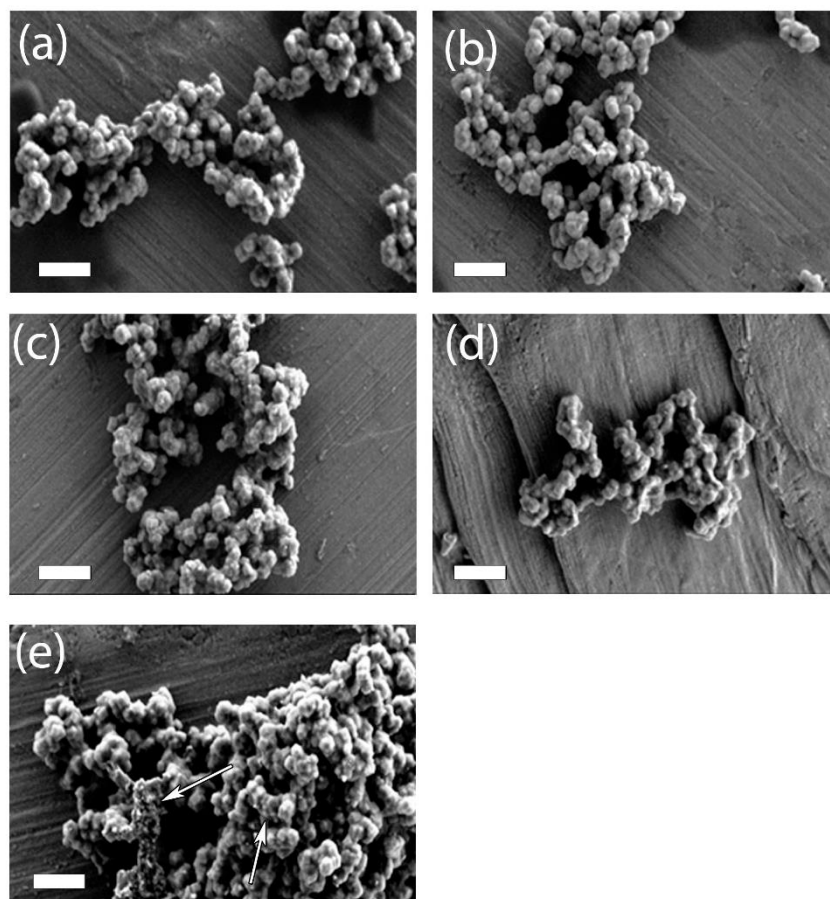


Figure S9. FESEM images of ZIF-8@PdNP-1 after (a) 10 min, (b) 20 min, (c) 30 min and (d) 40 min of EY reduction. White arrows in (d) highlight the etching of ZIF-8. Scale bars for all images are 1 μm .

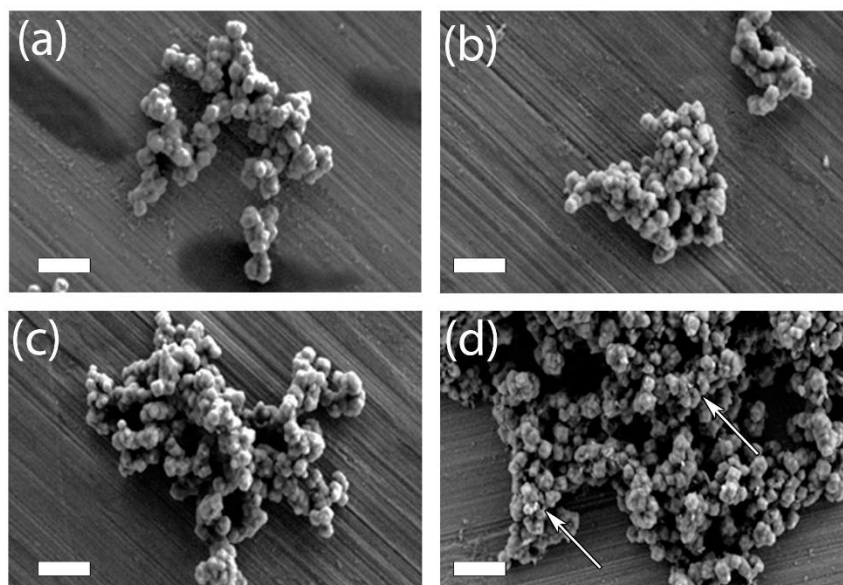


Figure S10. FESEM images of ZIF-8@PdNP-2 after (a) 10 min, (b) 20 min, (c) 30 min, (d) 40 min and (e) 50 min of 4-NP reduction. White arrows in (e) highlight the etching of ZIF-8. Scale bars for all images are 1 μm .

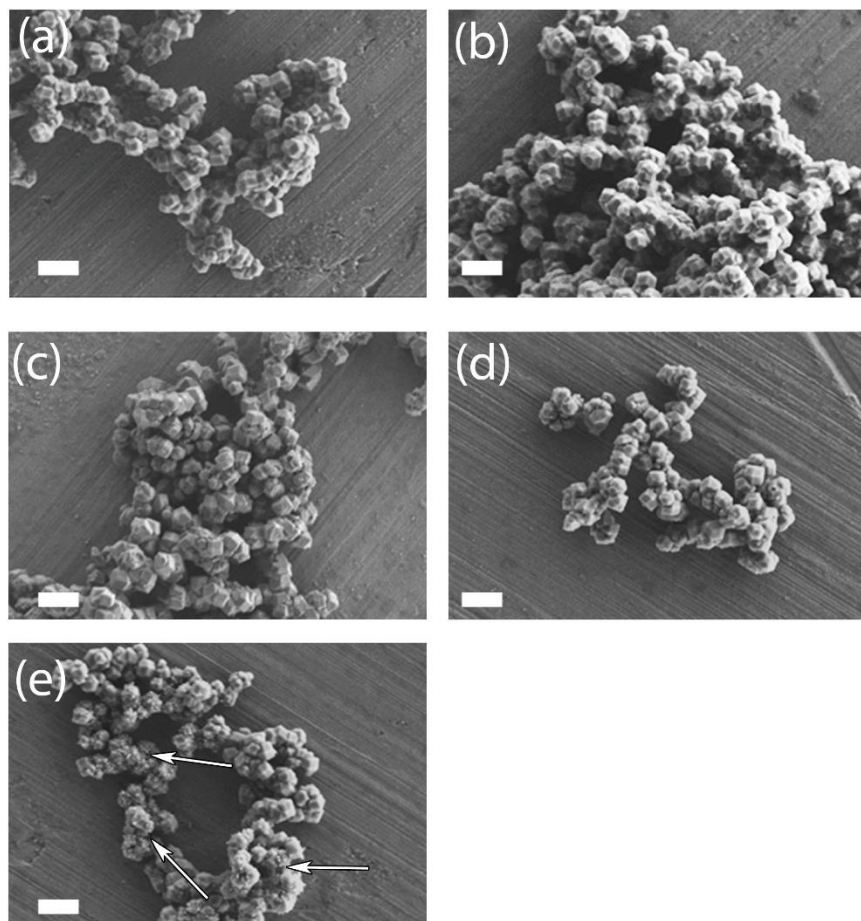


Figure S11. FESEM images of ZIF-8@PdNP-2 after (a) 10 min, (b) 20 min, (c) 30 min, (d) 40 min and (e) 50 min of EY reduction. White arrows in (e) highlight the etching of ZIF-8. Scale bars for all images are 1 μm .

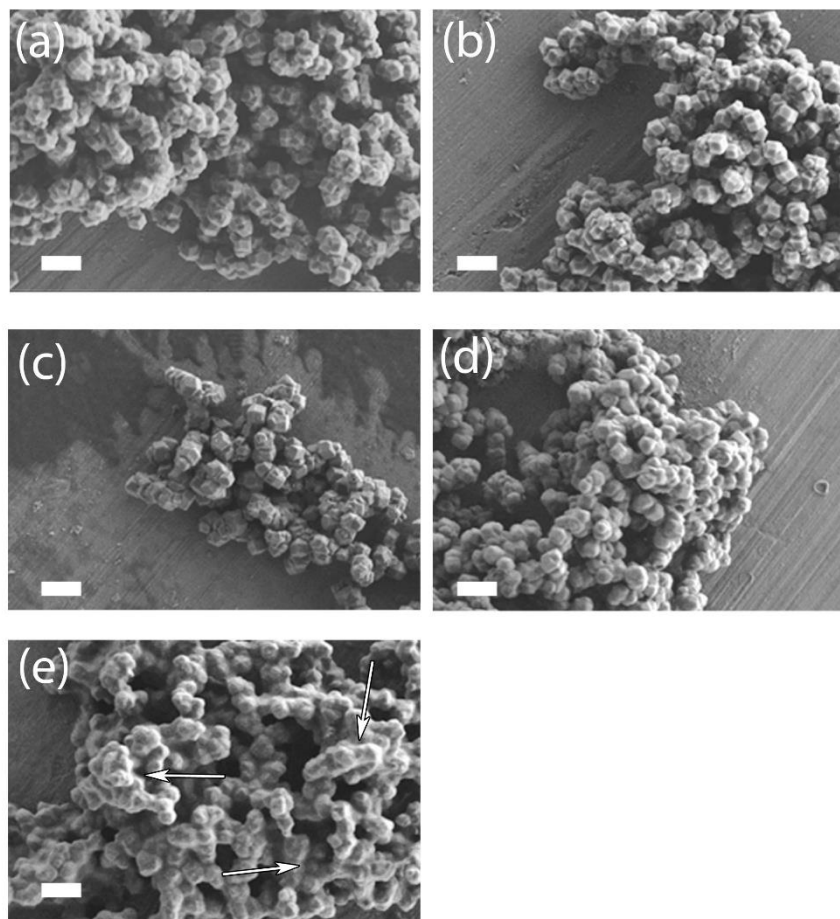


Figure S12. FESEM images of ZIF-8@PdNP-3 after (a) 10 min, (b) 20 min, (c) 30 min, (d) 40 min, (e) 50 min and (f) 60 min of 4-NP reduction. White arrows in (f) highlight the etching of ZIF-8. Scale bars for all images are 2 μm .

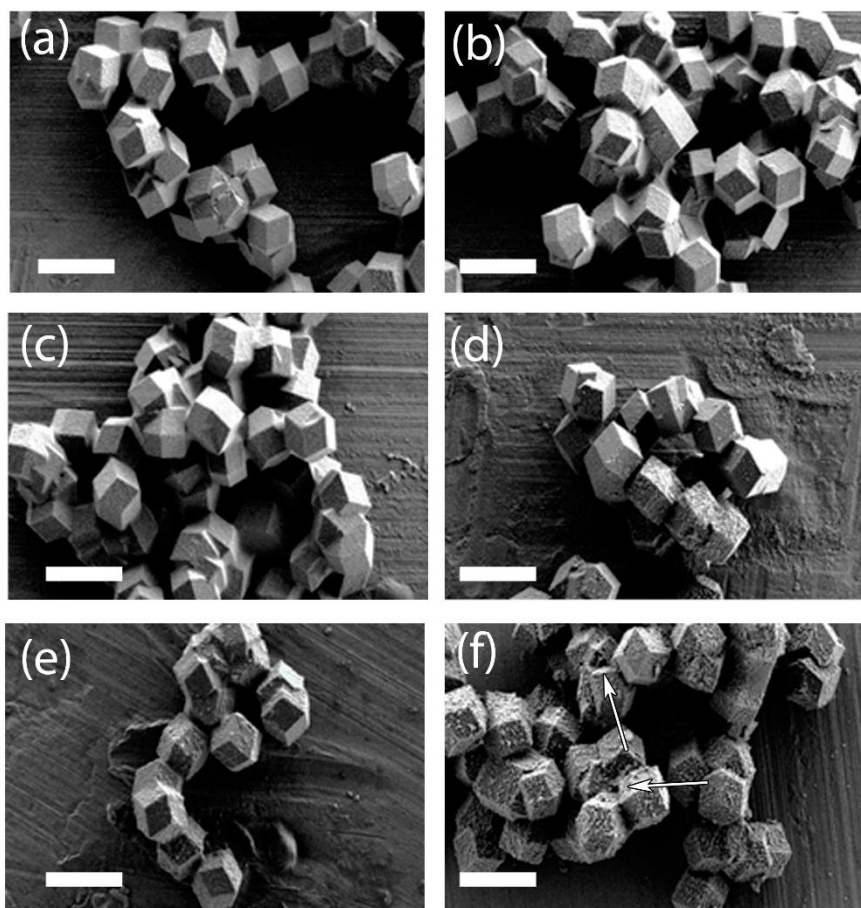


Figure S13. FESEM images of ZIF-8@PdNP-3 after (a) 10 min, (b) 20 min, (c) 30 min, (d) 40 min, (e) 50 min and (f) 60 min of EY reduction. White arrows in (f) highlight the etching of ZIF-8. Scale bars for all images are 2 μm .

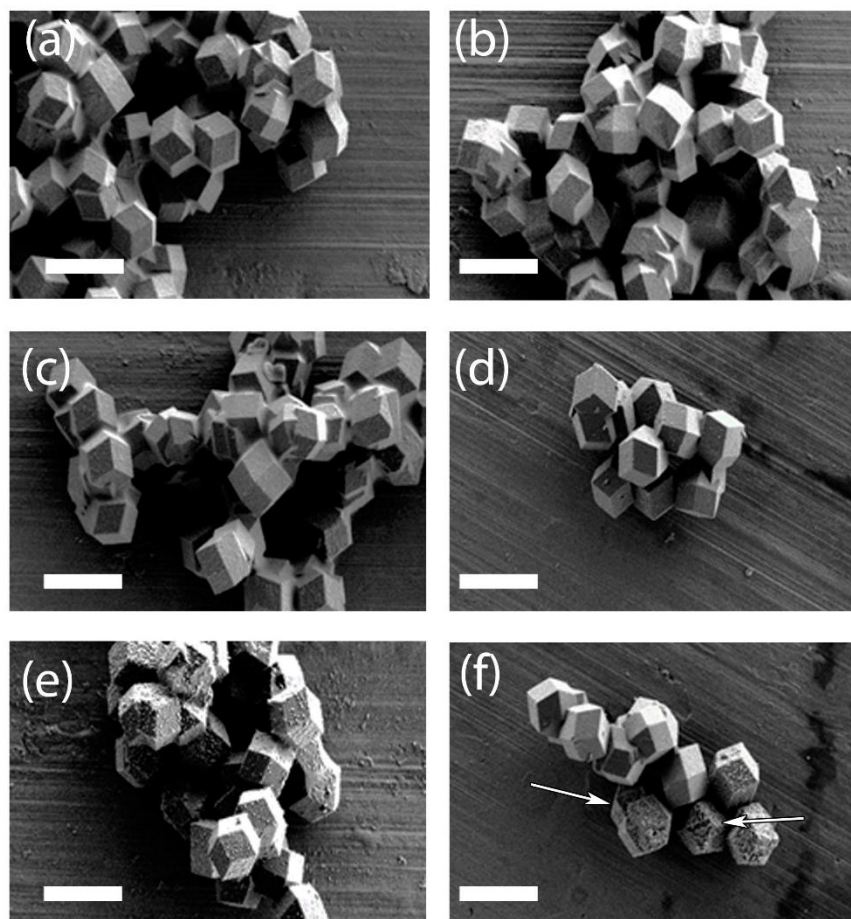


Figure S14. FESEM images of ZIF-8@PtNP-1 after (a) 10 min, (b) 20 min, (c) 30 min and (d) 40 min of 4-NP reduction. White arrows in (d) highlight the etching of ZIF-8. Scale bars for all images are 1 μm .

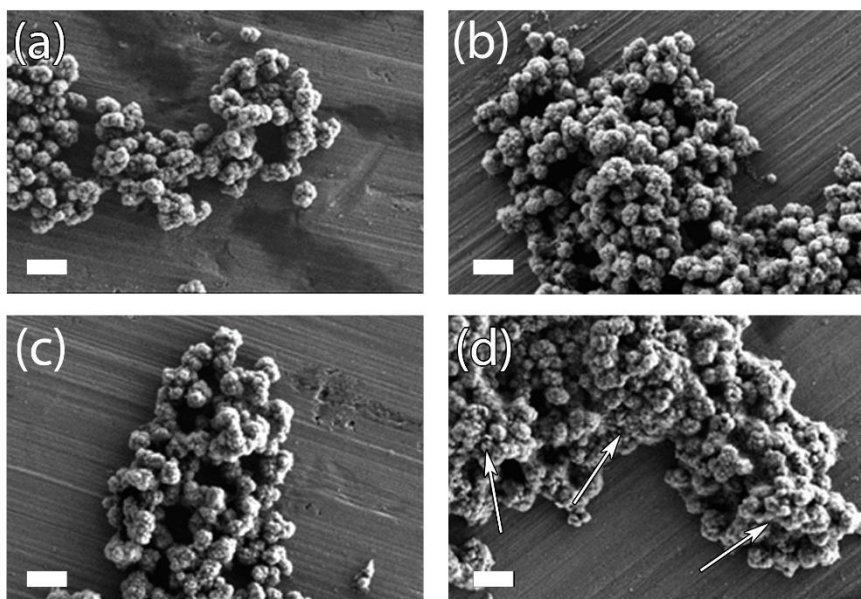


Figure S15. FESEM images of ZIF-8@PtNP-1 after (a) 10 min, (b) 20 min, (c) 30 min, (d) 40 min and (e) 50 min of EY reduction. White arrows in (e) highlight the etching of ZIF-8. Scale bars for all images are 1 μm .

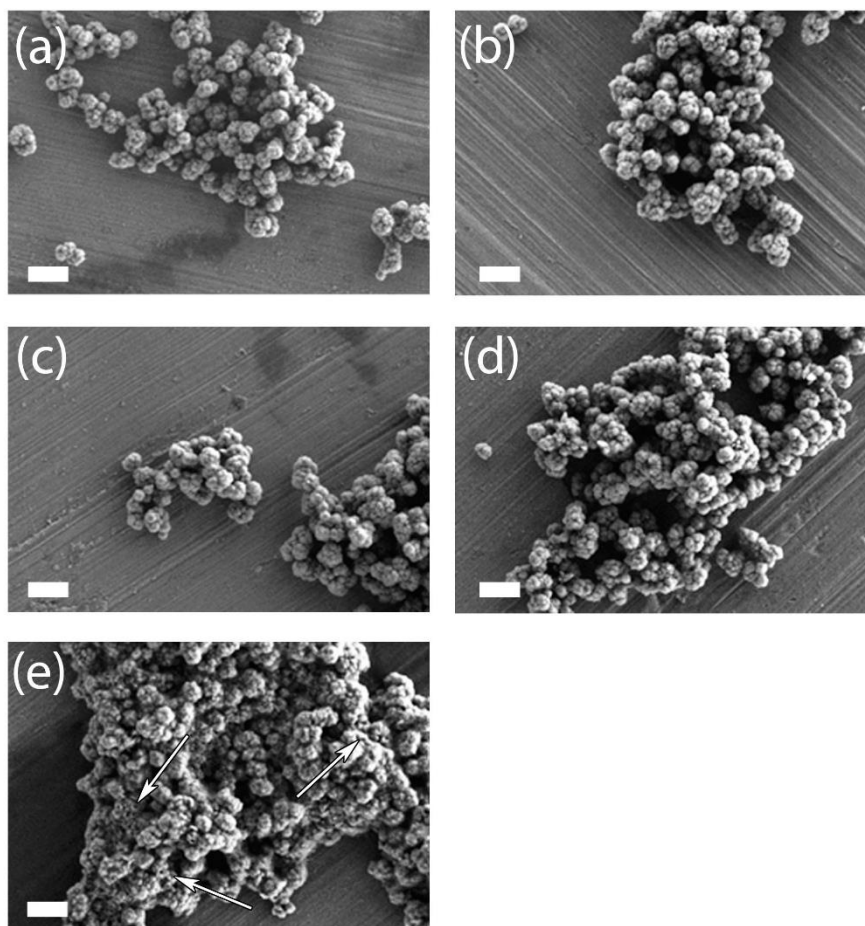


Figure S16. FESEM images of ZIF-8@PtNP-2 after (a) 10 min, (b) 20 min, (c) 30 min, (d) 40 min and (e) 50 min of 4-NP reduction. White arrows in (e) highlight the etching of ZIF-8. Scale bars for all images are 1 μm .

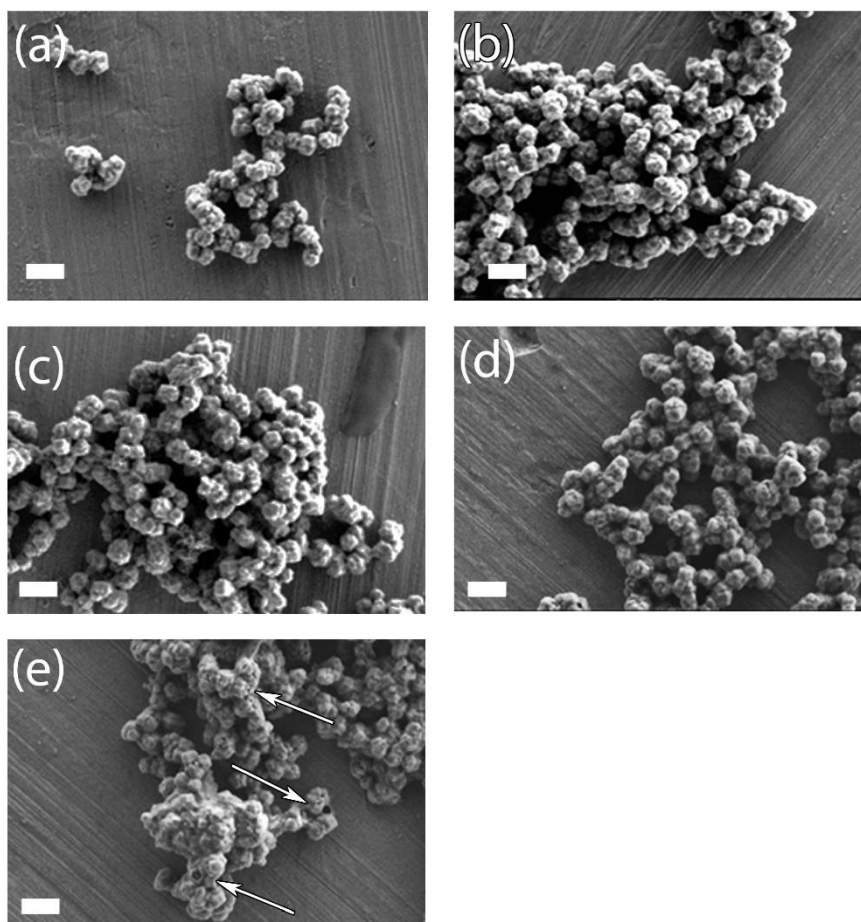


Figure S17. FESEM images of ZIF-8@PtNP-2 after (a) 10 min, (b) 20 min, (c) 30 min, (d) 40 min and (e) 50 min of EY reduction. White arrows in (e) highlight the etching of ZIF-8. Scale bars for all images are 1 μm .

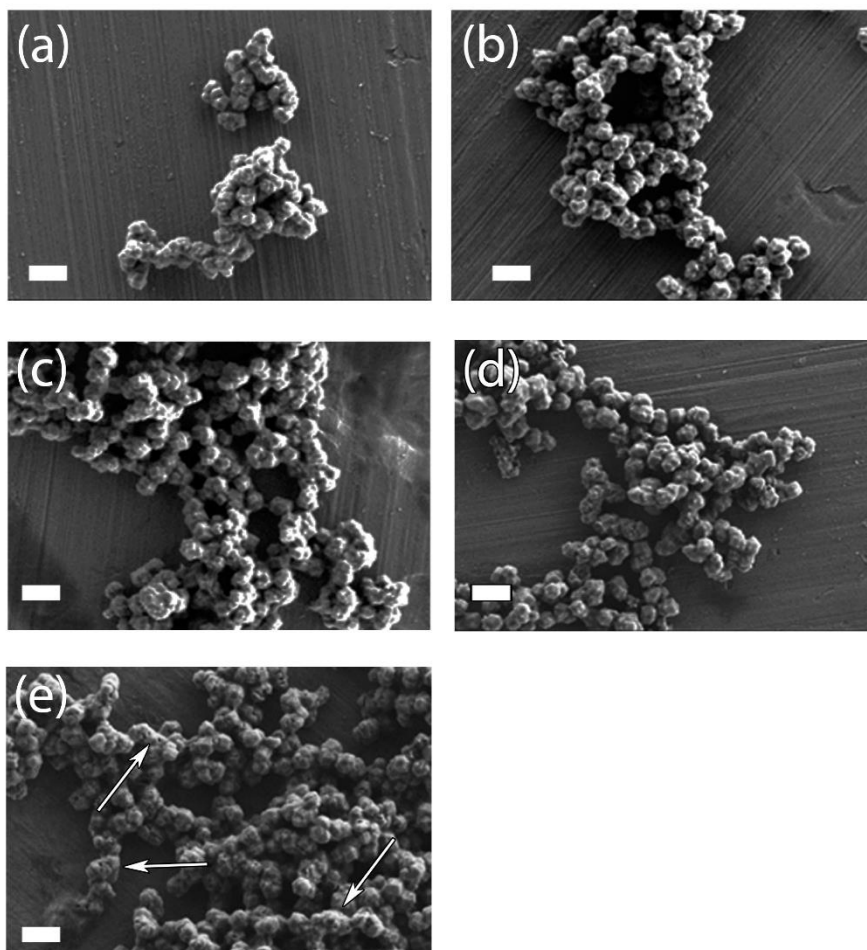


Figure S18. FESEM images of ZIF-8@PtNP-3 after (a) 10 min, (b) 20 min, (c) 30 min, (d) 40 min and (e) 50 min of 4-NP reduction. White arrows in (e) highlight the etching of ZIF-8. Scale bars for all images are 1 μm .

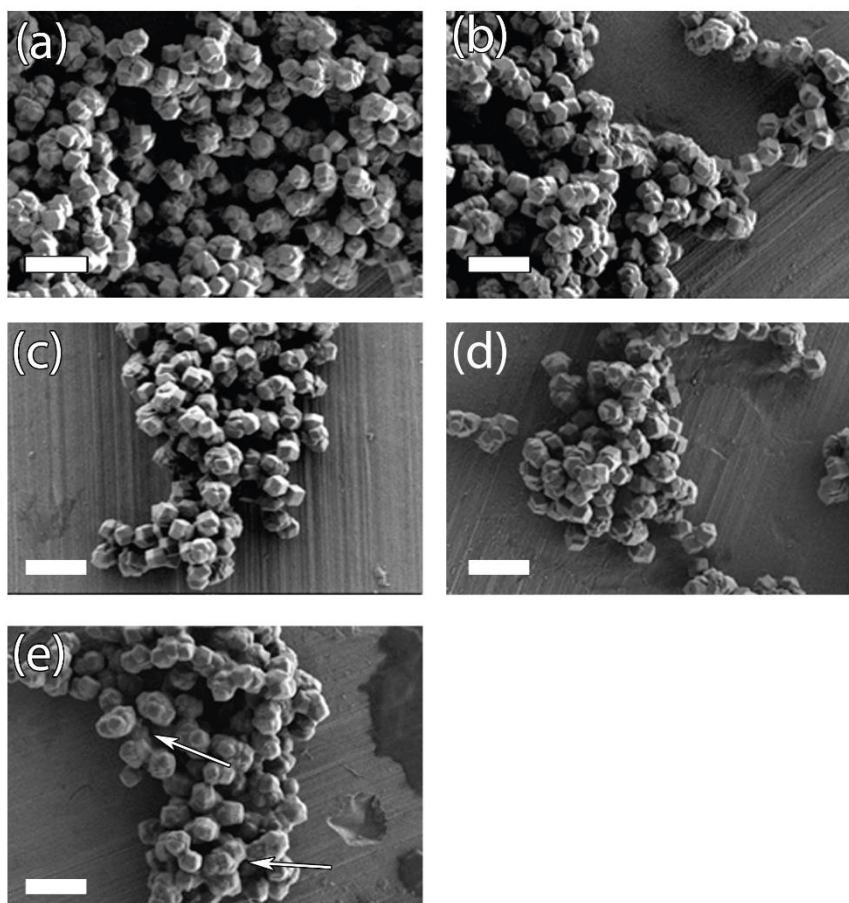


Figure S19. FESEM images of ZIF-8@PtNP-3 after (a) 10 min, (b) 20 min, (c) 30 min, (d) 40 min and (e) 50 min of EY reduction. White arrows in (e) highlight the etching of ZIF-8. Scale bars for all images are 1 μm .

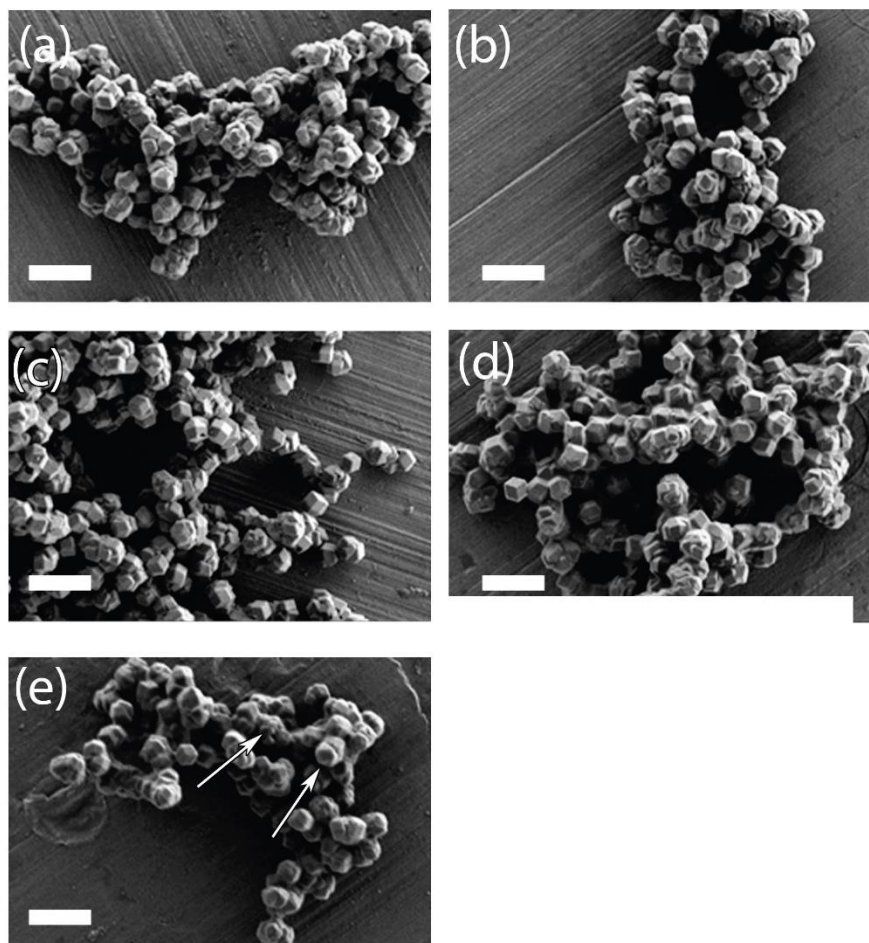


Figure S20. FESEM images of ZIF-8@PtNP-4 after (a) 10 min, (b) 20 min, (c) 30 min, (d) 40 min, (e) 50 min and (f) 60 min of 4-NP reduction. White arrows in (f) highlight the etching of ZIF-8. Scale bars for all images are 2 μm .

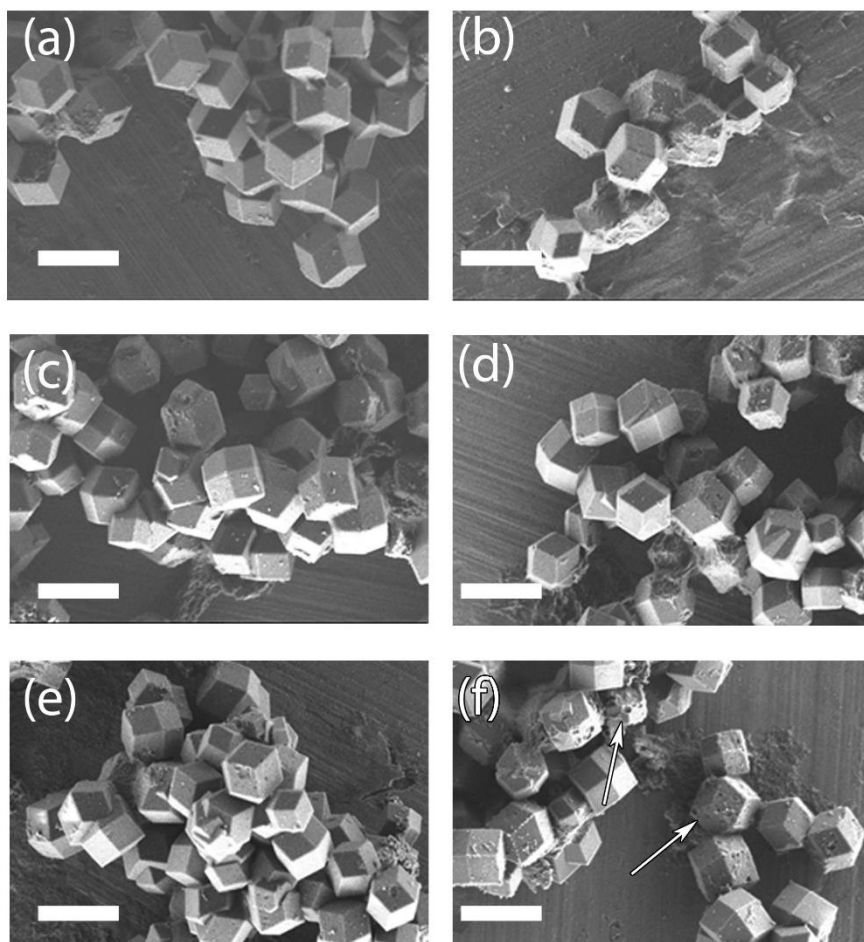


Figure S21. FESEM images of ZIF-8@PtNP-4 after (a) 10 min, (b) 20 min, (c) 30 min, (d) 40 min, (e) 50 min, (f) 60 min and (g) 70 min of EY reduction. White arrows in (g) highlight the etching of ZIF-8. Scale bars for all images are 2 μm .

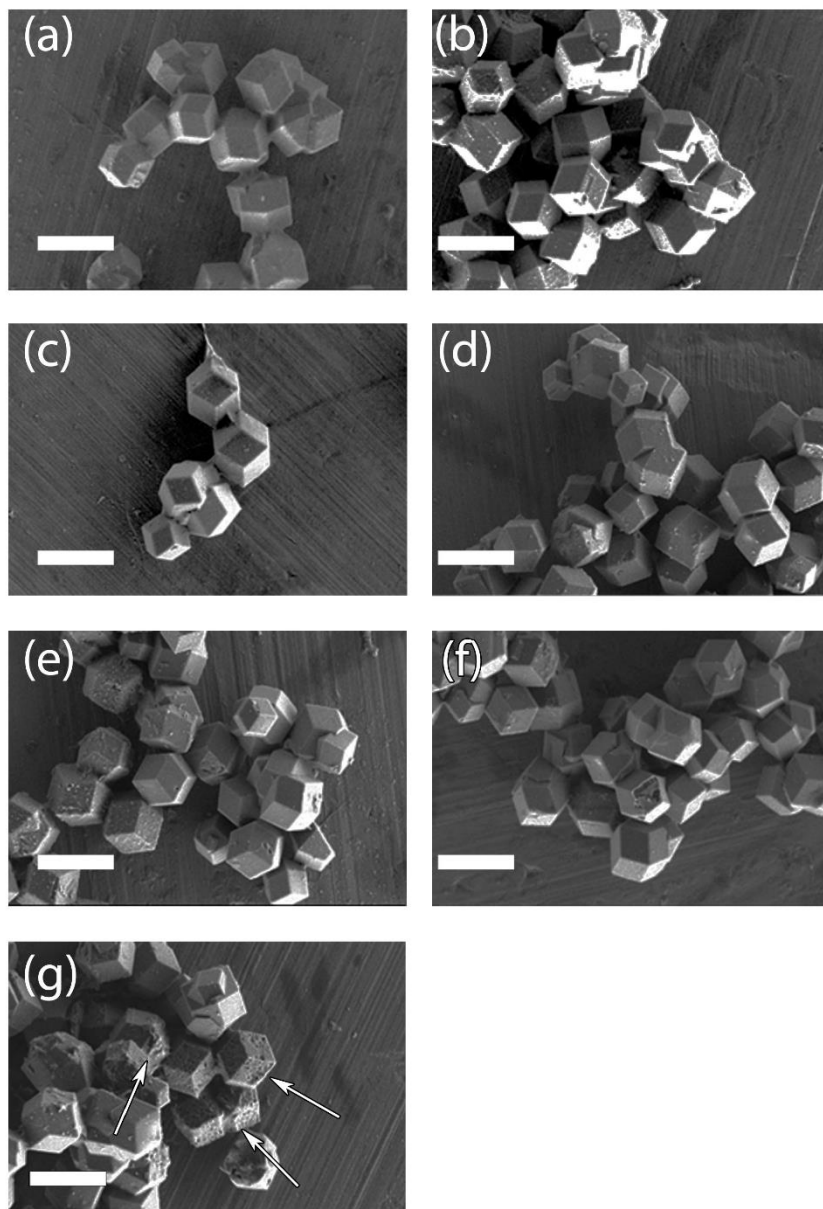


Figure S22. Representative X-Ray Powder Diffraction (XRPD) patterns of ZIF-8@PtNP-4 and ZIF-8@PdNP-3 composites after stopping the catalytic reactions, as compared to the simulated pattern for the crystal structure of ZIF-8 (black). These spectra confirm that these composites retain the crystallinity under the studied conditions.

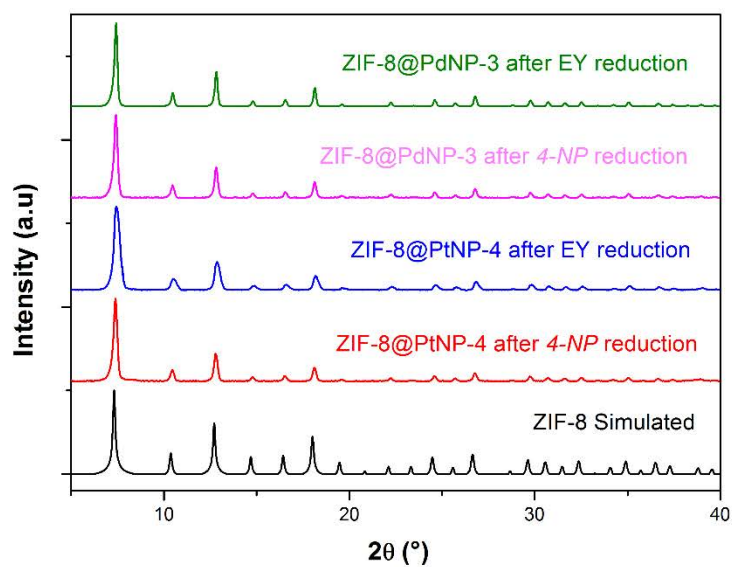
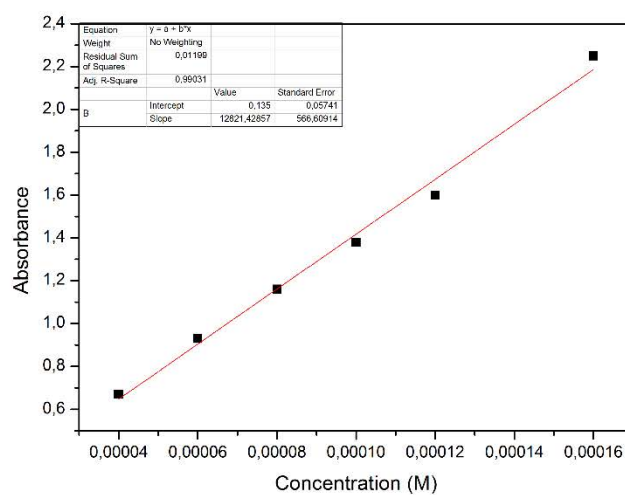


Figure S23. The calibration line of the absorbance maxima at wavelength, 400 nm, versus the 4-NP concentration, giving an extinction coefficient value of $12.8 \times 10^3 \text{ M}^{-1}\cdot\text{cm}^{-1}$.



Chapter 4 - Core-shell Au/CeO₂ Nanoparticles Supported in UiO-66 Beads Exhibiting Full CO Conversion at 100° C

Cite this: *J. Mater. Chem. A*, 2017, 5, 13966Received 6th April 2017
Accepted 12th June 2017

DOI: 10.1039/c7ta03006a

rsc.li/materials-a

Core-shell Au/CeO₂ nanoparticles supported in UiO-66 beads exhibiting full CO conversion at 100 °C†

A. Yazdi,^a A. Abo Markeb,^b L. Garzón-Tovar,^a J. Patarroyo,^a J. Moral-Vico,^b A. Alonso,^{*b} A. Sánchez,^b N. Bastus,^a I. Imaz,^a X. Font,^b V. Puntes^{†*acd} and D. Maspoch^{†*ad}

Hybrid core-shell Au/CeO₂ nanoparticles (NPs) dispersed in UiO-66 shaped into microspherical beads are created using the spray-drying continuous-flow method. The combined catalytic properties of nanocrystalline CeO₂ and Au in a single particle and the support and protective function of porous UiO-66 beads make the resulting composites show good performances as catalysts for CO oxidation ($T_{50} = 72$ °C; $T_{100} = 100$ °C) and recyclability.

Long-term exposure to carbon monoxide gas causes lethal damage to humans and animals.¹ In 2014 alone, 6381 kilotons of CO were released into the atmosphere, mainly from transportation, power plants and industrial activities.² To date, one of the most efficient solutions for mitigating CO emissions into the atmosphere is its catalytic oxidation to CO₂.^{3,4} Good-performance catalysts for CO oxidation are metal nanoparticles (NPs) such as Au, Pd, Pt and Ru NPs.^{5–8} These NPs are usually supported on/in zeolites,⁹ activated carbon,¹⁰ and metal oxides, including alumina,¹¹ mesoporous silica,¹² ceria,^{13–17} zirconia,¹⁸ titania,¹⁹ and iron oxides.³ These supports avoid NP aggregation and, eventually, enhance the catalytic activity of NPs. A remarkable case is the use of nanocrystalline CeO₂ to support Au NPs.^{20,21} In this particular composite, CeO₂ acts as an active support that enhances the catalytic performance of Au NPs for CO oxidation. Indeed, because CeO₂ has a high oxygen storage and release capacity²² and facile oxygen vacancy formation, its surface can be easily enriched with oxygen vacancies so that Au NPs can strongly bind to these vacancies.^{23,24} Also, the oxygen

vacancies in CeO₂ can create Ce³⁺ ions, opening a new CO oxidation pathway by O₂ adsorbed on Au–Ce³⁺ bridge sites.²³ Moreover, the interaction between the ceria and the metal NPs can prevent reorganization of the metallic atoms under operating conditions.²²

Inspired by these latter results, herein we show a fast method that enables integrating pre-designed core-shell Au/CeO₂ NPs^{25–27} into metal-organic frameworks (MOFs). Recently, MOFs have attracted much attention as new porous supports for catalytic NPs due to their exceptionally high surface areas, structural diversity and tailorable pore chemical functionalities.²⁸ For CO oxidation, Xu *et al.* have shown that ZIF-8 MOFs can support Au NPs to fully oxidize CO at a temperature of 225 °C.²⁹ Similarly, Pd and Pt NPs and hybrid Pd/Pt NPs supported on MIL-101, ZIF-8, UiO-67 and UiO-66 MOFs showed full CO conversion at temperatures ranging from 120 °C to 200 °C (Table 1).^{30–33} In this work, we combine the catalytic properties for CO oxidation of both nanocrystalline CeO₂ and Au counterparts in a single particle entity, which is supported in UiO-66 beads using the spray-drying continuous-flow method. This method allows the simultaneous synthesis and shaping of MOF beads while encapsulating the pre-synthesized NPs in a fast, continuous one-step process.^{34–36}

Table 1 Inorganic nanoparticles supported on MOFs for CO oxidation

Catalyst	NPs wt%	T_{50} (°C)	T_{100} (°C)	Ref.
UiO-66@Au/CeO ₂	7	72	100	This work
UiO-66@Au/CeO ₂	5.5	82	110	This work
UiO-67@Pt	5	100	120	33
MIL-101@Pt/Pd		160	175	30
MIL-101@Pt		160	175	30
UiO-66@Au/CeO ₂	2.8	98	180	This work
UiO-66@Pt	2	160	180	32
MIL-101@Pd		185	200	30
ZIF-8@Pt	2	170	200	31
ZIF-8@Au	5	170	225	29
UiO-66		369	440	This work

^aCatalan Institute of Nanoscience and Nanotechnology (ICN2), CSIC, The Barcelona Institute of Science and Technology, Campus UAB, Bellaterra, 08193 Barcelona, Spain. E-mail: victor.puntes@icn2.cat; daniel.maspoch@icn2.cat

^bDepartment of Chemical, Biological and Environmental Engineering, Escola d'Enginyeria, Universitat Autònoma de Barcelona, 08193 Bellaterra, Spain. E-mail: Amanda.Alonso@uab.cat

^cVall, d'Hebron Institut de Recerca (VHIR), 08035, Barcelona, Spain

^dICREA, Pg. Lluís Companys 23, 08010 Barcelona, Spain

† Electronic supplementary information (ESI) available. See DOI: 10.1039/c7ta03006a

Our method started with the synthesis of core-shell Au/CeO₂ (Ce : Au = 1 : 1) NPs in water following the simultaneous reduction/oxidation of Au and Ce precursors (ESI†). Synthesized NPs had an average particle size of 9.6 ± 2.0 nm and an Au core size of 4.2 ± 1.2 nm (Fig. S1, ESI†). Then, they were functionalized with PVP, allowing them to be transferred from water to dimethylformamide (DMF). This step enables the dispersion of Au/CeO₂ NPs in the solvent needed for synthesizing the UiO-66 beads. Afterwards, 100 mg of terephthalic acid, 3 mL of acetic acid, 4 mL of Au/CeO₂ NPs (concentration = 1 mg mL⁻¹) and 280 μL of Zr(OPrⁿ)₄ were sequentially mixed in 40 mL of DMF. Note here that ZrCl₄, which is the common salt used to synthesize UiO-66, was replaced by Zr(OPrⁿ)₄ because of the dissolution of CeO₂ in the acidic precursor solution when ZrCl₄ is utilized (Fig. S2, ESI†).³⁷ This mixture was injected into a coil flow reactor at a feed rate of 2.4 mL min⁻¹ at 115 °C. The resulting pre-heated solution was then spray dried at 180 °C and a flow rate of 336 mL min⁻¹ using a spray cap with a 0.5 mm diameter hole. The collected solid was dispersed in DMF and washed twice with DMF and ethanol.³⁴

A final step involved its calcination at 250 °C overnight in the presence of air. This calcination process facilitates the removal of PVP from the surface of Au/CeO₂ NPs. It also enhances the interfacial interaction of Au and CeO₂ and increases the crystallinity of CeO₂, which leads to an enhancement of the oxygen generation/storage capacity of ceria.^{38–40}

Field-emission scanning electron microscopy (FE-SEM) of the calcinated powder revealed the formation of spherical beads (average size = 3.4 ± 1.8 μm) formed by the assembly of nanocrystals of UiO-66 (Fig. 1a). X-ray powder diffraction (XRPD) indicated that the beads were pure crystalline UiO-66 (Fig. 1j). Fig. 1b and c show high angle annular dark field scanning transmission electron microscopy (HAADF-STEM) results of these beads, confirming the encapsulation of well-dispersed Au/CeO₂ NPs inside them. In addition, energy dispersive X-ray spectroscopy (EDX) mapping of the beads showed the homogeneous distribution of Au and Ce inside the beads (Fig. 1k). The content of Au/CeO₂ in this composite was estimated by digesting the powder in a mixture of concentrated HCl and HNO₃ and analysed by inductively coupled plasma optical emission spectrometry (ICP-OES), from which a Au/CeO₂ content of 2.8% (Ce: 1.28%, Au: 1.31%) in the composite (hereafter, UiO-66@Au/CeO₂-2.8) was determined. The comparison of this value to the initial percentage of Au/CeO₂ NPs added into the UiO-66 precursor solution leads to an encapsulation yield of 92%, confirming the efficiency of the spray drying method for incorporating Au/CeO₂ NPs into the UiO-66 beads. Finally, the adsorption capacity of UiO-66@Au/CeO₂-2.8 was determined. N₂ physical adsorption measurements showed a measured Brunauer Emmet Teller (BET) surface area (*A*_{BET}) of 1095 m² g⁻¹ (Fig. S3a, ESI†), very close to that of pristine UiO-66 superstructures.³⁷

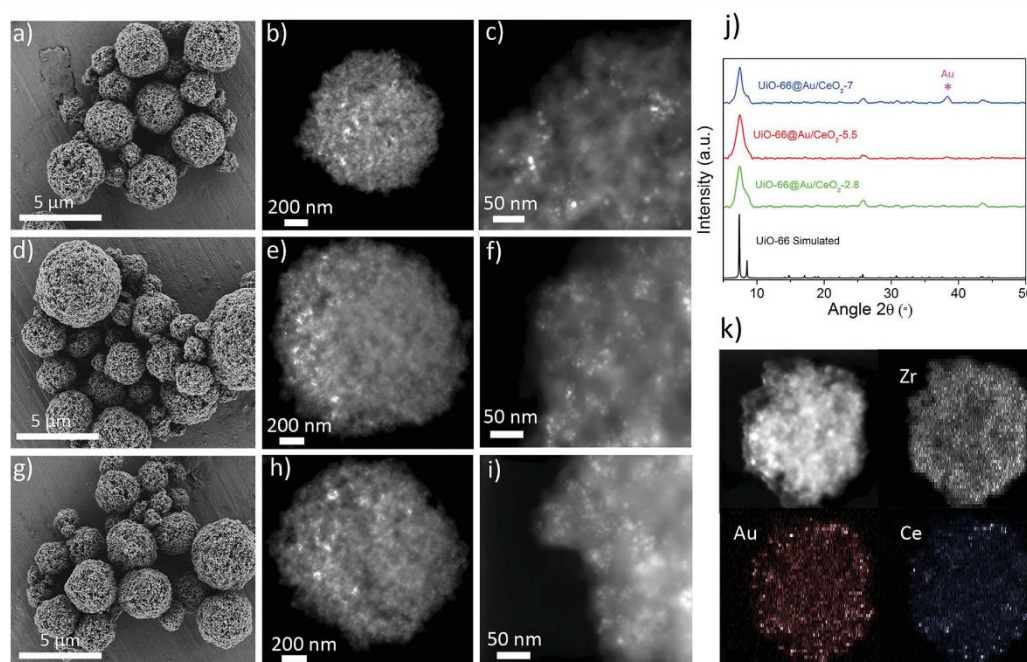


Fig. 1 (a–i) Representative FE-SEM and HAADF-STEM images of UiO-66@Au/CeO₂-2.8 (a–c), UiO-66@Au/CeO₂-5.5 (d–f) and UiO-66@Au/CeO₂-7 (g–i). (j) XRPD patterns of UiO-66@Au/CeO₂-2.8 (green), UiO-66@Au/CeO₂-5.5 (red) and UiO-66@Au/CeO₂-7 (blue) in comparison to the simulated pattern of UiO-66 (black). (k) Elemental mapping (Zr, Ce and Au) of the composite UiO-66@Au/CeO₂-2.8.

The catalytic activity of the UiO-66@Au/CeO₂-2.8 in CO oxidation was evaluated by the temperature-programmed oxidation method. The catalytic oxidation of CO was carried out in a fixed bed column reactor with dimensions of 9.0 cm in length and 0.5 cm in inner diameter set in a controlled temperature oven. 50 mg of the catalyst was packed into the column, and a mixture of gases consisting of 1% CO, 21% O₂ and 78% N₂ was allowed to pass through the column reactor at a constant flow rate of 100 mL min⁻¹. After that, the catalyst was heated up to the desired temperature and maintained until a steady state was achieved. Within this interval of time, a set of samples of the outlet gas were withdrawn and analyzed to determine the CO conversion.

In an initial step, the catalytic activity of UiO-66 beads without Au/CeO₂ NPs was measured as a control reaction. As expected, UiO-66 beads showed no conversion of CO to CO₂ up to 200 °C, and full conversion took place at 440 °C (Fig. S4, ESI†). In contrast, the catalytic activity of UiO-66@Au/CeO₂-2.8 was remarkably enhanced. As is shown in Fig. 2a, this composite showed a CO conversion starting at room temperature and exhibited a 50% (*T*₅₀) and a 100% (*T*₁₀₀) CO conversion at temperatures of 98 °C and 180 °C, respectively (Table 1).

It is known that, if no aggregation occurs, higher loading of NPs tends to increase the catalytic activity of this class of supported composites. To this end, we systematically synthesized a series of composites in which we increased the added amount of Au/CeO₂ NP dispersion (1 mg mL⁻¹) in the precursor solution to 8.5 mL, 12 mL and 16 mL. Again, FE-SEM and HAADF-STEM images revealed the formation of beads containing Au/CeO₂ NPs for all samples (Fig. 1d-i). However, the latter sample was discarded because it showed the presence of a high amount of non-encapsulated Au/CeO₂ NPs together with the beads as well as lower crystallinity of UiO-66 (Fig. S5, ESI†). For the first two compositions, XRPD patterns confirmed the formation of UiO-66 (Fig. 1j), from which Au/CeO₂ contents of 5.5% (Ce: 2.48%, Au: 2.50%) and 7% (Ce: 3.22%, Au: 3.18%) in the composites (hereafter, UiO-66@Au/CeO₂-5.5 and UiO-66@Au/CeO₂-7) were determined. These amounts correspond to 91% and 74% of encapsulation efficiency for UiO-66@Au/CeO₂-5.5 and UiO-66@Au/CeO₂-7, respectively. Finally, N₂ physical adsorption measurements confirmed that both composites are porous, showing measured BET surface areas of 1070 and 870 m² g⁻¹ (Fig. S3b and c, ESI†).

Ensuing temperature-programmed oxidation measurements confirmed a clear improvement of CO conversion for both new composites, achieving lower *T*₅₀ and *T*₁₀₀ values by increasing the percentage of Au/CeO₂ NPs (Fig. 2a). In the case of UiO-66@Au/CeO₂-5.5, *T*₅₀ and *T*₁₀₀ were found to be 82 °C and 110 °C, respectively. For UiO-66@Au/CeO₂-7, these temperatures decreased down to 72 °C and 100 °C. Remarkably, in this latter case, a CO conversion of 3.8% was achieved at room temperature. Moreover, for this latter reaction, the activation energy was found to be 40.2 kJ mol⁻¹, whereas the turnover frequency (TOF) values at temperatures of 30, 50, 75 and 100 °C were 10, 39, 106 and 204 h⁻¹, respectively (for comparison purposes, the TOF values of other reported catalysts based on Au NPs are given in Table S1, ESI†).

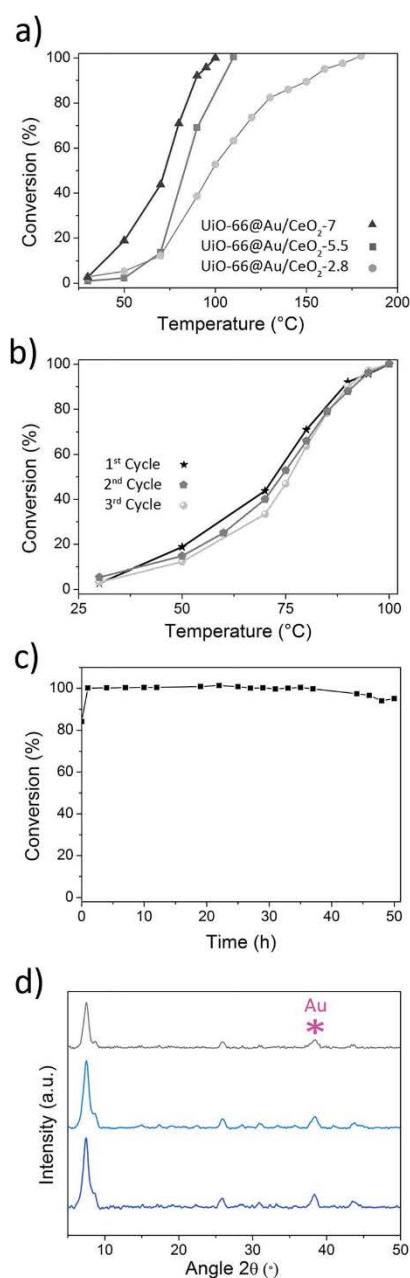


Fig. 2 (a) CO conversion rate as a function of reaction temperature for UiO-66@Au/CeO₂-2.8, UiO-66@Au/CeO₂-5.5 and UiO-66@Au/CeO₂-7. (b) CO conversion rate as a function of reaction temperature for three consecutive cycles over the UiO-66@Au/CeO₂-7 composite. (c) CO conversion rate at 100 °C for 12 hours over the UiO-66@Au/CeO₂-7 composite. (d) XRPD patterns of the as-synthesized UiO-66@Au/CeO₂-7 (blue) and after three temperature-programmed cycles (light blue) and 50 hours of continuous CO conversion (grey).

Finally, the recyclability of these composites was evaluated using the composite UiO-66@Au/CeO₂-7 that shows a lower T_{100} . Initially, we performed three cycles of catalysis without detecting any loss of activity (Fig. 2b). After these cycles, the stability of UiO-66@Au/CeO₂-7 was analyzed by XRPD that showed a complete retention of the crystallinity of UiO-66 (Fig. 2d), as also confirmed by its unaffected surface area ($A_{\text{BET}} = 850 \text{ m}^2 \text{ g}^{-1}$). Similarly, no sign of NP sintering or aggregation and alteration of the morphology of the beads was observed by STEM and FE-SEM (Fig. S6, ESI†). Then, the catalytic activity of the UiO-66@Au/CeO₂-7 sample was also studied for a longer period of time. For this, the conversion of CO was performed continuously at 100 °C for 50 hours, during which no loss of activity for the first 37 hours and a slight decrease of activity (5%) after 50 hours (Fig. 2c) were observed. We attributed this decrease in catalytic activity to a loss of crystallinity of UiO-66 (Fig. 2d) and its porosity capabilities ($A_{\text{BET}} = 670 \text{ m}^2 \text{ g}^{-1}$).

In conclusion, we have described the formation of a new composite based on the entrapment and dispersion of core-shell Au/CeO₂ NPs into microsized spherical, porous UiO-66 beads using the spray-drying continuous-flow method. The combination of nanocrystalline CeO₂ and Au allows accessing to CO conversion T_{50} and T_{100} as low as 72 °C and 100 °C. These values are to our knowledge one of the lowest CO conversion temperatures achieved using catalysts based on NPs supported on MOFs. In addition, UiO-66 provides enough protection to avoid NP sintering/aggregation. We consider this method as a general approach for making composites consisting of functional NPs dispersed in MOFs already shaped into spherical beads, as demonstrated by the fact that other composites made of Pd NPs dispersed into UiO-66 beads (Fig. S7, ESI†) were also fabricated and tested for CO oxidation.

Acknowledgements

This work was supported by the Spanish MINECO (projects PN MAT2015-65354-C2-1-R and MAT2015-70725-R), the Catalan AGAUR (projects 2014-SGR-80 and 2014-SGR-612), and the ERC under the EU FP7 (ERC-Co 615954). N. G. B. thanks the MINECO for her RyC grant RYC-2012-10991 and the financial support by the European Commission Seventh Framework Program (FP7) through the Marie Curie Career Integration Grant (322153-MINE). ICN2 acknowledges the support of the Spanish MINECO through the Severo Ochoa Centres of Excellence Programme, under Grant SEV-2013-0295.

Notes and references

- 1 R. A. Jones, J. A. Strickland, J. A. Stunkard and J. Siegel, *Toxicol. Appl. Pharmacol.*, 1971, **19**, 46–53.
- 2 Environment and Climate Change Canada, Canadian Environmental Sustainability Indicators: Air Pollutant Emissions, 2016, <http://www.ec.gc.ca/indicateurs-indicators/default.asp?lang=en&n=E79F4C12-1>.
- 3 L. Liu, F. Zhou, L. Wang, X. Qi, F. Shi and Y. Deng, *J. Catal.*, 2010, **274**, 1–10.
- 4 B. Qiao, A. Wang, X. Yang, L. F. Allard, Z. Jiang, Y. Cui, J. Liu, J. Li and T. Zhang, *Nat. Chem.*, 2011, **3**, 634–641.
- 5 M. S. Chen, Y. Cai, Z. Yan, K. K. Gath, S. Axnanda and D. W. Goodman, *Surf. Sci.*, 2007, **601**, 5326–5331.
- 6 J. Wang, Z. Wang and C.-J. Liu, *ACS Appl. Mater. Interfaces*, 2014, **6**, 12860–12867.
- 7 P. J. Berlowitz, C. H. F. Peden and D. W. Goodman, *J. Phys. Chem.*, 1988, **92**, 5213–5221.
- 8 E. M. C. Alayon, J. Singh, M. Nachtegaal, M. Harfouche and J. A. van Bokhoven, *J. Catal.*, 2009, **263**, 228–238.
- 9 W. Han, P. Zhang, Z. Tang and G. Lu, *Process Saf. Environ. Prot.*, 2014, **92**, 822–827.
- 10 L. Wang, Y. Zhang, Y. Lou, Y. Guo, G. Lu and Y. Guo, *Fuel Process. Technol.*, 2014, **122**, 23–29.
- 11 A. S. Ivanova, E. M. Slavinskaya, R. V. Gulyaev, V. I. Zaikovskii, O. A. Stonkus, I. G. Danilova, L. M. Plyasova, I. A. Polukhina and A. I. Boronin, *Appl. Catal., B*, 2010, **97**, 57–71.
- 12 H. Wang and C.-J. Liu, *Appl. Catal., B*, 2011, **106**, 672–680.
- 13 A. E. R. S. Khder, H. M. A. Hassan, M. A. Betiha, K. S. Khairou and A. A. Ibrahim, *React. Kinet., Mech. Catal.*, 2014, **112**, 61–75.
- 14 D. Zhang, X. Du, L. Shi and R. Gao, *Dalton Trans.*, 2012, **41**, 14455–14475.
- 15 W. Liu, X. Liu, L. Feng, J. Guo, A. Xie, S. Wang, J. Zhang and Y. Yang, *Nanoscale*, 2014, **6**, 10693–10700.
- 16 D. Zhang, Y. Qian, L. Shi, H. Mai, R. Gao, J. Zhang, W. Yu and W. Cao, *Catal. Commun.*, 2012, **26**, 164–168.
- 17 W. Liu, T. Deng, L. Feng, A. Xie, J. Zhang, S. Wang, X. Liu, Y. Yang and J. Guo, *CrystEngComm*, 2015, **17**, 4850–4858.
- 18 C. M. Olmos, L. E. Chinchilla, J. J. Delgado, A. B. Hungria, G. Blanco, J. J. Calvino and X. Chen, *Catal. Lett.*, 2015, **146**, 144–156.
- 19 J. Wang, S. A. Kondrat, Y. Wang, G. L. Brett, C. Giles, J. K. Bartley, L. Lu, Q. Liu, C. J. Kiely and G. J. Hutchings, *ACS Catal.*, 2015, **5**, 3575–3587.
- 20 S. Carrettin, P. Concepcion, A. Corma, J. M. Lopez Nieto and V. F. Puentes, *Angew. Chem., Int. Ed.*, 2004, **43**, 2538–2540.
- 21 M. Centeno, T. Ramirez Reina, S. Ivanova, O. Laguna and J. Odriozola, *Catalysts*, 2016, **6**, 158.
- 22 N. J. Divins, I. Angurell, C. Escudero, V. Perez-Dieste and J. Llorca, *Science*, 2014, **346**, 620–623.
- 23 H. Y. Kim, H. M. Lee and G. Henkelman, *J. Am. Chem. Soc.*, 2012, **134**, 1560–1570.
- 24 C. Zhang, A. Michaelides and S. J. Jenkins, *Phys. Chem. Chem. Phys.*, 2011, **13**, 22–33.
- 25 T. Mitsudome, M. Yamamoto, Z. Maeno, T. Mizugaki, K. Jitsukawa and K. Kaneda, *J. Am. Chem. Soc.*, 2015, **137**, 13452–13455.
- 26 F. Zhu, G. Chen, S. Sun and X. Sun, *J. Mater. Chem. A*, 2013, **1**, 288–294.
- 27 Y. H. Qu, F. Liu, Y. Wei, C. L. Gu, L. H. Zhang and Y. Liu, *Appl. Surf. Sci.*, 2015, **343**, 207–211.
- 28 P. Falcaro, R. Ricco, A. Yazdi, I. Imaz, S. Furukawa, D. Maspocho, R. Ameloot, J. D. Evans and C. J. Doonan, *Coord. Chem. Rev.*, 2016, **307**, 237–254.

- 29 H.-L. Jiang, B. Liu, T. Akita, M. Haruta, H. Sakurai and Q. Xu, *J. Am. Chem. Soc.*, 2009, **131**, 11302–11303.
- 30 A. Aijaz, T. Akita, N. Tsumori and Q. Xu, *J. Am. Chem. Soc.*, 2013, **135**, 16356–16359.
- 31 G. Lu, S. Li, Z. Guo, O. K. Farha, B. G. Hauser, X. Qi, Y. Wang, X. Wang, S. Han, X. Liu, J. S. DuChene, H. Zhang, Q. Zhang, X. Chen, J. Ma, S. C. Loo, W. D. Wei, Y. Yang, J. T. Hupp and F. Huo, *Nat. Chem.*, 2012, **4**, 310–316.
- 32 W. Zhang, G. Lu, C. Cui, Y. Liu, S. Li, W. Yan, C. Xing, Y. R. Chi, Y. Yang and F. Huo, *Adv. Mater.*, 2014, **26**, 4056–4060.
- 33 G.-l. Zhuang, J.-q. Bai, X. Zhou, Y.-f. Gao, H.-l. Huang, H.-q. Cui, X. Zhong, C.-L. Zhong and J.-g. Wang, *Eur. J. Inorg. Chem.*, 2017, **2017**, 172–178.
- 34 L. Garzon-Tovar, M. Cano-Sarabia, A. Came-Sanchez, C. Carbonell, I. Imaz and D. Maspoch, *React. Chem. Eng.*, 2016, **1**, 533–539.
- 35 A. Carné-Sánchez, I. Imaz, M. Cano-Sarabia and D. Maspoch, *Nat. Chem.*, 2013, **5**, 203–211.
- 36 J. P.-C. L. Garzon-Trovar, I. Imaz and D. Maspoch, *Adv. Funct. Mater.*, 2017, **27**, 1606424.
- 37 B. Rungtaweeworani, J. Baek, J. R. Araujo, B. S. Archanjo, K. M. Choi, O. M. Yaghi and G. A. Somorjai, *Nano Lett.*, 2016, **16**, 7645–7649.
- 38 B. He, Q. Zhao, Z. Zeng, X. Wang and S. Han, *J. Mater. Sci.*, 2015, **50**, 6339–6348.
- 39 L. Zhou, X. Li, Z. Yao, Z. Chen, M. Hong, R. Zhu, Y. Liang and J. Zhao, *Sci. Rep.*, 2016, **6**, 23900.
- 40 Y. Liu, H.-S. Chen, J. Li and P. Yang, *RSC Adv.*, 2015, **5**, 37585–37591.

Supplementary Information

Core-shell Au/CeO₂ nanoparticles supported in UiO-66 beads exhibiting full CO conversion at 100 °C

A. Yazdi, A. Abo Markeb, L. Garzon-Tovar, J. Patarroyo, J. Moral-Vico, A. Alonso, A. Sánchez, N. G. Bastús, I. Imaz, X. Font, V. Puentes and D. Maspoch

Experimental details

Materials

All reagents were purchased from Sigma-Aldrich and used without further purification. All gases were purchased from Carbueros Metálicos. Deionized water, obtained with a Milli-Q system (18.2 MQ cm), was used in all reactions.

Synthesis of PVP-Stabilized Au/CeO₂ Nanoparticles

Au/CeO₂ (Ce:Au = 1:1) NPs were synthesized in water following the simultaneous reduction/oxidation of Au and Ce precursors (N. Bastus, J. Patarroyo, J. Piella, V. Puntès, work submitted). More specifically, 400 ml of an aqueous solution containing sodium citrate (10 mM) was prepared and heated with a heating mantle in a three-neck round-bottomed flask for 15 minutes under vigorous stirring. A condenser was used to prevent the evaporation of the solvent. After boiling had commenced, HAuCl₄ (25 mM) and cerium (III) nitrate hexahydrate (25 mM) were sequentially injected to this solution. After cooling down to room temperature, 4 g of poly (vinylpyrrolidone) (PVP, M.W 10,000) in 200 ml of water was added dropwise to the NP solution while stirring and left overnight at room temperature. Then, 800 ml of acetone was added to the NP solution and left 24 hours at room temperature without stirring for precipitation of the NPs. After removing the supernatant, NPs were washed three times with DMF and finally, redispersed in DMF to give a colloidal solution of Au/CeO₂ NPs with a concentration of 1 mg/ml. The average size of synthesized Au/CeO₂ NPs was 12 ± 2.5 nm.

Synthesis of UiO-66@Au/CeO₂

100 mg of terephthalic acid (BDC), 3 ml of acetic acid, a volume of Au/CeO₂ NPs (concentration = 1 mg/ml; 4 ml for UiO-66@Au/CeO₂-2.8; 8.5 ml for UiO-66@Au/CeO₂-5.5; and 12.5 ml for UiO-66@Au/CeO₂-7) and 280 µl of Zr(OPrn)₄ were sequentially mixed in 40 ml DMF. These solutions were injected into a coil flow reactor (inner diameter: 3 mm) at a feed rate of 2.4 ml.min⁻¹ at 115° C. The resulting pre-heated solution was then spray dried at 180° C and a flow rate of 336 ml.min⁻¹ using a B-290 Mini Spray Dryer (BUCHI Labortechnik) using a spray cap with a 0.5 mm diameter hole. Then, the resulting solid was dispersed in DMF and washed twice with DMF and ethanol. The final product was calcined in the presence of air at 250° C for 12 hours. Encapsulation efficiency was calculated based on the initial amount of NPs in the precursors solution (4, 8.5 and 12 mg for UiO-66@Au/CeO₂-2.8, UiO-66@Au/CeO₂-5.5 and UiO-66@Au/CeO₂-7, respectively), the final mass of the

product after washing (144, 140 and 125 mg for UiO-66@Au/CeO₂-2.8, UiO-66@Au/CeO₂-5.5 and UiO-66@Au/CeO₂-7, respectively) and the Au/CeO₂ content determined by ICP-OES.

Synthesis of PVP-Stabilized Pd Nanoparticles

NaPdCl₂ (44 mg) was dissolved in 20 mL of ethylene glycol in the presence of 222 mg of PVP (MW = 55,000) in a three-neck round-bottomed flask. This solution was heated up to 180 °C for 10 minutes and, after cooling down to room temperature, 150 mL of acetone was added into it. Precipitated Pd NPs were then dispersed in DMF and washed twice with DMF by centrifugation. Finally, they were redispersed in 5 ml of DMF to give a colloidal solution of Pd NPs with a concentration of 0.8 mg/ml. The average size of synthesized Pd NPs was 3.3 ± 1.1 nm.

Synthesis of UiO-66@Pd

127 mg of ZrCl₄, 89 mg of BDC and 2 ml of PVP-stabilized Pd NPs solution with a concentration of 0.8 mg/ml were added to mixture of DMF (5 ml) and H₂O (0.4 ml). The resulting mixture was injected into a coil flow reactor (inner diameter: 3 mm) at a feed rate of 2.4 ml.min⁻¹ at 115° C. The resulting pre-heated solution was then spray dried at 180° C and a flow rate of 336 ml.min⁻¹ using a B-290 Mini Spray Dryer (BUCHI Labortechnik) using a spray cap with a 0.5 mm diameter hole. The resulting solid was dispersed in DMF and washed twice times with DMF and ethanol. Then, it was dispersed in ethanol and stirred at room temperature overnight and precipitated by centrifugation. The process was repeated one more time with ethanol. The final product was dried for 12 hours at 160° C under vacuum. Inductively Coupled Plasma – Optical Emission Spectroscopy (ICP-OES) showed a Pd content of 2.3 w.t. %.

Catalytic CO Oxidation Study

The catalytic oxidation of CO was carried out in a fixed bed column reactor with dimensions of 9.0 cm in length and 0.5 cm in inner diameter set in a controlled temperature oven. 50 mg of the catalyst was packed into the column, and a mixture of gases consisting of 1 % CO, 21 % O₂ and 78 % N₂ was passed through the column reactor at a fixed flow rate of 100 ml/min. After that, the catalyst was heated up to the desired temperature and maintained until a steady state was achieved. Within this interval of time, set of samples of the outlet gas were withdrawn and analyzed to determine the CO₂ produced. A Hewlett-Packard, GC-5890, gas chromatograph equipped with TCD detector using an Agilent J&W GC column, HP-Plot Q, was used to determine the CO₂. The produced CO₂ gas was determined based on the integration area of the CO₂ peak using the relevant calibration curve. The process of the effluent gas measurements was continued until 100 %

conversion of CO. Activation energy was calculated using the rate method [M. A. Shalabi, B. H. Harji, C. N. Kenney, *J. Chem. Technol. Biotechnol.*, 1996, **65**, 317–324], from which a value of 40.2 kJ/mol (with a R^2 value of 0.98) was determined.

Characterization

X-ray powder diffraction (XRPD) patterns were collected on an X'Pert PRO MPDP analytical diffractometer (Panalytical) at 45 kV, 40 mA using CuK α radiation (1.5419\AA). Nitrogen adsorption and desorption measurements were done at 77° K using an Autosorb-IQ-AG analyser (Quantachrome Instruments). Field-Emission Scanning Electron Microscopy (FE-SEM) images were collected on a FEI Magellan 400L scanning electron microscope at an acceleration voltage of 1.0–2.0 kV, using aluminum as support. High-angle annular dark-field scanning transmitted electron microscopy (HAADF-STEM) images were obtained with a FEI Tecnai G2 F20 at 200 kV. A Hewlett-Packard, GC-5890, gas chromatograph equipped with TCD detector using an Agilent J&W GC column, HP-Plot Q, was used to determine CO₂. Inductively Coupled Plasma – Optical Emission Spectroscopy (ICP-OES) measurements were performed using an ICP-OES Perkin-Elmer, model Optima 4300DV.

Figure S1. (a,b) HAADF-STEM and (c) XRPD pattern of core-shell Au/CeO₂ NPs (black) in comparison to simulate patterns of Au (red) and CeO₂ (blue). Histogram of the (d) overall diameter of Au/CeO₂, (e) Au core and (f) CeO₂ shell.

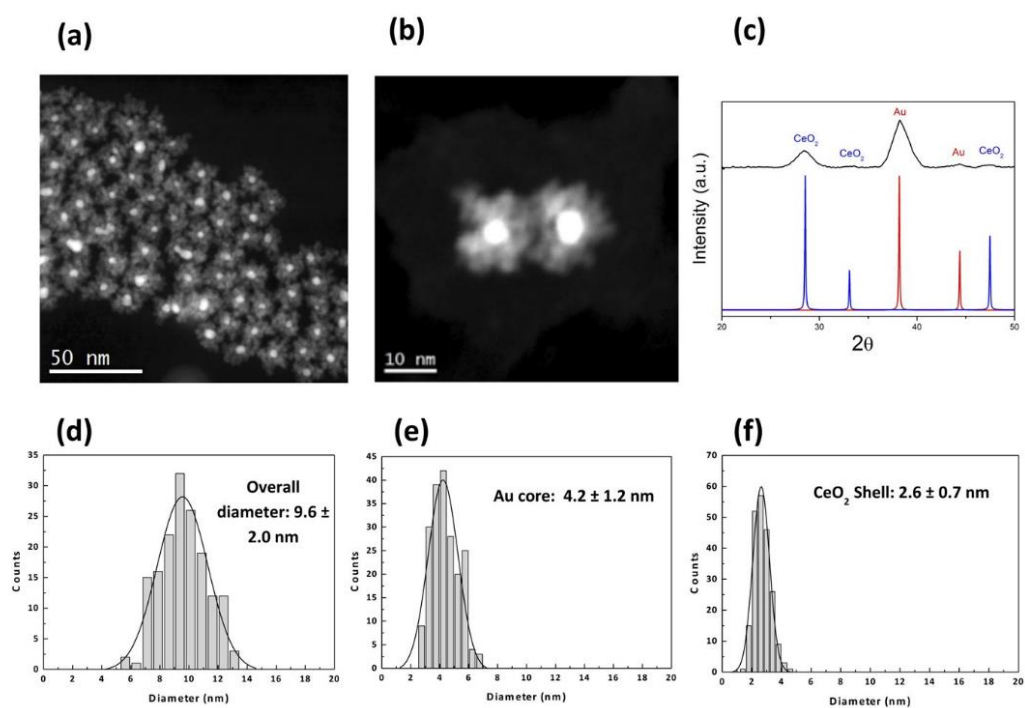


Figure S2. (a) HAADF-STEM and (b) XRPD pattern of UiO-66@Au (red) in comparison to simulated pattern of UiO-66 (black). Note here that, when we used $ZrCl_4$ as the metal salt to synthesize UiO-66@Au/CeO₂, the resulting acidic precursors solution (pH~1) at high temperature caused dissolution of CeO₂ in the process. As a result, a composite made of large Au NPs encapsulated into UiO-66 beads was produced. This phenomenon was confirmed by ICP-OES from which a Au content of 2.6 w.t. % and a Ce content of 0.02 w.t. % were found.

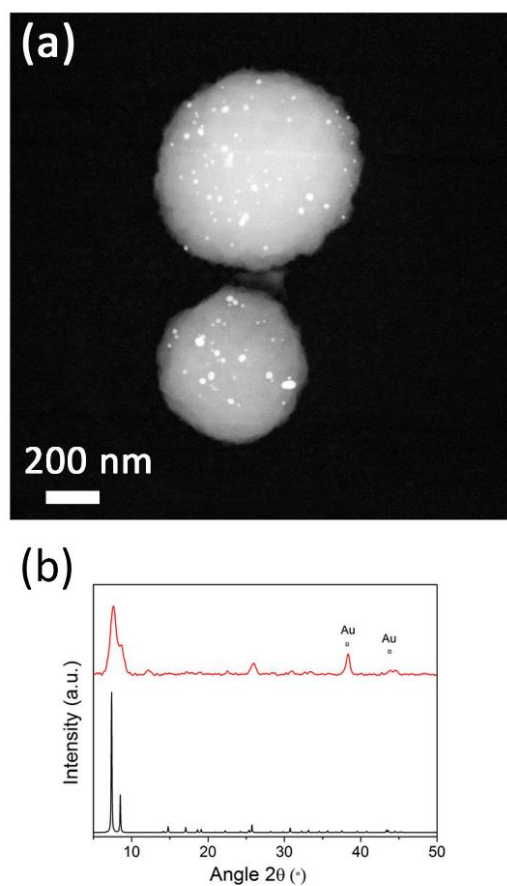


Figure S3. N₂ sorption isotherms collected at 77 K for (a) UiO-66@Au/CeO₂-2.8, (b) UiO-66@Au/CeO₂-5.5 and (c) UiO-66@Au/CeO₂-7. In this latter case, it is shown the isotherms collected before and after three temperature-programmed cycles and 50 hours of continuous CO conversion.

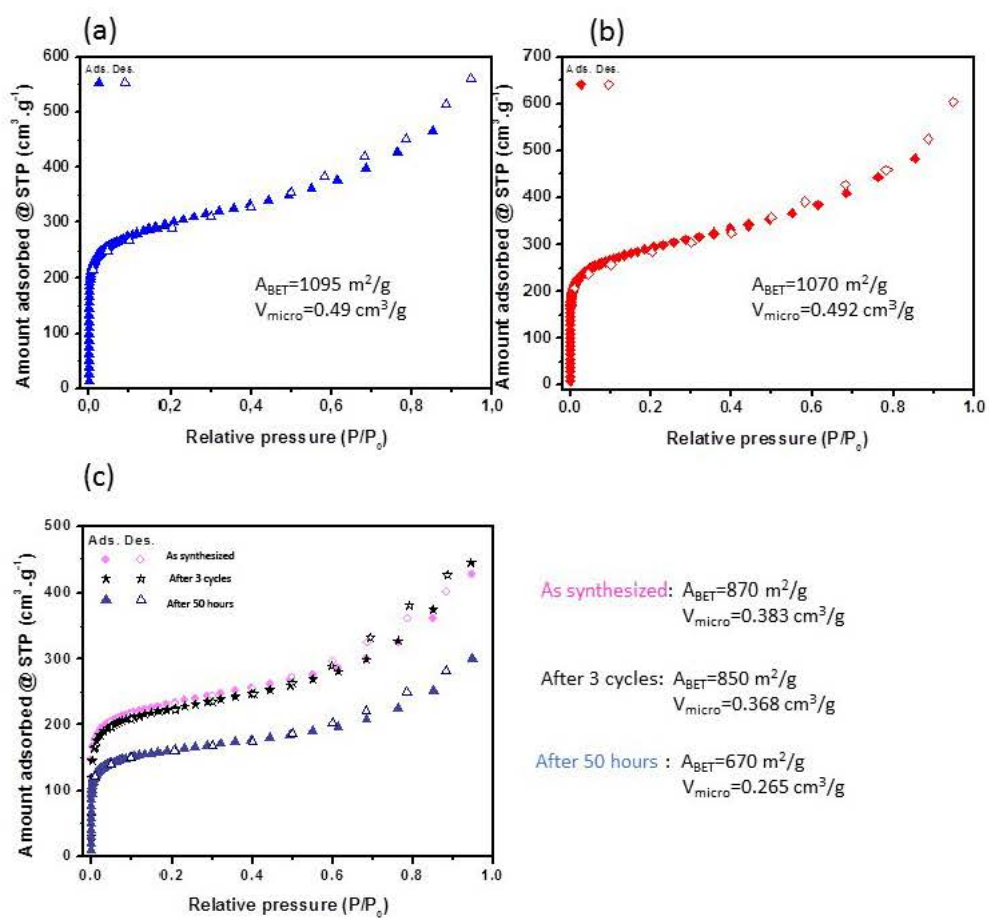


Figure S4. CO conversion rate as a function of reaction temperature for pristine UiO-66 beads.

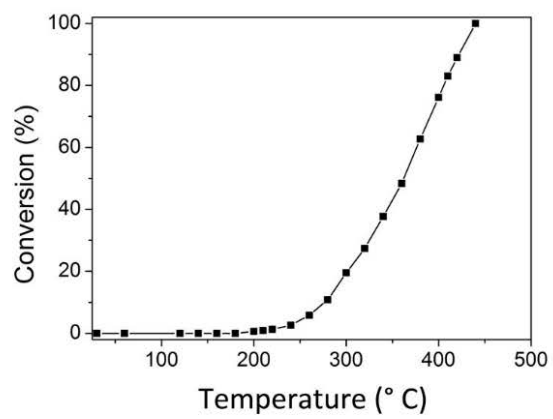


Figure S5. XRPD pattern of UiO-66@Au/CeO₂ synthesized with 16 ml of Au/CeO₂ NPs solution (red) in comparison to simulated pattern of UiO-66 (black).

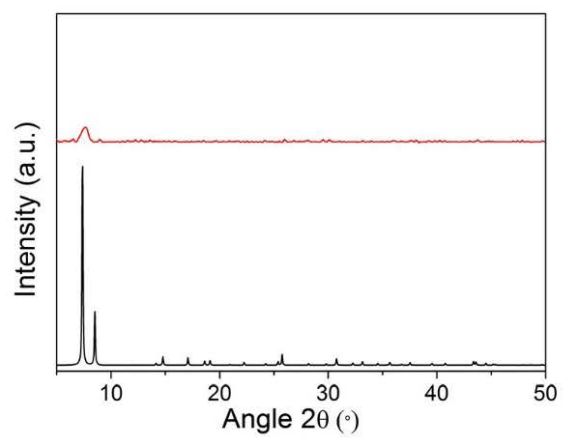


Figure S6. Stability test. (a,b) FE-SEM and (c) HAADF-STEM of UiO-66@Au/CeO₂-7 after three temperature-programmed cycles. (d,e) FE-SEM and (f) HAADF-STEM of UiO-66@Au/CeO₂-7 after 50 hours of continuous CO conversion.

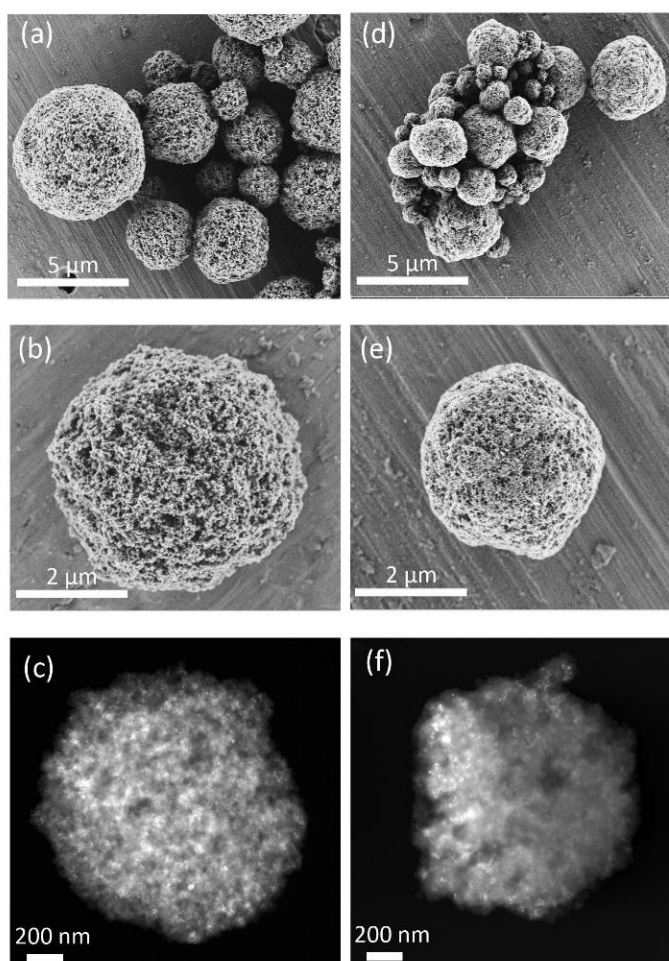


Figure S7. (a) HAADF-STEM, (b) FE-SEM and (c) XPDR pattern of UiO-66@Pd (red) in comparison to simulated pattern of UiO-66(black). (d) CO conversion rate as a function of reaction temperature for UiO-66@Pd, $T_{50} = 164$ °C and $T_{100} = 180$ °C.

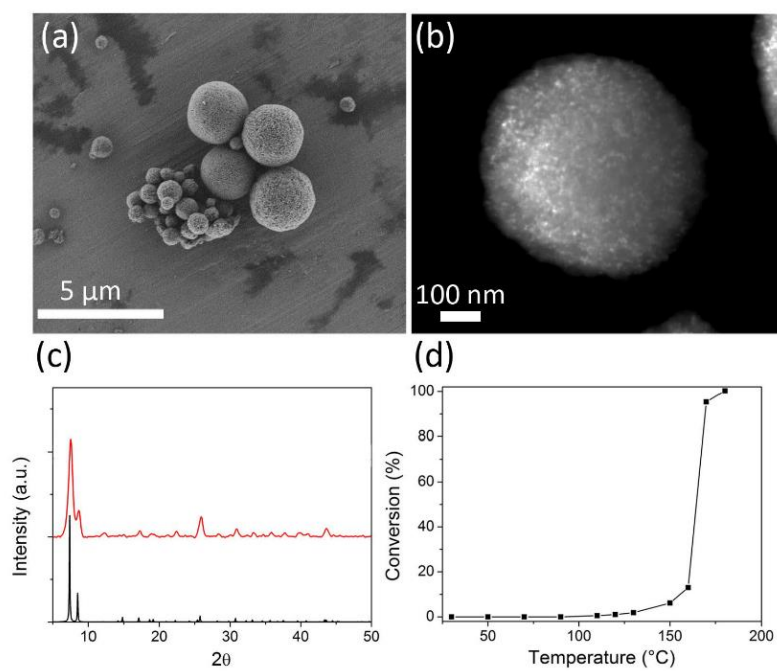


Table S1. Summary of catalysts based on Au NPs and their corresponding TOF values.

Material	T(°C)	Au NP size (nm)	TOF (h ⁻¹)	Reference
UiO-66@Au/CeO ₂	30	5	10	This work
	50	5	39	
	75	5	106	
	100	5	204	
2.32Au/ZnO _x /CeO ₂ -Al ₂ O ₃	25	5	1188	[1]
1.9Au/0.5ZnO/CeAl	25	5	1584	
1.82Au/1ZnO/Al	25	5	396	
1.7Au/1ZnO/CeAl	25	5	1836	
1.99Au/1.5ZnO/CeAl	25	5	1548	
1.57Au/0.5Fe ₂ O ₃ /CeAl	25	5.7	1152	
1.91 Au/1 Fe ₂ O ₃ /Al	25	5	72	
1.26 Au/1 Fe ₂ O ₃ /CeAl	25	18	4356	
Au/1.5 Fe ₂ O ₃ /CeAl	25	21	1368	
Pt/SiO ₂	177	10	36	
Al ₂ O ₃ -supported Pt	250	10	720	[3]
Al ₂ O ₃ -supported Pd	250	10	14400	
Al ₂ O ₃ -supported Rh	250	10	21600	
Au/TiO ₂ /Mo(100)	27	2.4	720*	[4]

*at a reaction time of 100min

[1] T. Ramirez Reina, S. Ivanova, M. I. Dominguez, M. A. Centeno, J. A. Odriozola, *Applied Catalysis A: General*, 2012, **419–420**, 58–66.

[2] N. W. Cant, *J. Catal*, 1980, **62**, 173-175.

[3] Y. F. Yu Yao, *J. Catal*, 1984, **87**, 152-162.

[4] A. K. Santra, D.W. Goodman, *Electrochimica Acta*, 2002, 47, **22-23**, 3595-3609.

Chapter 5 - Confining Functional Nanoparticles into Colloidal Imine-Based COF Spheres by a Sequential Encapsulation–Crystallization Method

■ Nanoparticle Encapsulation

Confining Functional Nanoparticles into Colloidal Imine-Based COF Spheres by a Sequential Encapsulation–Crystallization Method

David Rodríguez-San-Miguel^{+, [a]}, Amirali Yazdi^{+, [b]}, Vincent Guillerme^{, [b]}, Javier Pérez-Carvajal^{, [b]}, Víctor Puentes^{, [b, c]}, Daniel Maspoch^{, [b, c]} and Félix Zamora^{*, [a, d, e]}

Abstract: Here, a two-step method is reported that enables imparting new functionalities to covalent organic frameworks (COFs) by nanoparticle confinement. The direct reaction between 1,3,5-tris(4-aminophenyl)benzene and 1,3,5-benzenetricarbaldehyde in the presence of a variety of metallic/metal-oxide nanoparticles resulted in embedding of the nanoparticles in amorphous and non-porous imine-linked polymer organic spheres (NP@a-1). Post-treatment reactions of NP@a-1 with acetic acid under reflux led to crystalline and porous imine-based COF-hybrid spheres (NP@c-1). Interestingly, Au@c-1 and Pd@c-1 were found to be catalytically active.

The confinement of metallic and metal-oxide nanoparticles (NPs) in porous materials is a fruitful strategy to develop composites in which the porous matrix acts as a dispersive and protective medium for the NPs in addition to providing effective and selective accessibility to them. Owing to these properties, this class of composites shows promises for myriad appli-

cations, including heterogeneous catalysis,^[1] sensing,^[2] gas storage,^[3] plasmonics,^[4] remediation,^[5] batteries,^[6] biocides,^[7] magnetic refrigeration,^[8] and controlled guest release.^[9] To date, different porous materials have been explored for producing these composites, including activated carbon,^[10] silica,^[11] microporous zeolites,^[12] porous organic polymers,^[13] and, more recently, metal–organic frameworks (MOFs).^[14] Among the new porous materials available today, their covalent counterparts, covalent organic frameworks (COFs), are also emerging as attractive candidates for the elaboration of these composites. Similar to MOFs, COFs are attainable in various pore sizes and shapes with large surface areas and tailored pore surfaces. Despite their challenging crystallization,^[15] COFs show better thermal and chemical (e.g., aqueous, alkali, and acidic) stability, which can be a crucial feature for certain applications,^[16] for example, in heterogeneous catalysis, remediation, and biomedicine. Recently, NPs have been incorporated in COFs by infiltration of the NP precursors and subsequent growth of the NPs inside the pores.^[17] For MOFs, an alternative approach that has proved very productive for preparing a wide variety of MOF/NP composites is the encapsulation of pre-synthesized NPs into the MOF crystals.^[18] This approach allows control of the size, shape, and composition of the NPs and, therefore, their inherent properties.^[14a] It also allows improving their dispersion and controlling the number and localization of the NPs inside the MOF crystals.^[19] Thus far, however, the ability to apply this approach for COF particles has not yet been demonstrated, in part because of the incompatibility of the NP chemistry and that used to synthesize and crystallize COFs.

Here, we report a two-step strategy that enables the encapsulation of several types of NPs into imine-based COF spheres (Scheme 1). The first step is based on the encapsulation of NPs into amorphous imine-based spheres under mild conditions. This process resembles the traditional encapsulation technologies widely used for the entrapment of species into colloidal, amorphous, purely organic or metal–organic polymer spheres.^[20] The second step is based on the possibility to transform solid amorphous imine-like polymers into their crystalline COF analogues by exposing them to acidic conditions at 70 °C. Initially reported by Dichtel and co-workers,^[21] a variation of this method was recently used by Wang and co-workers^[17] to coat single iron oxide spheres (diameter: ca. 200–300 nm) with a layer of an imine-based COF for photothermal therapy. In the present study we show that this second crystallization step

[a] D. Rodríguez-San-Miguel, Dr. F. Zamora
Departamento de Química Inorgánica and Institute for Advanced Research in Chemical Sciences
Universidad Autónoma de Madrid
28049 Madrid (Spain)
E-mail: felix.zamora@uam.es

[b] A. Yazdi, V. Guillerme, Dr. J. Pérez-Carvajal, Prof. Dr. V. Puentes, Prof. Dr. D. Maspoch
Catalan Institute of Nanoscience and Nanotechnology (ICN2)
CSIC and The Barcelona Institute of Science and Technology
Campus UAB, Bellaterra, 08193 Barcelona (Spain)
E-mail: daniel.maspoch@icn2.cat

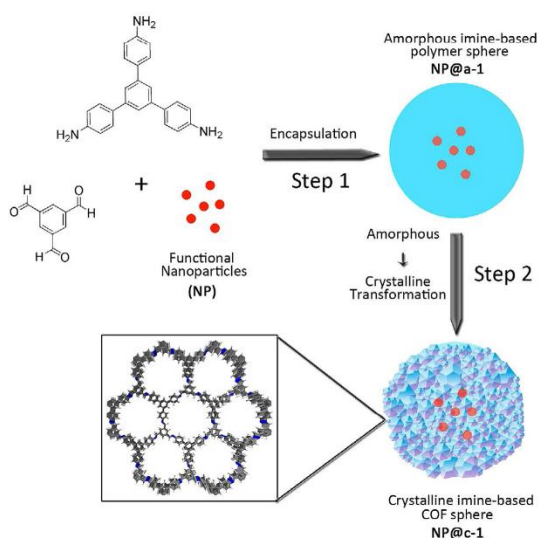
[c] Prof. Dr. V. Puentes, Prof. Dr. D. Maspoch
ICREA, Pg. Lluís Companys 23, 08010 Barcelona (Spain)

[d] Dr. F. Zamora
Instituto Madrileño de Estudios Avanzados en Nanociencia (IMDEA Nanociencia)
Cantoblanco, 28049 Madrid (Spain)

[e] Dr. F. Zamora
Condensed Matter Physics Center (IFIMAC)
Universidad Autónoma de Madrid
Madrid 28049 (Spain)

[*] These authors contributed equally to this work.

Supporting Information and the ORCID identification number(s) for the author(s) of this article can be found under <https://doi.org/10.1002/chem.201702072>.



Scheme 1. Schematic representation of the two-step encapsulation–crystallization process used to incorporate functional NPs into porous and crystalline COF spheres.

preserves the initial colloidal properties of the amorphous imine-based spheres and the dispersion, size, shape, and properties of the embedded NPs.

The design of our method began with the study of the formation of the amorphous imine-based polymer spheres and their subsequent transformation into their analogue porous COF spheres (see details in Ref. [22]). To this end, two trigonal building blocks, 1,3,5-tris(4-aminophenyl)benzene and 1,3,5-benzenetricarbaldehyde, were dissolved in an acetone/acetic acid mixture and stirred for 1 h at room temperature.^[22] The resulting yellow suspension was centrifuged (18407 rcf) for 2 min, the collected solid was washed twice with acetone and tetrahydrofuran, and finally dried for 48 h at room temperature and for 24 h at 150 °C under vacuum. Field-emission scanning (FESEM) and transmission (TEM) electron microscopy images and X-ray powder diffraction (XRPD) studies revealed that this fast condensation reaction produced the kinetically favorable, amorphous spheres with diameter of approximately 600 nm (hereafter called **amorphous-1** or **a-1**; Figure 1 a, c, i). The spectroscopic and analytical characterization of **a-1** agreed with those data already reported (Figures S1–S3 in the Supporting Information).^[22]

The formation of the more thermodynamically stable long-range-ordered structure was then achieved under reversible

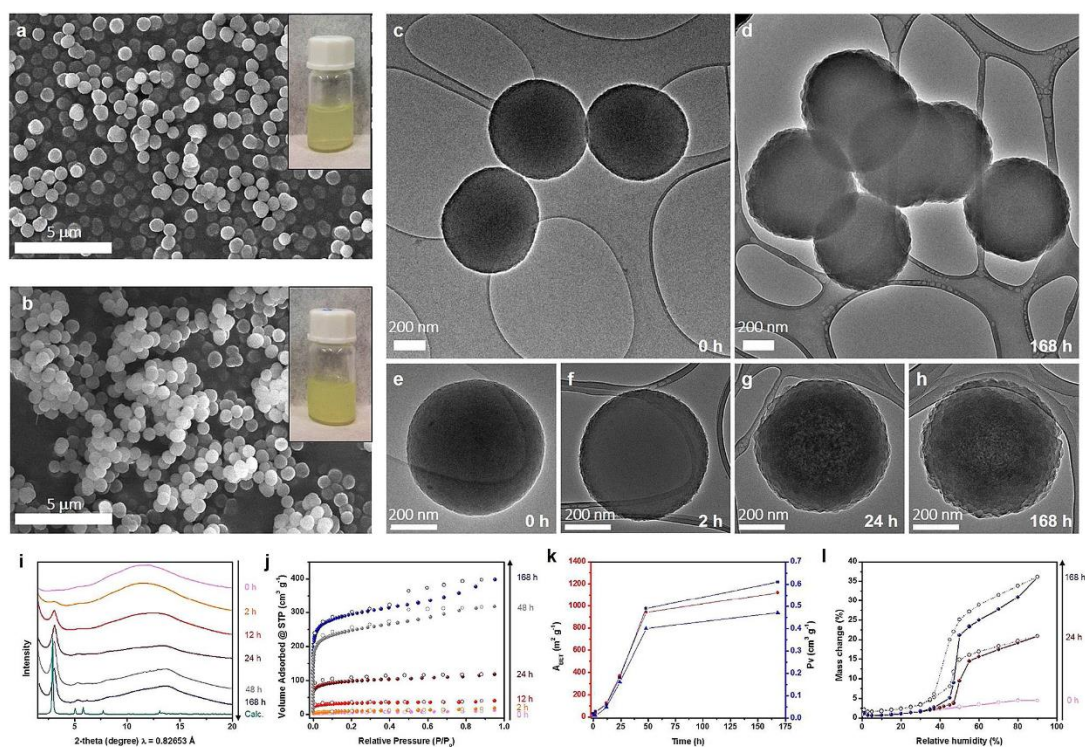


Figure 1. (a, b) Representative FESEM images of (a) **a-1** and (b) **c-1** spheres; insets show the corresponding photography of an aqueous colloidal solution; (c, d) TEM images of (c) **a-1** and (d) **c-1** spheres; (e–h) evolution of the roughness of the COF spheres at (e) $t = 0$ h, (f) 2 h, (g) 24 h, and (h) 168 h; (i–l) evolution of the (i) crystallinity, (j, k) porosity, and (l) water-sorption uptake during the amorphous-to-crystalline transformation; in (k), A_{BET} (red), micropore volume (blue), and total pore volume (black); in (l), water-sorption isotherms of **a-1** (pink), **a-1** treated for 24 h (magenta), and **c-1** (blue).

bond-formation conditions. For this, **a-1** spheres were treated with acetic acid containing a controlled amount of water under reflux in a mixture of mesitylene/dioxane for 2, 12, 24, 48, and 168 h. Then, each of the synthesized solids was collected by centrifugation (2348 rcf), washed with toluene, and dried for 48 h at room temperature and for 24 h at 150 °C under vacuum. The spectroscopic and analytical characterization of **c-1** did not show any significant change to that observed for its amorphous precursor **a-1** (Figures S1–S4 in the Supporting Information). The evolution of the amorphous-to-crystalline transformation was then followed by analyzing these solids by TEM, FESEM, XRPD, and gas- and water-sorption studies (Figure 1). TEM images showed submicrometric spheres (ca. 600 nm diameter) for all samples (Figure 1 c–h), thereby confirming that this treatment retained the shape and size of the initial **a-1** spheres. However, a closer look at the texture revealed a gradual increase in the roughness of the material for longer treatment times. XRPD clearly showed a gradual evolution of the crystallinity as a function of time (Figure 1 i) with the appearance of peaks that matched those calculated for the expected eclipsed COF structure (rather than the staggered) (Figure S6 in the Supporting Information).^[23] Thus, we assumed that the increase in roughness detected during the transition from **a-1** to the spheres treated for 168 h (hereafter called **crystalline-1** or **c-1**) was caused by the formation of crystalline domains based on COF nanolayers that were confined within the spheres (Figure 1 a–f).

This phenomenon was further confirmed by the calculation of the apparent Brunauer–Emmet–Teller (BET) area from N₂-sorption experiments performed at 77 K (Figures S7–S12 in the Supporting Information), showing a dramatic, gradual increase (Figure 1 j, k) from non-porous ($A_{\text{BET}} = 25 \text{ m}^2 \text{ g}^{-1}$, $V_t = 0.02 \text{ cm}^3 \text{ g}^{-1}$) for **a-1** up to highly porous for **c-1** ($A_{\text{BET}} = 1120 \text{ m}^2 \text{ g}^{-1}$, $V_t = 0.61 \text{ cm}^3 \text{ g}^{-1}$) after 168 h of treatment. The collected isotherms were found to be, according to IUPAC classification, type IV isotherms presenting H₂-type hysteresis loops. This behavior, commonly attributed to the presence of some mesoporosity, was in the present case more likely a result of some structural swelling as sometimes observed for this type of materials,^[24] or a combination of both.

In light of this porosity, we also investigated the CO₂ sorption (Figure S13 in the Supporting Information) and water-vapor sorption (Figure 1 l) properties of **a-1** and **c-1**. Similar to many amorphous polymers and despite its non-accessibility to N₂, **a-1** was found to be slightly porous to CO₂ with a total uptake (203 K, 760 Torr; 1 Torr \approx 133.322 Pa) of 3.9 mmol g⁻¹. As expected, **c-1** exhibited a much higher total uptake under similar conditions (14.3 mmol g⁻¹). The heats of adsorption (Q_{st}) derived from the isotherms collected at various temperatures between 258 and 298 K were found to be between 35 and 20 kJ mol⁻¹ for **a-1** and between 25 and 19 kJ mol⁻¹ for **c-1** (Figures S14 and S15 in the Supporting Information). These values are in the expected range of energies for a material without specific groups expected to interact with CO₂. The higher Q_{st} observed for the amorphous material can be attributed to a smaller pore size (**a-1** is non-porous to N₂).

Water-vapor sorption isotherms showed that the amorphous-to-crystalline transformation induced a gradual transition from hydrophobic to hydrophilic behavior (Figure 1 l). The water uptake of **a-1** increased monotonically, achieving a total uptake of only 0.04 g_{water} g_{COF}⁻¹. Interestingly, the development of porosity led to an increase of the uptake up to 0.21 and 0.37 g_{water} g_{COF}⁻¹ after 24 and 168 h of treatment, respectively. This behavior can be correlated with the gradual structural rearrangement from **a-1** into **c-1** upon treatment. The water isotherm of **c-1** can be described as type V, which is a typical behavior for porous materials with hydrophobic walls.^[25]

Once we confirmed that the chemical treatment leading to the rearrangement of the amorphous, non-porous **a-1** spheres into crystalline, highly porous **c-1** spheres could take place, we envisioned the use of the two-step process to confine NPs into COFs. In this process, the fast formation of **a-1** spheres should allow the encapsulation of NPs at room temperature. Then, because the NPs are encapsulated and protected, the amorphous-to-crystalline transformation at high temperatures should occur without compromising the properties of the NPs.

To prove the efficiency of this strategy, we initially started with the encapsulation of Fe₃O₄ NPs (9.8 ± 3.9 nm). These NPs were synthesized by using well-established methods, functionalized with polyvinylpyrrolidone (PVP), and dispersed in acetone.^[26] The Fe₃O₄ NPs were incorporated into the acetone/acetic acid mixture of the two trigonal building blocks, and the two-step process was reproduced by using the above-mentioned conditions. High-angle annular dark-field scanning transmission electron microscopy (HAADF-STEM) micrographs and XRPD studies of the solids collected after the first and second step showed the successful formation of Fe₃O₄@**a-1** and Fe₃O₄@**c-1** submicron spheres containing Fe₃O₄ NPs dispersed mostly in their center (Figure 2 a, b and Figure S16 in the Supporting Information). The chemical composition of

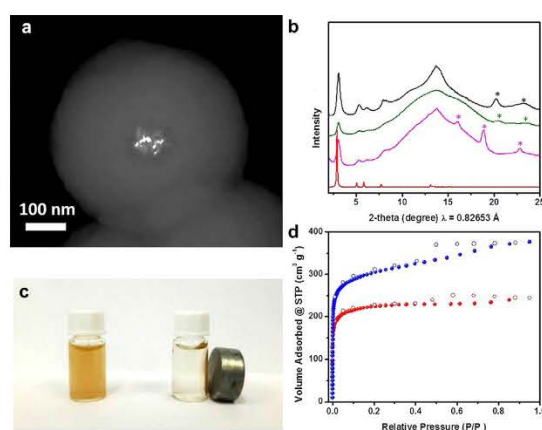


Figure 2. (a) HAADF-STEM image of a single Fe₃O₄@**c-1** sphere; (b) XRPD diagrams of Fe₃O₄@**c-1** (pink), Au@**c-1** (black), and Pd@**c-1** (green) composites in comparison to that simulated for the expected eclipsed **c-1** structure (red); stars highlight the presence of the characteristic peaks of the NPs; (c) visual observation of the magnetic nature of Fe₃O₄@**c-1** spheres; (d) N₂-sorption isotherms of **c-1** (blue) and Fe₃O₄@**c-1** spheres (red).

$\text{Fe}_3\text{O}_4@c-1$ spheres determined by energy-dispersive X-ray (EDX) microanalysis revealed that every sphere contained iron, oxygen, nitrogen, and carbon (Figure S18 in the Supporting Information). The content of iron in the composites was estimated by inductively coupled plasma optical emission spectrometry (ICP-OES), from which a Fe_3O_4 NP content of 7.6% w/w in the composite was determined. In addition, colloidal $\text{Fe}_3\text{O}_4@c-1$ spheres showed magnetic attraction when they were exposed to a magnet (Figure 2c). Therefore, it could be concluded that NPs encapsulated within the COF spheres were the initial Fe_3O_4 NPs, and, consequently, that the two-step process did not modify the properties of the embedded NPs. Also, the permanent porosity of $\text{Fe}_3\text{O}_4@c-1$ spheres was evaluated by N_2 sorption at 77 K. As expected, the sample was found to be porous, with an apparent BET area lower than that of the **c-1** spheres (Figure 2d, $A_{\text{BET}} = 880 \text{ m}^2 \text{ g}^{-1}$, $V_t = 0.38 \text{ cm}^3 \text{ g}^{-1}$).

We then extended the use of this process to the encapsulation of other types of NPs. By using the same strategy, **c-1** spheres containing Au ($9.0 \pm 2.4 \text{ nm}$) and Pd ($3.3 \pm 1.1 \text{ nm}$) NPs were prepared (Figure 3). As shown by XRPD measurements, both composites exhibited the characteristic peaks of **c-1** as well as the diffraction peaks associated with the NPs (Figure 2b). Moreover, EDX microanalysis confirmed the presence of Au and Pd in the **Au@c-1** and **Pd@c-1** composites, respectively (Figures S20 and S22 in the Supporting Information).

This type of metallic NP/COF composites should be very useful for heterogeneous catalysis. However, for this to be a reality, the porous COF matrix should allow the accessibility of molecules to the embedded NPs. As a proof-of-concept, we studied this accessibility by using both **Au@c-1** and **Pd@c-1** composites for the catalytic reduction of 4-nitrophenol (4-NP) into 4-aminophenol (4-AP) in the presence of NaBH_4 as a reducing agent. The catalytic reactions were conducted by mixing two aqueous solutions of NaBH_4 and 4-NP with an aqueous dispersion of **Pd@c-1** (Pd: 1.1% w/w) or **Au@c-1** (Au: 3.5% w/w) and followed by UV/Vis spectroscopy (Figure 3). As control experiments, we also reproduced the same reaction by using **c-1** (without NPs) and the amorphous **Au@a-1** and **Pd@a-1** hybrids as catalyst. In these latter cases, no catalytic activity was observed (Figure 3 and Figure S24 in the Supporting Information). For the **Au@c-1** and **Pd@c-1** hybrids, however, their catalytic activity was confirmed by the reduction of the peak at 400 nm as well as the appearance of a new peak at 305 nm, corresponding to 4-AP (Figure 3). 4-NP was fully reduced into 4-AP after 10 min for **Au@c-1** and after 14 min for **Pd@c-1**. These results are comparable to previously reported reductions of 4-NP by NP/MOF (mainly, ZIF-8 and UiO-66) hybrids but slightly less active than an Au@carbon yolk-shell nanocomposite,^[27] and confirm the accessibility of molecules to the embedded NPs.

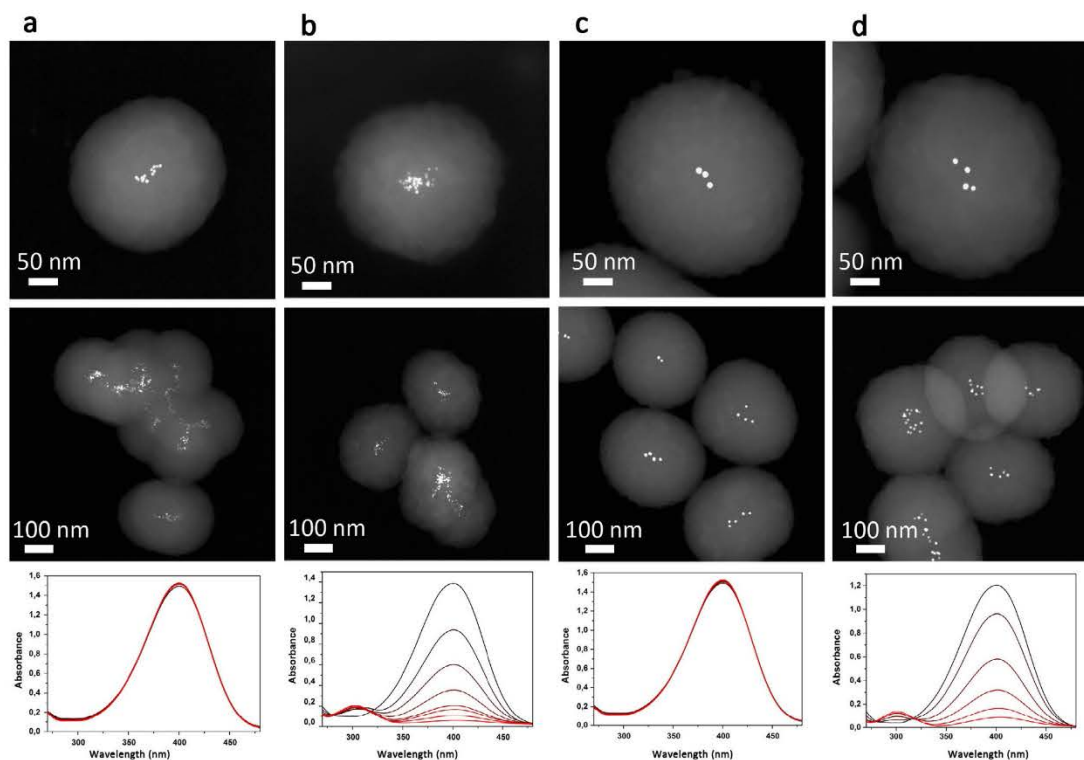


Figure 3. HAADF-STEM images (first row: single sphere; second row: general view) of (a) **Pd@a-1**, (b) **Pd@c-1**, (c) **Au@a-1**, and (d) **Au@c-1** composites. Third row shows the UV/Vis evolution of 4-NP reduction by using the corresponding composites as catalysts. Each spectrum was collected in intervals of 2 min.

In summary, we have demonstrated an efficient and simple two-step procedure to encapsulate several types of NPs into porous and crystalline imine-based COF spheres. This strategy could be extended to a broad range of NPs and their mixtures, and also to encapsulate molecular species. As a proof-of-concept we have also shown the ability of Au@c-1 and Pd@c-1 hybrids to catalyze the reduction of 4-nitrophenol into 4-aminophenol, which confirms the diffusion of reactants and products through the COF spheres to the embedded metallic NPs. This last result suggests potential applications in selective catalysis, remediation, and molecular delivery.

Acknowledgements

This work was supported by the Spanish MINECO (projects PN MAT2016-77608-C3-1-P and MAT2015-65354-C2-1-R), the Catalan AGAUR (project 2014 SGR 80), and the ERC under the EU FP7 (ERC-Co 615954). V.G. is grateful to the Generalitat de Catalunya for a Beatriu de Pinós fellowship (2014 BP-B 00155). A.Y. and ICN2 acknowledge the support of the Spanish MINECO through the Severo Ochoa Centers of Excellence Program, under Grant SEV-2013-0295.

Conflict of interest

The authors declare no conflict of interest.

Keywords: covalent organic frameworks • crystallization • encapsulation • hybrids • nanoparticles

- [1] a) C. Belver, J. Bedia, J. J. Rodriguez, *Appl. Catal. B* **2015**, *176–177*, 278–287; b) Y. Mei, Y. Lu, F. Polzer, M. Ballauff, M. Drechsler, *Chem. Mater.* **2007**, *19*, 1062–1069; c) S. Ikeda, S. Ishino, T. Harada, N. Okamoto, T. Sakata, H. Mori, S. Kuwabata, T. Torimoto, M. Matsumura, *Angew. Chem. Int. Ed.* **2006**, *45*, 8200–8203; *Angew. Chem.* **2006**, *118*, 8380–8383.
- [2] M. Segev-Bar, H. Haick, *ACS Nano* **2013**, *7*, 8366–8378.
- [3] C. Zlotea, R. Campesi, F. Cuevas, E. Leroy, P. Dibandjo, C. Volkringer, T. Loiseau, G. Férey, M. Latroche, *J. Am. Chem. Soc.* **2010**, *132*, 2991–2997.
- [4] D. Batra, S. Seifert, L. M. Varela, A. C. Y. Liu, M. A. Firestone, *Adv. Funct. Mater.* **2007**, *17*, 1279–1287.
- [5] a) J. Yang, H. Zhang, M. Yu, I. Emmanuelawati, J. Zou, Z. Yuan, C. Yu, *Adv. Funct. Mater.* **2014**, *24*, 1354–1363; b) F. He, D. Zhao, J. Liu, C. B. Roberts, *Ind. Eng. Chem. Res.* **2007**, *46*, 29–34; c) S. Saha, A. Pal, S. Kundu, S. Basu, T. Pal, *Langmuir* **2010**, *26*, 2885–2893.
- [6] R. Zou, Q. Liu, G. He, M. F. Yuen, K. Xu, J. Hu, I. P. Parkin, C.-S. Lee, W. Zhang, *Adv. Energy Mater.* **2016**, *6*, 160–163.
- [7] a) P. Lalueva, D. Carmona, M. Monzón, M. Arruebo, J. Santamaría, *Microporous Mesoporous Mater.* **2012**, *156*, 171–175; b) J. Pérez-Carvajal, P. Lalueva, C. Casado, C. Téllez, J. Coronas, *Appl. Clay Sci.* **2012**, *56*, 30–35.
- [8] A. Zelenáková, P. Hrubovčák, O. Kapusta, V. Zelenák, V. Franco, *Appl. Phys. Lett.* **2016**, *109*, 122412.
- [9] a) C.-Y. Lai, B. G. Trewyn, D. M. Jeftinija, K. Jeftinija, S. Xu, S. Jeftinija, V. S. Y. Lin, *J. Am. Chem. Soc.* **2003**, *125*, 4451–4459; b) P. Yang, S. Gai, J. Lin, *Chem. Soc. Rev.* **2012**, *41*, 3679–3698; c) K. H. Min, K. Park, Y.-S. Kim, S. M. Bae, S. Lee, H. G. Jo, R.-W. Park, I.-S. Kim, S. Y. Jeong, K. Kim, I. C. Kwon, *J. Controlled Release* **2008**, *127*, 208–218.
- [10] a) C. He, S. Wu, N. Zhao, C. Shi, E. Liu, J. Li, *ACS Nano* **2013**, *7*, 4459–4469; b) M. Kim, K. Sohn, H. B. Na, T. Hyeon, *Nano Lett.* **2002**, *2*, 1383–1387.
- [11] a) F. Caruso, M. Spasova, V. Salgueiriño-Maceira, L. M. Liz-Marzán, *Adv. Mater.* **2001**, *13*, 1090–1094; b) J. Kim, J. E. Lee, J. Lee, J. H. Yu, B. C. Kim, K. An, Y. Hwang, C.-H. Shin, J.-G. Park, J. Kim, T. Hyeon, *J. Am. Chem. Soc.* **2006**, *128*, 688–689.
- [12] a) G. Yang, N. Tsubaki, J. Shamoto, Y. Yoneyama, Y. Zhang, *J. Am. Chem. Soc.* **2010**, *132*, 8129–8136; b) J. Chen, Z. Feng, P. Ying, C. Li, *J. Phys. Chem. B* **2004**, *108*, 12669–12676.
- [13] A. G. Skirtach, C. Dejugnat, D. Braun, A. S. Susha, A. L. Rogach, W. J. Parak, H. Möhwald, G. B. Sukhorukov, *Nano Lett.* **2005**, *5*, 1371–1377.
- [14] a) P. Falcaro, R. Ricco, A. Yazdi, I. Imaz, S. Furukawa, D. Maspoche, R. Ameloot, J. D. Evans, C. J. Doonan, *Coord. Chem. Rev.* **2016**, *307*, 237–254; b) C. M. Doherty, D. Buso, A. J. Hill, S. Furukawa, S. Kitagawa, P. Falcaro, *Acc. Chem. Res.* **2014**, *47*, 396–405; c) M. Mukoyoshi, H. Kobayashi, K. Kusada, M. Hayashi, T. Yamada, M. Maesato, J. M. Taylor, Y. Kubota, K. Kato, M. Takata, T. Yamamoto, S. Matsumura, H. Kitagawa, *Chem. Commun.* **2015**, *51*, 12463–12466.
- [15] D. Beaudoin, T. Maris, J. D. Wuest, *Nat. Chem.* **2013**, *5*, 830–834.
- [16] J. L. Segura, M. J. Mancheno, F. Zamora, *Chem. Soc. Rev.* **2016**, *45*, 5635–5671.
- [17] J. Tan, S. Namuangruk, W. F. Kong, N. Kungwan, J. Guo, C. C. Wang, *Angew. Chem. Int. Ed.* **2016**, *55*, 13979–13984; *Angew. Chem.* **2016**, *128*, 14185–14190.
- [18] G. Lu, S. Z. Li, Z. Guo, O. K. Farha, B. G. Hauser, X. Y. Qi, Y. Wang, X. Wang, S. Y. Han, X. G. Liu, J. S. DuChene, H. Zhang, Q. C. Zhang, X. D. Chen, J. Ma, S. C. J. Loo, W. D. Wei, Y. H. Yang, J. T. Hupp, F. W. Huo, *Nat. Chem.* **2012**, *4*, 310–316.
- [19] a) L. Chen, Y. Peng, H. Wang, Z. Gu, C. Duan, *Chem. Commun.* **2014**, *50*, 8651–8654; b) S. Li, F. Huo, *Small* **2014**, *10*, 4371–4378.
- [20] a) I. Imaz, J. Hernandez, D. Ruiz-Molina, D. Maspoche, *Angew. Chem. Int. Ed.* **2009**, *48*, 2325–2329; *Angew. Chem.* **2009**, *121*, 2361–2365; b) Y. Zhang, D. Rochefort, *J. Microencapsulation* **2010**, *27*, 703–713.
- [21] B. J. Smith, N. Hwang, A. D. Chavez, J. L. Novotney, W. R. Dichtel, *Chem. Commun.* **2015**, *51*, 7532–7535.
- [22] D. Rodríguez-San-Miguel, J. J. Corral-Pérez, E. Gil-González, D. Cuellas, J. Arauzo, V. M. Monsalvo, V. Carcelén, F. Zamora, *CrystEngComm* **2017**, <https://doi.org/10.1039/C6CE02200F>.
- [23] A. de la Peña Ruigómez, D. Rodríguez-San-Miguel, K. C. Stylianou, M. Cavallini, D. Gentili, F. Liscio, S. Milita, O. M. Roscioni, M. L. Ruiz-González, C. Carbonell, D. Maspoche, R. Mas-Ballesté, J. L. Segura, F. Zamora, *Chem. Eur. J.* **2015**, *21*, 10666–10670.
- [24] a) R. Dawson, A. I. Cooper, D. J. Adams, *Prog. Polym. Sci.* **2012**, *37*, 530–563; b) V. Guillerme, Ł. J. Weseliński, M. Alkordi, M. I. H. Mohideen, Y. Belmabkhout, A. J. Cairns, M. Eddaoudi, *Chem. Commun.* **2014**, *50*, 1937–1940.
- [25] a) M. F. de Lange, K. J. F. M. Verouden, T. J. H. Vlugt, J. Gascon, F. Kapteijn, *Chem. Rev.* **2015**, *115*, 12205–12250; b) S. Paranthaman, F.-X. Couderc, A. H. Fuchs, *Phys. Chem. Chem. Phys.* **2010**, *12*, 8123–8130; c) J. Canivet, J. Bonnefoy, C. Daniel, A. Legrand, B. Coasne, D. Farrusseng, *New J. Chem.* **2014**, *38*, 3102–3111.
- [26] X. Liu, Z. Ma, J. Xing, H. Liu, *J. Magn. Magn. Mater.* **2004**, *270*, 1–6.
- [27] a) Z. Li, H. C. Zeng, *Chem. Mater.* **2013**, *25*, 1761–1768; b) W. Zhang, G. Lu, C. Cui, Y. Liu, S. Li, W. Yan, C. Xing, Y. R. Chi, Y. Yang, F. Huo, *Adv. Mater.* **2014**, *26*, 4056–4060; c) R. Liu, S. M. Mahurin, C. Li, R. R. Unocic, J. C. Idrobo, H. Gao, S. J. Pennycook, S. Dai, *Angew. Chem. Int. Ed.* **2011**, *50*, 6799–6802; *Angew. Chem.* **2011**, *123*, 6931–6934.

Manuscript received: May 9, 2017

Accepted manuscript online: May 16, 2017

Version of record online: June 13, 2017

Supporting Information

Confining Functional Nanoparticles into Colloidal Imine-Based COFSpheres by a Sequential Encapsulation–Crystallization Method

David Rodriguez-San-Miguel⁺,^[a] Amirali Yazdi⁺,^[b] Vincent Guillerm,^[b] Javier
Perez-Carvajal,^[b] Victor Puentes,^[b, c] Daniel MasPOCH,^{*[b, c]} and Felix
Zamora^{*[a, d, e]}

MATERIALS AND METHODS

1,3,5-benzenetricarboxaldehyde (BTCA) was obtained from Manchester Organics. 1,3,5-tris-(4-aminophenyl)benzene (TAPB) was prepared according to literature procedures.^[1] Other chemicals and solvents were obtained from Sigma-Aldrich and used without further purification unless specified.

Attenuated Total Reflection Fourier Transform Infrared Spectroscopy: ATR-FT-IR spectroscopy was recorded in a Perkin Elmer Spectrum 100 with a PIKE Technologies MIRacle Single Reflection Horizontal ATR accessory with a spectral range of 4000-650 cm^{-1} .

Solid-State ^{13}C CP-MAS Nuclear Magnetic Resonance Spectroscopy. Solid-state nuclear magnetic resonance (NMR) spectra were recorded at room temperature on a Bruker AV 400 WB spectrometer using a triple channel 4 mm probe with zirconia rotors and a Kel-F cap. Cross-polarization with MAS (CP-MAS) was used to acquire ^{13}C data at 100.61 MHz. The spectral width of the pulse sequence was 35 kHz. The ^1H excitation pulse was 3 μs . The CP contact time was 3.5 ms. High power two-pulse phase modulation (TPPM) ^1H decoupling was applied during data acquisition using a decoupling frequency of 80 kHz. Recycle delays were 4 s. The sample spinning rate was 10 kHz.

Thermogravimetry. Thermogravimetric analyses of samples were run on a Thermobalance TGA Q-500 thermal gravimetric analyzer with samples held in a platinum pan under nitrogen atmosphere. A 10 K min^{-1} ramp rate was used.

Elemental Analysis: Elemental analyses were obtained using LECO CHNS-932 elemental analyzer.

Field-Emission Scanning Electron Microscopy: Field-emission scanning electron microscopy (FE-SEM) images were collected on a scanning electron microscope (FEI Magellan 400L XHR) at an acceleration voltage of 1.0 kV, using aluminium as a support.

Transmission Electron Microscopy: High-Angle Annular Dark-Field Scanning Transmission Electron Microscopy (HAADF-STEM) and TEM images and Energy Dispersive X-ray Spectroscopy (EDX) composition profiles were collected on a Transmission Electron Microscope FEI Tecnai G2 F20 at 200 kV.

Powder X-Ray Diffraction: Powder X-ray diffraction (PXRD) data were collected at 100 K at XALOC beamLine at ALBA synchrotron^[2] ($\lambda = 0.82653 \text{ \AA}$). Data were integrated and scaled using the Fit2D program.^[3]

Inductively Coupled Plasma - Mass Spectrometry: ICP-MS measurements were performed using an ICP-MS Agilent Series 7500.

Gas Adsorption: Volumetric N_2 and CO_2 sorption isotherms were collected at 77 K (N_2) and 203 K, 258 K, 273 K, 288 K, 298 K (CO_2) using an ASAP 2020 HD (Micromeritics). Temperature was controlled by a liquid nitrogen bath (77 K) or Lauda Proline RP 890 chiller (203 K – 298 K). As recommended by Rouquerol (COPS X conference, Characterization Of Porous Solids, Granada, 2014), Brunner Emmet Teller (BET) area and total pore volumes are selected preferentially to Langmuir model for the evaluation and comparison of the porosity of MOFs. BET areas (A_{BET}) were calculated using MicroActive software within an appropriate pressure range in order to keep the C constant positive, using the criteria recommended by Rouquerol *et al.*^[4] The micropore volumes (V_{t}) were calculated at

$P/P_0 = 0.3$, whereas the total pore volumes (V_t) were calculated at $P/P_0 = 0.95$. Samples were outgassed for 12 h under secondary vacuum at 150°C.

UV-Visible Spectroscopy: UV-visible spectra were acquired with a Shimadzu UV-2400 spectrophotometer. Samples were placed in a cell, and spectral analysis was performed at room temperature.

Dynamic Light Scattering: Dynamic light scattering (DLS) spectra were acquired with a Zetasizer Nano ZS. Samples were dispersed in water and placed in a cell, and spectral analysis was performed at room temperature.

SYNTHETIC PROCEDURES

a-1 Spheres: BTCA (46 mg, 0.28 mmol) was dissolved in 15 mL of acetone and 3 mL of acetic acid. Separately, TAPB (100 mg, 0.28 mmol) was also dissolved in 15 mL of acetone. The resulting solutions were mixed and stirred for 1 h. A turbid yellow suspension was formed. The reaction mixture was centrifuged at 18407 rcf for 2 min. The supernatant was removed and the yellow solid was washed twice with 20 mL of acetone and twice with 20 mL of tetrahydrofuran (THF), isolating it by means of centrifugation at 18407 rcf for 2 min. Finally, the solid was allowed to dry in ambient conditions for 48 h and under vacuum at 150 °C for 24 h to produce 116 mg (85 % yield) of yellow powder. Elemental analysis calculated for $C_{33}H_{21}N_3 \cdot H_2O$: C: 83.02 %; H: 4.82 %; N: 8.81 %. Found: C: 82.97 %; H: 4.88 %; N: 8.56 %.

c-1 Spheres: a-1 (116 mg) was dispersed in a mixture of 10.5 mL of 1,4-dioxane, 2.1 mL of mesitylene, 2.1 mL of water and 3.1 mL of acetic acid and heated for 7 days. After cooling, the mixture was centrifuged at 2348 rcf for 3 min. The supernatant was removed and the yellow solid was washed with toluene (20 + 12 mL), isolating it by means of centrifugation at 2348 rcf for 3 min. Finally, the solid was allowed to dry in ambient conditions for 48 h and under vacuum at 150 °C for 24 h to produce 112 mg (97 % yield) of yellow powder. Elemental analysis calculated for $C_{33}H_{21}N_3 \cdot H_2O$: C: 83.02 %; H: 4.82 %; N: 8.81 %. Found: C: 83.20 %; H: 4.91 %; N: 8.22 %.

PVP Stabilized Gold Nanoparticles: A solution of 2.2 mM sodium citrate in Milli-Q water (150 mL) was heated with a heating mantle in a 250 mL three-necked round-bottomed flask for 15 min under vigorous stirring. A condenser was utilized to prevent the evaporation of the solvent. After boiling had commenced, 1 mL of $HAuCl_4$ (25 mM) was injected. The colour of the solution changed from yellow to bluish gray and then, to soft pink in 10 min. Under these conditions, the resulting particles (9 ± 2.4 nm, $\sim 3 \times 10^{12}$ NPs/mL) were coated with negatively charged citrate ions and hence, they were well suspended in H_2O . After the gold nanoparticle solution was cooled to room temperature, a solution of 0.5 g poly(vinylpyrrolidone) (PVP, MW = 40,000) in water (20 mL) was added dropwise to the gold nanoparticle solution under continuous stirring, and the mixture was further stirred at room temperature for 24 h. Then, 600 mL of acetone were added to this mixture and left overnight. The supernatant was removed, and the resulting nanoparticles were washed one time with methanol and twice with acetone, and finally dispersed in 10 mL of acetone at a concentration of $0.6 \text{ mg} \cdot \text{mL}^{-1}$.^[5]

PVP Stabilized Palladium Nanoparticles: Na_2PdCl_4 (44 mg) was dissolved in 20 mL of ethylene glycol in the presence of 222 mg of poly(vinylpyrrolidone) (PVP, MW = 55,000) in a three-neck round-bottomed flask. This solution was heated up to 180 °C for 10 min and, after cooling down to room temperature, 150 mL of acetone was added to the as-synthesized PVP stabilized palladium

nanoparticles. Then, the precipitated nanoparticles were dispersed in ethanol, washed twice with ethanol and once with acetone, and finally redispersed in acetone to give a colloidal solution of palladium nanoparticles at a concentration of $0.5 \text{ mg}\cdot\text{mL}^{-1}$. The average size of the palladium nanoparticles was $3.3 \pm 1.1 \text{ nm}$.

PVP Stabilized Iron Oxide Nanoparticles: Iron oxide magnetic nanoparticles were prepared by the conventional co-precipitation method. 4 g of $\text{FeCl}_3\cdot 6\text{H}_2\text{O}$, 1.25 g of $\text{FeCl}_2\cdot 4\text{H}_2\text{O}$ and 300 mg of poly (vinylpyrrolidone) (PVP, MW = 55,000) were dissolved in 50 mL of Milli-Q water under nitrogen under vigorous stirring at 80°C . Then, 0.5 mL of NH_4OH (15 M) was added and the solution was heated for another 1.5 h. After cooling, the nanoparticles were sequentially washed with Milli-Q water and ethanol several times. Finally, nanoparticles were washed twice with acetone and the cleaned nanoparticles were dispersed in acetone at a concentration of $1 \text{ mg}\cdot\text{mL}^{-1}$.^[6] The average size of the iron oxide nanoparticles was $9.8 \pm 3.9 \text{ nm}$.

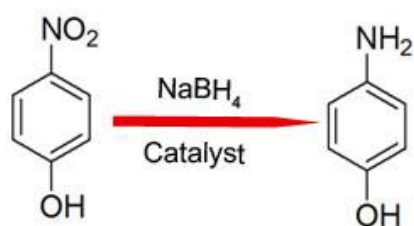
Au@c-1 Spheres: BTCA (20 mg, 0.12 mmol) was dissolved in 1.33 mL of gold nanoparticle suspension, 5.33 mL of acetone and 1.33 mL of acetic acid. Separately, TAPB (43 mg, 0.12 mmol) was also dissolved in 1.33 mL of gold nanoparticle suspension and 5.33 mL of acetone. The resulting solutions were mixed and stirred for 1 h. A pink precipitate was formed in a turbid salmon suspension. The reaction mixture was centrifuged at 24 rcf for 5 min. The turbid salmon supernatant was removed and the pink solid was washed twice with 9 mL of acetone and twice with 9 mL of THF, isolating it by means of centrifugation for 5 min at 94 rcf. The solid was dispersed in a mixture of 5.25 mL of 1,4-dioxane, 1.05 mL of mesitylene, 1.05 mL of water and 1.56 mL of acetic acid and heated for 7 days. After cooling, the mixture was centrifuged at 2348 rcf for 3 min. The supernatant was removed and the solid was washed with thrice with 6 mL of toluene, isolating it by means of centrifugation at 2348 rcf for 3 min. Finally, the solid was allowed to dry in ambient conditions for 48 h and under vacuum at 80°C for 24 h to produce 8.5 mg of brownish-pink powder.

Pd@c-1 Spheres: BTCA (20 mg, 0.12 mmol) was dissolved in 1.33 mL of palladium nanoparticle suspension, 5.33 mL of acetone and 1.33 mL of acetic acid. Separately, TAPB (43 mg, 0.12 mmol) was also dissolved in 1.33 mL of palladium nanoparticle suspension and 5.33 mL of acetone. The resulting solutions were mixed and stirred for 1 h. A black precipitate was formed in a turbid yellow suspension. The reaction mixture was centrifuged at 24 rcf for 5 min. The turbid yellow supernatant was removed and the black solid was washed twice with 9 mL of acetone and twice with 9 mL of THF, isolating it by means of centrifugation for 5 min at 94 rcf. The solid was dispersed in a mixture of 5.25 mL of 1,4-dioxane, 1.05 mL of mesitylene, 1.05 mL of water and 1.56 mL of acetic acid and heated for 7 days. After cooling, the mixture was centrifuged at 2348 rcf for 3 min. The supernatant was removed and the yellow solid was washed with thrice with 6 mL of toluene, isolating it by means of centrifugation at 2348 rcf for 3 min. Finally, the solid was allowed to dry in ambient conditions for 48 h and under vacuum at 80°C for 24 h to produce 10 mg of yellow powder.

Fe_3O_4 @c-1 Spheres: BTCA (150 mg, 0.93 mmol) was dissolved in 25 mL of iron oxide nanoparticle suspension, 25 mL of acetone and 10 mL of acetic acid. Separately, TAPB (325 mg, 0.93 mmol) was also dissolved in 25 mL of iron oxide nanoparticle suspension and 25 mL of acetone. The resulting solutions were mixed and ultrasonicated for 1 h. A brown precipitate was formed in a turbid yellow suspension. The turbid yellow supernatant was removed by means of magnetic decantation. The brown solid was washed thrice with 30 mL of acetone and twice with 30 mL of THF. The solid was dispersed in a mixture of 34.25 mL of 1,4-dioxane, 6.85 mL of mesitylene, 6.85 mL of water and 10.2 mL of acetic acid and heated for 7 days. After cooling, the supernatant was removed by means of magnetic decantation and the solid was washed once with 25 mL of ethanol and twice with 20 mL of toluene.

Finally, the solid was allowed to dry in ambient conditions for 48 h and afterwards was dried under vacuum at 80 °C for 24 h to produce 142 mg of a yellow powder.

4-nitrophenol (4-NP) Reduction: The catalytic reactions were conducted by mixing 0.5 mL of an aqueous solution of NaBH_4 (1.3 M) with 3.0 mL of an aqueous solution of 4-NP (0.125 mM). After 2 min, 0.2 mL of an aqueous solution of 0.15 mg mL^{-1} of **Pd@a-1/Pd@c-1** or 0.4 mL of an aqueous solution of 0.15 mg mL^{-1} of **Au@a-1/Au@c-1** were injected into the reaction mixture. The catalytic reaction was then followed every 2 min by UV-vis spectroscopy in the range of 280–460 nm.



CHARACTERIZATION

Figure S1. ATR-FT-IR spectra of monomers **BTCA** (red) and **TAPB** (blue), of **a-1** (orange) and of **c-1** (green). The most significant changes are highlighted: Disappearance of N-H stretching bands between 3300-3500 cm^{-1} , decrease of the intensity of C=O stretching band at 1689 cm^{-1} , and appearance of C=N stretching band at 1623 cm^{-1} .

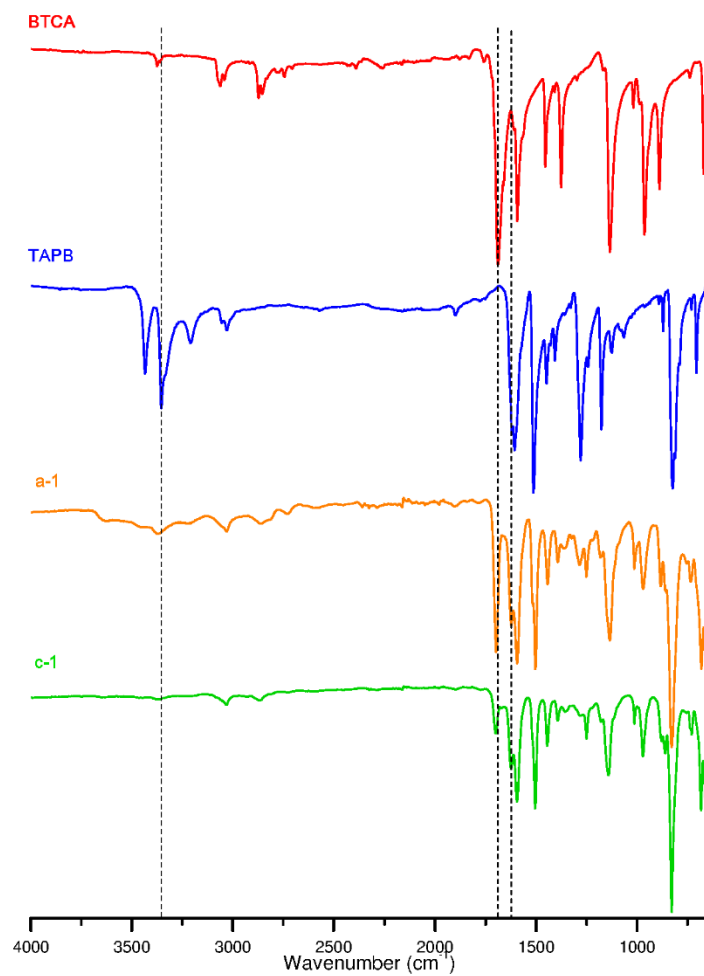
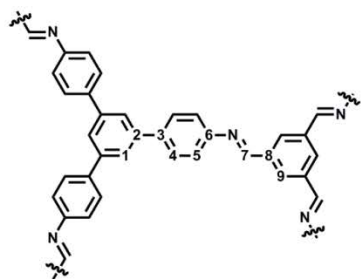
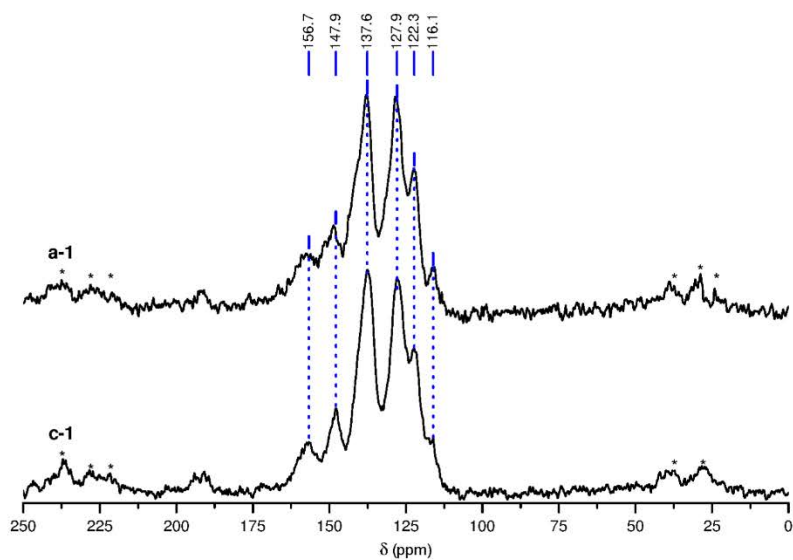


Figure S2. (Top) Solid-state ^{13}C CP-MAS NMR spectra of **a-1** (top), and **c-1** (bottom). Asterisks denote spinning sidebands. (Below) Representation of the imine-based structure and the corresponding assignment of the ^{13}C CP-MAS NMR peaks.



Signal (ppm)	Assignment
156.7	7
147.9	6
137.6	2, 3, 8
127.9	4, 9
122.3	1
116.1	5

Figure S3. TGA trace for a-1.

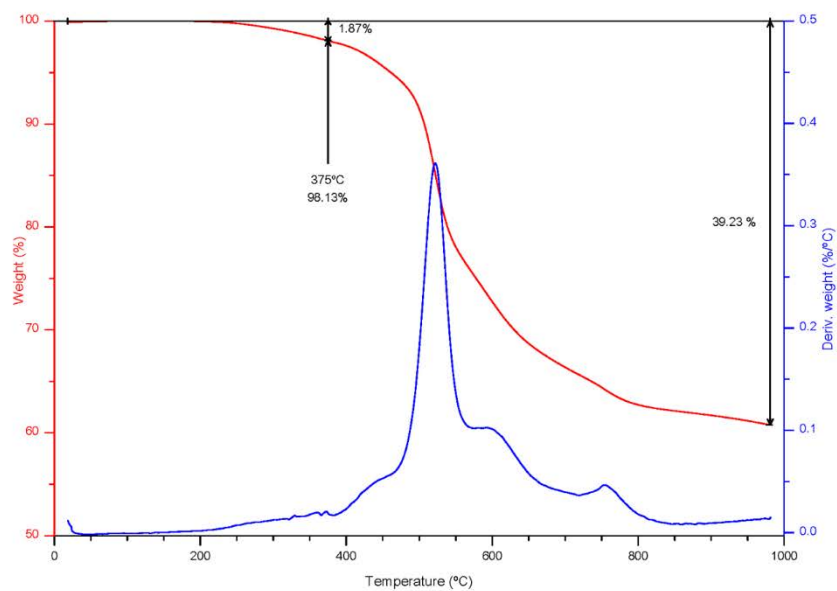


Figure S4. TGA trace for c -1.

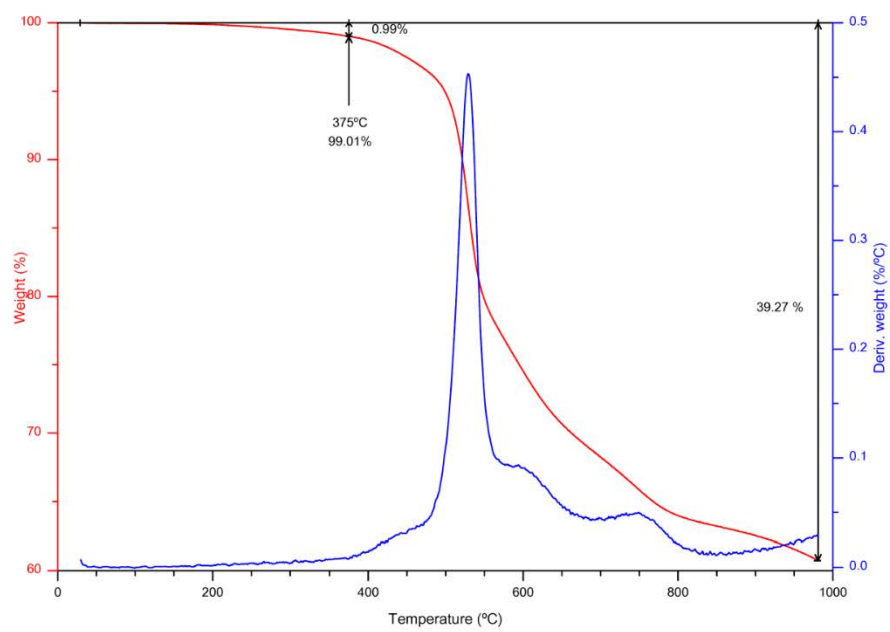


Figure S5. Dynamic Light Scattering (DLS) measurements of an aqueous colloidal solution of (a) **a-1** and (b) **c-1**.

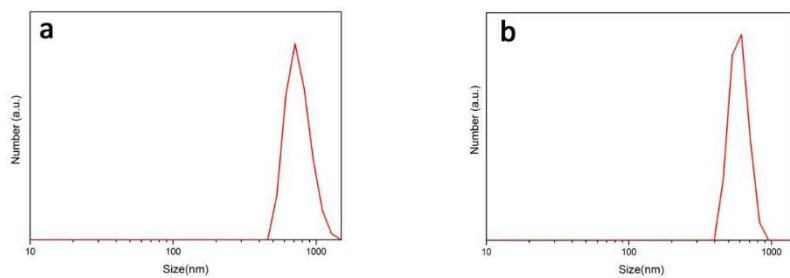


Figure S6. Comparison of calculated PXRD diagram of the staggered (green) and eclipsed (red) COF with experimental PXRD diagram of c-1 (black).

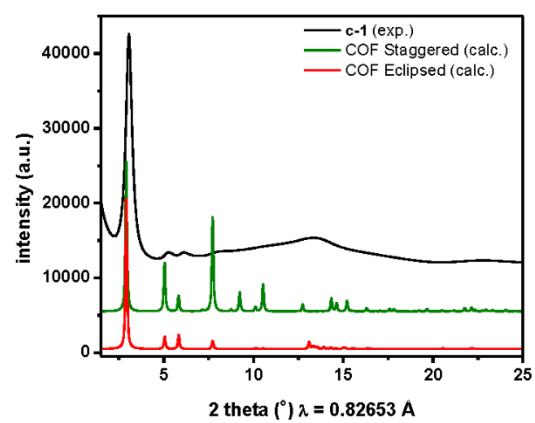
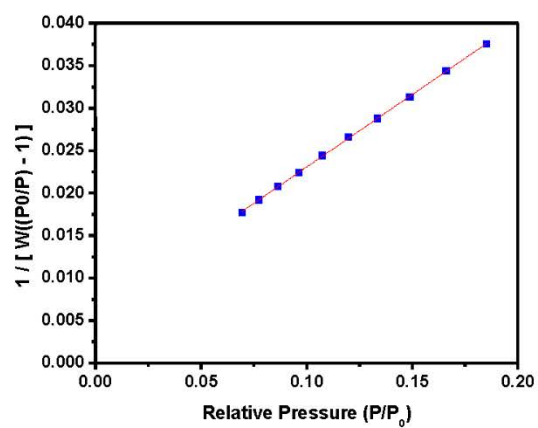
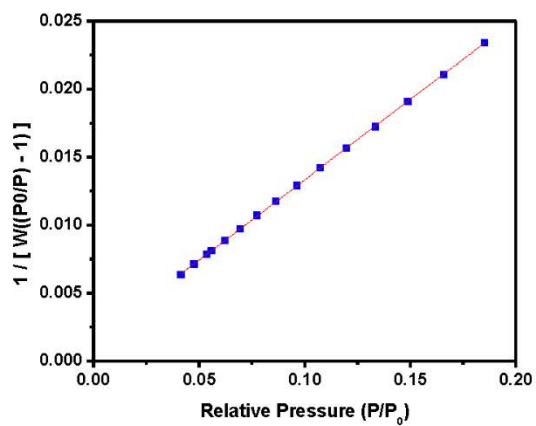


Figure S7. BET plot for N₂ sorption in a-1.



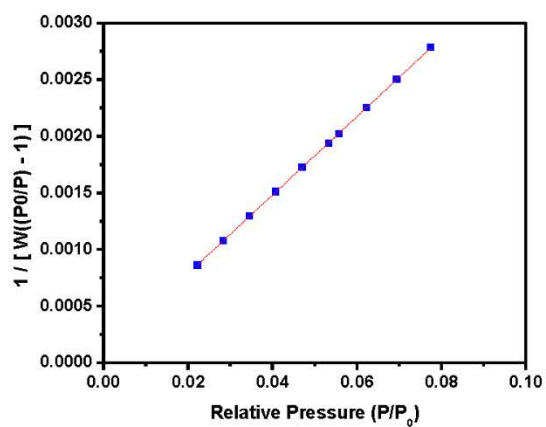
BET surface area: 24.6012 ± 0.1231 m²/g
Slope: 0.170959 ± 0.000878 g/cm³ STP
Y-intercept: 0.005966 ± 0.000109 g/cm³ STP
C: 29.655030
Qm: 5.6521 cm³/g STP
Correlation coefficient: 0.9998944
Molecular cross-sectional area: 0.1620 nm²

Figure S8. BET plot for N₂ sorption in the 2 h-treated a-1.



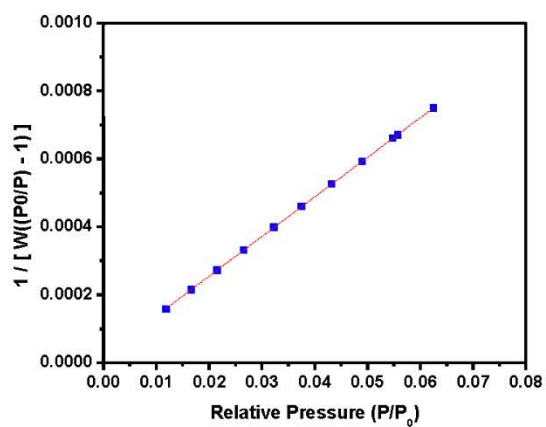
BET surface area: 36.3728 ± 0.0568 m²/g
Slope: 0.118157 ± 0.000186 g/cm³ STP
Y-intercept: 0.001509 ± 0.000020 g/cm³ STP
C: 79.312496
Qm: 8.3566 cm³/g STP
Correlation coefficient: 0.9999839
Molecular cross-sectional area: 0.1620 nm²

Figure S9. BET plot for N₂ sorption in the 12 h-treated a-1.



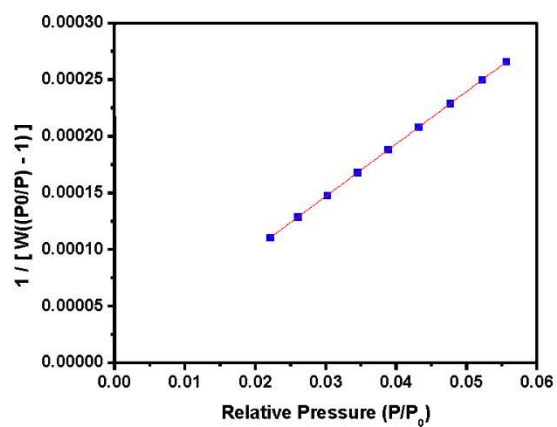
BET surface area: 125.0931 ± 0.2662 m²/g
Slope: 0.034702 ± 0.000074 g/cm³ STP
Y-intercept: 0.000092 ± 0.000004 g/cm³ STP
C: 377.146553
Qm: 28.7400 cm³/g STP
Correlation coefficient: 0.9999818
Molecular cross-sectional area: 0.1620 nm²

Figure S10. BET plot for N₂ sorption in the 24 h-treated a-1.



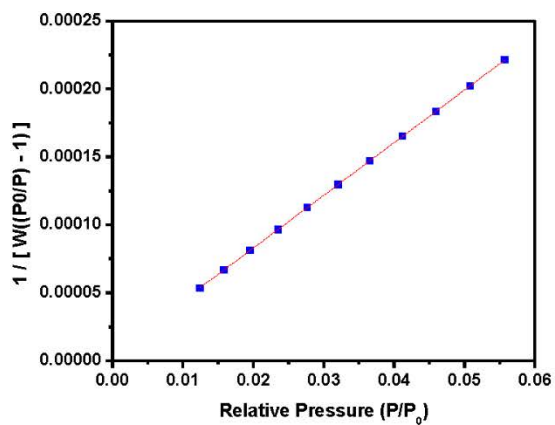
BET surface area: 372.3449 ± 0.5171 m²/g
Slope: 0.011669 ± 0.000016 g/cm³ STP
Y-intercept: 0.000021 ± 0.000001 g/cm³ STP
C: 554.396981
Qm: 85.5458 cm³/g STP
Correlation coefficient: 0.9999913
Molecular cross-sectional area: 0.1620 nm²

Figure S11. BET plot for N₂ sorption in the 48 h-treated a-1.



BET surface area: 938.3967 ± 0.3102 m²/g
Slope: 0.004630 ± 0.000002 g/cm³ STP
Y-intercept: 0.000008 ± 0.000000 g/cm³ STP
C: 585.016261
Qm: 215.5956 cm³/g STP
Correlation coefficient: 0.9999996
Molecular cross-sectional area: 0.1620 nm²

Figure S12. BET plot for N₂ sorption in c-1 (168 h-treated).



BET surface area: 1121.6708 ± 0.7206 m²/g
Slope: 0.003875 ± 0.000002 g/cm³ STP
Y-intercept: 0.000005 ± 0.000000 g/cm³ STP
C: 709.057482
Qm: 257.7026 cm³/g STP
Correlation coefficient: 0.9999981
Molecular cross-sectional area: 0.1620 nm²

Figure S13. CO₂ sorption isotherms collected at 203 K, 258 K, 273 K, 288 K and 298 K for a-1 (left) and c-1 (right).

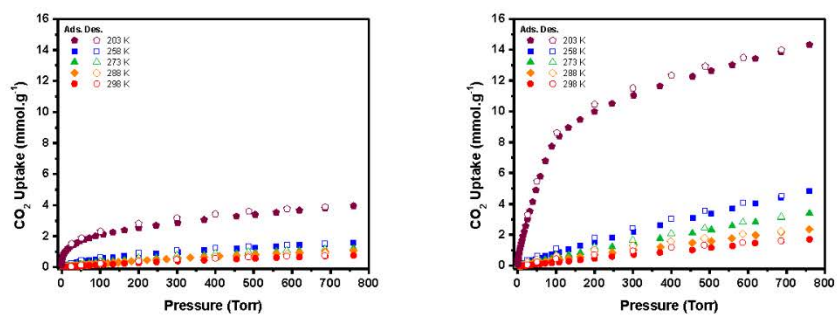


Figure S14. Heats of adsorption of CO₂ for a-1 (left), calculated from the isotherms derived from CO₂ adsorption isotherms collected at 258 K, 273 K, 288 K and 298 K (right).

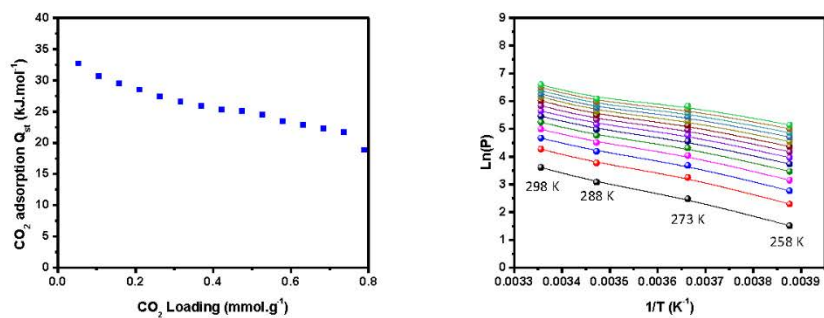


Figure S15. Heats of adsorption of CO₂ for c-1 (left), calculated from the isotherms derived from CO₂ adsorption isotherms collected at 258 K, 273 K and 298 K (right).

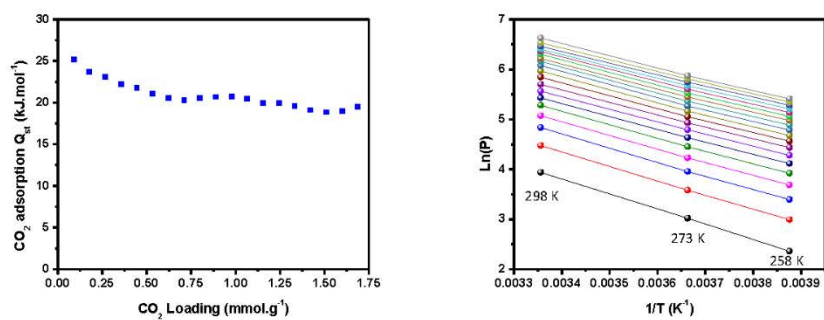


Figure S16. HAADF-STEM images of (a) $\text{Fe}_3\text{O}_4@a-1$ and (b) $\text{Fe}_3\text{O}_4@c-1$. Scale bars are 200 nm.

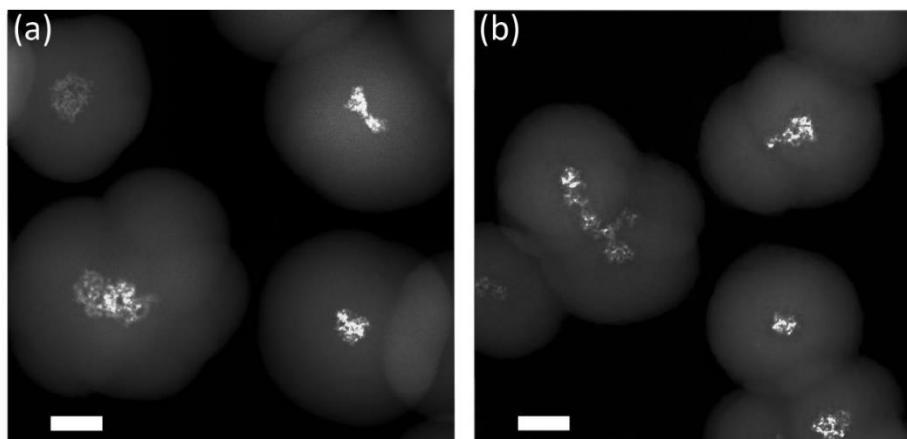


Figure S17. Comparison of calculated PXRD diagram of c-1 (red) and experimental PXRD diagram of Fe₃O₄ NPs (blue) with Fe₃O₄@c-1 (black).

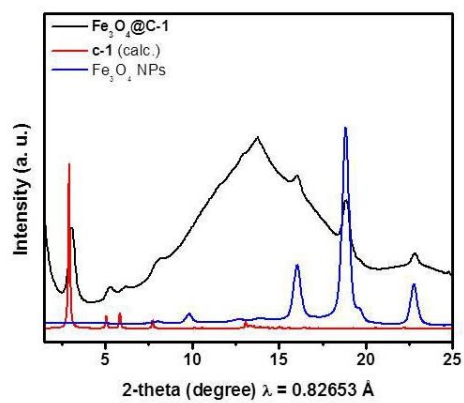


Figure S18. EDX of Fe₃O₄@c-1.

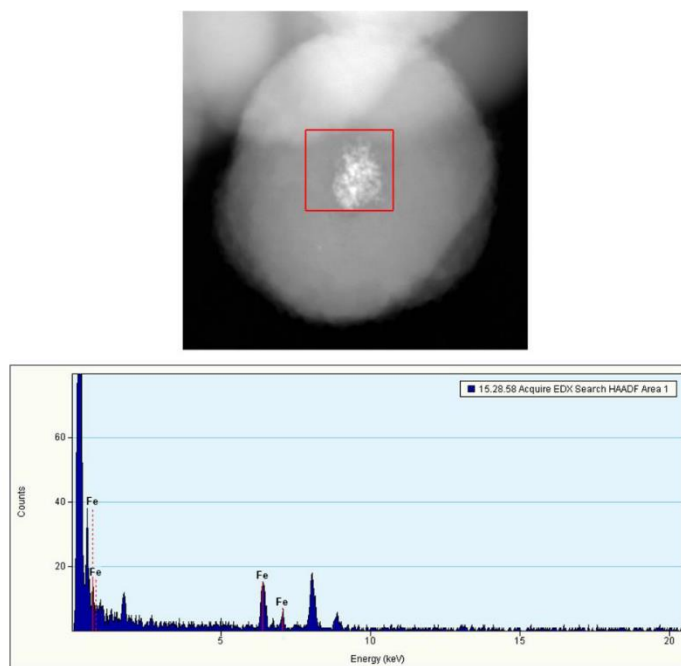


Figure S19. Comparison of calculated PXRD diagram of c-1 (red) and Au NPs (blue) with experimental PXRD diagram of Au@c-1 (black).

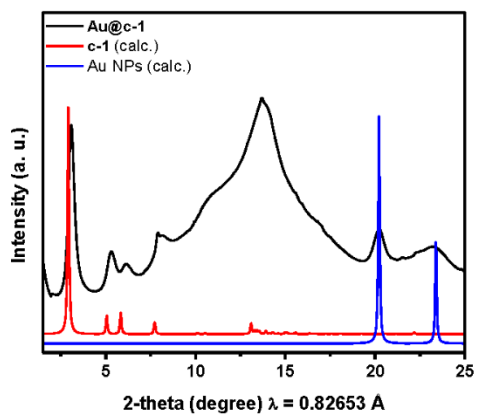


Figure S20. EDX of Au@c-1.

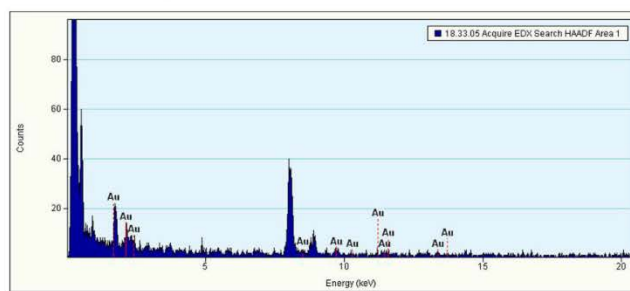
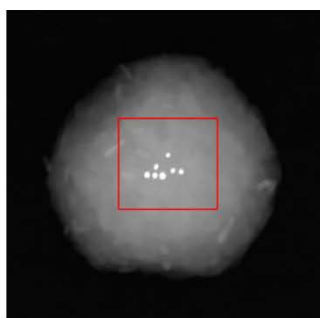


Figure S21. Comparison of calculated PXRD diagram of c-1 (red) and Pd NPs (blue) with experimental PXRD diagram of Pd@c-1 (black).

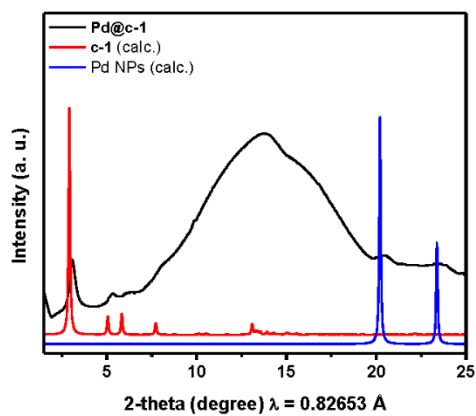


Figure S22. EDX of (a) Pd@c-1.

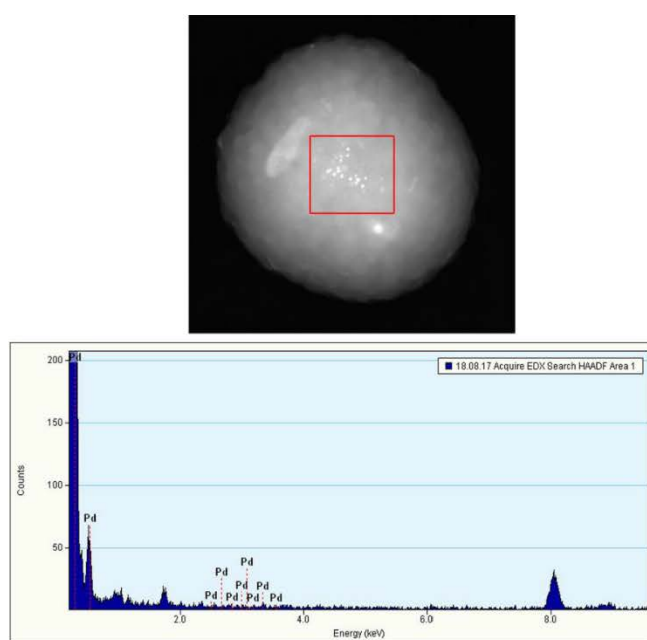


Figure S23. Scanning electron microscopy (SEM) and HAADF-STEM images of (a,b) Pd@c-1 and (c,d) Au@c-1 after 4-NP reduction.

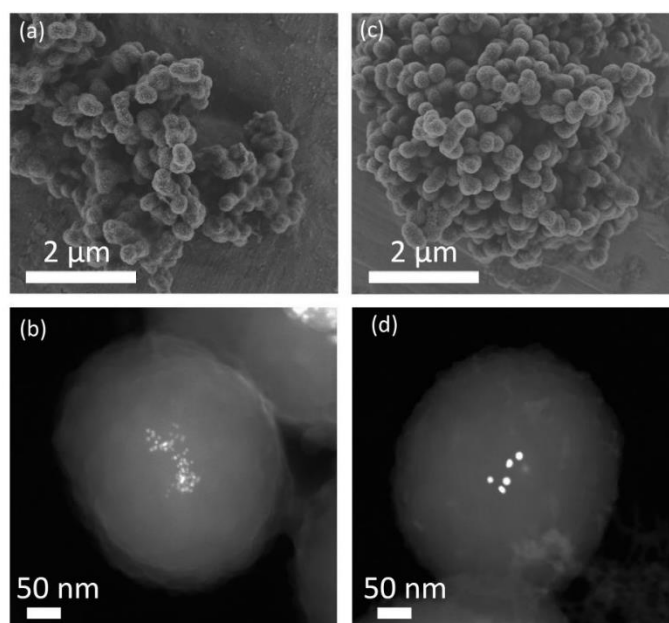
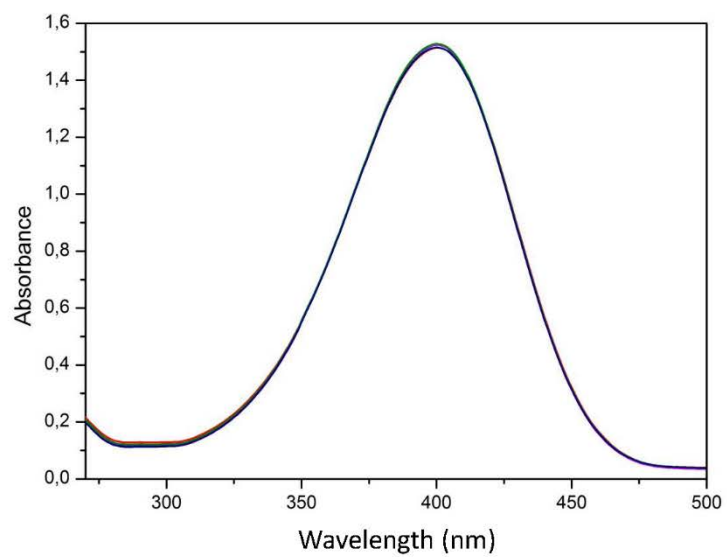


Figure S24. Reduction of 4-*NP* in presence of c-1 after 16 min of treatment.



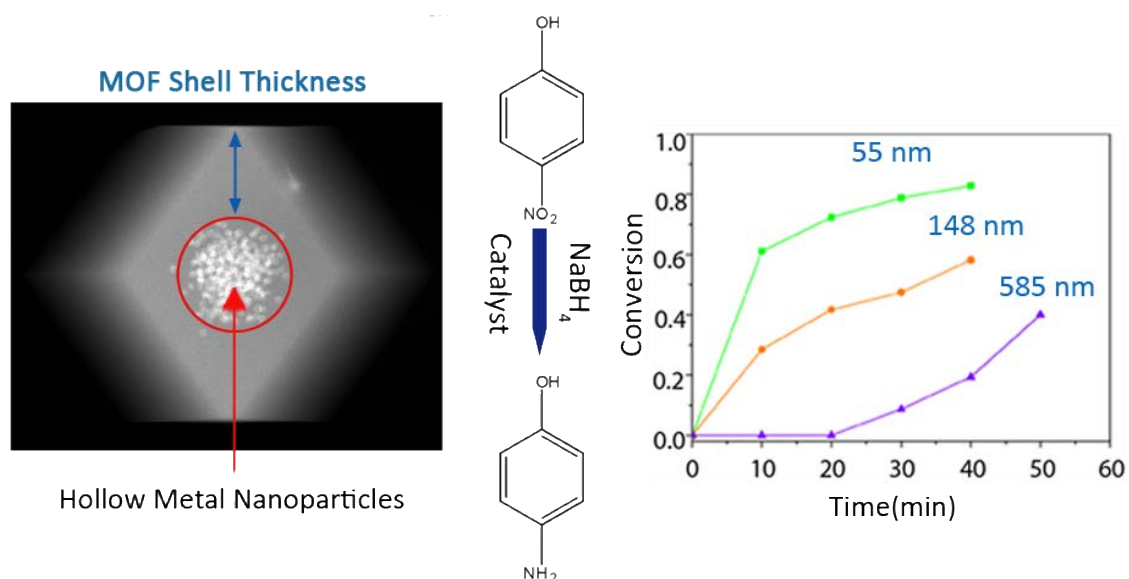
REFERENCES

- [1] A. D. Ruigomez, D. Rodriguez-San-Miguel, K. C. Stylianou, M. Cavallini, D. Gentili, F. Liscio, S. Milita, O. M. Roscioni, M. L. Ruiz-Gonzalez, C. Carbonell, D. MasPOCH, R. Mas-Balleste, J. L. Segura, F. Zamora, *Chem-Eur J* **2015**, *21*, 10666-10670.
- [2] J. Juanhuix, F. Gil-Ortiz, G. Cuni, C. Colldelram, J. Nicolas, J. Lidon, E. Boter, C. Ruget, S. Ferrer, J. Benach, *J. Sync. Rad.* **2014**, *21*, 679-689.
- [3] A. P. Hammersley, *ESRF Intern. Rep.* **1997**, *ESRF97HA02T*, "FIT2D: An Introduction and Overview".
- [4] F. Rouquerol, J. Rouquerol, K. Sing, *Adsorption by Powders & Porous Solids: Principles, Methodology and Applications*, Academic Press, London, **1999**.
- [5] N. G. Bastús, J. Comenge, V. Puentes, *Langmuir* **2011**, *27*, 11098-11105.
- [6] X. Liu, Z. Ma, J. Xing, H. Liu, *J. Mag. Mag. Mater* **2004**, *270*, 1-6.

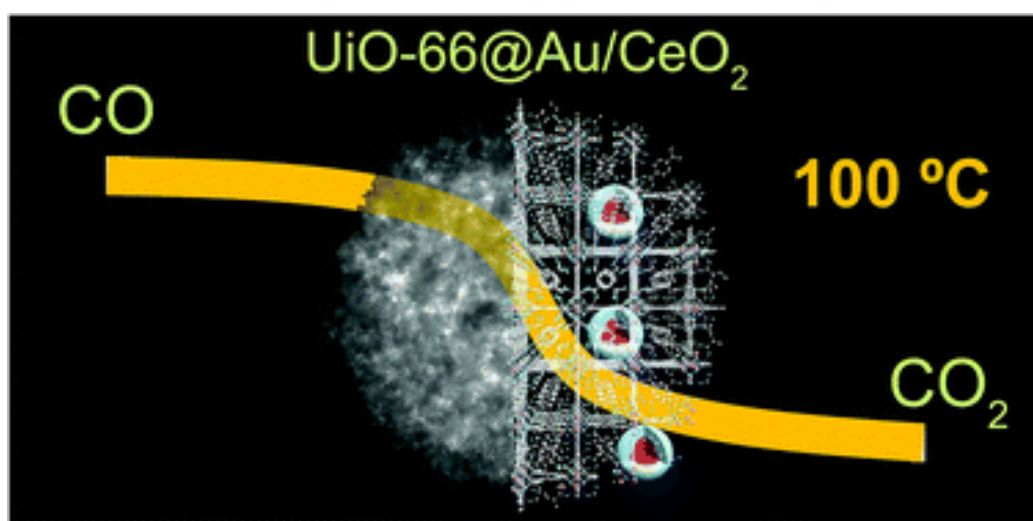
Conclusion

The main objective of this PhD Thesis has been the optimization and the development of synthetic methodologies to encapsulate iNPs into COFs and MOFs, which have been found to be an effective catalyst used in various reactions.

In the first part of this work, we encapsulated hollow Pt or Pd nanoparticles into ZIF-8, making a series of composites in which the ZIF-8 shell thickness and crystal size have been systematically varied. The concentration of the ZIF-8 precursors tuned the variation of these parameters. We demonstrated that, by lowering the concentration of Zn^{2+} and 2-MiM (6.5 mM) in the encapsulation process, we could obtain a nano-size ZIF-8 (197 nm). On the contrary, by increasing the concentration of the precursors, we were able to increase the size of the crystal and the shell thickness up to 1832 nm and 585 nm, respectively. Furthermore, we have demonstrated that the MOF shell thickness is an important parameter to be considered when MOF@iNP composites are used as catalysts. To evaluate the catalytic performance of the synthesized composites, two model reactions with different molecule size were chosen (reduction of 4-NP and EY). The results demonstrated that the composites with thicker shells have lower conversion efficiencies given for at a certain time. Our findings suggest that decreasing the size (at the nanoscale) of these composites should facilitate the production of faster and more efficient catalysts. However, the smaller the composite, the lower the stability in time, which could prevent their recyclability.

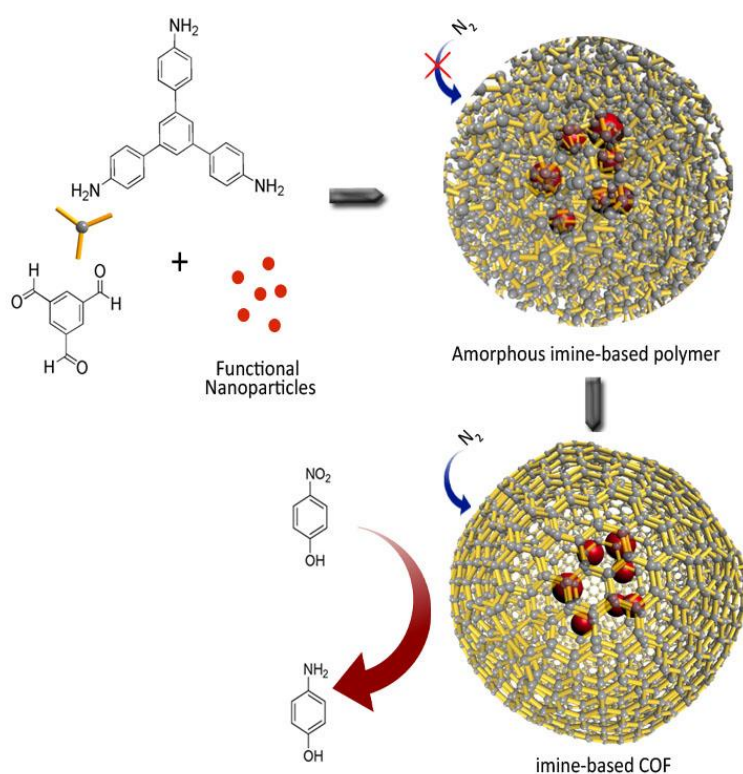


In addition, we have described the formation of a new composite, based on the entrapment and dispersion of core-shell Au/CeO₂ NPs into microsized spherical, porous UiO-66 beads using the spray-drying continuous-flow method. This method allowed achieving an encapsulation yield of 92%, with a high loading of NPs (7.7 w.t). Subsequently, the synthesized composites were used as a catalyst for CO oxidation reaction. The combination of nanocrystalline CeO₂ and Au facilitated CO conversion T₅₀ and T₁₀₀ as low as 72 °C and 100° C. These values are the lowest temperature reported for the full conversion of CO to CO₂ in the MOF@iNP based catalysts. In addition, UiO-66 provides enough protection to avoid NPs sintering/aggregation during the catalysis process. This protection enabled us to recycle the catalyst several times and using it for a long period of conversion (50 hours) without losing any significant catalytic activity. We consider this method a general approach for making composites, consisting of functional NPs dispersed in MOFs already shaped into spherical beads.



Finally, we have demonstrated an efficient and simple two-step procedure to encapsulate several types of iNPs into porous and crystalline COF spheres. The first step was based on encapsulation of PVP-capped iNPs (Au, Pd and Fe₃O₄) into an amorphous imine-based polymer. Thenceforth, the amorphous polymers with the embedded iNPs were exposed to acidic conditions at high temperature to transform into crystalline and porous

imine-based COF@iNPs. Remarkably, the size and the shape of the iNPs were not affected by the transformation conditions. This strategy could be extended to a broad range of iNPs and their mixtures, and to encapsulate molecular species. Furthermore, as a proof of concept, we have also shown the ability of crystalline COF@Au and crystalline COF@Pd hybrids to catalyze the reduction of 4-nitrophenol into 4-aminophenol. This reduction activity was not observed in the amorphous imine-based polymers composites, with the same encapsulated iNPs. This phenomenon confirmed that the diffusion of reactants and products only occurred in the porous and crystalline COF spheres. This last result suggests potential applications in selective catalysis, remediation, and molecular delivery.



All the results obtained during this PhD showed the importance of the development of the synthetic methods for encapsulation of iNPs into MOFs and COFs for heterogeneous catalysis. Encapsulation is one of the most sophisticated methods to pair iNPs with MOFs and COFs. However, there are some parameters that have to be taken into account when carrying out encapsulation procedures. In this PhD Thesis, we demonstrated that the control of the crystal size and the shell thickness of MOFs (in the encapsulation process) enhances the

activity and the stability of the composites in different catalytic reactions. In addition, we introduced a more efficient and faster continuous-flow technique to encapsulate iNPs in MOFs via spray-drying methodology. The result of using this technique for the encapsulation process proved to be an extremely effective catalyst for CO oxidation. Indeed, these results presented here could open new possibilities for producing MOFs@iNP catalysts via spray-drying for more ambitious and complex reactions. Finally, in this work, we presented that the encapsulation of iNPs can be extended to other crystalline porous materials such as COFs. We demonstrated that the encapsulated functional iNPs were accessible by testing COFs@iNP composites as a catalyst for a model reaction. Certainly, these results open a new path for potential applications in selective catalysis, remediation, and molecular delivery due to the diverse structure and porosity of COFs.

Appendix

In this appendix of this PhD thesis, four additional works are presented. These manuscripts are related to the main objectives in a border sense, but nonetheless, add insights to the fields of MOFs.

The first work was a review based on applications of MOF@iNPs which was entitled “Application of metal and metal oxide nanoparticles@MOFs”.

The second work presented was elaborated during my Master Thesis. It was focused on the synthesis of sixteen known MOFs in nano range size. Uncoated MOF nanoparticles were assessed for cytotoxicity to HepG2 and MCF7 cells *in vitro*, and for toxicity to zebrafish embryos *in vivo*. These results have been reported in the manuscript entitled “Synthesis, Culture Medium Stability, and In Vitro and In Vivo Zebrafish Embryo Toxicity of Metal-Organic Framework Nanoparticles”.

The third work was based on the continuous, one-step spray-drying synthesis of several members of isorecticular MOF family such as $[\text{SiF}_6]^{2-}$ and $[\text{TiF}_6]^{2-}$. This article was entitled “Continuous One-Step Synthesis of Porous M- XF_6 -Based Metal-Organic and Hydrogen-Bonded Frameworks”.

The fourth work demonstrated the synthesis of (multi)-layered zeolitic imidazolate framework (ZIF-8/-67) composite particles via a sequential deconstruction–reconstruction process with an introduction of functional inorganic nanoparticles onto the crystal surface. This article was entitled “Sequential Deconstruction–Reconstruction of Metal-Organic Frameworks: An Alternative Strategy for Synthesizing (Multi)-Layered ZIF Composites”.



Contents lists available at ScienceDirect

Coordination Chemistry Reviews

journal homepage: www.elsevier.com/locate/ccr

Review

Application of metal and metal oxide nanoparticles@MOFs

Paolo Falcaro^{a,*}, Raffaele Ricco^a, Amirali Yazdi^b, Inhar Imaz^b, Shuhei Furukawa^c, Daniel MasPOCH^{b,d}, Rob Ameloot^e, Jack D. Evans^f, Christian J. Doonan^{f,**}^a CSIRO Manufacturing Flagship, Private Bag 10, Clayton South, VIC 3169, Australia^b Institut Català de Nanociència i Nanotecnologia (ICN2), Campus de la UAB, Edifici ICN2 08193 Bellaterra, Spain^c Institute for Integrated Cell-Material Sciences (WPI-iCeMS), Kyoto University, Yoshida, Sakyo-ku, Kyoto 606-8501, Japan^d Institució Catalana de Recerca i Estudis Avançats (ICREA), 08100 Barcelona, Spain^e Centre for Surface Chemistry and Catalysis, University of Leuven, Celestijnenlaan 200F, 3001 Leuven, Belgium^f Department of Chemistry, School of Physical Sciences, The University of Adelaide, North Terrace Campus, Adelaide SA 5005, Australia

Contents

1. Introduction	238
2. NP@MOFs for gas storage and separation.....	238
2.1. Hydrogen storage	239
2.2. Noble gas separation	240
3. NP@MOFs for catalysis	241
3.1. Oxidation of CO	241
3.2. Oxidations of alcohols and hydrocarbons	241
3.3. Hydrogen generation	244
3.4. Hydrogenation of olefines	244
3.5. Carbon–carbon coupling	244
4. NP@MOFs for sensing	244
4.1. Size-selective sensors	244
4.2. Gas selective-sensors	245
4.3. Ion-selective sensors	245
4.4. Photonic crystal sensors	246
5. NP@MOFs for sequestration and separation	247
5.1. Sequestration of pollutants	247
5.2. Uptake and degradation	248
5.3. Stationary phases for separations	248
6. NP@MOFs for controlled release	249
7. Future outlook	251
Acknowledgements	252
References	252

ARTICLE INFO

Article history:

Received 12 June 2015

Received in revised form 6 August 2015

Accepted 7 August 2015

Available online 15 August 2015

Keywords:

Composites

Metal–Organic Frameworks

Nanoparticles

Applications

Nanoparticles@MOFs

ABSTRACT

Composites based on Metal–Organic Frameworks (MOFs) are an emerging class of porous materials that have been shown to possess unique functional properties. Nanoparticles@MOFs composites combine the tailorable porosity of MOFs with the versatile functionality of metal or metaloxide nanoparticles. A wide range of nanoparticles@MOFs have been synthesised and their performance characteristics assessed in molecular adsorption and separation, catalysis, sensing, optics, sequestration of pollutants, drug delivery, and renewable energy. This review covers the main research areas where nanoparticles@MOFs have been strategically applied and highlights the scientific challenges to be considered for their continuing development.

© 2015 Published by Elsevier B.V.

* Corresponding author. Tel.: +61 395452968.

** Corresponding author. Tel.: +61 883135770.

E-mail addresses: Paolo.Falcaro@csiro.au (P. Falcaro), christian.doonan@adelaide.edu.au (C.J. Doonan).<http://dx.doi.org/10.1016/j.ccr.2015.08.002>

0010-8545/© 2015 Published by Elsevier B.V.

1. Introduction

Metal-Organic Frameworks (MOFs), also called Porous coordination Polymers (PCPs), are of significant interest to chemists due to their exceptionally high surface areas and structural diversity. Furthermore, the modular approach to their synthesis, allows for the preparation of porous networks with precisely tailored chemical and physical attributes [1–5]. These unique features have led researchers to explore combining MOFs with other functional materials to form novel composites with advanced properties [6]. Indeed, ceramics, metal nanoparticles, polymers and biomolecules have been combined with MOFs to afford new materials that have demonstrated unprecedented performance in the areas of catalysis [7], molecular separations [8], sensing [9], plasmonics [10], gas storage [11], controlled guest release [12,13], and protection of biomacromolecules [14]. The most widely studied of these composite systems are based on integrating metal and metal oxide nanoparticles with MOFs. This may be attributed to the versatility of the synthetic approaches for metal oxide (ceramic) and metallic nanomaterials. For example, metal and metal oxide nanoparticles can be prepared by infiltrating the precursors in the pre-formed porous MOF crystals, either via the vapor or liquid phase [1,15]. Particle formation is subsequently triggered within the MOF by the application of heat [16,17], reducing agents [18,19] or radiation [20,21] (Fig. 1a). Alternatively, because the mild synthetic conditions typically used to synthesize MOFs do not affect the chemical composition, structure and morphology of most metal or metal oxide nanoparticles [22], in the resulting composite, the MOF encapsulates the functional nanoparticles (Fig. 1b).

A conceptually different, emerging approach termed pseudomorphic replication relies on the preparation of core-shell inorganic particles where the core is the 'functional' nanoparticles and the shell is a feedstock material for the inorganic node

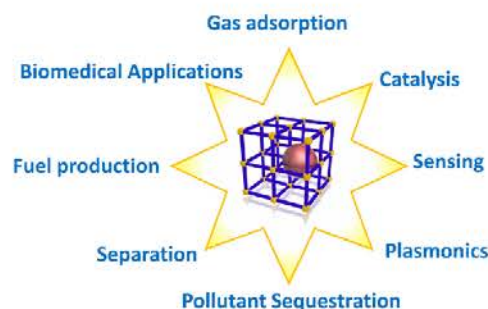


Fig. 2. Schematic illustration of different applications of nanoparticles@MOFs.

of the MOF [13]. Under judiciously controlled conditions, the shell reacts rapidly with the organic precursor ligands to grow the MOF network around the core nanoparticles (Fig. 1c) [23]. Finally, pre-formed MOFs and nanoparticles can be combined to form clusters of the two components (Fig. 1d).

The focus of this review is to canvass the variety of applications that have been explored for nanoparticles@MOF composites and to highlight how this unique combination leads to materials with enhanced performance characteristics in the areas of gas adsorption, catalysis, sensing, microelectronics, sequestration, delivery and biomedical applications, fuel production and separation (Fig. 2).

2. NP@MOFs for gas storage and separation

MOFs have been thoroughly investigated for their application to the storage and separation of a number of gases, including hydrogen, carbon dioxide and methane [24–26]. To improve the relatively weak physisorption forces, researchers have applied their efforts

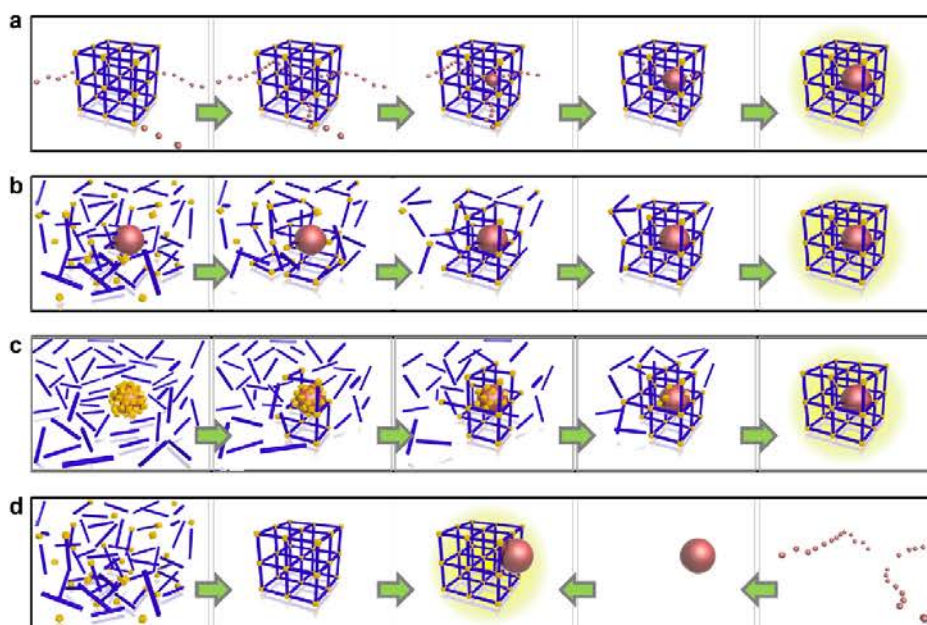


Fig. 1. Different synthetic approaches for the preparation of nanoparticles@MOF composites: (a) infiltration in preformed MOFs, (b) self-assembly of MOFs encapsulating the nanoparticles, (c) pseudomorphic replication converting a ceramic shell of a core-shell nanoparticle into a MOF, (d) individual preparation of MOFs and nanoparticles and subsequent mixing.

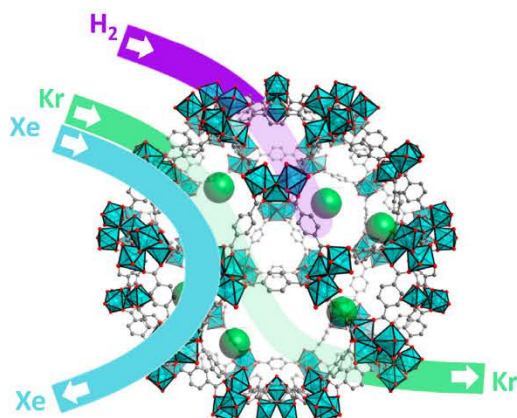


Fig. 3. Schematic illustration of nanoparticles@MOFs for gas adsorption (H_2) and gas separation (Kr and Xe).

to tuning pore sizes, modifying pore chemistry and generating co-ordinatively unsaturated metal sites [15,27]. In addition, combining metal and metal oxide nanoparticles with MOFs has shown promise towards increasing the interactions with adsorbates that would normally have extremely weak interactions with the pore surfaces such as hydrogen and noble gases. Here we highlight examples where the introduction of nanoparticles into MOFs has been successfully employed to enhance gas adsorption and separation (Fig. 3).

2.1. Hydrogen storage

Alternative energy sources are in high demand given the present concerns of climate change, energy security and pollution. One such alternative is hydrogen gas as it can be produced from domestic resources and can be used to power fuel cells as zero-emission energy generators. Despite the advantages of hydrogen as a fuel source there are concerns over safe storage methods at high pressures, especially for automotive applications. There are a number of strategies that mitigate this issue, one of which is storing hydrogen within porous frameworks. Most porous materials store hydrogen by way of weak van der Waals interactions [28], however, transition metals can adsorb hydrogen via a metallic bonding and dissociation processes, described conceptually in Fig. 4a. The combination of high surface areas and enhanced adsorption enthalpy at a metal surface suggests that metal/metal oxide@MOF composites are promising materials for hydrogen storage.

An early example of metal/metal oxide@MOF composites for hydrogen storage was reported by Yang and Li who demonstrated that a physical mixture of MOF and Pt supported on active carbon significantly enhances hydrogen uptake capacity at room temperature [29]. Remarkably, the increase in adsorption does not follow the weighted average of MOF and Pt/C. The observed enhancement is attributed to the so-called ‘hydrogen spillover’ effect (Fig. 4b) where hydrogen molecules dissociate at the metal cluster, then move to the carbon support and subsequently to the organic components of the MOF [30]. This effect has been demonstrated in a number of MOFs [31–35], furthermore, *ab initio* calculations have been applied in an effort to understand the mechanism of this postulated adsorption process [36–39]. Recently, however, Luzan and Talyzin reported that the spillover effect from Pt/C catalyst to MOF was irreproducible [40], and Hirscher has commented it may be below the detection limit of the gas adsorption apparatus [41]. Yang and co-workers note that the methodology to maximize spillover

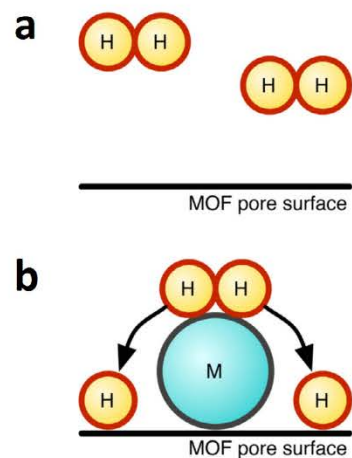


Fig. 4. (a) Hydrogen adsorption on MOFs usually occurs by weak van der Waals interactions. The introduction of metal nanoparticles allows for the stronger mechanism (b) where dissociation and subsequent ‘spillover’ may occur.

depends on a number of experimental factors involved in sample preparation [42].

Despite the questionable mechanism of hydrogen spillover in physical mixtures of MOFs with Pt/C, work focused on more structurally well-defined metal nanoparticles@MOF composites has shown promising results. For example, Pd nanoparticles loaded in MOF-5 (1 wt% loading) and in SNU-3 (3 wt% loading) demonstrated increased hydrogen adsorption at low pressure and temperature [43,44]. Pd@SNU-3 also showed an increase in hydrogen uptake at room temperature and high pressure compared to SNU-3, however calculated isosteric heats of adsorption indicated that the Pd@SNU-3 possessed a lower enthalpy of adsorption for H_2 . This result further highlights that the mechanism of action in these materials is not comprehensively understood. Materials with significantly higher Pd content have been described by Latrouche and co-workers, who were able to produce MIL-100(Al) embedded with 10 wt% metallic Pd [18]. These high loadings gave rise to a decrease in surface area and pore volume as indicated by nitrogen adsorption experiments. This would be anticipated due to the pore volume consumed by Pd nanoparticles. Consistent with the lower pore volume of these samples, the 77 K hydrogen capacity of the Pd@MIL-100(Al) samples were less than that of the bare framework. However, the room temperature hydrogen uptake capacity was significantly improved; 0.35 wt% at room temperature and 4 MPa. These values are approximately double that of MIL-100(Al). Characterization by X-ray diffraction revealed that the high capacity at room temperature is partially explained by formation of Pd hydride that occurs readily at room temperature. Recently, Kitagawa and co-workers have significantly improved hydrogen storage capacity of Pd nanoparticles by employing a MOF coating [11]. Here, samples of Pd nanocrystals were successfully covered in the HKUST-1 leading to a drastic increase in the storage capacity and kinetics of hydrogen adsorption compared to the base Pd nanocubes (Fig. 5). Notably, at elevated temperatures HKUST-1 shows no appreciable hydrogen adsorption. Further investigations by X-ray photoelectron spectroscopy (XPS) suggest the enhanced hydrogen storage capacity in the composite material is a result of electron transfer from Pd nanocrystals to the HKUST-1 coating. This approach is widely applicable to other metal nanoparticles@MOF systems and may provide a general method to enhance the reactivity of nanoparticles.

Pt nanoparticles are known to afford extremely strong interactions with hydrogen. For example, Pd black is able to absorb and

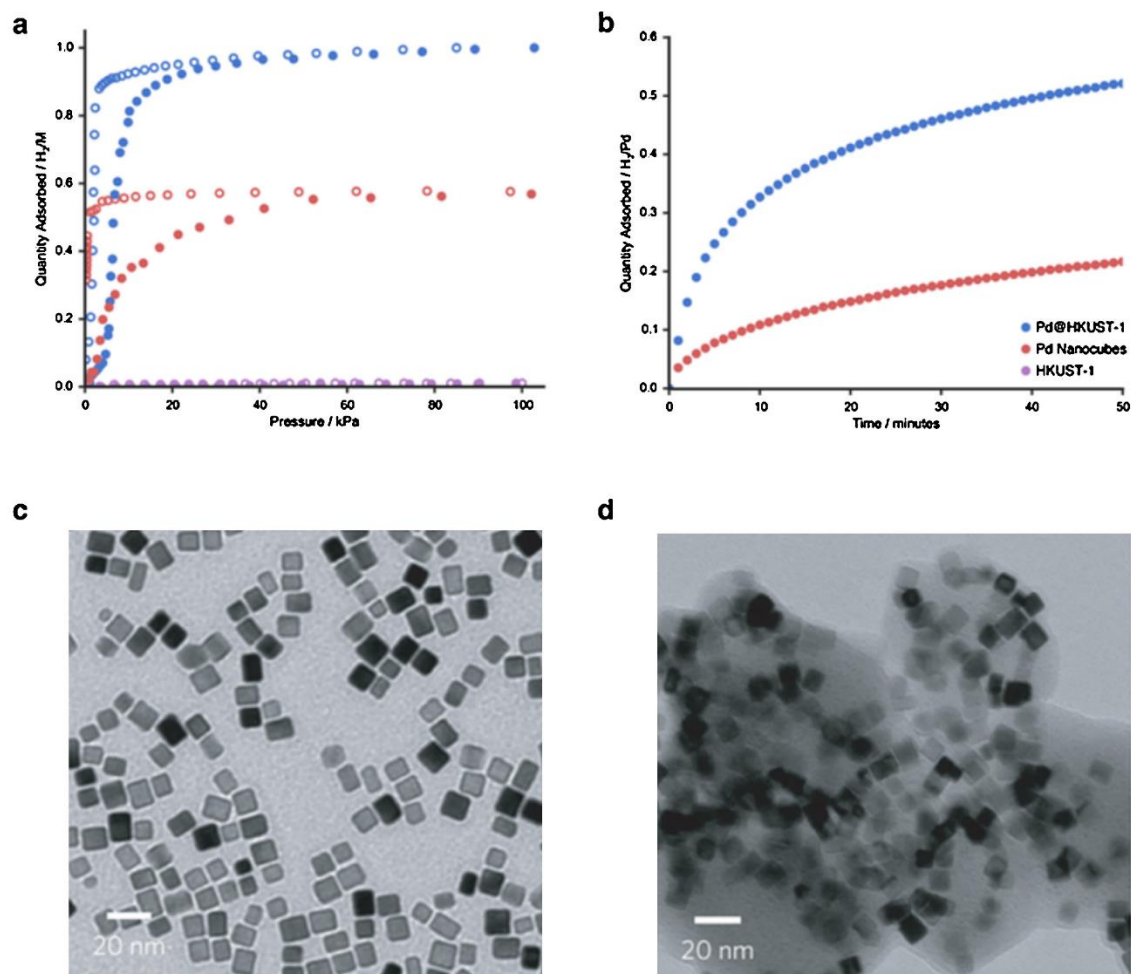


Fig. 5. Hydrogen adsorption isotherms (desorption is shown by open symbols) for bare Pd nanocubes, HKUST-1 and Pd@HKUST-1 at 303 K (a) and hydrogen adsorption profiles at 303 K at a pressure of 101.3 kPa over a period of 50 minutes (b). TEM images of Pd nanocubes (c) and Pd@HKUST-1 (d). Reproduced from ref. [11].

desorb hydrogen at room temperature, however, hydrogen cannot be desorbed from Pt black at room temperature under evacuation [28]. Inspired by the results of Yang and Li's bridged Pt/C and MOF materials [29], Senker et al. were able to synthesize samples of ultra-high surface area MOF-177 loaded with 43 wt% Pt nanoparticles [45]. The resulting composite was reported to adsorb 2.5 wt% of hydrogen at room temperature at 144 bar. This gives rise to a storage capacity of $62.5 \text{ g}_{\text{H}_2} \text{ L}^{-1}$, which is close to that of liquid hydrogen at $70 \text{ g}_{\text{H}_2} \text{ L}^{-1}$. Unfortunately, subsequent cycles show decreasing capacity that can be explained by passivation of the Pt surface by stable Pt-H moieties.

Overall, research into hydrogen adsorption in these materials highlights the advantages of combining the strong adsorption potential of metal nanoparticles and high surface areas of MOFs. However, for this area to progress further work needs to be focused on elucidating the mechanism of action for hydrogen adsorption, especially with respect to the observed hydrogen spillover effect [30]. A better understanding of these systems will facilitate the hypothesis driven design of novel composites for H_2 storage.

2.2. Noble gas separation

Molecular separation of Kr and Xe is important as reprocessing nuclear fuel requires the removal of radioactive ^{85}Kr from Xe in the off-gas [46]. Currently, separation of these gases is achieved by cryogenic distillation. This process is extremely energy intensive owing to the low boiling points of Kr and Xe at -153°C and -108°C , respectively. Similar to hydrogen, noble gases interact very weakly with the surfaces of porous materials. This has motivated researchers to use metal nanoparticles as a strategy towards enhancing uptake capacity. Groose and co-workers reported that Ag clusters in X- and Y-type zeolites gave rise to a higher uptake of Xe, when compared to the original sodium ion containing zeolites, and was dependent on Ag loading [47]. Subsequently, Thallapally et al. were able to produce Ag nanoparticles in MOF-74(Ni) with up to 6.59 wt% Ag [48]. The Xe and Kr adsorption of these materials showed the Xe capacity at 1 bar and room temperature was increased by 15.6% when compared to the bare framework (Fig. 6). Importantly, the introduction of Ag to MOF-74(Ni) did not significantly increase the Kr capacity, as it is less polarizable than Xe.

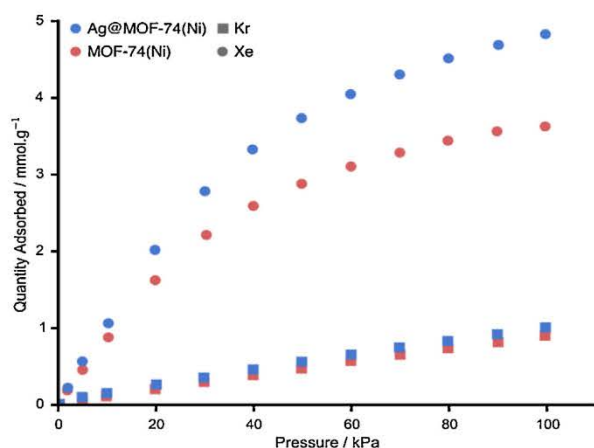


Fig. 6. Xe and Kr isotherms for bare MOF-74(Ni) and a sample of Ag@MOF-74(Ni) loaded with 1.47 wt% Ag. Reproduced from ref. [48].

Accordingly, the adsorption selectivity (calculated from the pure gas isotherms and a 50:50 mixture) was double that of the benchmark activated-carbon was achieved. These extremely promising results suggest that metal nanoparticle@MOF composites should be further investigated for their potential application to noble gas separations.

3. NP@MOFs for catalysis

Metal nanoparticles are highly attractive materials for catalysis due to the larger surface area/unit volume ratio as compared to their bulk metal analogues that are traditionally used in industrial catalysis [49,50]. However, there are still some major barriers for the widespread use of nanoparticles as catalysts. Some of these drawbacks include a tendency to aggregate, low recyclability, and difficulty recovering the nanoparticles from the reaction media. To overcome these problems, metal nanoparticles are typically immobilized on or in supports [51]. A common strategy is to use porous materials with well-defined pore characteristics; in this way, the partition between the exterior and the interior pore structure permits the selective gating of the molecules that reach, and therefore react with the nanoparticles [52]. Porous materials also have the advantage of confining and protecting the nanoparticles, thus facilitating their recovery from the bulk solution and preventing particle aggregation. In this context, the regular porosity of MOFs together with the possibility to tailor their pore size, shape and chemical functionality makes them an excellent platform to support active metal nanoparticles for heterogeneous catalysis [53].

Table 1 summarizes some reactions already tested using MOF supported metal nanoparticles as catalysts, highlighting the nature of the MOF and the nanoparticle, the nanoparticle size, and the weight percentage of the nanoparticle in the MOF. These studies are largely based on oxidation, hydrogenation, C–C coupling and H₂ production reactions (Fig. 7). However, other important catalytic processes are now being investigated. For example the catalytic synthesis of methanol from CO₂ and H₂, using Cu nanoparticles stabilized into MOF-5, was demonstrated by Fischer et al., who found a maximum 70 μmol_{MeOH} g⁻¹ cat h⁻¹ methanol production [54]. More recently, complex cascade reactions involving Knoevenagel condensations and subsequent hydrogenations were successfully catalyzed using IRMOF-3 supported Pd nanoparticles [53].

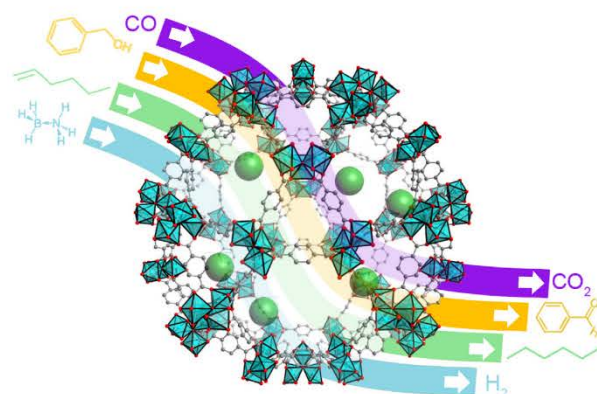


Fig. 7. Schematic Illustration of some representative reactions catalyzed by MOF supported metal nanoparticles.

3.1. Oxidation of CO

Among the oxidation processes, oxidation of carbon monoxide to carbon dioxide has been extensively studied because of the high toxicity of carbon monoxide and its importance in fuel cell technology, where the preferential oxidation of carbon monoxide in excess of hydrogen is a key process for the production of clean fuel [55]. Overall, MOF supported nanoparticles have showed good performance for carbon monoxide oxidation at elevated temperatures. For example, Xu, Hupp, and Gascón groups reported that Au and Pt nanoparticles supported in ZIF-8 and NH₂-MIL-101(Al) afford the total conversion of carbon monoxide to carbon dioxide at around 200 °C [7,56,57]. Importantly, the reaction temperature can be reduced to 100–150 °C by incorporating Pt, Pd and Cu nanoparticles within MIL-101 and Pd nanoparticles within MOF-5 [58–60]. Additionally, the total conversion of carbon monoxide to carbon dioxide was observed when CuO/CeO₂ nanoparticles were formed, *in situ*, within HKUST-1 [61].

3.2. Oxidations of alcohols and hydrocarbons

MOF supported metal nanoparticles have been also used as catalysts for aerobic alcohol oxidation reactions which are considered as key reactions in 'green' organic synthesis. These processes usually require temperatures above 100 °C (under solvent free conditions), or the presence of a large excess of a base. The majority of these investigations employ Au and Pd nanoparticles supported in different MOFs. Fischer and co-workers first studied the oxidation of benzyl alcohol to benzyl aldehyde using Ru and Au nanoparticles [62], and Au/ZnO and Au/TiO₂ nanoparticles [63] supported on MOF-5. For the Ru nanoparticles, which could be easily converted to RuO_x by oxidation with diluted O₂ gas inside MOF-5, the conversion of benzyl alcohol was low (25%). This was attributed to the structural decomposition of MOF-5 during the oxidation reaction. However, in the case of Au and hybrid Au/ZnO and Au/TiO₂ nanoparticles, the authors observed better performance (conversion ranges of 50–70%) when a base was added to accelerate the oxidation reactions by deprotonation of the alcohol. These results were in contrast to those obtained by Ishida et al., who reported that Au nanoparticles embedded in MOF-5 activate the oxidation reaction with base (conversion = 100%) but also without base (conversion = ~70%) [64].

A variety of alcohol oxidation reactions have been investigated by the group of Li. Here, catalytic activity of a series of composites was assessed that were made from different combinations of MOFs (DUT-5, UiO-66, MOF-253, UiO-67, and MIL-101(Cr))

Table 1
List of MOF supported metal nanoparticle catalysts by reaction and substrate.

MOF composite	Nanoparticle	Weight (%)	Size (nm)	Conv. (%) ^a	Ref.
<i>Oxidation</i>					
CO					
ZIF-8	Pt	3.4	2.5 ± 4.1	100	[7]
ZIF-8	Au	5	4.2 ± 2.6	100	[56]
MIL-101-NH ₂ (Al)	PTA/Pt			100	[57]
MIL-101(Cr)	Cu/Pd	2.9	2–6	100	[58]
MIL-101(Cr)	Pt/Pd	2.9	3–9	100	[59]
MOF-5	Pd	0.19		65	[60]
HKUST-1	CuO/CeO ₂		5–15	100	[61]
MIL-101(Cr)	Pt	2/1/5	1.8 ± 0.2	100	[99]
Ra-MOF	Pd	3.6	1.8 ± 0.3	100	[100]
<i>Alcohols</i>					
MOF-5	Ru	30	1.5–1.7	25	[62]
MOF-5	Au/ZnO–Au/TiO ₂ –Au	1–20	2.7–20	50/68/74	[63]
MOF-5/MIL-53(Al)	Au		1.5 ± 0.7	99	[64]
DUT-5/UiO-66/MOF-253	Pt	0.5	1.5–2	99	[65]
UiO-67	Pd	1	3 ± 0.5	99	[66]
MIL-101(Cr)	Au	0.5	2.3 ± 1.1	100	[67]
ZIF-8	Au	30	3.7	81	[68]
UiO-66–NaBH ₄	Au		5–7	94	[69]
MOF-177	Pt	43	2–3		[45]
UiO-66–NH ₂	Au	1.8	2.8–3.1	94	[101]
UiO-66	Au	8		54	[102]
MIL-101(Cr)	Pd	0.35	2.5 ± 0.5	99	[103]
<i>Cyclohexane</i>					
MIL-101(Cr)/MIL-53(Cr)	Au	4.64/4.63	4.8 ± 2.9	30/31	[70]
MIL-101(Cr)	Au/Pd	1	2.4 ± 0.6	51	[71]
<i>Benzyllic hydrocarbons</i>					
HKUST-1	Fe ₃ O ₄	28.78	20		[72]
<i>Benzyl-amine</i>					
UiO-66–NaBH ₄	Au	5–7		53	[69]
<i>Ethylene</i>					
ZIF-8	Pt/Pd	4.95/2.70	6.2	94	[73]
<i>Hydrogenation</i>					
<i>Ketones</i>					
MIL-101(Cr)	Pt		1.5–2.5	97–98	[85]
MIL-101(Cr)	Pd	15	2–3.5	100	[86]
MIL-101(Cr)	Pd	42–45	1.7	100	[89]
<i>1-Hexene</i>					
ZIF-8	Pt	0.23–0.74	2–3	95	[83]
<i>1-Hexyne</i>					
ZIF-8	Pt	1	2.7	100	[84]
<i>1,4-Butynediol</i>					
ZIF-8	Pd	5	4–6	98	[104]
<i>Styrene</i>					
MIL-101(Cr)	Pd	1	1.5	80–100	[82]
MOF-5	Pt	1		97	[43]
MesMOF-1	Ni	20	1.1	99	[105]
<i>Toluene</i>					
MIL-101-NH ₂ (Al)	PTA/Pt				[57]
<i>Acetylene</i>					
MIL-101(Cr)	Pd	1	1.5	80–100	[82]
<i>Nitroarenes/Nitrobenzene</i>					
MIL-101(Cr)	Pt	1	1.5–2.5	100	[88]
MesMOF-1	Ni	20, 35	1.1, 1.4–1.9	100	[105]
<i>Phenol</i>					
MIL-101(Cr)-MIL-53(Cr)	Pd	4.3/4.9	2.5/4.3	100	[87]
<i>Nitrophenol</i>					
ZIF-8	Au	10–15	2–3	100	[106]
ZIF-8	Au/Ag	2/2		100	[107]
MIL-100(Fe)	Au			100	[108]
<i>Cyclohexanone/Cycloheptanone</i>					
MIL-101	Ni/Pd	18	2.5–3.5	80/100	[109]
<i>Octane</i>					
MIL-101(Cr)	Pt	1.2	5 ± 0.5	100	[90]

Table 1 (Continued)

MOF composite	Nanoparticle	Weight (%)	Size (nm)	Conv. (%) ^a	Ref.
<i>2,3,5-trimethylbenzoquinone</i> MIL-101(Cr)	Pd	2	2–3	100	[91]
<i>Benzene/cyclohexene</i> MOF-5	Ru	0.98	2	99	[110]
<i>Other olefins</i> HKUST-1	Au/Pt		100	25	[111]
<i>2,16. Vanillin</i> MIL-101(Cr)	Pd	2	1.8 ± 0.2	45	[112]
<i>Dehalogenation of aryl chlorides</i> MIL-101-NH ₂ (Cr) C–C coupling	Pd	0.62	2.49	98	[92]
<i>Suzuki-Miyaura coupling</i> MIL-101(Cr)	Pd	1	1.9 ± 0.7	82	[93]
MIL-53-NH ₂ (Al)	Pd	1	3.12	99	[94]
MIL-101-NH ₂ (Cr)	Pd	8	2–3	99	[95]
MCoS-1	Pd	1	2–3	97	[96]
<i>Ullman coupling</i> MIL-101(Cr)	Pd	1	1.9 ± 0.7	99	[93]
<i>Sonogashira reaction</i> MCoS-1	Pd	1	2–3	94	[96]
MOF-5	Pd	3	3–6	100	[97]
<i>Heck reaction</i> MIL-53-NH ₂ (Fe)	Pd	0.96	3.2	83	[98]
<i>Hydrogen generation</i> IRMOF-3	Pd	2	35	100	[53]
MIL-101(Cr)	Ni/Au		1.8 ± 0.2	100	[74]
ZIF-8	Ni	19	2.7 ± 0.7	100	[75]
ZIF-8	Ni/Pt	1–3	2.2 ± 0.3	100	[76]
MIL-101-EDA(Cr)	Au/Pd	13.7/1.5	2–3	100	[77]
MIL-125-NH ₂	Pd	0.5	3.1		[78]
MIL-101-NH ₂ (Cr)	Pt	1.5	3.75 ± 0.5		[79]
HKUST-1	Pd	0.86	4.3 ± 1.1	100	[113]
<i>Other</i> <i>Reduction of Cr(VI)</i> UiO-66-NH ₂	Pd	0.93	3–6	100	[114]
MIL-101(Cr)	Pt	2	2.6	100	[115]
<i>Methanol synthesis</i> MOF-5	Pd/Cu	36/13	1–2		[54]
MOF-5	Cu/ZnO	1.4/40	1–3		[116]
<i>Conversion of methylcyclopentane</i> UiO-66	Pt	0.4	2.5	100	[117]
<i>Synthesis of arylamines</i> MIL-101(Cr)	Pd/Pt				[118]
<i>Aminocarbonylation</i> ZIF-8	Pd	1	4–9	99	[119]
MOF-5	Pd	1	3–12	92	[120]
<i>Indole synthesis</i> MIL-101(Cr)	Pd	3	2.6	67	[121]
<i>Phenylation of naphthalene</i> MOF-5	Pd	2.3	20	65	[122]
<i>Direct arylation</i> MIL-101(Cr)	Pd	0.5	2.6 ± 0.5	85	[123]

^a Maximum conversion value reached (or reported).

and metal nanoparticles (Pt, Pd and Au). Overall, they showed that the confined metal nanoparticles were highly active in this type of oxidations under base free conditions (conversions up to 100%). The authors attributed these results to the electron donation and confinement effects offered by MOFs [65–67]. Other systems including Au nanoparticles supported in ZIF-8 and UiO-66 and Pt nanoparticles supported in MOF-177 also showed very good catalytic activity for the conversion of alcohols to aldehydes [44,68,69].

Beyond alcohols, the oxidation of hydrocarbons has also been catalyzed using MOF supported nanoparticles. Hydrocarbons have

been selectively oxidized, with molecular oxygen as the oxidant, by Au, Au/Pd, Fe₃O₄ or Pt/Pd nanoparticles immobilized in several MOFs (MIL-101 (Cr), MIL-53 (Cr), HKUST-1 and ZIF-8) [70–73]. For example, Huang et al. studied the activity of ZIF-8 supported bimetallic Pt/Pd nanoparticles for the photoactivated oxidation-degradation of ethylene to CO₂ and H₂O [73]. This nanocomposite showed excellent synergistic photocatalytic activity (conversion = 94%), which was to the authors contend due to the fact that ZIF-8, in addition to serving as a support to prevent particle aggregation, has an excellent capacity to adsorb ethylene and thus promote its photodegradation to CO₂ and H₂O.

3.3. Hydrogen generation

One of the biggest challenges in chemistry today is the energy efficient generation of H₂. With this goal in mind, Xu and co-workers evaluated the activity of Au, Ni and hybrid Au/Ni nanoparticles in MIL-101 and of Ni nanoparticles in ZIF-8 for the catalytic dehydrogenation of ammonia borane to generate H₂. In this case complete dehydrogenation was observed [74,75]. Other reactions for hydrogen production have also been evaluated. Singh and Xu successfully studied the generation of H₂ by decomposition of hydrazine in aqueous solution using ZIF-8 supported Ni-Pt bimetallic nanoparticles [76]. In addition, the same group and Martis et al. proved that it was possible to catalyze the dehydrogenation of formic acid using bare and amine-functionalized MIL-101-ethylenediamine supported Au-Pd bimetallic nanoparticles [77] and amine-functionalized MIL-125 supported Pd nanoparticles [78]. Recently, water splitting to produce H₂ using Pt nanoparticles embedded into MIL-101-NH₂ (Cr) was also evaluated. A maximum turnover of 110 mol_{H₂} mol_{cat}⁻¹ was achieved when the loading of Pt nanoparticles was 0.5% [79]. Finally, the photocatalytic properties of Pt@MOFs were also tested for H₂ production. Here, Lin's group first studied the photocatalytic performance of Pt nanoparticles embedded into two UiO frameworks functionalized with [Ir(ppy)₂(bpy)]⁺ (where ppy is 2-phenyl-pyridine and bpy is 2,2'-bipyridine) complexes, and found that high Ir-based turnover numbers [defined as $n(1/2H_2)/n(Ir)$] of 3400 and 7000 were achieved when irradiated under visible light (>420 nm). Under these conditions, the [Ir(ppy)₂(bpy)^{•+}] radicals generated by triethylamine-mediated photoreduction could transfer electrons to Pt nanoparticles to reduce protons for H₂ production [80]. Also, Matsuoka's group found that Pt nanoparticles photodeposited on amino-functionalized MIL-125(Ti) were able to photocatalyze the generation of H₂, reaching a total production of 33 μmol H₂ when this system was immersed in an aqueous solution containing triethanolamine at room temperature while being subjected to visible-light (>420 nm) for 9 h. In this case, the reaction proceeded through the light absorption by the organic linker forming the MOF followed by the electron transfer to the photocatalytically active titanium-oxo cluster. In this system, Pt nanoparticles acted as cocatalysts [81].

3.4. Hydrogenation of olefines

A fourth vast family of catalytic reactions studied using MOF supported metal nanoparticles as catalysts is the hydrogenation of alkenes [82,83], alkynes [82,84], ketones [85,86], and aromatics [43,82,87]; all of which are key processes in chemical industry. As can be seen in Table 1, the most active metal nanoparticles for these reactions are Pt and Pd, and the most promising MOF support is MIL-101 most probably due to its stability and large pore channels. Using this combination, excellent conversion rates (~100%) for the hydrogenation of ketones, aromatic molecules, alkenes, alkynes and nitro compounds have been observed [82,85–92].

3.5. Carbon–carbon coupling

Finally, the last ensemble of reactions that have been catalyzed by MOF supported NPs concern the C–C coupling reactions. Such transformations include Suzuki–Miyaura [93–96], Sonogashira [96,97], Ullmann [93], and Heck [98] reactions. Compared to other metal nanoparticles, Pd offers undoubtedly the best conversion rates in C–C coupling and thus Pd@MOF composites are primarily tested for these types of catalytic reactions. An illustrative example was reported by Yuan et al., who developed a very efficient Pd@MIL-101(Cr) catalyst for water mediated Suzuki–Miyaura and Ullmann coupling reactions. This catalyst showed high stability,

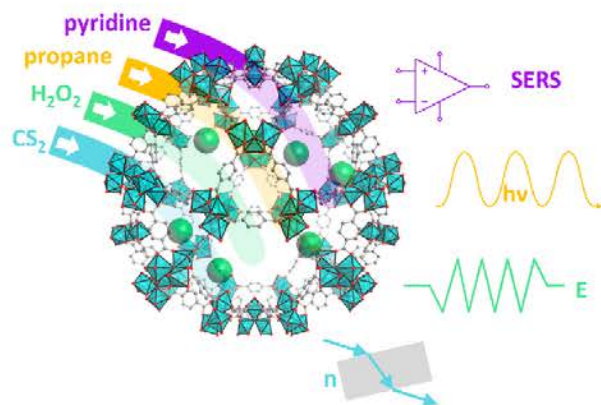


Fig. 8. Schematic illustration of Nanoparticles@MOFs for sensing different analytes (left side) entering in the frameworks. The analyte, as a host, interacts with the composite that could amplify the Raman signal (SERS), affect the luminescent properties, induce changes in the electrical or optical (refractive index) properties.

low metal leaching and high activities (conversion = 100%) over a large number of cycles [93].

4. NP@MOFs for sensing

A wide range of applications, including chemical threat detection, medical diagnostics, food/drink quality control, explosives and pollutants detection, requires sensors that detect specific molecules or elements with high selectivity, sensitivity, and speed of analysis [124–126]. Typical transduction mechanisms are changes in the electrical, photophysical or mechanical properties of the sensor material when it interacts with the analyte (sensing, Fig. 8). Metal nanoparticles have been widely investigated as sensor components because their physical properties (mainly optical, electrochemical or photoelectrochemical) are readily modulated upon interaction with molecules [127,128]. Recently, MOFs have been proposed as a novel class of support for chemical probes, as pre-concentrators, and as molecular filters and templates. In this respect, MOFs act in an analogous way to other porous materials, such as mesoporous silica or zeolites. However, MOFs offer greater possibilities for tailoring the pore size and chemistry in order to enhance the adsorption of targeted molecules or elements [129].

4.1. Size selective sensors

One of the most promising strategies for designing highly selective/sensitive sensors is to synthesize metal/metaloxide MOF composites in order to combine their complementary properties [130]. To date, most of these sensors are constructed by embedding metal nanoparticles in the MOF crystals. Thus, the working mechanism relies on the target molecule diffusing to the embedded metal nanoparticles, through the MOF pores, where interaction causes a detectable change in physical properties. According to this mechanism, the properties of the MOFs are expected to play a major role on the final performance of the sensor. For example, the uniform pore size and resulting size-selectivity of MOFs enabled the development of sensors in which the MOFs act as size-exclusion filters [131]. A pioneering example of this type of sensors was recently reported by Sugikawa et al. [10], who synthesized a MOF-5 supported Au nanorod sensor that showed Surface-Enhanced Raman Scattering (SERS) behavior when contacted with certain pyridine derivatives (Fig. 9a). SERS is a powerful vibrational spectroscopy technique that allows the detection of sub-attomolar quantities of analyte due to the million-fold Raman scattering enhancement

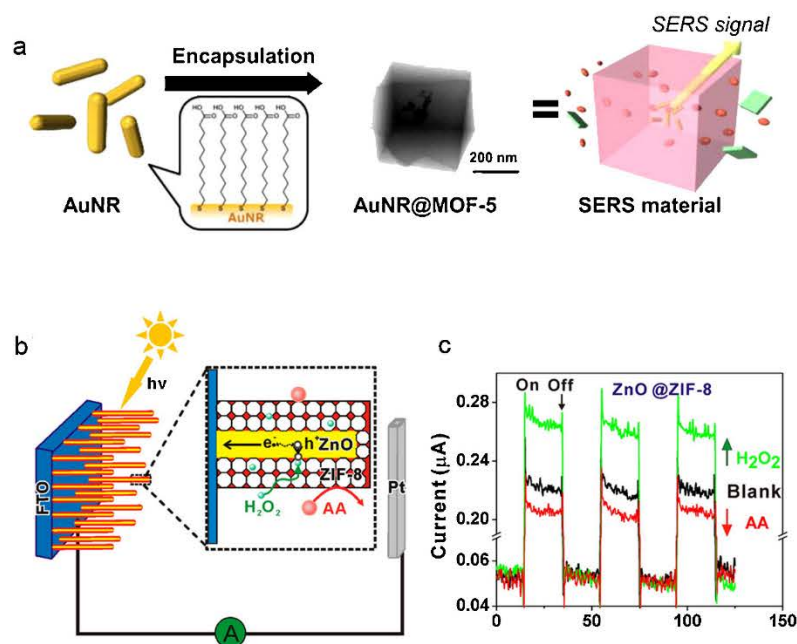


Fig. 9. (a) Schematic illustration of SERS sensing activity of MOF-5 supported Au nanorods. Reproduced from [10]. (b) Schematic diagram of ZIF-8 supported ZnO nanorods PEC sensors with selectivity to H₂O₂. (c) Photocurrent response of this sensor in the presence of H₂O₂ (0.1 mM) and ascorbic acid (0.1 mM). Reproduced from [137].

occurring when the analytes are adsorbed on metal nanoparticles (e.g. plasmonic Au nanorods) [132–134]. Interestingly, Sada's group showed that the SERS signal enhancement occurred only for certain types of pyridine derivatives, such as pyridine and 2,6-bipyridine, but not for poly(4-vinylpyridine). This selectivity was attributed to the fact that small molecules such as pyridine and 2,6-bipyridine can diffuse into the pores of MOF-5 and reach the embedded Au nanorods. On the contrary, bulky poly(4-vinylpyridine) molecules cannot diffuse into MOF-5 and cannot interact with Au nanorods. Very recently, a similar strategy was used to follow the metalation of a porphyrin-based MOF [135]. In this study, SERS-active Ag nanoparticles were wrapped with crystals of this MOF.

Other size-selective sensors composed of MOFs and metal nanoparticles have been reported. These systems were used to monitor electrochemical changes of Pt nanoparticles [136], photoelectrochemical changes of ZnO nanorods [137] and luminescence changes of CdSe quantum dots. Xu et al. showed the possibility to selectively detect H₂O₂ using UiO-66 supported Pt nanoparticles [136]. One of the main concerns for a H₂O₂ electrochemical sensor is the presence of other physiological species such as ascorbic acid, uric acid and some carbohydrate compounds, which can be also oxidized along with H₂O₂ molecules on the electrode surface and cause interference. This issue was solved by embedding the Pt nanoparticles into UiO-66, which acts as a size-exclusion filter allowing only H₂O₂ molecules to diffuse in, while excluding the bulkier interfering ascorbic acid, uric acid, and carbohydrate compounds. Selective photoelectrical detection of H₂O₂ was demonstrated using a similar approach, by coating ZnO nanorods with ZIF-8 (Fig. 9b) [137]. Here, the ZIF-8 network also acts as a size-exclusion filter preventing the diffusion of ascorbic acid molecules while allowing diffusion of the smaller H₂O₂ molecules to the ZnO nanorods. Illuminating the sample with 380 nm light engendered a photocurrent response that arises from the oxidation of H₂O₂ by photogenerated holes on the surface of ZnO nanorods (Fig. 9c). Finally, Falcaro and co-workers

demonstrated the size selective detection of ethanethiol compared to a larger linear copolymer *n*-isopropyl acrylamide/acrylic acid/*t*-butyl acrylamide mercaptane, by following the quenching effect of luminescent CdSe quantum dots embedded into MOF-5 [9,138]. The same group grew MOF-5 around Co NPs and subsequent infiltration with a dye enabled the fabrication of a repositionable sensor for the detection of aromatic amines [139].

4.2. Gas selective-sensors

In addition to size selective sensors, the potential of MOFs to tune the chemical functionality of their pores for the selective adsorption of certain species also paves new ways to create chemically selective sensors when combined with responsive metal nanoparticles. For example, it is well-known that MOF-5 is selective towards CO₂ in a gas mixture because the polarizability and quadrupole moment of CO₂ leads to electrostatic attraction between CO₂ molecules and the aromatic rings of MOF-5 [140]. Using this property, Tang's group synthesized a Au@MOF-5 SERS sensor able to selectively detect CO₂ in the presence of various gases [141].

4.3. Ion-selective sensors

Recent advances have led to selective sensors based on other mechanisms; e.g., taking advantage of the low chemical stability of some MOFs. Using this approach, Zhao et al. developed a sensor selective for phosphate ions by embedding ZnO quantum dots into MOF-5 [142]. The working mechanism of this sensor was simple: MOF-5 degrades in the presence of phosphate ions, thus liberating the ZnO nanoparticles, that recover their original fluorescence that was quenched when embedded. The authors showed the selectivity of this sensor for phosphates by exposing it to various other anions, resulting in a much lower fluorescence signal.

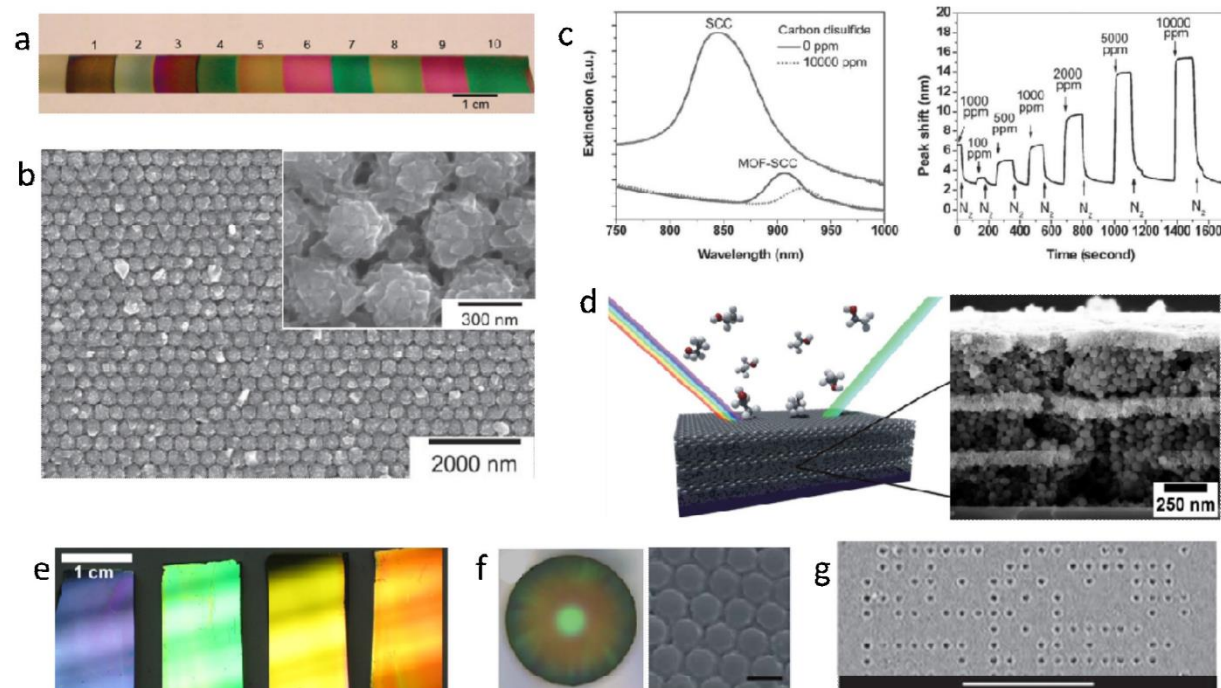


Fig. 10. MOF-based photonic crystals for label-free optical sensing. (a) Photograph of a series of ZIF-8 films of various thicknesses grown on silicon substrates. Reproduced from [143]. (b) SEM images of the MOF-silica photonic crystals prepared by step-by-step deposition of HKUST-1. Inset: high magnification. (c) Left: Near-IR extinction spectra of the MOF-silica photonic crystal (MOF-SCC) and the bare silica colloidal (SCC) crystal film before and after exposure to 10 000 ppm CS₂. Right: Response of MOF-silica photonic crystal to a series of CS₂ vapors of various concentrations versus time. Reproduced from [146]. (d) Left: Schematic representation of a Bragg stack. Right: SEM images of a Bragg stack prepared by alternating spin-coating nanoparticulate suspensions of ZIF-8 and TiO₂, resulting in a layer thickness of approx. 200 nm and 50 nm for ZIF-8 and TiO₂, respectively. Reproduced from [152]. (e) Photographs of step-by-step HKUST-1/ITO hybrid materials with different thicknesses. The stripes are caused by the light source. Reproduced from [156]. (f) Left: Optical image of a MOF-5/silica composite sphere with a diameter of 200 μm. Right: Corresponding SEM image showing the uniform silica spheres with interstitial MOF-5. Scale bar: 300 nm. Reproduced from [157]. (g) Transmission optical microscopy image of a metallic silver dot pattern deposited inside a single MOF-5 crystal. Scale bar: Scale bar: 25 μm. Reproduced from [148].

4.4. Photonic crystal sensors

Color change is another attractive sensing mechanism, as it can be readily detected, in some cases even with the naked eye. Solvatochromism/vapochromism and luminescence color or intensity shifts have been reported for MOFs upon guest accommodation [129]. However, such behavior is based on specific responsive elements in the lattice that might not be compatible with fine-tuning the adsorption properties to detect different analytes. Therefore, a more flexible approach would require fine-tuning the MOF adsorption behavior without having to take the preservation of color change capabilities into account. In this context, Lu et al. demonstrated sensing based on the color change of the light reflecting off of a thin ZIF-8 film on a flat surface (Fig. 10a) [143]. The underlying principle is Fabry-Pérot interference, which occurs when incident light undergoes multiple reflections off of two parallel surfaces separated by a distance on the order of the wavelength of light. The wavelengths at which constructive interference occurs, which determines the color of the reflected light, depends on the refractive index of the film. Since the refractive index of a microporous material increases when guests are accommodated in the pores, the concentration of propane in N₂ correlates with the interference peak shifts.

The performance of interference-based sensors can be improved by alternating high- and low-refractive index materials. Label-free optical sensors of this type are referred to as 'photonic crystals' [144]. Metal and metal oxide nanoparticles composite can be used as effective materials for sensing applications due to

the difference between the refractive index of the MOF and the encapsulated inorganic nanoparticles. Lu et al. first illustrated this depositing a conformal HKUST-1 coating on an array of uniform carboxylic acid terminated silica spheres, using a step-by-step protocol (Fig. 10b) [145,146]. When exposed to carbon disulphide (CS₂) vapors, the wavelength of the light reflecting off of the photonic crystal shifted gradually with increasing CS₂ concentrations while a bare silica colloidal crystal did not generate a response (Fig. 10c). Similar three-dimensional photonic crystals can also be fabricated using regular assemblies of uniform polymer beads instead of silica spheres [147]. Infiltration of such polymer colloidal crystal templates with MOF precursor solutions [148] and subsequent dissolution of the polymer template results in photonic crystals where the alteration of high- and low-refractive index components is ensured by the continuous MOF structure and regularly spaced air gaps therein, respectively [149,150]. Similar behavior is observed in stacked layers of well-formed and uniform MOF crystallites [151].

Another approach for the fabrication of photonic MOF-based sensors, requires alternating layers of high- and low-refractive index materials stacked on top of each other, to yield one-dimensional photonic crystals or Bragg stacks. Although these are not discrete nanoparticles imbedded within MOF crystals, but rather superstructures that requires both nanoparticle and MOF components localized in different layers, we will briefly discuss such composites to highlight this emerging application. The Bragg stack reflectivity can be enhanced by increasing the number of layers, or by the judicious choice of materials to increase the refractive index contrast. Hinterholzinger et al. demonstrated Bragg stacks

based on ZIF-8 and high-refractive index TiO_2 [152]. Two fabrication methods were employed: (1) alternating spin-coating of nanoparticulate suspensions of both materials and (2) alternating ZIF-8 growth and spin-coating of TiO_2 particles. While the former technique yields a high degree of textural mesoporosity in both layer types, in addition to the ZIF-8 microporosity, the latter method results in Bragg stacks featuring continuous ZIF-8 layers (Fig. 10d). Alcohols too large to efficiently enter the ZIF-8 pores triggered small and large responses in the sensors obtained with method 1 and 2, respectively. These tests indicate that to enable molecular sieving in a photonic crystal, continuous MOF films are preferred. Nevertheless, the particle spin-coating method remains popular, mainly because of its simplicity and general applicability [153,154]. For instance, Hu et al. demonstrated how Bragg stacks of the flexible MIL-88B- NH_2 and TiO_2 can be used for the determination of the EtOH content of aqueous solutions of the alcohol [153]. Ranft et al. showed how the response from three spin-coated MOF- TiO_2 Bragg stacks with different adsorption preferences could be combined to generate a unique signature for each analyte and thus enhance specificity in comparison to that of the individual sensors [154].

The deposition of both the MOF layer and high-refractive index component as continuous films provides the highest reflectivity MOF-based Bragg stacks. Thus far only two cases of monolithic MOF-based Bragg stacks have been demonstrated. Lu et al. showed how metal sputtering in combination with the ZIF-8 film growth method led to one-dimensional photonic crystals [146,155]. The Bragg stack with the highest reflectivity reported to date (ca. 80%) was created by Liu et al. by alternating the sputtering of indium tin oxide (ITO) and the deposition of HKUST-1 layers via the step-by-step protocol (Fig. 10e) [156].

One potential issue with the practical implementation of photonic crystals is the angle-dependency of the observed color [155]. Cui et al. proposed an interesting approach to fabricate color shift sensors exhibiting full angle independence that work similarly to the three-dimensional photonic crystals discussed above [157] (Fig. 10f).

Another exciting development is the demonstration by Ameloot et al. of depositing metallic microstructures within single crystals of a photoactive MOF material in a programmed fashion [148]. This method enables the fabrication of three-dimensional metal dot arrays arranged in an arbitrary pattern within a MOF crystal (Fig. 10g), thus resulting in a regular arrangement of high- and low-refractive index materials. Since the generation of such arrays is fully computer-controlled, fine-tuning the optical response for photonic sensing applications should be straightforward.

5. NP@MOFs for sequestration and separation

The high and tunable porosity of MOFs eases the penetration, accumulation, and separation of various species not only from gas but also from liquid phase. Nanoparticles embedded inside MOF structures can impart additional functionalities. For example, enabling the recollection using a magnetic field of the MOF used as a sorbent for pollutants, using the photocatalytic properties for their degradation, or acting a support that facilitate the separation of organic compounds (Fig. 11).

5.1. Sequestration of pollutants

MOFs have shown great potential for the removal of carcinogenic polycyclic aromatic hydrocarbons (PAHs), heavy metals, pesticides, dyes, radionuclides and other toxic chemicals [158–164]. Introducing additional functionality via magnetic nanoparticles can be achieved by synthesizing magnetic framework

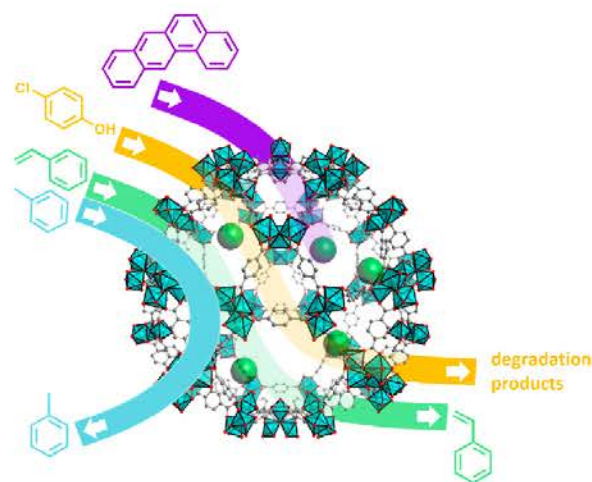


Fig. 11. Schematic illustration of metal/metaloxide nanoparticles@MOF for pollutant sequestrations and degradation, and separation.

composites (MFCs) [165]. There are two main advantages provided by the magnetic particles. Firstly, they facilitate positioning the porous material using an external magnetic force. This can have application to simple magnetic recovery in a batch reactor to more precise localization in microfluidic devices. Secondly, magnetic nanoparticles afford a magneto-thermal effect when exposed to an alternate magnetic field which can be exploited to release guests from the pores of the MFCs [166]. We note that the surface area of the MFCs are lower compared to the parent MOF due to the gravimetric contribution of the particles that, under optimized conditions, lies in the range of 3–5 wt% (e.g. 4% using Co nanoparticles [139]).

The use of MFCs for the sequestration of polycyclic aromatic hydrocarbons (PAHs) has been reported by Doherty et al. [167] and Huo and Yan [168] in 2012. Yan demonstrated that silica coated magnetic iron oxide and MIL-101(Cr) could be mixed and used for the efficient recovery (81–96%) of six different PAHs from water, while Doherty et al. showed that cobalt and nickel ferrites superparamagnetic nanofibers directly embedded into MOF-5 crystals afforded a 1.3 mmol g^{-1} uptake of benz[a]anthracene (Fig. 12a). In 2013, the group of Maspoeh [169] synthesized iron oxide embedded in the copper based MOF HKUST-1 using a spray-drying method. The resulting spherical magnetic framework composite was used for capturing dibenzothiophene (DBT) from iso-octane with a remarkable extraction capacity of 200 g kg^{-1} (Fig. 12b). Chen and co-workers [72] investigated using core-shell magnetic spheres, made with a magnetic iron oxide core and a MIL-100(Fe) MOF shell, towards the sequestration of polychlorinated biphenyls (PCBs) from water. This MOF composite yielded excellent recovery (above 81%) of the PCB, and it was also being able to reach a very low limit of detection (down to 1.07 ng L^{-1}), suitable for harvesting trace amounts of pollutant.

A second important application in environmental remediation is related to inorganic pollutants, such as heavy metals [170,171]. This is due to the environmental and health issues connected with the contamination from, particularly Pb, Hg, Ni, Cr, and Cd. Additionally, the efficient sequestration of certain rare heavy metals such as Ag, Au, Pd, and Pt is of interest because of their high economic value. Examples of MFCs exploited for the collection of dangerous heavy metals have been reported by Sohrabi et al. [172], Wang et al. [173], and Taghizadeh et al. [174]. All these studies used modified silica-coated, iron oxide nanoparticles embedded into HKUST-1. Sohrabi

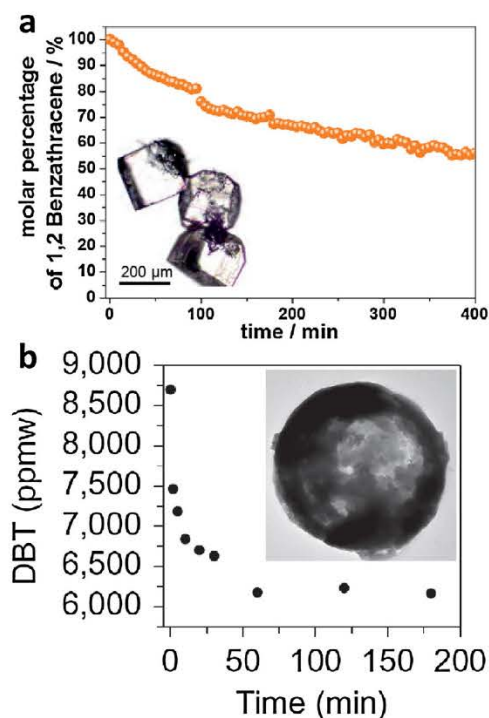


Fig. 12. (a) Change in molar percentage of benz[a]anthracene during time due to the uptake performed by $\text{CoFe}_2\text{O}_4/\text{MOF-5}$ composite (in the inset). Reproduced from [167]; (b) Time dependence of the dibenzothiophene capture by Iron oxide nanoparticle@HKUST-1 superstructure (in the inset) obtained by spray-drying. Reproduced from [169].

explored the optimization of Cd(II) and Pb(II) ions uptake using pyridine grafted on the surface of the magnetic particles. Excellent extraction values of ca. 190 mg g^{-1} were reported. Wang et al. chose post-functionalization of magnetite@HKUST-1 with dithizone as a strategy for the sequestration of Pb(II) obtaining a modest uptakes of 1.67 mg g^{-1} . Based on a very similar system to Sohrabi [172], Taghizadeh studied the uptake of Cd(II), Pb(II), Ni(II), and Zn(II), reported sequestration values between 98 (Ni) and 206 (Zn) mg g^{-1} . The capture of high value heavy metals by MFCs has been canvassed in the work of Falcaro et al. [175] and Bagheri et al. [176]. In the first case, a composite based on a MOF made of two linkers (terephthalic acid and 2-aminoterephthalic acid) and Co nanoparticles was used to selectively harvest Ag(I) ions from a microchannel, in which the MFCs were moved from a dodecanol filled zone to a silver enriched methanol one. It was posited that sequestration of Ag(I) ions was due to the presence of the amino groups in the MOF pores. Finally, the nanocomposite was moved to a third channel filled with dodecanol for recovery. In the work of Bagheri et al. [176], the aforementioned pyridine functionalized iron oxide magnetic particles embedded into HKUST-1 were used to collect Pd from water with a maximum absorption capacity of 105 mg g^{-1} .

5.2. Uptake and degradation

A different strategy in environmental remediation is the concomitant removal and degradation of pollutants, particularly with respect to noxious organic agents. In this case, the high uptake capacity afforded by the MOF and the potential of the embedded nanoparticles to decompose pollutant molecules are utilised.

In 2013, Shen et al. [114] proposed a pioneering study that described the simultaneous uptake and degradation of toxic species, such as hexavalent chromium and model dyes, using Pd@NH₂-UiO66. In this composite, small Pd nanoparticles (3–6 nm) were homogeneously generated within the pores of a preformed amino functionalized UiO-66 MOF. Under a 420 nm visible light irradiation, this system was able to photo-catalytically reduce the carcinogenic Cr(VI) to Cr(III) within 90 min at a pH range of 1–5, demonstrating superior performance when compared with bare NH₂-UiO66 and N-doped titania. More interestingly, the same system was investigated toward the complete degradation of methyl orange (MO) and methylene blue (MB). Here, the measured conversion was modest when using either the dye (5% for MO and 38% for MB) or the Cr(VI) alone. However, this conversion drastically enhanced when the dye was added to the reaction system: Cr(VI) reduction increased from initial 70% to 79% in presence of MO, and from 70% to nearly 100% in presence of MB, demonstrating a beneficial synergistic effect.

Among the different active materials with degradation capabilities, titania particles are extensively used as efficient photocatalytic nanomaterials, especially for self-cleaning surfaces [177,178]. For such purpose, Hu and co-workers [179] studied the TiO₂@MIL-101(Cr) composite, which was prepared by post-infiltration of different amounts of *tert*-butyl titanate into the MOF cavities. The resulting titania was then converted to the more photocatalytically active anatase phase by thermal treatment. The composite demonstrated higher adsorption of formaldehyde than the titania alone due to the high surface area of MIL-101(Cr). Additionally, the titania was able to degrade the pollutant using a 100 W lamp at 365 nm. The composite with 14.5 wt% TiO₂ was found to be the most efficient with ca. 80% of product destroyed within 200 min. Furthermore, the same material was successfully used for the degradation of *o*-xylene with analogous results.

A recent example of one-pot uptake and degradation carried out by a NP@MOF composite was reported by Cai's group [180]. In this work, Fe-doped MOF-5 was prepared around pre-synthesized 60 nm Co₃O₄ nanoparticles, using Fe(acac)₃ as the source of iron (Fig. 13a) [181]. The high porosity and open pore network of the MOF structure enables fast molecule diffusion, thus rapidly concentrating the pollutant species (in this case, 4-chlorophenol) and exposing it to the catalytic nanoparticles for its degradation. In this case, the degradation was mediated by potassium peroxy-monosulfate (Oxone), which was diffused into the MOF pores. The as-prepared yolk-shell catalyst was highly active with a removal efficiency of 4-chlorophenol over 99% within 150 min even after four successive cycles (Fig. 13b).

5.3. Stationary phases for separations

Due to their crystalline structure and high porosity, MOFs have recently emerged as candidates for analytical and chromatographic separations [182]. Separation by adsorption is more energy efficient than distillation, but to date limited examples with acceptable selectivity have been reported [183]. Silica is the most common stationary phase used in normal phase chromatography and therefore, a natural step forward is to combine silica and MOFs to achieve better performances. Bradshaw's group [8] introduced a sphere-on-sphere (SOS) technique to immobilize small engineered 200 nm silica nanospheres on 5.5 μm silica microspheres. The SOS system with carboxylic groups acted as scaffold for the subsequent growth of HKUST-1 crystals, and the obtained SOS-COOH@HKUST-1 composite (Fig. 14a and b) was packed in a high-performance liquid chromatography (HPLC) column. The results indicated that the composite was able to separate a mixture of toluene, ethylbenzene and styrene using heptanes/dichloromethane 95:5, whereas the neat SOS-COOH showed no separation properties (Fig. 14c and

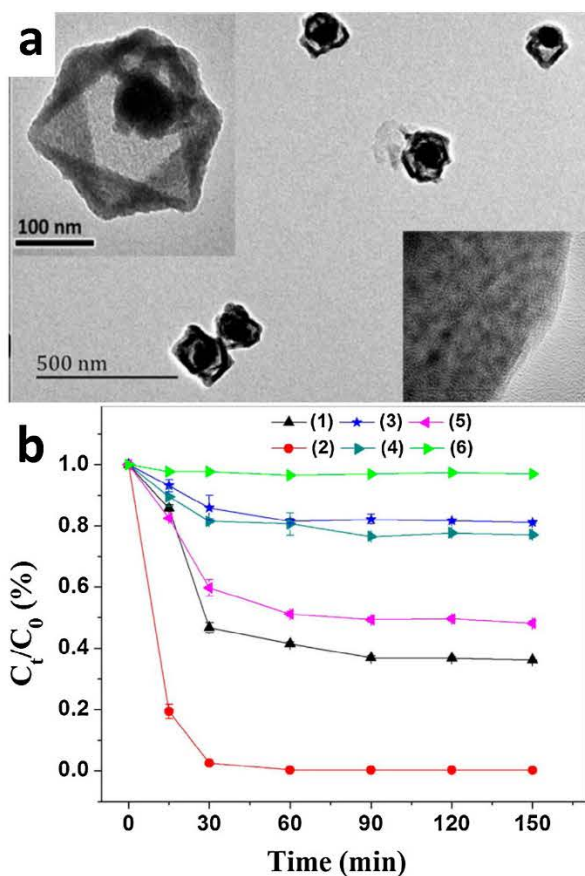


Fig. 13. (a) TEM image of yolk-shell $\text{Co}_3\text{O}_4@Fe\text{-MOF-5}$. The insets are closer observations of the composite; (b) Removal of 4-chlorophenol within 2.5 h for bare NPs activated with Oxone (1), yolk-shell composite activated with Oxone (2), composite alone (3), hollow MOF with Oxone (4), solid core-shell composite with Oxone (5), and Oxone only.

Reproduced from ref. [180].

d). Moreover, the same composite was used, after dichloromethane or toluene pre-conditioning for 24 h, to successfully separate xylene isomers using heptane as the mobile phase. Silvestre et al. [184] used layer-by-layer epitaxy to grow HKUST-1 on magnetic silica nanocubes, producing a magnetic framework composite with high surface area ($1150 \text{ m}^2 \text{ g}^{-1}$) after 200 coating cycles. The obtained material was used for HPLC chromatography, showing an appreciable, although incomplete separation of toluene and pyridine. In both cases, the presence of MOFs was found important to enhance, and in some case achieve optimal separation performance.

6. NP@MOFs for controlled release

Molecular delivery is an application of current interest in MOF chemistry [185,186]. In contrast to gas storage and separation, where the focus is to optimise the attractive forces between the framework and guest, the possibility to control the molecular delivery of guests represents an additional challenge. The majority of studies in this area describe the *spontaneous release* of molecules from the pores [187–190]. This process is driven by the molecular diffusion where, ultimately, the concentration of guest molecules in the pores and external environment reaches equilibrium. This strategy is most suitable for long-term drug release. However, if

the release of guests can be triggered by an external stimulus (Fig. 15), further opportunities would arise in more complex systems in cell biology or biomedicine. MOF composites seem to be an effective platform for controlled drug release. Three strategies for triggered release of molecules have been explored using MOF composites: (1) Introduction of photo-switchable molecules into the pore networks that gives rise to guest release upon irradiation [191,192]; (2) Immobilization of target molecules into pore surfaces via photo-labile moieties that undergo controlled photolysis and release of the entrapped molecules [193,194]. We noted that both of these strategies require the specific chemical modifications to the pores' surface; and (3) Exploitation of metal/metal oxide nanoparticles@MOFs nanoparticles where external stimuli, such as a magnetic field or light, causes release of molecules by localized heating. The advantage of this approach relies on the wide variety of frameworks of different pore size and chemistry that can be used to prepare these metal/metal oxide nanoparticles@MOF composites.

Incorporating magnetic metal nanoparticles into MOFs is an example of a metal/metal oxide nanoparticles@MOF composite designed for controlled molecular release [165]. In addition to providing a mechanism for localised heating, the magnetic nanoparticle facilitates spatial control of the composite via the external magnetic field. To this end, Qiu and co-workers have reported the synthesis of $\text{Fe}_3\text{O}_4@HKUST-1$ nanocomposites loaded with nimesulide (NIM), a potential anticancer drug for pancreatic cancer treatment (Fig. 16a and b) [195]. This MOF composite maintained its magnetic characteristics at 300 K, thus demonstrating its potential for use in biological systems. Furthermore, these nanocomposites could be positioned using a magnet in aqueous solution as shown in Fig. 16c. The spontaneous release of NIM over 11 days was examined in physiological saline (aqueous NaCl solution) at 37°C (Fig. 16d); however, controlled release of the drug via an alternating magnetic field was not demonstrated. We note that HKUST-1 is known to be water sensitive [196], hence the spontaneous release of NIM may be attributed to the decomposition of HKUST-1.

A similar study was also reported by Li and co-workers using $\gamma\text{-Fe}_2\text{O}_3@MIL-53(\text{Al})$. In this case, the measured residual magnetization of $\gamma\text{-Fe}_2\text{O}_3@MIL-53(\text{Al})$ indicated that the $\gamma\text{-Fe}_2\text{O}_3$ nanoparticles were superparamagnetic [197]. Here the spontaneous release of ibuprofen as a model drug over 7 days was reported. However, the stability of this composite in physiological saline solution was not assessed. Given the higher stability of MIL-53(Al) in water [198] than in phosphate buffer saline, it can be expected that the spontaneous release of the drug was regulated by pore diffusion. Kaskel and co-workers further exploited the properties of magnetic nanoparticles into MOFs by triggering the release of molecules via induced magnetic heating (Fig. 17) [166]. In this experiment, $\gamma\text{-Fe}_2\text{O}_3@HKUST-1$ was suspended in ethanol and, under a magnetic field strength of 1.7 kA m^{-1} at a frequency of 183 kHz, a temperature increase from 23°C to 40°C was measured in less than 10 minutes. A specific absorption rate (SAR) for ibuprofen was determined to be 11.1 W g^{-1} . Because $\gamma\text{-Fe}_2\text{O}_3@HKUST-1$ showed temperature dependent release kinetics of ibuprofen (passing from $4.4 \times 10^{-6} \text{ mmol s}^{-1}$ at 20°C to $6.6 \times 10^{-6} \text{ mmol s}^{-1}$ at 40°C), the high SAR value will effectively contribute to the release of drugs induced by an external magnetic field. Accordingly, real-time monitoring of drug release under an external magnetic field should be investigated to fully evaluate the potential of this system.

Gold nanorods (GNRs) are known to generate heat by absorption of near infrared light, the so-called photothermal conversion effect [199]. Furukawa and co-workers demonstrated the synthesis of core-shell type mesoscopic composites of $\text{GNR}@[\text{Al}(\text{OH})(1,4\text{-ndc})_n]$ from $\text{GNR}@alumina$ via coordination replication (Fig. 18)

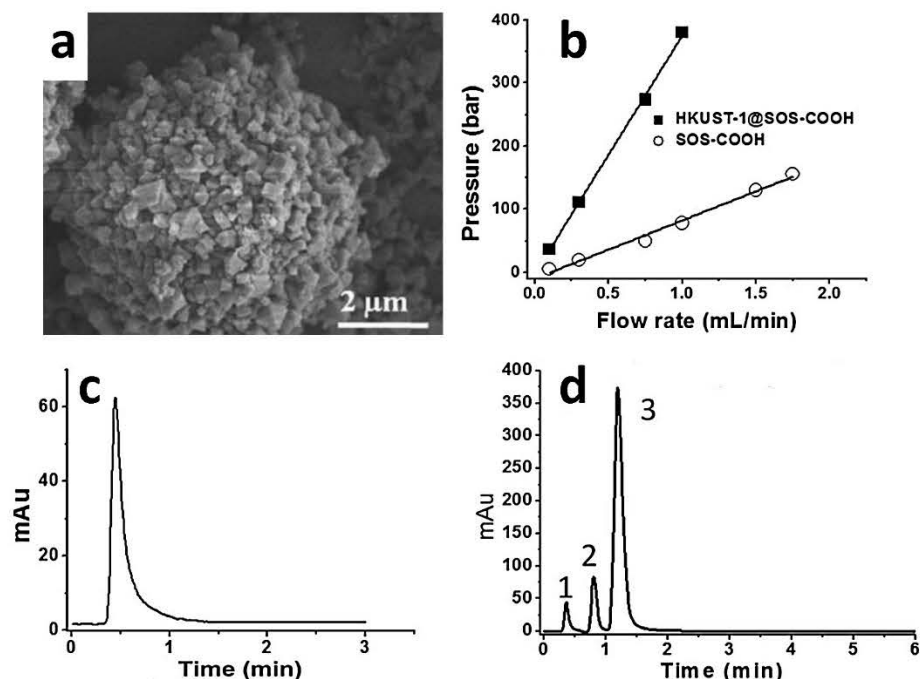


Fig. 14. (a) SEM of SOS-COOH@HKUST-1 particles; (b) back-pressure vs flow rate measured for columns packed with SOS-COOH particles (empty circles) and SOS-COOH@HKUST-1 particles (black squares) using heptanes as mobile phase; (c) chromatogram showing that column packed with SOS-COOH particles was not able to separate a mixture of ethylbenzene and styrene; (d) chromatogram obtained using column packed SOS-COOH@HKUST-1 particle in heptane/DCM 95:5 as mobile phase, for the separation of toluene (1), ethylbenzene (2), and styrene (3).

Reproduced from ref. [8].

[13]. In this case, anthracene was selected as the model guest specie as it can be easily monitored by fluorescence spectroscopy. Interestingly, spontaneous release (i.e. leakage) of anthracene from the pores was not observed in cyclohexane. However, molecular release was confirmed under near infrared light (750 nm) irradiation. Most of molecules (ca. 70%) were released from the pores of $[Al(OH)(1,4\text{-ndc})_n]$ in 2 h. This work represents the highest level of control achieved for the triggered release of molecules from metal nanoparticles@MOFs.

As shown here, the hybridization of MOFs with metal nanoparticles is a promising strategy for inducing molecular release via a

non-destructive external stimulus (magnetic field, near IR light). However, there are still very few examples of metal nanoparticles@MOFs for delivery applications and further proof-of-concept model systems will be essential to a comprehensive understanding of their chemistry and potential for real biological application. The key elements that need to be addressed are the following: (1) careful experimental design that directly monitors molecular release under external stimuli; (2) development of physiologically stable non-toxic MOFs; and (3) understanding the host-guest interactions between the MOFs and selected drugs, so that controlled release can be realised without drug leakage.

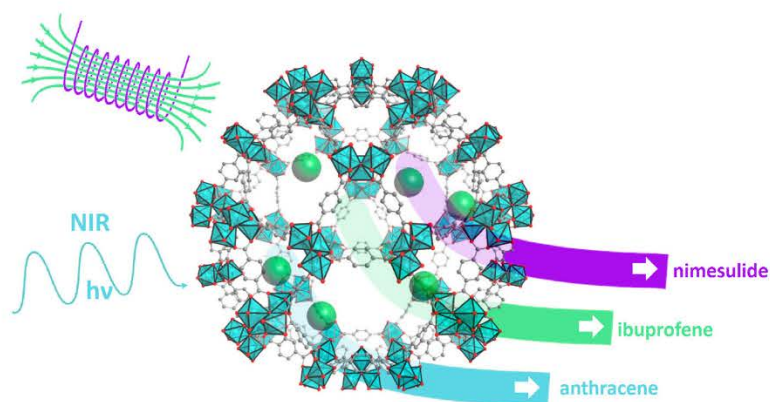


Fig. 15. Schematic illustration of controlled molecular release from metal/metal oxide nanoparticles@MOF. Thanks to the capability of magnetic iron oxide nanoparticles or gold nanorods, which convert magnetic field or near IR into heat, respectively, the release of trapped molecules can be initiated by physical stimuli.

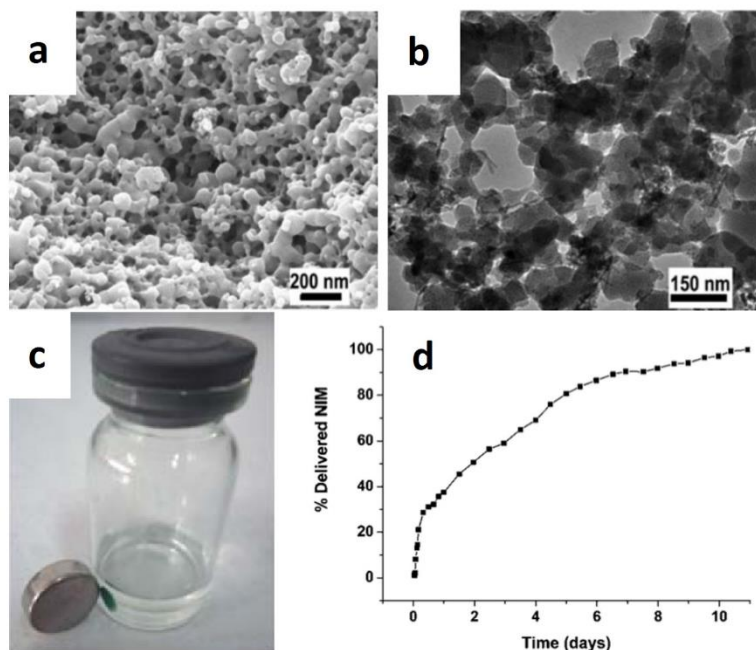


Fig. 16. (a) SEM and (b) TEM images of Fe_3O_4 @HKUST-1 composites. (c) NIM loaded Fe_3O_4 @HKUST-1 composites attracted by a magnet. (d) Spontaneous release of NIM from Fe_3O_4 @HKUST-1 in physiological saline solution at 37°C . Reproduced from ref. [195].

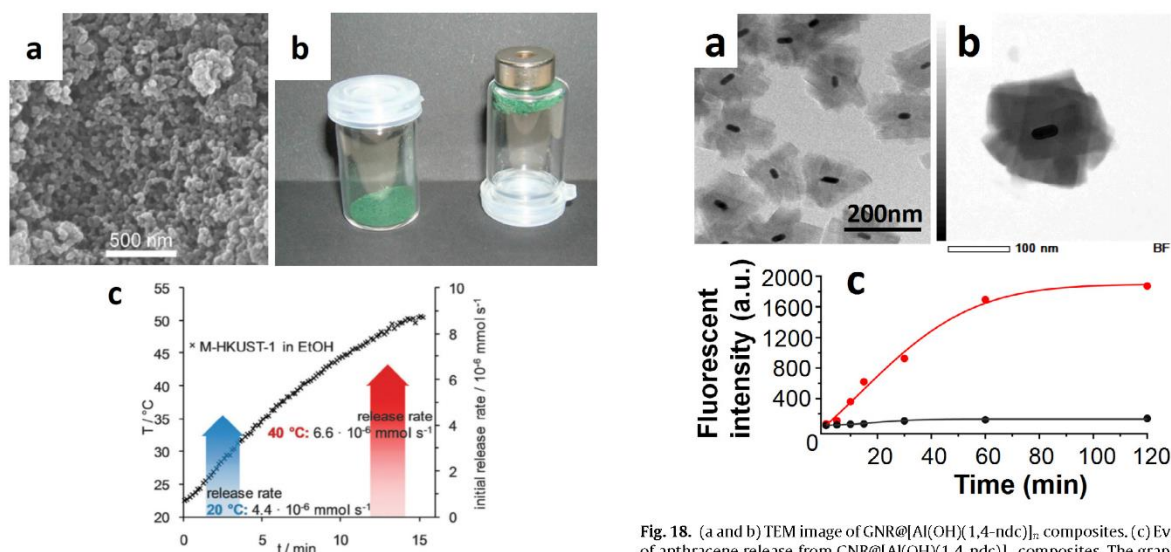


Fig. 17. (a) SEM image of $g\text{-Fe}_2\text{O}_3$ @HKUST-1 composites. (b) Fe_3O_4 @HKUST-1 composites attracted by a magnet. (c) Magnetic heating curve of 324 mg of $g\text{-Fe}_2\text{O}_3$ @HKUST-1 composites in 30 mL of ethanol at 183 kHz and a field strength of 1.7 kA m^{-1} . The arrows indicate the initial release rates for ibuprofen at 20 and 40°C , respectively. Reproduced from ref. [166].

7. Future outlook

In this review we have shown how nanocomposites obtained by the judicious combination of metal/metal oxide nanoparticles with MOFs can be used as advanced materials for wide variety of

Fig. 18. (a and b) TEM image of $\text{GNR@[Al(OH)(1,4-ndc)]}_2$ composites. (c) Evaluation of anthracene release from $\text{GNR@[Al(OH)(1,4-ndc)]}_2$ composites. The graph shows liner plots for fluorescence intensity maxima of the released anthracene versus time with (red) and without (black) light irradiation at 750 nm . Reproduced from ref. [13].

applications including gas adsorption, separation, catalysts, molecular sieve and repositionable sensors, environmental remediation, and drug-delivery. Importantly, these nanocomposites are now being explored for more sophisticated and emerging technologies such as microfluidics where the nanocomposites can be used as micro-carriers [175], photocatalysts for H_2 production [200], or biomedical applications where ‘up-conversion’ properties can facilitate photoregulated drug release [201].

Despite the amount of studies proposed in the literature, we posit that we are at the early stage of this emerging research field. We base this notion on the following: (1) the potential for integrating sophisticated inorganic nano-systems with a variety of properties including plasmonic, electro- and thermo-chromic, up- and down-conversion properties into the composites; (2) the ever and increasing number of MOFs possessing customized chemical functionalities and tailored pore size and arrangement; (3) the rapid progress in the preparation methods for nanoparticles and MOFs that will further facilitate their integration; and (4) the potential to engineer multicomponent nanocomposite systems that can incorporate multiple nanoparticles within different MOFs systems. Finally, in order to fully realize the potential of this area, a fundamental understanding of the mechanisms that imbue the composites with their unique properties (e.g. spill over effect, heat transfer mechanisms, and energy gap modulation) must be pursued. This will help to build a solid platform towards the engineering of these exciting and novel materials for practical applications.

Acknowledgements

P.F. and C.J.D. gratefully acknowledges the Australian Research Council for funding DECRA DE120102451 and Future Fellowships FT100100400, respectively. D.M., I.I. and A.Y. thank the EC FP7 ERC-Co 61594.

References

- [1] H. Deng, C.J. Doonan, H. Furukawa, R.B. Ferreira, J. Towne, C.B. Knobler, B. Wang, O.M. Yaghi, *Science* 327 (2010) 846.
- [2] S. Kitagawa, R. Kitaura, S. Noro, *Angew. Chem. Int. Ed.* 43 (2004) 2334.
- [3] H. Furukawa, K.E. Cordova, M. O'Keefe, O.M. Yaghi, *Science* 341 (2013) 974.
- [4] M. O'Keefe, O.M. Yaghi, *Chem. Rev.* 112 (2012) 675.
- [5] V. Guillemin, D. Kim, J.F. Eubank, R. Luebke, X. Liu, K. Adil, M.S. Lah, M. Eddaoudi, *Chem. Soc. Rev.* 43 (2014) 6141.
- [6] Q.-L. Zhu, Q. Xu, *Chem. Soc. Rev.* 43 (2014) 5468.
- [7] G. Lu, S. Li, Z. Guo, O.K. Farha, B.G. Hauser, X. Qi, Y. Wang, X. Wang, S. Han, X. Liu, J.S. DuChene, H. Zhang, Q. Zhang, X. Chen, J. Ma, S.C.J. Loo, W.D. Wei, Y. Yang, J.T. Hupp, F. Huo, *Nat. Chem.* 4 (2012) 310.
- [8] A. Ahmed, M. Forster, R. Clowes, D. Bradshaw, P. Myers, H. Zhang, *J. Mater. Chem. A* 1 (2013) 3276.
- [9] P. Falcaro, A.J. Hill, K.M. Nairn, J. Jasieniak, J.I. Mardel, T.J. Bastow, S.C. Mayo, M. Gimona, D. Gomez, H.J. Whitfield, R. Ricco, A. Patelli, B. Marmiroli, H. Amenitsch, T. Colson, L. Villanova, D. Buso, *Nat. Commun.* 2 (2011) 237.
- [10] K. Sugikawa, S. Nagata, Y. Furukawa, K. Kokado, K. Sada, *Chem. Mater.* 25 (2013) 2565.
- [11] G. Li, H. Kobayashi, J.M. Taylor, R. Ikeda, Y. Kubota, K. Kato, M. Takata, T. Yamamoto, S. Toh, S. Matsumura, H. Kitagawa, *Nat. Mater.* 13 (2014) 802.
- [12] R. Ameloot, F. Vermoortele, W. Vanhove, M.B.J. Roeffaers, B.F. Sels, D.E. De Vos, *Nat. Chem.* 3 (2011) 382.
- [13] K. Khaletskaya, J. Reboul, M. Meilikhov, M. Nakahama, S. Diring, M. Tsujimoto, S. Isoda, F. Kim, K. Kamei, R.A. Fischer, S. Kitagawa, *J. Am. Chem. Soc.* 135 (2013) 10998.
- [14] K. Liang, R. Ricco, C.M. Doherty, M.J. Styles, S. Bell, N. Kirby, S. Mudie, D. Haylock, A.J. Hill, C.J. Doonan, P. Falcaro, *Nat. Commun.* 6 (2015) 7240.
- [15] J.D. Evans, C.J. Sumbly, C.J. Doonan, *Chem. Soc. Rev.* 43 (2014) 5933.
- [16] S. Rösler, R.A. Fischer, *CryStEngComm* 17 (2015) 199.
- [17] S. Hermes, F. Schröder, S. Amirjalayer, R. Schmid, R.A. Fischer, *J. Mater. Chem.* 16 (2006) 2464.
- [18] C. Zlotea, R. Campesi, F. Cuevas, E. Leroy, P. Dibandjo, C. Volkringer, T. Loiseau, G. Férey, M. Latroche, *J. Am. Chem. Soc.* 132 (2010) 2991.
- [19] M. Saikia, D. Bhuyan, L. Saikia, *New J. Chem.* 39 (2015) 64.
- [20] R.J.T. Houk, B.W. Jacobs, F.E. Gabaly, N.N. Chang, A.A. Talin, D.D. Graham, S.D. House, I.M. Robertson, M.D. Allendorf, *Nano Lett.* 9 (2009) 3413.
- [21] L. He, L.F. Dumée, D. Liu, L. Velleman, F. She, C. Banos, J.B. Davies, L. Kong, *RSC Adv.* 5 (2015) 10707.
- [22] C.M. Doherty, D. Buso, A.J. Hill, S. Furukawa, S. Kitagawa, P. Falcaro, *Acc. Chem. Res.* 47 (2014) 396.
- [23] J. Reboul, S. Furukawa, N. Horike, M. Tsotsalas, K. Hirai, H. Uehara, M. Kondo, N. Louvain, O. Sakata, S. Kitagawa, *Nat. Mater.* 11 (2012) 717.
- [24] J.L.C. Rowsell, O.M. Yaghi, *Angew. Chem. Int. Ed.* 44 (2005) 4670.
- [25] K. Sumida, D.L. Rogow, J.A. Mason, T.M. McDonald, E.D. Bloch, Z.R. Herm, T.-H. Bae, J.R. Long, *Chem. Rev.* 112 (2012) 724.
- [26] T. Düren, L. Sarkisov, O.M. Yaghi, R.Q. Snurr, *Langmuir* 20 (2004) 2683.
- [27] M. Eddaoudi, J. Kim, N. Rosi, D. Vodak, J. Wachter, M. O'Keefe, O.M. Yaghi, *Science* 295 (2002) 469.
- [28] M. Yamauchi, H. Kobayashi, H. Kitagawa, *ChemPhysChem* 10 (2009) 2566.
- [29] Y. Li, R.T. Yang, *J. Am. Chem. Soc.* 128 (2006) 726.
- [30] R. Prins, *Chem. Rev.* 112 (2012) 2714.
- [31] N.R. Stuckert, L. Wang, R.T. Yang, *Langmuir* 26 (2010) 11963.
- [32] Y. Li, R.T. Yang, *J. Am. Chem. Soc.* 128 (2006) 8136.
- [33] Y.-Y. Liu, J.-L. Zeng, J. Zhang, F. Xu, L.-X. Sun, *Int. J. Hydrog. Energy* 32 (2007) 4005.
- [34] X.M. Liu, S. Rather, Q. Li, A. Lueking, Y. Zhao, J. Li, *J. Phys. Chem. C* 116 (2012) 3477.
- [35] C.-S. Tsao, M.-S. Yu, C.-Y. Wang, P.-Y. Liao, H.-L. Chen, U.-S. Jeng, Y.-R. Tzeng, T.-Y. Chung, H.-C. Wu, *J. Am. Chem. Soc.* 131 (2009) 1404.
- [36] Y. Li, F.H. Yang, R.T. Yang, *J. Phys. Chem. C* 111 (2007) 3405.
- [37] A. Mavrandonakis, W. Klöpffer, *J. Phys. Chem. C* 112 (2008) 3152.
- [38] Y. Li, F.H. Yang, R.T. Yang, *J. Phys. Chem. C* 112 (2008) 3155.
- [39] K. Lee, Y.-H. Kim, Y.Y. Sun, D. West, Y. Zhao, Z. Chen, S.B. Zhang, *Phys. Rev. Lett.* 104 (2010) 236101.
- [40] S.M. Luzan, A.V. Talyzin, *Microporous Mesoporous Mater.* 135 (2010) 201.
- [41] M. Hirscher, *Microporous Mesoporous Mater.* 135 (2010) 209.
- [42] Y. Li, L. Wang, R.T. Yang, *Microporous Mesoporous Mater.* 135 (2010) 206.
- [43] M. Sabo, A. Henschel, H. Fröde, E. Klemm, S. Kaskel, *J. Mater. Chem.* 17 (2007) 3827.
- [44] Y.E. Cheon, M.P. Suh, *Angew. Chem. Int. Ed.* 48 (2009) 2899.
- [45] S. Proch, J. Herrmannsdörfer, R. Kempe, C. Kern, A. Jess, L. Seyfarth, J. Senker, *Chem.-Eur. J.* 14 (2008) 8204.
- [46] D. Banerjee, A.J. Cairns, J. Liu, R.K. Motkuri, S.K. Nune, C.A. Fernandez, R. Krishna, D.M. Strachan, P.K. Thallapally, *Acc. Chem. Res.* 48 (2015) 211.
- [47] R. Grosse, R. Burmeister, B. Boddenberg, A. Gedeon, J. Fraissard, *J. Phys. Chem.* 95 (1991) 2443.
- [48] J. Liu, D.M. Strachan, P.K. Thallapally, *Chem. Commun.* 50 (2013) 466.
- [49] J.A. Kent (Ed.), *Kent and Riegel's Handbook of Industrial Chemistry and Biotechnology*, Springer US, Boston, MA, 2007.
- [50] L. Lloyd, *Handbook of Industrial Catalysts*, Springer US, Boston, MA, 2011.
- [51] R.M. Rioux, H. Song, J.D. Hoefelmeyer, P. Yang, G.A. Somorjai, *J. Phys. Chem. B* 109 (2005) 2192.
- [52] D. Astruc, F. Lu, J.R. Aranzues, *Angew. Chem. Int. Ed.* 44 (2005) 7852.
- [53] S. Hermes, M.-K. Schröter, R. Schmid, L. Khodair, M. Muhler, A. Tissler, R.W. Fischer, R.A. Fischer, *Angew. Chem. Int. Ed.* 44 (2005) 6237.
- [54] M. Zhao, K. Deng, L. He, Y. Liu, G. Li, H. Zhao, Z. Tang, *J. Am. Chem. Soc.* 136 (2014) 1738.
- [55] M. Homel, T.M. Gür, J.H. Koh, A.V. Virkar, *J. Power Sources* 195 (2010) 6367.
- [56] H.-L. Jiang, B. Liu, T. Akita, M. Haruta, H. Sakurai, Q. Xu, *J. Am. Chem. Soc.* 131 (2009) 11302.
- [57] E.V. Ramos-Fernandez, C. Pieters, B. van der Linden, J. Juan-Alcañiz, P. Serra-Crespo, M.W.G.M. Verhoeven, H. Niemantsverdriet, J. Gascon, F. Kapteijn, *J. Catal.* 289 (2012) 42.
- [58] M.S. El-Shall, V. Abdelsayed, A.E.R. Khder, H.M.A. Hassan, H.M. El-Kaderi, T.E. Reich, *J. Mater. Chem.* 19 (2009) 7625.
- [59] A. Aijaz, T. Akita, N. Tsumori, Q. Xu, *J. Am. Chem. Soc.* 135 (2013) 16356.
- [60] W. Kleist, M. Maciejewski, A. Baiker, *Thermochim. Acta* 499 (2010) 71.
- [61] J.M. Zamoro, N.C. Pérez, E.E. Miró, C. Casado, B. Seoane, C. Téllez, J. Coronas, *Chem. Eng. J.* 195–196 (2012) 180.
- [62] F. Schröder, D. Esken, M. Cokoja, M.W.E. van den Berg, O.I. Lebedev, G. Van Tendeloo, B. Walaszek, G. Buntkowsky, H.-H. Limbach, B. Chaudret, R.A. Fischer, *J. Am. Chem. Soc.* 130 (2008) 6119.
- [63] M. Müller, S. Turner, O.I. Lebedev, Y. Wang, G. van Tendeloo, R.A. Fischer, *Eur. J. Inorg. Chem.* 2011 (2011) 1876.
- [64] T. Ishida, M. Nagaoka, T. Akita, M. Haruta, *Chem.-Eur. J.* 14 (2008) 8456.
- [65] H. Liu, L. Chang, L. Chen, Y. Li, *J. Mater. Chem. A* 3 (2015) 8028.
- [66] L. Chen, H. Chen, R. Luque, Y. Li, *Chem. Sci.* 5 (2014) 3708.
- [67] H. Liu, Y. Liu, Y. Li, Z. Tang, H. Jiang, *J. Phys. Chem. C* 114 (2010) 13362.
- [68] D. Esken, S. Turner, O.I. Lebedev, G. Van Tendeloo, R.A. Fischer, *Chem. Mater.* 22 (2010) 6393.
- [69] K. Leus, P. Concepcion, M. Vandichel, M. Meledina, A. Grirrane, D. Esquivel, S. Turner, D. Poelman, M. Waroquier, V.V. Speybroeck, G.V. Tendeloo, H. García, P.V.D. Voort, *RSC Adv.* 5 (2015) 22334.
- [70] Z. Sun, G. Li, L. Liu, H. Liu, *Catal. Commun.* 27 (2012) 200.
- [71] J. Long, H. Liu, S. Wu, S. Liao, Y. Li, *ACS Catal.* 3 (2013) 647.
- [72] X. Chen, N. Ding, H. Zang, H. Yeung, R.-S. Zhao, C. Cheng, J. Liu, T.-W.D. Chan, *J. Chromatogr. A* 1304 (2013) 241.
- [73] Y. Huang, Y. Zhang, X. Chen, D. Wu, Z. Yi, R. Cao, *Chem. Commun.* 50 (2014) 10115.
- [74] Q.-L. Zhu, J. Li, Q. Xu, *J. Am. Chem. Soc.* 135 (2013) 10210.
- [75] P.-Z. Li, K. Aranishi, Q. Xu, *Chem. Commun.* 48 (2012) 3173.
- [76] A.K. Singh, Q. Xu, *ChemCatChem* 5 (2013) 3000.
- [77] X. Gu, Z.-H. Lu, H.-L. Jiang, T. Akita, Q. Xu, *J. Am. Chem. Soc.* 133 (2011) 11822.
- [78] M. Martis, K. Mori, K. Fujiwara, W.-S. Ahn, H. Yamashita, *J. Phys. Chem. C* 117 (2013) 22805.
- [79] M. Wen, K. Mori, T. Kamegawa, H. Yamashita, *Chem. Commun.* 50 (2014) 11645.
- [80] C. Wang, K.E. deKrafft, W. Lin, *J. Am. Chem. Soc.* 134 (2012) 7211.
- [81] Y. Horiuchi, T. Toyao, M. Saito, K. Mochizuki, M. Iwata, H. Higashimura, M. Anpo, M. Matsuoka, *J. Phys. Chem. C* 116 (2012) 20848.
- [82] A. Henschel, K. Gedrich, R. Kraehnert, S. Kaskel, *Chem. Commun.* 45 (2008) 4192.
- [83] P. Wang, J. Zhao, X. Li, Y. Yang, Q. Yang, C. Li, *Chem. Commun.* 49 (2013) 3330.
- [84] C.J. Stephenson, J.T. Hupp, O.K. Farha, *Inorg. Chem.* 2 (2015) 448.

- [85] H. Pan, X. Li, D. Zhang, Y. Guan, P. Wu, J. Mol. Catal. Chem. 377 (2013) 108.
- [86] J. Hermannsdörfer, M. Friedrich, R. Kempe, Chem.-Eur. J. 19 (2013) 13652.
- [87] D. Zhang, Y. Guan, E.J.M. Hensen, L. Chen, Y. Wang, Catal. Commun. 41 (2013) 47.
- [88] W. Du, G. Chen, R. Nie, Y. Li, Z. Hou, Catal. Commun. 41 (2013) 56.
- [89] J. Hermannsdörfer, R. Kempe, Chem.-Eur. J. 17 (2011) 8071.
- [90] H. Khajavi, H.A. Stil, H.P.C.E. Kuipers, J. Gascon, F. Kapteijn, ACS Catal. 3 (2013) 2617.
- [91] X. Zhao, Y. Jin, F. Zhang, Y. Zhong, W. Zhu, Chem. Eng. J. 239 (2014) 33.
- [92] Y. Huang, S. Liu, Z. Lin, W. Li, X. Li, R. Cao, J. Catal. 292 (2012) 111.
- [93] B. Yuan, Y. Pan, Y. Li, B. Yin, H. Jiang, Angew. Chem. Int. Ed. 49 (2010) 4054.
- [94] Y. Huang, Z. Zheng, T. Liu, J. Lü, Z. Lin, H. Li, R. Cao, Catal. Commun. 14 (2011) 27.
- [95] V. Pascanu, Q. Yao, A. Bermejo Gómez, M. Gustafsson, Y. Yun, W. Wan, L. Samain, X. Zou, B. Martin-Matute, Chem.-Eur. J. 19 (2013) 17483.
- [96] A.S. Roy, J. Mondal, B. Banerjee, P. Mondal, A. Bhaumik, S.M. Islam, Appl. Catal. Gen. 469 (2014) 320.
- [97] S. Gao, N. Zhao, M. Shu, S. Che, Appl. Catal. Gen. 388 (2010) 196.
- [98] Y. Huang, S. Gao, T. Liu, J. Lü, X. Lin, H. Li, R. Cao, ChemPlusChem 77 (2012) 106.
- [99] A. Aijaz, A. Karkamkar, Y.J. Choi, N. Tsumori, E. Rönnebro, T. Autrey, H. Shioyama, Q. Xu, J. Am. Chem. Soc. 134 (2012) 13926.
- [100] J.Y. Kim, M. Jin, K.J. Lee, J.Y. Cheon, S.H. Joo, J.M. Kim, H.R. Moon, Nanoscale Res. Lett. 7 (2012) 461.
- [101] Y. Luan, Y. Qi, H. Gao, N. Zheng, G. Wang, J. Mater. Chem. A 2 (2014) 20588.
- [102] J. Zhu, P.C. Wang, M. Lu, Appl. Catal. Gen. 477 (2014) 125.
- [103] G. Chen, S. Wu, H. Liu, H. Jiang, Y. Li, Green Chem. 15 (2012) 230.
- [104] M. Zhang, Y. Yang, C. Li, Q. Liu, C.T. Williams, C. Liang, Catal. Sci. Technol. 4 (2014) 329.
- [105] T.-H. Park, A.J. Hickman, K. Koh, S. Martin, A.G. Wong-Foy, M.S. Sanford, A.J. Matzger, J. Am. Chem. Soc. 133 (2011) 20138.
- [106] Z. Li, H.C. Zeng, Chem. Mater. 25 (2013) 1761.
- [107] H.-L. Jiang, T. Akita, T. Ishida, M. Haruta, Q. Xu, J. Am. Chem. Soc. 133 (2011) 1304.
- [108] F. Ke, J. Zhu, L.-G. Qiu, X. Jiang, Chem. Commun. 49 (2013) 1267.
- [109] J. Hermannsdörfer, M. Friedrich, N. Miyajima, R.Q. Albuquerque, S. Kümmel, R. Kempe, Angew. Chem. Int. Ed. 51 (2012) 11473.
- [110] Y. Zhao, J. Zhang, J. Song, J. Li, J. Liu, T. Wu, P. Zhang, B. Han, Green Chem. 13 (2011) 2078.
- [111] Y. Liu, W. Zhang, S. Li, C. Cui, J. Wu, H. Chen, F. Huo, Chem. Mater. 26 (2014) 1119.
- [112] A. Aijaz, Q.-L. Zhu, N. Tsumori, T. Akita, Q. Xu, Chem. Commun. 51 (2015) 2577.
- [113] M. Gulcan, M. Zahmakiran, S. Özkur, Appl. Catal. B Environ. 147 (2014) 394.
- [114] L. Shen, W. Wu, R. Liang, R. Lin, L. Wu, Nanoscale 5 (2013) 9374.
- [115] M. Yadav, Q. Xu, Chem. Commun. 49 (2013) 3327.
- [116] M. Müller, S. Hermes, K. Köhler, M.W.E. van den Berg, M. Muhler, R.A. Fischer, Chem. Mater. 20 (2008) 4576.
- [117] K. Na, K.M. Choi, O.M. Yaghi, G.A. Somorjai, Nano Lett. 14 (2014) 5979.
- [118] F.G. Cirujano, A. Leyva-Pérez, A. Corma, F.X. Lladrós, Xamena, ChemCatChem 5 (2013) 538.
- [119] T.T. Dang, Y. Zhu, J.S.Y. Ngiam, S.C. Ghosh, A. Chen, A.M. Seayad, ACS Catal. 3 (2013) 1406.
- [120] T.T. Dang, Y. Zhu, S.C. Ghosh, A. Chen, C.L.L. Chai, A.M. Seayad, Chem. Commun. 48 (2012) 1805.
- [121] H. Li, Z. Zhu, F. Zhang, S. Xie, H. Li, P. Li, X. Zhou, ACS Catal. 1 (2011) 1604.
- [122] Y.K. Park, S.B. Choi, H.J. Nam, D.-Y. Jung, H.C. Ahn, K. Choi, H. Furukawa, J. Kim, Chem. Commun. 46 (2010) 3086.
- [123] Y. Huang, Z. Lin, R. Cao, Chem.-Eur. J. 17 (2011) 12706.
- [124] L. Rimai, J.H. Visser, E.M. Logothetis, A. Samman, in: Polym. Sens., American Chemical Society, 1998, p. 102.
- [125] D. Wencel, T. Abel, C. McDonagh, Anal. Chem. 86 (2014) 15.
- [126] S. Joo, R.B. Brown, Chem. Rev. 108 (2008) 638.
- [127] F. Xiao, J. Song, H. Gao, X. Zan, R. Xu, H. Duan, ACS Nano 6 (2012) 100.
- [128] M. Segev-Bar, H. Haick, ACS Nano 7 (2013) 8366.
- [129] L.E. Kreno, K. Leong, O.K. Farha, M. Allendorf, R.P. Van Duyne, J.T. Hupp, Chem. Rev. 112 (2012) 1105.
- [130] J. Lei, R. Qian, P. Ling, L. Cui, H. Ju, TrAC Trends Anal. Chem. 58 (2014) 71.
- [131] M. Dincă, J.R. Long, J. Am. Chem. Soc. 127 (2005) 9376.
- [132] B. Sharma, R.R. Frontier, A.-I. Henry, E. Ringe, R.P. Van Duyne, Mater. Today 15 (2012) 16.
- [133] M. Schierhorn, S.J. Lee, S.W. Boettcher, G.D. Stucky, M. Moskovits, Adv. Mater. 18 (2006) 2829.
- [134] Y. Sawai, B. Takimoto, H. Nabika, K. Ajito, K. Murakoshi, J. Am. Chem. Soc. 129 (2007) 1658.
- [135] Y. Zhao, N. Kormienko, Z. Liu, C. Zhu, S. Asahina, T.-R. Kuo, W. Bao, C. Xie, A. Hexemer, O. Terasaki, P. Yang, O.M. Yaghi, J. Am. Chem. Soc. 137 (2015) 2199.
- [136] Z. Xu, L. Yang, C. Xu, Anal. Chem. 87 (2015) 3438.
- [137] W. Zhan, Q. Kuang, J. Zhou, X. Kong, Z. Xie, L. Zheng, J. Am. Chem. Soc. 135 (2013) 1926.
- [138] D. Buso, J. Jasieniak, M.D.H. Lay, P. Schiavuta, P. Scopece, J. Laird, H. Amenitsch, A.J. Hill, P. Falcaro, Small 8 (2012) 80.
- [139] P. Falcaro, F. Normandin, M. Takahashi, P. Scopece, H. Amenitsch, S. Costacurta, C.M. Doherty, J.S. Laird, M.D.H. Lay, F. Lisi, A.J. Hill, D. Buso, Adv. Mater. 23 (2011) 3901.
- [140] J.-R. Li, J. Sculley, H.-C. Zhou, Chem. Rev. 112 (2012) 869.
- [141] L. He, Y. Liu, J. Liu, Y. Xiong, J. Zheng, Y. Liu, Z. Tang, Angew. Chem. Int. Ed. 52 (2013) 3741.
- [142] D. Zhao, X. Wan, H. Song, L. Hao, Y. Su, Y. Lv, Sens. Actuators B Chem. 197 (2014) 50.
- [143] G. Lu, J.T. Hupp, J. Am. Chem. Soc. 132 (2010) 7832.
- [144] P. Innocenzi, L. Malfatti, P. Falcaro, Water Droplets to Nanotechnology, RSC Publishing, Cambridge, UK, 2013.
- [145] O. Shekha, H. Wang, S. Kowarik, F. Schreiber, M. Paulus, M. Tolan, C. Sternemann, F. Evers, D. Zacher, R.A. Fischer, C. Wöll, J. Am. Chem. Soc. 129 (2007) 15118.
- [146] G. Lu, O.K. Farha, L.E. Kreno, P.M. Schoenoecker, K.S. Walton, R.P. Van Duyne, J.T. Hupp, Adv. Mater. 23 (2011) 4449.
- [147] Y. Wu, F. Li, Y. Xu, W. Zhu, C. Tao, J. Cui, G. Li, Chem. Commun. 47 (2011) 10094.
- [148] R. Ameloot, M.B.J. Roelofs, G. De Cremer, F. Vermoortele, J. Hofkens, B.F. Sels, D.E. De Vos, Adv. Mater. 23 (2011) 1788.
- [149] Y. Wu, F. Li, W. Zhu, J. Cui, C. Tao, C. Lin, P.M. Hannam, G. Li, Angew. Chem. Int. Ed. 50 (2011) 12518.
- [150] R. Ameloot, E. Gobechiya, H. Uji-i, J.A. Martens, J. Hofkens, L. Alaerts, B.F. Sels, D.E. De Vos, Adv. Mater. 22 (2010) 2685.
- [151] C. Cui, Y. Liu, H. Xu, S. Li, W. Zhang, P. Cui, F. Huo, Small 10 (2014) 3672.
- [152] F.M. Hinterholzinger, A. Ranft, J.M. Feckl, B. Rühle, T. Bein, B.V. Lotsch, J. Mater. Chem. 22 (2012) 10356.
- [153] Z. Hu, C. Tao, F. Wang, X. Zou, J. Wang, J. Mater. Chem. C 3 (2015) 211.
- [154] A. Ranft, F. Niekiel, I. Pavlichenko, N. Stock, B.V. Lotsch, Chem. Mater. 27 (2015) 1961.
- [155] G. Lu, O.K. Farha, W. Zhang, F. Huo, J.T. Hupp, Adv. Mater. 24 (2012) 3970.
- [156] J. Liu, E. Redel, S. Walheim, Z. Wang, V. Oberst, J. Liu, S. Heissler, A. Welle, M. Moosmann, T. Scherer, M. Bruns, H. Gliemann, C. Wöll, Chem. Mater. 27 (2015) 1991.
- [157] J. Cui, N. Gao, C. Wang, W. Zhu, J. Li, H. Wang, P. Seidel, B.J. Ravoo, G. Li, Nanoscale 6 (2014) 11995.
- [158] E. Zanchetta, L. Malfatti, R. Ricco, M.J. Styles, F. Lisi, C.J. Coghlan, C.J. Doonan, A.J. Hill, G. Brusatin, P. Falcaro, Chem. Mater. 27 (2015) 690.
- [159] Q.-R. Fang, D.-Q. Yuan, J. Sculley, J.-R. Li, Z.-B. Han, H.-C. Zhou, Inorg. Chem. 49 (2010) 11637.
- [160] E. Tahmasebi, M.Y. Masoomi, Y. Yamini, A. Morsali, Inorg. Chem. 54 (2015) 425.
- [161] X. Zhu, B. Li, J. Yang, Y. Li, W. Zhao, J. Shi, J. Gu, ACS Appl. Mater. Interfaces 7 (2015) 223.
- [162] M. Majumder, P. Sheath, J.I. Mardel, T.G. Harvey, A.W. Thornton, A. Gonzago, D.F. Kennedy, I. Madsen, J.W. Taylor, D.R. Turner, M.R. Hill, Chem. Mater. 24 (2012) 4647.
- [163] C.W. Abney, K.M.L. Taylor-Pashow, S.R. Russell, Y. Chen, R. Samantary, J.V. Lockard, W. Lin, Chem. Mater. 26 (2014) 5231.
- [164] J.B. DeCoste, G.W. Peterson, Chem. Rev. 114 (2014) 5695.
- [165] R. Ricco, L. Malfatti, M. Takahashi, A.J. Hill, P. Falcaro, J. Mater. Chem. A 1 (2013) 13033.
- [166] M.R. Lohe, K. Gedrich, T. Freudenberg, E. Kockrick, T. Dellmann, S. Kaskel, Chem. Commun. 47 (2011) 3075.
- [167] C.M. Doherty, E. Knystautes, D. Buso, L. Villanova, K. Konstas, A.J. Hill, M. Takahashi, P. Falcaro, J. Mater. Chem. 22 (2012) 11470.
- [168] S.-H. Huo, X.-P. Yan, Analyst 137 (2012) 3445.
- [169] A. Carné-Sánchez, I. Imaz, M. Cano-Sarabia, D. Maspoch, Nat. Chem. 5 (2013) 203.
- [170] L. Järup, Br. Med. Bull. 68 (2003) 167.
- [171] G.W. Bryan, W.J. Langston, Environ. Pollut. 76 (1992) 89.
- [172] M.R. Sohrabi, Z. Matbouie, A.A. Asgharinezhad, A. Dehghani, Microchim. Acta 180 (2013) 589.
- [173] Y. Wang, J. Xie, Y. Wu, H. Ge, X. Hu, J. Mater. Chem. A 1 (2013) 8782.
- [174] M. Taghizadeh, A.A. Asgharinezhad, M. Pooladi, M. Barzin, A. Abbaszadeh, A. Tadjarodi, Microchim. Acta 180 (2013) 1073.
- [175] P. Falcaro, F. Lapierre, B. Marmiroli, M. Styles, Y. Zhu, M. Takahashi, A.J. Hill, C.M. Doherty, J. Mater. Chem. C 1 (2012) 42.
- [176] A. Bagheri, M. Taghizadeh, M. Behbahani, A. Akbar Asgharinezhad, M. Salarian, A. Dehghani, H. Ebrahimezhad, M.M. Amini, Talanta 99 (2012) 132.
- [177] E.I. Cedillo-González, R. Ricco, M. Montorsi, M. Montorsi, P. Falcaro, C. Siligardi, Build. Environ. 71 (2014) 7.
- [178] M. Pelaez, N.T. Nolan, S.C. Pillai, M.K. Seery, P. Falaras, A.G. Kontos, P.S.M. Dunlop, J.W.J. Hamilton, J.A. Byrne, K. O'Shea, M.H. Entezari, D.D. Dionysiou, Appl. Catal. B Environ. 125 (2012) 331.
- [179] Y. Hu, Z. Huang, L. Zhou, D. Wang, G. Li, J. Sep. Sci. 37 (2014) 1482.
- [180] T. Zeng, X. Zhang, S. Wang, H. Niu, Y. Cai, Environ. Sci. Technol. 49 (2015) 2350.
- [181] Z. Zhang, Y. Chen, X. Xu, J. Zhang, G. Xiang, W. He, X. Wang, Angew. Chem. Int. Ed. 53 (2014) 429.
- [182] Z.-Y. Gu, C.-X. Yang, N. Chang, X.-P. Yan, Acc. Chem. Res. 45 (2012) 734.
- [183] M. Palomino, A. Cantón, A. Corma, S. Leiva, F. Rey, S. Valencia, Chem. Commun. (2007) 1233.
- [184] M.E. Silvestre, M. Franzreb, P.G. Weidler, O. Shekha, C. Wöll, Adv. Funct. Mater. 23 (2013) 1210.
- [185] R.C. Huxford, J. Della Rocca, W. Lin, Curr. Opin. Chem. Biol. 14 (2010) 262.
- [186] P. Horcajada, R. Gref, T. Baati, P.K. Allan, G. Maurin, P. Couvreur, G. Férey, R.E. Morris, C. Serre, Chem. Rev. 112 (2012) 1232.
- [187] P. Horcajada, T. Chalati, C. Serre, B. Gillet, C. Sebrie, T. Baati, J.F. Eubank, D. Heurtaux, P. Clayette, C. Kreuz, J.-S. Chang, Y.K. Hwang, V. Marsaud, P.-N. Bories, L. Cynober, S. Gil, G. Férey, P. Couvreur, R. Gref, Nat. Mater. 9 (2010) 702.

Metal–Organic Frameworks

Synthesis, Culture Medium Stability, and In Vitro and In Vivo Zebrafish Embryo Toxicity of Metal–Organic Framework Nanoparticles

Àngels Ruyra,^[a, b] Amiralí Yazdí,^[a] Jordi Espín,^[a] Arnau Carné-Sánchez,^[a] Nerea Roher,^[b] Julia Lorenzo,^[b, c] Inhar Imaz,^[a] and Daniel MasPOCH^{*, [a, d]}

Abstract: Metal–organic frameworks (MOFs) are among the most attractive porous materials available today. They have garnered much attention for their potential utility in many different areas such as gas storage, separation, catalysis, and biomedicine. However, very little is known about the possible health or environmental risks of these materials. Here, the results of toxicity studies on sixteen representative uncoated MOF nanoparticles (nanoMOFs), which were assessed for cytotoxicity to HepG2 and MCF7 cells in vitro, and for

toxicity to zebrafish embryos in vivo, are reported. Interestingly, there is a strong correlation between their in vitro toxicity and their in vivo toxicity. NanoMOFs were ranked according to their respective in vivo toxicity (in terms of the amount and severity of phenotypic changes observed in the treated zebrafish embryos), which varied widely. Altogether these results show different levels of toxicity of these materials; however, leaching of solubilized metal ions plays a main role.

Introduction

Metal–organic frameworks (MOFs) are porous materials built from the controlled crystallization of metal ions or higher nuclearity metal clusters with multifunctional organic ligands.^[1–3] When assembled at the nanoscale, they are called nanoMOFs. Analogously to other classes of nanoparticles, nanoMOFs show size-dependent properties (e.g., different adsorption kinetics or better dispersibility compared with their bulk analogues),^[1] which can be exploited in numerous practical applications, in-

cluding traditional storage^[4] and catalysis,^[5,6] and in newer areas such as sensors,^[7] functional membranes and thin-films,^[8,9] and in biomedical applications such as drug-delivery,^[10–12] NO absorption,^[13,14] and contrast agents.^[15] The ever-increasing interest in nanoMOFs (and in their bulk analogues) should ultimately lead to their widespread production and use. However, little is known about the safety of these nanomaterials to humans and to the environment. Thus, before any nanoMOF can be adopted for practical use, its Environmental Health and Safety (EHS) profile must be determined.

Prior to the work we report here, other groups had already explored the in vitro toxicity of certain bare nanoMOFs in cells. In 2008, Lin et al. assayed the cytotoxicity of amorphous disuccinato-cisplatin/Tb^{III} nanoparticles (size: ca. 60 nm) to HT-29 human colon adenocarcinoma cells, observing no appreciable cytotoxicity.^[16] Starting in 2010, Horcajada, Gref, Serre et al. evaluated the in vitro toxicity of several Fe^{III}-based nanoMOFs (e.g., nanoMIL-53, nanoMIL-88, nanoMIL-100, and nanoMIL-101; size: 90–200 nm) to various cell lines, including mouse macrophage J774.A1, human leukemia (CCRF-CEM), human multiple myeloma (RPMI-8226) and human cervical adenocarcinoma (HeLa) cells, and low cytotoxicities were generally found.^[10,17–20] Roughly in parallel, Junior et al. assayed nanoZIF-8 (size: 200 nm) against three human cell lines (mucoepidermoid carcinoma of lung [NCI-H292], colorectal adenocarcinoma [HT-29], and promyelocytic leukemia [HL-60]), and found that at the highest tested concentration (109 μM), it was not cytotoxic to any of them.^[11] However, Horcajada et al. recently observed cytotoxicity of nanoZIF-8 (size: 90 nm) to HeLa and J774 cell lines, reporting IC₅₀ values of 436 and 109 μM, respectively.^[18] They also reported that Zr^{IV}-based UiO-66 (size:

[a] Dr. À. Ruyra,^{*} A. Yazdí,^{*} J. Espín,^{*} Dr. A. Carné-Sánchez, Dr. I. Imaz, Prof. Dr. D. MasPOCH
ICN2 (ICN-CSIC)
Institut Català de Nanociència i Nanotecnologia
Esfera UAB, 08193 Bellaterra, Barcelona (Spain)
E-mail: daniel.masPOCH@icn.cat

[b] Dr. À. Ruyra,^{*} Dr. N. Roher, Dr. J. Lorenzo
Institut de Biotecnologia i de Biomedicina
Parc de Recerca UAB
Campus Universitat Autònoma de Barcelona
08193 Bellaterra, Barcelona (Spain)

[c] Dr. J. Lorenzo
Departament de Bioquímica i de Biologia Molecular
Campus Universitat Autònoma de Barcelona
08193 Bellaterra, Barcelona (Spain)

[d] Prof. Dr. D. MasPOCH
Institució Catalana de Recerca
i Estudis Avançats (ICREA)
08100 Barcelona (Spain)

[*] These authors contributed equally.

Supporting information for this article is available on the WWW under <http://dx.doi.org/10.1002/chem.201405380>.

100 nm) was more toxic, showing IC_{50} values of 239 (HeLa) and $36 \mu\text{M}$ (J774).

The aforementioned results were obtained from *in vitro* studies only. Importantly, the only *in vivo* studies on nanoMOFs reported to date were done in Wistar female rats.^[10,20] In these studies, the rats were given one of three Fe^{III} -based nanoMOFs (nanoMIL-88, nanoMIL-100, or nanoMIL-101) by intravenous injection, and subsequently analyzed for various parameters (e.g., serum, enzymatic, histological, etc.). The results revealed a lack of severe acute or sub-acute toxicity.

In this communication, we report combined *in vitro* (HepG2 and MCF7 cells) and *in vivo* (zebrafish embryos) studies on the toxicity of sixteen archetypical, uncoated nanoMOFs. As shown in Figure 1, the selected nanoMOFs comprise: MIL-100 [$\text{Fe}_3\text{O}(\text{H}_2\text{O})_2\text{Cl}(\text{btc})_2$] (**1**; btc: 1,3,5-benzenetricarboxylic acid);^[21] MIL-101 [$\text{Fe}_3\text{Cl}(\text{H}_2\text{O})_2\text{O}(\text{NH}_2\text{-bdc})_3$] (**2**; $\text{NH}_2\text{-bdc}$: 2-aminobenzene-1,4-dicarboxylic acid);^[22] MOF-5 [$\text{Zn}_4\text{O}(\text{bdc})_3$] (**3**; bdc: 1,4-benzenedicarboxylic acid);^[23] and MOF-74 (also called CPO-27 family) [$\text{M}_2(\text{dhbdc})$] (**4–9**; M: Zn^{II} , Cu^{II} , Ni^{II} , Co^{II} , Mn^{II} , and Mg^{II} ; dhbdc: 2,5-dihydroxy-1,4-benzenedicarboxylic acid);^[24] ZIF-7 [$\text{Zn}(\text{Ph-im})_2$] (**10**; Ph-im: benzylimidazole);^[25] ZIF-8 [$\text{Zn}(\text{Me-im})_2$] (**11**; Me-im: 2-methylimidazole);^[25] UiO-66 [$\text{Zr}_6\text{O}_4(\text{OH})_4(\text{bdc})_6$] (**12**); UiO-66- NH_2 [$\text{Zr}_6\text{O}_4(\text{OH})_4(\text{NH}_2\text{-bdc})_6$] (**13**);^[26] UiO-67 [$\text{Zr}_6\text{O}_4(\text{OH})_4(\text{bpdc})_6$] (**14**; bpdc: biphenyl-4,4'-dicarboxylic acid);^[26] HKUST-1 [$\text{Cu}_3(\text{btc})_2$] (**15**);^[27] and NOTT-100 (also called MOF-505) [$\text{Cu}_2(\text{bptc})$] (**16**; bptc: 3,3',5,5'-biphenyl-tetracarboxylic acid).^[28]

We screened the nanoMOFs for cytotoxicity to the two aforementioned cell lines (using standard *in vitro* methodologies), performed *in vivo* studies in zebrafish (as an *in vivo* model appropriate for comparative studies on mammalian biology), and finally the results from each study were compared. Zebrafish is recognized by the National Institute of Environmental Health Science (NIEHS, USA) and the Institute for Environment and Sustainability (IES, Europe) as an excellent system in which to study environmental toxicity,^[29,30] and is accepted by the National Institutes of Health (NIH, USA) as an alternative model for exploring human diseases.^[29–31] Furthermore, zebrafish embryo assays do not raise major ethical questions regarding vertebrate experimentation. Based on our results, we ranked the nanoMOFs according to their *in vivo* toxicity (in terms of the amount and severity of phenotypic changes in the treated zebrafish embryos). We found that this ranking parallels the *in vitro* toxicity rankings for both cell lines, and that the toxicity depends strongly on the solubility of the nanoMOFs and on their subsequent release of metal ions.

Results and Discussion

Synthesis and characterization of the nanoMOF library

We and other groups have previously reported several methods for synthesizing nanoMOFs.^[1,32,33] By using solvo- and

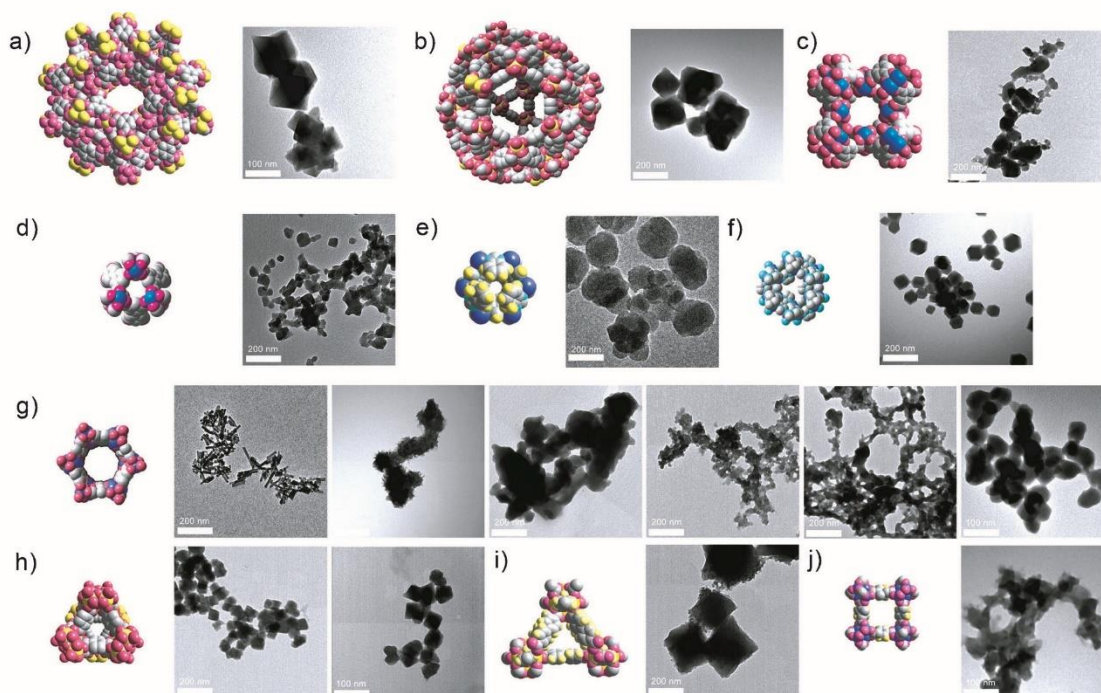


Figure 1. Representation of the crystal structures and corresponding TEM images of the synthesized nanoMOFs: a) nanoMIL-100; b) nanoMIL-101; c) nanoHKUST-1; d) nanoNOTT-100; e) nanoZIF-7; f) nanoZIF-8; g) the nanoM-MOF-74 family (from left to right, M = Co, Ni, Mg, Cu, Mn and Zn); h) nanoUiO-66 (left) and nanoUiO-66- NH_2 (right); i) nanoUiO-67; and j) nanoMOF-5.

hydro-thermal reactions reported previously, we prepared the following nanoMOFs: nanoMIL-100 (size: 143 ± 23 nm), nanoMIL-101 (size: 170 ± 50 nm), nanoM-MOF-74s ($M = \text{Zn}^{\text{II}}$; size: 35 ± 9 nm; $M = \text{Cu}^{\text{II}}$, size: 20 ± 8 nm; $M = \text{Ni}^{\text{II}}$, size: 111 ± 38 nm; $M = \text{Co}^{\text{II}}$, size: 112 ± 26 nm; $M = \text{Mn}^{\text{II}}$, size: 51 ± 18 nm; $M = \text{Mg}^{\text{II}}$, size: 122 ± 34 nm), nanoUiO-66 (size: 66 ± 34 nm), nanoUiO-66-NH₂ (size: 73 ± 32 nm), and nanoUiO-67 (size: 180 ± 30 nm). We employed fast precipitation to prepare nanoZIF-8 (size: 80 ± 15 nm) in water, nanoZIF-7 (size: 170 ± 20 nm) in *N,N*-dimethylformamide (DMF), and nanoMOF-5 (size: 85 ± 34 nm) in DMF; the latter, by slowly adding a base into the precursor solution. Finally, we used our recently developed spray-drying technique^[34] to synthesize nanoHKUST-1 (size: 75 ± 28 nm) and nanoNOTT-100 (size: 45 ± 18 nm). Details on all the syntheses are provided in the Supporting Information.

Once synthesized, all the nanoMOFs were cleaned to remove any impurities (including trace amounts of toxic solvents from the syntheses), dried at 80 °C overnight, and finally redispersed in dimethyl sulfoxide (DMSO) to form stable colloids (concentrations: 25 to 100 mM) for the *in vitro* and *in vivo* toxicity studies. Transmission electron microscopy (TEM; Figure 1) and X-ray powder diffraction (XRPD) of the resulting colloids demonstrated that all selected nanoMOFs were obtained as homogeneous nanoscale crystals and that their XRPD patterns were fully coincident with the simulated patterns calculated from atomic coordinates (see Figure S1 in the Supporting Information). In addition, all colloidal dispersions were characterized by dynamic light scattering (DLS) studies to confirm the crystal size measured from the TEM images, as well as the homogeneity of each sample and the absence of any aggregation of the nanocrystals in solution (see Figures S2 and S3 in the Supporting Information).

Stability of the nanoMOFs in culture medium

The stability of all the nanoMOFs in the culture medium containing 10% fetal bovine serum (FBS) was studied. Each nanoMOF colloid was separately dispersed in the medium at a final concentration of 10 mM, and then incubated at 37 °C for 24 h. The resulting solids were then collected by centrifugation, dried, weighed, and finally characterized by XRPD.

The robustness of the crystal structure of each nanoMOF was evaluated by comparing the initial and final XRPD spectra (see Figure S4 in the Supporting Information). Furthermore, the XRPD spectra were used to check for any other crystalline species that might have formed in the event that the nanoMOFs had degraded. Each supernatant was also characterized by inductively coupled plasma-optical emission spectrometry (ICP-OES) to estimate the amount of metal ion that had leaked from the nanoMOF and dissolved into the culture medium. Table 1 shows all the values extracted from this study. These data clearly indicate that all the nanoMOFs were at least partially soluble in the culture medium, although the degree of solubility varied widely by structure. The data also reveal that some of the nanoMOFs had become amorphous in the culture medium, having undergone structural rearrangements and/or reactions that generated new inorganic species.

Table 1. NanoMOFs classified according to their degradation in the culture medium containing 10% fetal bovine serum (FBS).

nanoMOF	[M _i] [μM] ^[a]	Deg _{min} [%] ^[b]	XRPD analysis
UiO-67	215.6 ± 6.3	0.3 ± 0.0	amorphous
MIL-100	316.2 ± 46.1	1.1 ± 0.2	stable
MIL-101	310.4 ± 90.1	1.1 ± 0.3	amorphous
UiO-66	1099.8 ± 105.3	1.8 ± 0.2	stable
UiO-66-NH ₂	1567.5 ± 183.1	2.6 ± 0.3	stable
ZIF-7	448.5 ± 23.4	4.5 ± 0.2	stable
MOF-5	3108.6 ± 634.1	7.8 ± 1.6	new crystalline species
Mn-MOF-74	2651.4 ± 73.6	13.3 ± 0.4	loss of crystallinity; new crystalline species (MnCO ₃)
Co-MOF-74	3258.1 ± 58.8	16.2 ± 0.3	loss of crystallinity
ZIF-8	1916.2 ± 75.4	19.1 ± 0.8	stable
Zn-MOF-74	5442.6 ± 130.6	27.2 ± 0.5	stable
HKUST-1	9168.6 ± 137.5	30.3 ± 0.5	loss of crystallinity
Ni-MOF-74	7014.3 ± 174.9	35.1 ± 0.9	stable
NOTT-100	7967.5 ± 152.8	39.4 ± 0.8	loss of crystallinity
Cu-MOF-74	9556.8 ± 689.9	47.9 ± 3.4	loss of crystallinity
Mg-MOF-74	12573.7 ± 273.9	62.9 ± 1.4	loss of crystallinity

[a] The concentration of the corresponding metal ions solubilized after the incubation of each nanoMOF at 37 °C for 24 h was determined by ICP-OES. [b] The minimum percentage of degradation (deg_{min}(%)) was calculated as follows: deg_{min}(%) = ([M_i] · V · S) / n_{MOF}; where V is the volume of DMEM, S is the stoichiometric ratio of nanoMOF to metal ion, and n_{MOF} is the number of moles of initial nanoMOF.

The most soluble nanoMOF in the culture medium was nanoMg-MOF-74 (12573 ± 274 μM Mg^{II}), which corresponds to 62.9% of its constituent Mg^{II}, and the least soluble, nanoUiO-67 (216 ± 6 μM Zr^{IV}), which corresponds to 0.3% of its constituent Zr^{IV}. Despite their vastly different levels of solubility, they each lost crystallinity and became amorphous upon contact with the culture medium.

NanoZIF-7 was poorly soluble in culture medium (449 ± 23 μM dissolved Zn^{II} ions, corresponding to 4.5% of its constituent Zn^{II}), whereas nanoZIF-8 was more soluble, showing a leakage of 1916 ± 75 μM Zn^{II} (19.1% of its constituent Zn^{II}). Interestingly, after incubation of each one in the culture medium, their respective crystal structures remained unaltered. NanoUiO-66 and nanoUiO-66-NH₂ were also very stable (see Figure S4), having released only 1100 ± 105 μM Zr^{IV} (1.8% of the constituent Zr^{IV}) and 1568 ± 183 μM of Zr^{IV} (2.6% of the constituent Zr^{IV}), respectively. In the case of nanoMIL-100 and nanoMIL-101, the concentrations of dissolved Fe^{III} ions were only 316 ± 46 μM Fe^{III} (1.1% of the constituent Fe^{III}) and 310 ± 90 μM (1.1% of the constituent Fe^{III}), respectively. Although upon incubation both compounds became amorphous, upon subsequent exposure to ethanol, nanoMIL-100 recovered its crystallinity, which confirmed the robustness of its framework (see Figure S4).

The two Cu^{II}-based nanoMOFs (nanoHKUST-1 and nanoNOTT-100) were relatively soluble, releasing 9169 ± 138 μM Cu^{II} (30.3% of its constituent Cu^{II}) and 7968 ± 153 μM Cu^{II} (39.4% of its constituent Cu^{II}). This degradation was clearly accompanied by a loss of crystallinity, which, in the XRPD patterns, is evidenced by the disappearance of most of the char-

acteristic peaks. Similarly, the nanoM-MOF-74 family exhibited moderate to high solubility: nanoCu-MOF-74 released $9557 \pm 690 \mu\text{M}$ Cu^{II} (47.9% of its constituent Cu^{II}); nanoNi-MOF-74, $7014 \pm 175 \mu\text{M}$ Ni^{II} (35.1% of its constituent Ni^{II}); nanoZn-MOF-74, $5443 \pm 131 \mu\text{M}$ Zn^{II} (27.2% of its constituent Zn^{II}); nanoCo-MOF-74, $3258 \pm 59 \mu\text{M}$ Co^{II} (16.2% of its constituent Co^{II}); and nanoMn-MOF-74, $2651 \pm 74 \mu\text{M}$ Mn^{II} (13.3% of its constituent Mn^{II}). Upon incubation in the culture medium, all of these nanoMOFs suffered a loss of crystallinity, with nanoCu-MOF-74, nanoCo-MOF-74, and nanoMn-MOF-74 exhibiting the greatest loss.

We would like to note that the proportion of metal ion (relative to the constituent amount of the tested nanoMOF) found in solution cannot always be directly related to the degradation of the nanoMOF. This is because degradation sometimes leads to formation of new, insoluble species. In our study, such species—provided that they were crystalline—were detectable by XPRD. Such was the case with nanoMn-MOF-74, the XPRD spectrum of which after incubation in culture medium indicated the formation of MnCO_3 (see Figure S5 in the Supporting Information). The formation of MnCO_3 was further studied by analyzing the powder resulting from the incubation, which confirmed the generation of new (rod-like) particles (see Figure S5). Electron-diffraction analysis (by TEM) of one of these particles revealed a diffraction that was pattern identical to that expected for MnCO_3 (see Figure S5). Formation of new species was also observed in the XPRD patterns for nanoCo-MOF-74, nanoMg-MOF-74, and nanoMOF-5. Unfortunately, in those cases, the new species could not be identified. NanoMOF-5 released $3108 \pm 634 \mu\text{M}$ Zn^{II} (7.8% of its constituent Zn^{II}), but its XPRD spectrum revealed the formation of a new, insoluble crystalline species, and lacked the characteristic peak of nanoMOF-5 itself (see Figure S4).

Given the above findings, we reasoned that the percentage of solubilized metal ions relative to the constituent amount of the tested nanoMOF represents the minimum percentage of degradation, because the ions might have further reacted to form insoluble species in the culture medium. Here, we would like to mention that four of the most structurally robust nanoMOFs (nanoMIL-100, nanoMIL-101, nanoUiO-66, and nanoUiO-66-NH₂) actually underwent greater degradation in culture medium than that detected by analyzing the solubilized metal ions. In these cases, the weight-loss values (calculated by comparing the post- and pre-weight values, and expressed as a percentage) were much higher than were the corresponding values for relative percentage of solubilized metal ions: $25.8 \pm 2.5\%$ for nanoMIL-100 (1.1%); $10.3 \pm 4.1\%$ for nanoMIL-101 (1.1%); $14.7 \pm 0.3\%$ for nanoUiO-66 (1.8%); and $10.1 \pm 0.8\%$ for nanoUiO-66-NH₂ (2.6%). We have tentatively attributed these differences to insoluble, amorphous metal-containing species resulting from the reaction of the released metal ions in the cell culture media. In fact, this phenomenon has previously been observed for Zn^{II} metal ions in cell culture media: for instance, ZnO nanoparticles have been reported to release Zn^{II} into cell culture media or serum, which then rapidly reacts to form a poorly soluble, amorphous nanostructured Zn^{II} -carbonate-phosphate precipitate.^[35,36]

In vitro cytotoxicity of the nanoMOF components

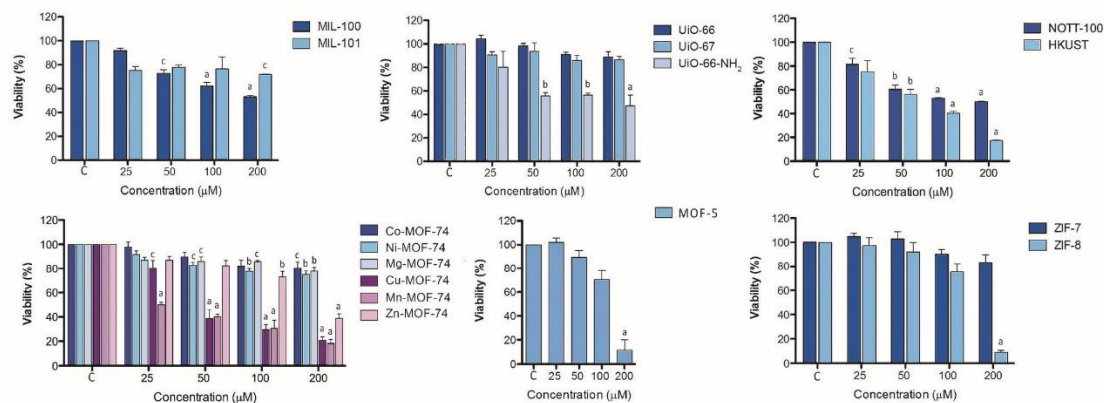
The cytotoxicity of each organic ligand and each metal ion (as a chloride salt; except for MgSO_4) used to build the nanoMOFs was individually evaluated in HepG2 cells, using the XTT assay. The cells were exposed to a single organic ligand or metal salt at doses ranging from 1 to 200 μM for 24 h (see Figure S6 and S7). None of the organic ligands showed any significant cytotoxicity, even at the highest dose, nor did the Co^{II} , Ni^{II} , Zn^{II} , Zr^{IV} or Mg^{II} salts: cell viabilities were greater than 75% in all cases. In contrast, the Cu^{II} and Mn^{II} salts exhibited high cytotoxicity, even at low doses (5 to 10 μM); and Fe^{III} showed moderate to high cytotoxicity from 25 to 200 μM , respectively.

In vitro cytotoxicity of the nanoMOFs

The effect of each nanoMOF on cell viability was tested in HepG2 cells and in MCF7 cells using the XTT assay, at doses ranging from 25 to 200 μM , for 24 h and 72 h. Firstly, prior to the assay, the DMSO colloid of a given nanoMOF was mixed with the cell culture medium. We would like to mention that the formation and use of these colloids is an intermediate but necessary step for minimizing any possible aggregation of nanoMOFs in the cell-culture medium. However, despite this step, many of the nanoMOFs still gradually agglomerated in both media, forming soft agglomerates. Thus, under these conditions, we were unable to differentiate between toxicity arising from single nanocrystals of each nanoMOF and toxicity arising from their corresponding agglomerates.

For most of the nanoMOFs, their respective cytotoxicity depended on the cell type and on the concentration (see Figure 2 and Figure S8 in the Supporting Information). Interestingly, some of the nanoMOFs (Co-MOF-74, Mg-MOF-74, UiO-66, and UiO-67) showed little or no cytotoxicity, even at the highest dose (200 μM). Within the nanoMOF-74 family, the cytotoxicity of each member varied according to the metal component (Figure 2): those containing Co, Ni or Mg showed no marked cytotoxicity to either of the cell lines after 24 h of incubation, whereas those containing Cu, Mn or Zn showed high levels of cytotoxicity at the highest dose (200 μM). The viability levels observed in the cells exposed to the latter were $20.9 \pm 2.7\%$ (HepG2) and $38.2 \pm 0.3\%$ (MCF7) for nanoCu-MOF-74; $18.3 \pm 3.0\%$ (HepG2) and $32.4 \pm 3.8\%$ (MCF7) for nanoMn-MOF-74; and $38.8 \pm 3.6\%$ (HepG2) and $57.6 \pm 0.6\%$ (MCF7) for nanoZn-MOF-74. These results were generally consistent with those observed at 72 h (see Figure S8), although some differences were identified. For example, the cytotoxicity of nanoNi-MOF-74 to MCF7 cells was higher after 72 h, whereas that of nanoCu-MOF-74 to the same cells, and that of nanoZn-MOF-74 to HepG2 cells, were each lower after 72 h. NanoMIL-100 and -101 showed little to moderate toxicity to each cell line after 24 and 72 h. However, at its highest dose (200 μM) and 24 h incubation, nanoMIL-100 provoked a substantial decrease ($53.2 \pm 1.0\%$) in the viability of the HepG2 cells. After 72 h, nanoMIL-101 also led to a decrease in the viability ($41.8 \pm 7.3\%$) of HepG2 cells. None of the nanoUiO MOFs exhibited substantial cytotoxicity at either incubation time, except for

HepG2



MCF7

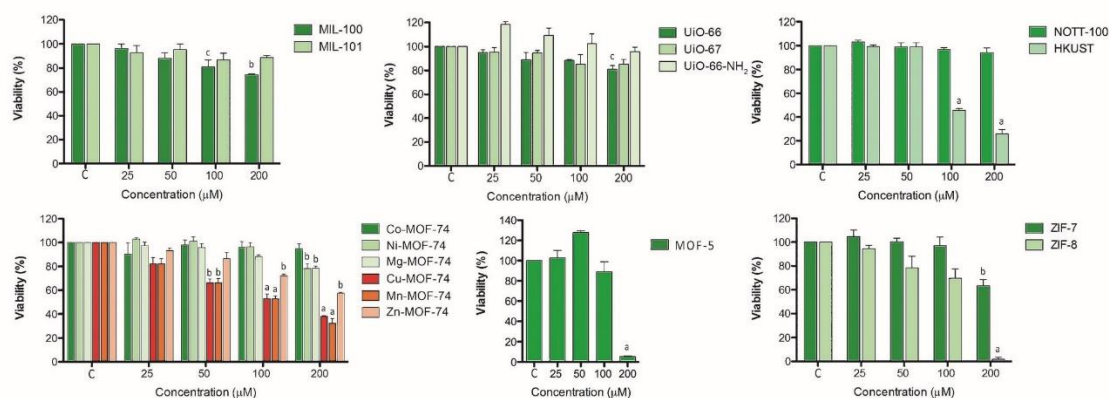


Figure 2. In vitro cytotoxicity of nanoMOFs to human cells. Cell viability of MCF7 or HepG2 cells after 24 h incubation with a single nanoMOF at one of various concentrations (25 to 200 μM). Untreated cells were used as controls (marked as C). Data represent the mean \pm standard error of the mean (SEM) of three independent experiments. Significant differences from the control are marked accordingly (^a $p < 0.05$, ^b $p < 0.01$, ^c $p < 0.005$).

nanoUiO-66-NH₂ at the highest dose (200 μM) and 24 h incubation, this material showed moderate cytotoxicity to HepG2 cells ($47.2 \pm 9.4\%$ viability). The results for the nanoZIF family of MOFs varied widely: nanoZIF-7 was not cytotoxic to the HepG2 cells and moderately cytotoxic to the MCF7 cells, whereas nanoZIF-8 was highly cytotoxic to both. Both nanoHKUST-1 and nanoNOTT-100 were highly cytotoxic to both cell lines at both incubation times: for example, at 200 μM and 24 h incubation, nanoHKUST-1 was highly toxic to HepG2 cells ($17.4 \pm 0.5\%$ viability). The only exception was nanoNOTT-100 at 200 μM after 24 h incubation in MCF7 cells ($94.2 \pm 4.0\%$ viability). Lastly, at 200 μM and 24 or 72 h incubation time, nanoMOF-5 was highly cytotoxic to both cell lines.

The toxicity of nanomaterials is widely accepted to derive from their chemical composition, through mechanisms such as dissolution and consequent release of toxic components (e.g., metal ions) or generation of reactive oxygen species, and/or to stress or stimuli caused by their surface reactivity, their size

and/or their shape.^[37] Although distinguishing between these mechanisms is not trivial, our results indicate that the toxicity of nanoMOF crystals is strongly related to their solubility and, therefore, to the release of solubilized (toxic) metal ions.

The solubility tests on the sixteen nanoMOFs confirmed that they are all at least partially soluble in cell culture media and show minimum percentage of degradation in solution, ranging from 0.3% (nanoUiO-67) to 62.9% (nanoMg-MOF-74). This degradation induces the release of their constituent metal ions and organic ligands into the media.

Given that free metal ions, rather than free organic ligands, have previously been imputed as the toxic agents in MOFs,^[18] we focused our attention on the metal ions solubilized in the media. Indeed, we found that the most cytotoxic nanoMOFs in our assays were those that released sufficiently high amounts of soluble metal ions known to be moderately or highly cytotoxic in their free form (e.g., Cu^{II}, Mn^{II}, and Fe^{III}). For example, nanoCu-MOF-74, nanoHKUST-1, and nanoNOTT-100, all of

which are built from Cu^{II} ions, were highly soluble and toxic in our tests. We believe that this toxicity, similarly to that observed with other soluble nanomaterials,^[36–40] might be attributed to the release and subsequent cellular uptake of Cu^{II} ions. For example, nanoCu-MOF-74 was highly cytotoxic and provoked a rapid toxic effect: at nanoCu-MOF-74 concentrations of 50 and 100 μM , and 24 h of incubation, the viability of treated HepG2 cells had decreased to approximately 40 and approximately 30%, respectively. This result is consistent with our cytotoxicity studies on free Cu^{II} ions (see Figure S6): for example, at a Cu^{II} concentration of 50 μM and 24 h of incubation, the viability of treated HepG2 cells had dropped to 23.9%. Assuming a similar rate of release of Cu^{II} over the entire range of concentrations, this viability value for Cu^{II} alone corresponds to approximately 50 μM of nanoCu-MOF-74 (47.9% of constituent Cu^{II} lost; 38.7% cell viability for the same incubation time), approximately 55 μM of nanoHKUST-1 (30.3% of constituent Cu^{II} lost; cell viability: < 60%) and approximately 63 μM of nanoNOTT-100 (39.4% of constituent Cu^{II} lost; cell viability: < 60%) (see Figure 2). We observed a similar correlation between the cytotoxicity of free metal ions and the corresponding nanoMOFs in our studies on free Mn^{II} ions and on nanoMn-MOF-74. At the lowest concentration (25 μM) and 24 h of incubation, this nanoMOF caused the viability of HepG2 cells to decrease to 49.9%. At this concentration, a release of approximately 3 μM Mn^{II} (13.3% of the constituent Mn^{II}) would be expected, which would correlated to cell viabilities of between 30 and 70%.

Unlike the aforementioned cases, the nanoMOFs that release significant amounts of soluble metal ions, but whose free constituent metal ion did not show cytotoxicity in the free form at the working concentrations [Co^{II} , Ni^{II} , or Mg^{II}], showed little or no toxicity. These include nanoMg-MOF-74, nanoCo-MOF-74, and nanoNi-MOF-74. Similarly, those nanoMOFs that do not release significant amounts of soluble metal ions showed low cytotoxicity. These include nanoMIL-100, nanoMIL-101, nanoUiO-66, nanoUiO-66- NH_2 , nanoUiO-67, and nanoZIF-7. The only exceptions to this trend were three of the Zn^{II} -based nanoMOFs: nanoZn-MOF-74, nanoZIF-8, and nanoMOF-5. In all three cases, we expected the concentration of Zn^{II} ions released from the nanoMOF to be lower than the maximum working concentration of 200 μM (at which free Zn^{II} ions did not show any significant cytotoxicity; in fact, the in vitro toxic concentration of Zn^{II} ions has been reported to be ca. 400 μM).^[41] However, all three nanoMOFs caused high cytotoxicity at 200 μM . Interestingly, these results are consistent with recent studies on nanoIRMOF-3 that showed cytotoxicity to PC12 cells; in that study, cell viability was approximately 55% at 122 μM and < 20% at 488 μM .^[42] They are also consistent with findings from studies on ZnO or Zn nanoparticles, the toxicity of which could not be imputed solely to their release of Zn^{II} ions into solution.^[43] In fact, several authors have suggested that Zn nanoparticles might generate reactive oxygen species that induce oxidative stress^[36,44–46] or that exhibit body burden or size effects; any of these factors might have contributed to the cytotoxicity that we observed in the Zn^{II} -based nanoMOFs.

In vivo toxicity in zebrafish embryos

We then evaluated the in vivo toxicity of nine of the sixteen nanoMOFs in zebrafish (*Danio rerio*) embryo, and subsequently compared the results to those corresponding to the in vitro assays. Zebrafish embryos have been used extensively to assay the in vivo toxicity of nanoparticles because they are comparable to mammalian systems and amenable to medium-to-high-throughput screening.^[47–50] Zebrafish embryos exposed to different concentrations (1 to 200 μM) of a suspension of a single nanoMOF were assessed for several toxicity parameters every 24 h until 120 h post-fertilization (hpf): these include mortality, hatching rate, and appearance of abnormal phenotypes (e.g., low pigmentation, pericardial/yolk-sac edema, delayed development, bent spine, etc.).

We chose nine nanoMOFs for in vivo evaluation to represent a wide spectrum of cytotoxicity from the in vitro assays, including nontoxic or barely cytotoxic (nanoUiO-66, nanoUiO-67, and nanoCo-MOF-74, and nanoMg-MOF-74), moderately cytotoxic (nanoZIF-7, nanoMIL-100, and nanoMIL-101), and highly cytotoxic (nanoZIF-8 and nanoHKUST-1). To rule out any effects provoked by the 0.5% DMSO present in the three nanoMOF suspensions (1 μM , 20 μM and 200 μM), we also assessed its toxicity. At a final concentration of 0.5% in E3 medium, DMSO was found to have no visible effects on normal larvae development after 120 h exposure: no differences in survival rate, hatching rate, or phenotype were observed between the DMSO-treated group of larvae and the negative (untreated) control group.

Figure 3a shows the cumulative mortality of embryos from the assays. We found that at 120 h post fertilization (hpf), the vast majority of nanoMOFs had not altered embryo viability. Hence, the viabilities of the embryos exposed to nanoCo-MOF-74, nanoMg-MOF-74, nanoUiO-66, nanoUiO-67, nanoMIL-100, and nanoMIL-101 were not significantly different to those of the control (DMSO-treated) group. In contrast, nanoZIF-7, nanoZIF-8, and nanoHKUST-1 provoked significant decreases in embryo survival (Figure 3 and S9). NanoZIF-7 was slightly toxic at 200 μM (embryo viability at 120 hpf: 79.2%); nanoZIF-8 was more toxic at the same concentration (embryo viability at 120 hpf: 33.3%); and nanoHKUST-1 was extremely toxic at this concentration (viability: 0%); in fact, even at 20 μM nanoHKUST-1, none of the embryos treated with this nanoMOF had survived by 48 hpf (viability: 0%).

We quantified the hatching rate of the embryos in the nanoMOF-treated group and the control group. As shown in Figure 3b and c, some of the nanoMOF-treated group exhibited a significant concentration-dependent hatching delay. Many previous studies have reported that fish embryos exposed to nanoparticles exhibit delayed hatching,^[40,47,51] although whether this delay is caused by the whole nanoparticles themselves or by their released constituent materials remains unknown.^[52,53] Some researchers have proposed that the delay might be caused by interactions between the nanoparticles and the zebrafish hatching enzyme, which is crucial for digesting the inner layer of the chorion (the membrane surrounding the embryo).^[52,54]

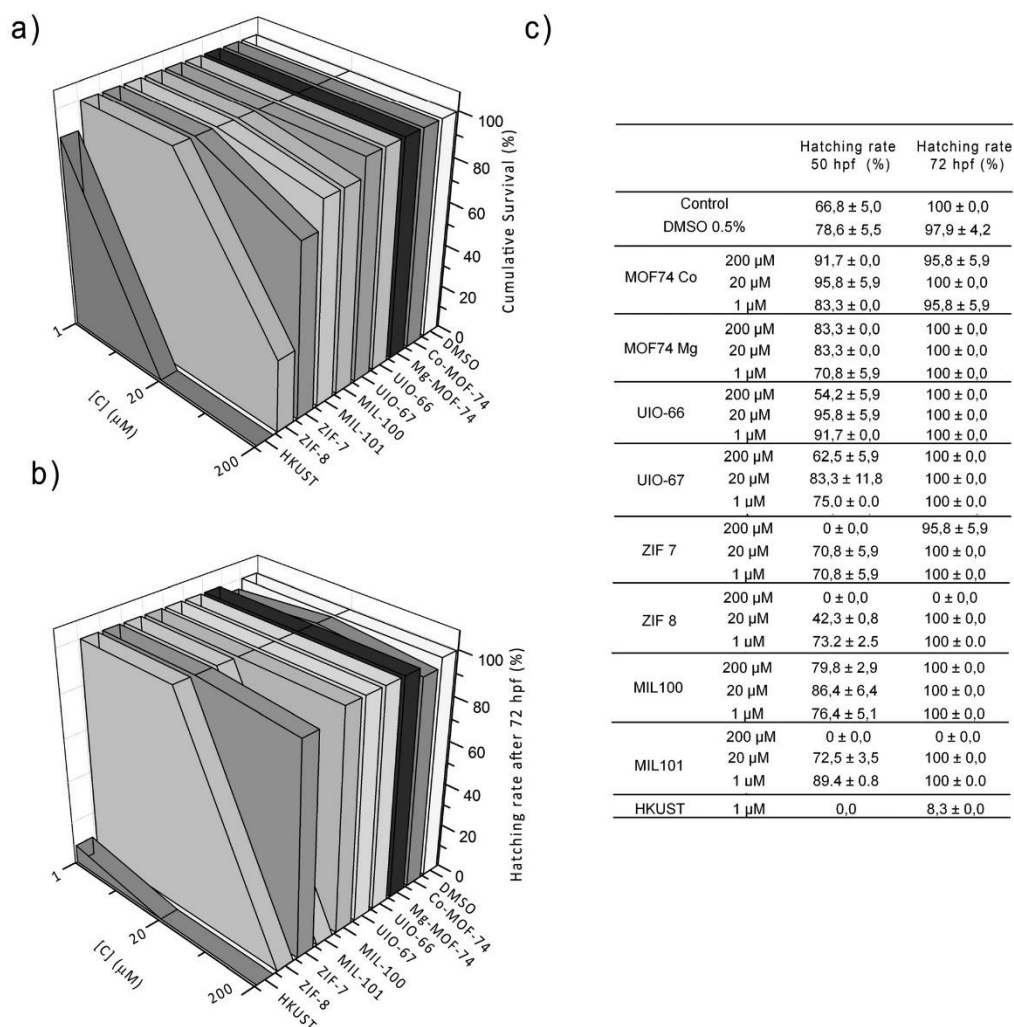


Figure 3. In vivo toxicity of nanoMOFs to zebrafish embryos. a) Cumulative survival of zebrafish larvae at 120 h post-fertilization (hpf) after exposure to a single nanoMOF at one of three concentrations (1, 20, or 200 μM). b) Concentration-dependent (1, 20, or 200 μM) effects of nanoMOFs on the hatching rates of zebrafish embryos at 120 hpf. c) Quantification of hatching rates (%) at 50 and 72 hpf.

When incubated under normal conditions, control embryos hatched from their chorion between 48 and 72 hpf (Figure 3c), exhibiting slightly accelerated hatching, similar to an effect that has been previously reported.^[55] However, the embryos incubated with nanoZIF-7 or nanoHKUST-1 hatched significantly later than did the control embryos (Figure 3b and c, and Figure S10 in the Supporting Information), and of these two treated groups, only the nanoZIF-7 group reached 100% hatching rate. In the case of nanoHKUST-1, the hatching delay was only quantified at a nanoHKUST-1 dose of 1 μM , because no embryos survived at the higher doses. Interestingly, embryos exposed to the highest dose (200 μM) of nanoZIF-8 or nanoMIL-101 did not hatch at all by 120 hpf. It is important to mention here that nanoZIF-8 has an effect on the survival at this high-

est dose (200 μM). No significant hatching delay was observed in the groups exposed to nanoCo-MOF-74, nanoMg-MOF-74, nanoUiO-66, nanoUiO-67, or nanoMIL-100.

To further characterize the in vivo toxicity of nanoMOFs, we also quantified the morphological defects observed on the treated embryos after they had hatched (Figure 4 and Figure S11 in the Supporting Information). No significant malformations were found in the embryos that had been exposed to nanoMg-MOF-74; significant levels of yolk sac edema were found in the nanoCo-MOF-74, nanoUiO-66, nanoUiO-67, and nanoZIF-7 groups; concentration-dependent yolk sac edemas and significant pericardial edema was found in the nanoMIL-100 group. No further putative morphological defects could be detected in the groups exposed to 200 μM of nanoZIF-8 or

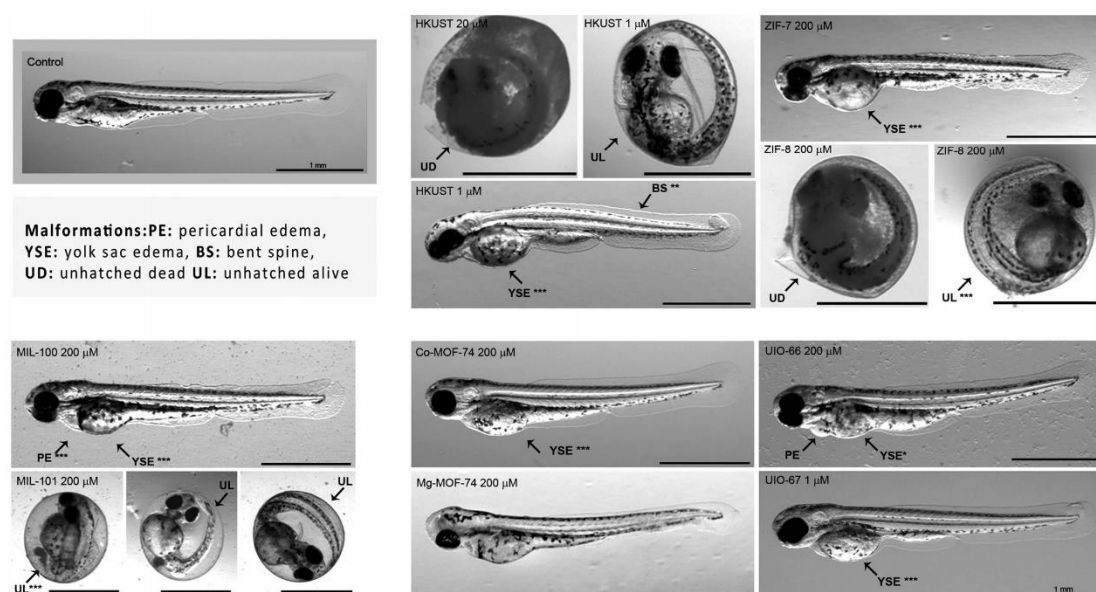


Figure 4. Malformations in zebrafish embryos that had been exposed to nanoMOFs. Representative images of embryos were taken after continuous exposure to nanoMOFs (72 hpf). The malformations were imaged and quantified. Significant differences from the control are marked accordingly (** $p < 0.01$, *** $p < 0.005$).

nanoMIL-101, due to their inability to hatch, although some morphological malformations were observed in the groups exposed to lower doses of nanoZIF-8 (pericardial edema, yolk-sac edema and bent spine) or nanoMIL-101 (yolk sac edema) (see Figure S11). Interestingly, significant levels of pericardial edema, yolk-sac edema, and bent spine were observed in the group that had been exposed to nanoHKUST-1 at the low dose of $1 \mu\text{M}$; however, the malformations in the groups exposed to higher doses were not characterized because none of the embryos had survived.

Ranking of the in vivo toxicity of nanoMOFs

To compare the in vivo toxicity of the nine studied nanoMOFs, we quantified their in vivo effects on the zebrafish embryos using a scoring system that was first described by Peterson et al.^[56,30] and subsequently modified by Nel et al.^[47] Thus, we

scored the amount and severity of the phenotypic changes, on a scale from 0 to 4, whereby 0 = normal phenotype; 1 = a minor phenotypic change; 2 = multiple moderate alterations; 3 = severe embryo deformation; and 4 = no survival (see Table 2). The nanoMOFs scored as follows: 0 (nanoMg-MOF-74); 1 (nanoCo-MOF-74, nanoUiO-66, and nanoUiO-67); 2 (nanoMIL-100 and nanoZIF-7); 3 (nanoZIF-8 and nanoMIL-101); and 4 (nanoHKUST-1).

Comparison of the in vitro toxicity and the in vivo toxicity results for the nanoMOFs

We found a strong correlation between the in vitro toxicity results and the in vivo toxicity results for the nine nanoMOFs that were tested in both assays (Table 3). The only deviation from this trend was that observed for nanoMIL-101, which was

Score	Attributes	nanoMOF	Morphological defects	Physiological defects
0	no morphological or physiological defects	nanoMg-MOF-74		
1	single morphological/physiological defect	nanoCo-MOF-74, nanoUiO-66 and nanoUiO-67	yolk sac edema	
2	multiple morphological and physiological defects	nanoMIL-100 and nanoZIF-7	pericardial and yolk sac edema, bent spine	mortality, reduced hatching rate
3	severe multiple morphological and physiological defects	nanoMIL-101 and nanoZIF-8	pericardial and yolk sac edema, bent spine	mortality, embryos failed to hatch
4	embryos do not survive	nanoHKUST-1	disintegrated embryo	

Table 3. Qualitative comparison between the in vitro and in vivo toxicity of the nanoMOFs studied in both assays.

Grade of toxicity	In vitro	In vivo
–		(0) nanoMg-MOF-74
+	nanoMg-MOF-74, nanoCoMOF-74, nanoUiO-66 and nanoUiO-67	(1) nanoCoMOF-74, nanoUiO-66 and nanoUiO-67
++	nanoMIL-100, nanoZIF-7 and nanoMIL-101	(2) nanoMIL-100 and nanoZIF-7
+++	nanoZIF-8	(3) nanoZIF-8 and nanoMIL-101
++++	nanoHKUST-1	(4) nanoHKUST-1

more toxic to zebrafish embryos (adverse effect on hatching) than it was to HepG2 or MCF7 cells.

Conclusion

We have assessed the in vitro toxicity and in vivo toxicity of a series of representative, uncoated, nanoscale metal-organic frameworks (nanoMOFs). We first screened sixteen nanoMOFs against two human cell lines (HepG2 and MCF7), and then screened a diverse set of nine of these nanoMOFs in zebrafish embryos. We found a strong correlation between the in vitro toxicity results and the in vivo toxicity results, with nanoMg-MOF-74 being the least toxic in both assays. The only exception to this trend was nanoMIL-101, which was more toxic to embryos than to cell cultures. Our findings suggest that degradation of nanoMOFs in solution generates metal ions that strongly determine the toxicity of these nanomaterials. However, other factors might also influence the toxicity of nanoMOFs, including the formation of other species upon degradation, or certain crystal parameters (e.g., size, shape, charge, etc.). We affirm that more studies on the possible environmental and health risks of nanoMOFs must be performed before these new nanomaterials can be exploited for practical use.

Experimental Section

Materials

All reagents and solvents used in the nanoMOF syntheses were purchased from Sigma-Aldrich and Romil, respectively, and were used without any further purification.

NanoMOF synthesis

The nanoMOFs were prepared by using modified versions of reported methods.^[1,32,33] The general procedures are detailed in the Supporting Information.

NanoMOF characterization

We characterized the synthesized nanoMOFs by XRPD, to determine their purity, and by transmission electron microscopy (TEM), field-emission scanning electron microscopy (FESEM) and dynamic light scattering (DLS), to determine their size distribution.

Stability studies

A carefully weighed sample of each nanoMOF was separately dispersed in 10 mL of DMEM medium with 10% FBS to achieve a final concentration of 10 mM. Each mixture was incubated at 37 °C for 24 h with gentle stirring, and then centrifuged for 5 min at 10000 rpm (Alegria 64R, Beckman Coulter). Each supernatant was characterized by ICP-OES with an Optima 4300DV unit (Perkin-Elmer)

to determine the amount of solubilized metal ions. In parallel, each pellet was washed with 10 mL of deionized water to remove buffer salts, and then centrifuged. This process was repeated with methanol, and the resulting solids were dried in an oven at 90 °C overnight, weighed and finally, characterized by XRPD. All the experiments were performed in triplicate.

Evaluation of the in vitro toxicity of the nanoMOFs and their constituent components to HepG2 and MCF7 cells

Human hepatocyte (HepG2) and breast cancer (MCF7) cell lines were separately incubated with a single nanoMOF, and then the effects of the nanoMOFs on cell viability were assessed by using the XTT (2,3-bis-(2-methoxy-4-nitro-5-sulphophenyl)-2H-tetrazolium-5-carboxanilide) cell viability assay^[37] after 24 and 72 h incubation time. The cells were cultured in either DMEM (Dulbecco's modified Eagle's medium, Invitrogen; for HepG2 cells) or DMEM F12 (for MCF7 cells), containing GlutaMax 1 and supplemented with 10% (v/v) heat-inactivated fetal bovine serum (FBS) (Invitrogen) at 37 °C, 5% CO₂ and 95% humidity. The cells were seeded into 96-well plates (cell density: 4.0 × 10³ cells/well), incubated for 24 h, and then exposed to fresh medium containing a DMSO suspension of the desired nanoMOF (concentrations: 25 to 200 μM). At 24 and 72 h incubation, aliquots of 20 μL of XTT solution were added to each well, and the resulting color was quantified (λ = 450 nm) in a spectrophotometric plate-reader (PerkinElmer Victor3V). Cell viability was expressed as a percentage of the control level. All the measurements were performed in triplicate, in three independent experiments. The same procedure was employed to separately evaluate the cytotoxicity of each nanoMOF component (metal salt or organic ligand) to HepG2 cells, except at a concentration range from 1 to 200 μM and at 24 h incubation time. Differences among the data were analyzed by using one-way ANOVA, followed by Tukey's post test (*p* < 0.001).

Exposure of zebrafish embryos to nanoMOFs

Adult zebrafish (*Danio rerio*) were maintained in tanks with recirculating water under a 14 h light/10 h dark cycle at 28 °C. Male and female zebrafish were set up in pairs for breeding in breeding tanks. A grid insert in the tanks enabled the resulting embryos to fall to the bottom, avoiding parental predation. The embryos were collected in E3 medium (5 mM NaCl, 0.17 mM KCl, 0.33 mM CaCl₂, 0.33 mM MgSO₄ and 0.1% Methylene Blue), rinsed carefully to remove debris, and kept at 28 °C in an incubator. The embryos were visually assessed with a microscope (Olympus, CKX31, Japan) for viability and developmental stage, and the selected healthy specimens were plated into 96-well plates at 1 embryo/well. Starting at 5 h post-fertilization, the embryos were exposed to 200 μL/well of a solution of a single nanoMOF at different concentrations

(1, 20, and 200 μM ; final concentration of DMSO in E3 medium: 0.5%), or to a DMSO control solution (0.5% DMSO in E3 medium), or to E3 medium alone (negative control). The embryos were assessed for hatching rate, cumulative mortality and malformations at 24, 48, 72, 96, and 120 hpf. Screening for morphological defects included the assessment of abnormally developed eyes; lack of somite formation; delayed development; pericardial edema; yolk-sac edema; irregular pigmentation; tail malformation; and/or a bent spine. The most frequently found malformations (pericardial edema, yolk-sac edema, and bent spine), were quantified. Embryos with abnormal morphologies were anaesthetized with ethyl 3-aminobenzoate methanesulfonate (160 ppm MS-222, Sigma), transferred onto microscope slides, and then photographed in a Leica Stereomicroscope MZ FLIII. Each condition was tested in 24 individuals. All experimental procedures were submitted to the Ethical Committee of the Universitat Autònoma de Barcelona, and the procedures follow the International Guiding Principles for Research Involving Animals.

Acknowledgements

We acknowledge financial support from the MINECO, Spain, (projects MAT2012-30994 and CTQ2011-16009-E) and from EU FP7 (project ERC-Co 615954). We also thank the Servei de Microscopia of the UAB and Dr. Belén Ballesteros of ICN2. I.I. and N.R. thank the MINECO for Ramón y Cajal grants.

Keywords: metal-organic frameworks · microporous materials · nanoparticles · toxicology · zebrafish

- [1] A. Carné, C. Carbonell, I. Imaz, D. MasPOCH, *Chem. Soc. Rev.* **2011**, *40*, 291–305.
- [2] H. Furukawa, K. E. Cordova, M. O’Keeffe, O. M. Yaghi, *Science* **2013**, *341*, 974–980.
- [3] W. Lin, W. J. Rieter, K. M. L. Taylor, *Angew. Chem. Int. Ed.* **2009**, *48*, 650–658; *Angew. Chem.* **2009**, *121*, 660–668.
- [4] D. Tanaka, A. Henke, K. Albrecht, M. Moeller, K. Nakagawa, S. Kitagawa, J. Groll, *Nat. Chem.* **2010**, *2*, 410–418.
- [5] K. H. Park, K. Jang, S. U. Son, D. A. Sweigart, *J. Am. Chem. Soc.* **2006**, *128*, 8740–8741.
- [6] L. J. Zhang, F. L. Jiang, Y. F. Zhou, W. T. Xu, M. C. Hong, *Tetrahedron* **2013**, *69*, 9237–9244.
- [7] W. J. Rieter, K. M. L. Taylor, W. Lin, *J. Am. Chem. Soc.* **2007**, *129*, 9852–9853.
- [8] T. Rodenas, M. van Dalen, E. García-Pérez, P. Serra-Crespo, B. Zornoza, F. Kapteijn, J. Gascon, *Adv. Funct. Mater.* **2014**, *24*, 249–256.
- [9] Y.-S. Li, H. Bux, A. Feldhoff, G.-L. Li, W.-S. Yang, J. Caro, *Adv. Mater.* **2010**, *22*, 3322–3326.
- [10] a) P. Horcajada, T. Chalati, C. Serre, B. Gillet, C. Sebrie, T. Baati, J. F. Eubank, D. Heurtaux, P. Clayette, C. Kreuz, J. S. Chang, Y.-K. Hwang, V. Marsaud, P. N. Bories, L. Cynober, S. Gil, G. Férey, P. Couvreur, R. Gref, *Nat. Mater.* **2010**, *9*, 172–178; b) W. Morris, W. E. Briley, E. Auyeung, M. D. Cabezas, C. A. Mirkin, *J. Am. Chem. Soc.* **2014**, *136*, 7261–7264.
- [11] I. B. Vasconcelos, T. G. da Silva, G. C. G. Militao, T. A. Soares, N. A. Rodrigues, M. O. Rodrigues, N. B. da Costa Jr., R. O. Freire, S. A. Junior, *RSC Adv.* **2012**, *2*, 9437–9442.
- [12] J. Zhuang, C.-H. Kuo, L.-Y. Chou, D.-Y. Liu, E. Weerapana, C.-K. Tsung, *ACS Nano* **2014**, *8*, 2812–2819.
- [13] S. Diring, D. O. Wang, C. Kim, M. Kondo, Y. Chen, S. Kitagawa, K.-I. Kamei, S. Furukawa, *Nat. Commun.* **2013**, *4*, 2684.
- [14] N. J. Hinks, A. C. McKinlay, B. Xiao, P. S. Wheatley, R. E. Morris, *Microporous Mesoporous Mater.* **2010**, *129*, 330–334.
- [15] a) J. Della Rocca, W. Lin, *Eur. J. Inorg. Chem.* **2010**, 3725–3734; b) G. A. Pereira, J. A. Peters, F. A. Almeida Paz, J. Rocha, C. F. G. C. Geraldies, *Inorg. Chem.* **2010**, *49*, 2969–2974; c) A. Foucault-Collet, K. A. Gogick, K. A. White, S. Villette, A. Pallier, G. Collet, C. Kieda, T. Li, S. J. Geib, N. L. Rosi, S. Petoud, *Proc. Natl. Acad. Sci.* **2013**, *110*, 17199–17204; d) A. Carné-Sánchez, C. S. Bonnet, I. Imaz, J. Lorenzo, É. Tóth, D. MasPOCH, *J. Am. Chem. Soc.* **2013**, *135*, 17711–17714.
- [16] W. J. Rieter, K. M. Pott, K. M. L. Taylor, W. Lin, *J. Am. Chem. Soc.* **2008**, *130*, 11584–11585.
- [17] T. Baati, L. Njim, F. Neffati, A. Kerkeni, M. Bouttemi, R. Gref, M. F. Najjar, A. Zakhama, P. Couvreur, C. Serre, P. Horcajada, *Chem. Sci.* **2013**, *4*, 1597–1607.
- [18] C. Tamames-Tabar, D. Cunha, E. Imbuluzqueta, F. Ragon, C. Serre, M. J. Blanco-Prieto, P. Horcajada, *J. Mater. Chem. B* **2014**, *2*, 262–271.
- [19] T. Chalati, P. Horcajada, P. Couvreur, C. Serre, M. Ben Yahia, G. Maurin, R. Gref, *Nanomedicine* **2011**, *6*, 1683–1695.
- [20] P. Horcajada, R. Gref, T. Baati, P. K. Allan, G. Maurin, P. Couvreur, G. Férey, R. Morris, C. Serre, *Chem. Rev.* **2012**, *112*, 1232–1268.
- [21] P. Horcajada, S. Surble, C. Serre, D.-Y. Hong, Y.-K. Seo, J. S. Chang, J. M. Grenèche, *Chem. Commun.* **2007**, 2820–2822.
- [22] S. Bauer, C. Serre, T. Devic, P. Horcajada, J. Marrot, G. Férey, N. Stock, *Inorg. Chem.* **2008**, *47*, 7568–7576.
- [23] H. Li, M. Eddaoudi, M. O’Keeffe, O. M. Yaghi, *Nature* **1999**, *402*, 276–279.
- [24] a) N. L. Rosi, J. Kim, M. Eddaoudi, B. Chen, M. O’Keeffe, O. M. Yaghi, *J. Am. Chem. Soc.* **2005**, *127*, 1504–1518; b) P. D. C. Dietzel, Y. Morita, R. Blom, H. Fjellvåg, *Angew. Chem. Int. Ed.* **2005**, *44*, 6354–6358; *Angew. Chem.* **2005**, *117*, 6512–6516.
- [25] a) K. S. Park, Z. Ni, A. P. Côte, J. Y. Choi, R. Huang, F. J. Urbe-Romo, H. K. Chae, M. O’Keeffe, O. M. Yaghi, *Proc. Natl. Acad. Sci. USA* **2006**, *103*, 10186–10191; b) X.-C. Huang, Y.-Y. Lin, J.-P. Zhang, X.-M. Chen, *Angew. Chem. Int. Ed.* **2006**, *45*, 1557–1559; *Angew. Chem.* **2006**, *118*, 1587–1589.
- [26] J. H. Cavka, S. Jakobsen, U. Olsbye, N. Guillou, C. Lamberti, S. Bordiga, K. P. Lillerud, *J. Am. Chem. Soc.* **2008**, *130*, 13850–13851.
- [27] S. S.-Y. Chui, S. M.-F. Lo, J. P. H. Charmant, A. G. Orpen, I. D. Williams, *Science* **1999**, *283*, 1148–1150.
- [28] B. Chen, N. W. Ockwig, A. R. Millward, D. S. Contreras, O. M. Yaghi, *Angew. Chem. Int. Ed.* **2005**, *44*, 4745–4749; *Angew. Chem.* **2005**, *117*, 4823–4827.
- [29] C. Parnig, *Curr. Opin. Drug Discov. Devel.* **2005**, *8*, 100–106.
- [30] O. Bar-Ilan, R. M. Albrecht, V. E. Fako, D. Y. Furgeson, *Small* **2009**, *5*, 1897–1910.
- [31] S. Lin, Y. Zhao, A. E. Nel, S. Lin, *Small* **2013**, *9*, 1608–1618.
- [32] M. Sindoro, N. Yanai, A.-Y. Jee, S. Granick, *Acc. Chem. Res.* **2014**, *47*, 459–469.
- [33] J. Della Rocca, D. Liu, W. Lin, *Acc. Chem. Res.* **2011**, *44*, 957–968.
- [34] A. Carné-Sánchez, I. Imaz, M. Cano-Sarabia, D. MasPOCH, *Nat. Chem.* **2013**, *5*, 203–211.
- [35] T. W. Turney, M. B. Duriska, V. Jayaratne, A. Elbaz, S. J. O’Keefe, A. S. Hastings, T. J. Piva, P. F. A. Wright, B. N. Feltis, *Chem. Res. Toxicol.* **2012**, *25*, 2057–2066.
- [36] C. Shen, S. A. James, M. D. de Jonge, T. W. Turney, P. F. A. Wright, B. N. Feltis, *Toxicol. Sci.* **2013**, *136*, 120–130.
- [37] T. J. Brunner, P. Wick, P. Manser, P. Spohn, R. N. Grass, L. K. Limbach, A. Bruinink, W. J. Stark, *Environ. Sci. Technol.* **2006**, *40*, 4374–4381.
- [38] Y.-N. Chang, M. Zhang, L. Xia, J. Zhang, G. Xing, *Materials* **2012**, *5*, 2850–2871.
- [39] M. Ates, J. Daniels, Z. Arslan, I. O. Farah, H. F. Rivera, *Environ. Sci. Processes Impacts* **2013**, *15*, 225–233.
- [40] W. Bai, Z. Zhang, W. Tian, X. He, Y. Ma, Y. Zhao, Z. Chai, *J. Nanopart. Res.* **2010**, *12*, 1645–1654.
- [41] R. D. Palmiter, *Proc. Natl. Acad. Sci. USA* **2004**, *101*, 4918–4923.
- [42] F. Ren, B. Yang, J. Cai, Y. Jiang, J. Xu, S. Wang, *J. Hazardous Mater.* **2014**, *271*, 283–291.
- [43] V. Valdiglesias, C. Costa, G. Kiliç, S. Costa, E. Pásaro, B. Laffon, J. P. Teixeira, *Environ. Int.* **2013**, *55*, 92–100.
- [44] A. Nel, T. Xia, L. Mädler, N. Li, *Science* **2006**, *311*, 622–627.
- [45] T. Xia, M. Kovochich, J. Brant, M. Hotze, J. Sempf, T. Oberley, C. Sioutas, J. I. Yeh, M. R. Wiesner, A. E. Nel, *Nano Lett.* **2006**, *6*, 1794–1807.
- [46] J. She, Z. Xiao, Y. Yang, S. Deng, J. Chen, G. Yang, N. Xu, *ACS Nano* **2008**, *2*, 2015–2022.
- [47] S. George, T. Xia, R. Rallo, Y. Zhao, Z. Ji, S. Lin, X. Wang, H. Zhang, B. France, D. Schoenfeld, R. Damoiseaux, R. Liu, S. Lin, K. A. Bradley, Y. Cohen, A. Nel, *ACS Nano* **2011**, *5*, 1805–1817.

- [48] X. Zhao, K. J. Ong, J. D. Ede, J. L. Stafford, K. W. Ng, G. G. Goss, S. C. J. Loo, *Small* **2013**, *9*, 1734–1741.
- [49] B. J. Shaw, R. D. Handy, *Environ. Int.* **2011**, *37*, 1083–1097.
- [50] S. Lin, X. Wang, Z. Ji, C. H. Chang, Y. Dong, H. Meng, Y.-P. Liao, M. Wang, T.-B. Song, S. Kohan, T. Xia, J. I. Zink, S. Lin, A. E. Nel, *ACS Nano* **2014**, *8*, 4450–4464.
- [51] J. Cheng, E. Flahaut, S. H. Cheng, *Environ. Toxicol. Chem.* **2007**, *26*, 708–716.
- [52] T. Xia, Y. Zhao, T. Sager, S. George, S. Pokhrel, N. Li, D. Schoenfeld, H. Meng, S. Lin, X. Wang, M. Wang, Z. Ji, J. I. Zink, L. Mädler, V. Castranova, S. Lin, A. E. Nel, *ACS Nano* **2011**, *5*, 1223–1235.
- [53] X. Zhu, J. Wang, X. Zhang, Y. Chang, Y. Chen, *Nanotechnology* **2009**, *20*, 195103–195112.
- [54] K. J. Ong, X. Zhao, M. E. Thistle, T. J. MacCormack, R. J. Clark, G. Ma, Y. Martinez-Rubi, B. Simard, J. S. C. Loo, J. G. C. Veinot, G. G. Goss, *Nanotoxicology* **2014**, *8*, 295–304.
- [55] K. Fent, C. J. Weisbroda, A. Wirth-Heller, U. Pieles, *Aquat. Toxicol.* **2010**, *100*, 218–228.
- [56] T. C. King Heiden, E. Dengler, W. J. Kao, W. Heideman, R. E. Peterson, *Toxicol. Appl. Pharmacol.* **2007**, *225*, 70–79.
- [57] A. H. Cory, T. C. Owen, J. A. Barltrop, J. G. Cory, *Cancer Commun.* **1991**, *3*, 207–212.

Received: September 23, 2014
Published online on December 11, 2014

Metal-organic Frameworks | Hot Paper |

Continuous One-Step Synthesis of Porous M-XF₆-Based Metal-Organic and Hydrogen-Bonded Frameworks

Vincent Guillerm,^[a] Luis Garzón-Tovar,^[a] Amirali Yazdi,^[a] Inhar Imaz,^[a] Jordi Juanhuix,^[b] and Daniel MasPOCH^{*,[a, c]}

Abstract: Metal-organic frameworks (MOFs) built up from connecting M-XF₆ pillars through N-donor ligands are among the most attractive adsorbents and separating agents for CO₂ and hydrocarbons today. The continuous, one-step spray-drying synthesis of several members of this isorecticular MOF family varying the anionic pillar (XF₆ = [SiF₆]²⁻ and [TiF₆]²⁻), the N-donor organic ligand (pyrazine and 4,4'-bipyridine) and the metal ion (M = Co, Cu and Zn) is demonstrated here. This synthetic method allows them to be obtained in the form of spherical superstructures assembled from nanosized crystals. As confirmed by CO₂ and N₂ sorption studies, most of the M-XF₆-based MOFs synthesised

through spray-drying can be considered "ready-to-use" sorbents as they do not need additional purification and time consuming solvent exchange steps to show comparable porosity and sorption properties with the bulk/single-crystal analogues. Stability tests of nanosized M-SiF₆-based MOFs confirm their low stability in most solvents, including water and DMF, highlighting the importance of protecting them once synthesised. Finally, for the first time it was shown that the spray-drying method can also be used to assemble hydrogen-bonded open networks, as evidenced by the synthesis of MPM-1-TIFSIX.

Introduction

The environmental impact associated with energy demand is a major problem worldwide.^[1] For example, CO₂ emission caused by humanity-CO₂ concentration at the South Pole recently passed the milestone of 400 ppm for the first time in the last 4 million years^[2]—contributes highly to climate change. In this sense, 2016 has also been the first year that the weekly average CO₂ concentration monitored in the Mona Loa observatory did not go below this key value, meaning that the average global temperature is likely to increase more than the 1.5 °C warming threshold.^[3]

To address the current and future energy needs while mitigating the environmental impact, one of the strategies has been the development of efficient CO₂ capture, storage, and separation materials for achieving cleaner combustible sup-

plies.^[4] These materials mainly include zeolites, activated carbons, metal-organic frameworks (MOFs) and covalent-organic frameworks (COFs).^[5] Among these innovative materials, an old-fashioned class of fluorinated materials^[6] have recently been brought back to the spotlight by the Eddaoudi and Zaworotko groups thanks to their exceptional uptake and selectivity towards CO₂ and hydrocarbons.^[7] These MOFs (Figure 1) are constructed from the assembly of pre-made M-XF₆ pillars (M = Co, Ni, Cu, Zn; X = Si, Ti, Sn, Zr, Ge, V, Ga) with N-donor type ligands (e.g., pyrazine (pyz), pyridyl-based ligands etc.).

However, despite these great developments, the scientific community and industry still need to join their efforts in transferring these materials from the laboratory to industry. A very important step here is the optimisation of their fabrication.^[8] This fabrication must always aim for fast and scalable one-step processes that produce ready-to-use products without the need of additional purification and drying steps. Here we report a synthetic method that allows production of several isorecticular M-XF₆-based CO₂ sorbents fulfilling all these requirements.

Our team recently introduced a well-established industrial spray-drying (SD) technique as a new synthetic way to prepare various MOFs (Scheme S1 in Supporting Information).^[8,9] The SD technique is a scalable and fast method allowing continuous synthesis of MOFs in the form of spherical superstructures or beads based on the assembly of nanosized crystals.^[9c] The strong expertise acquired from these previous studies, among several reports suggesting the capital importance of the formation of the inorganic secondary building unit (SBU) for the nucleation and growth of MOFs,^[10] convinced us that pre-made

[a] Dr. V. Guillerm, L. Garzón-Tovar, A. Yazdi, Dr. I. Imaz, Prof. Dr. D. MasPOCH
Catalan Institute of Nanoscience and Nanotechnology (ICN2)
CSIC and The Barcelona Institute of Science and Technology
Campus UAB, Bellaterra, 08193 Barcelona (Spain)
E-mail: daniel.masPOCH@icn2.cat

[b] Dr. J. Juanhuix
ALBA Synchrotron
Cerdanyola del Vallès, 08290 Barcelona (Spain)

[c] Prof. Dr. D. MasPOCH
ICREA
Pg. Lluís Companys 23, 08010 Barcelona (Spain)

Supporting information and the ORCID identification numbers for the authors of this article can be found under <https://doi.org/10.1002/chem.201605507>.

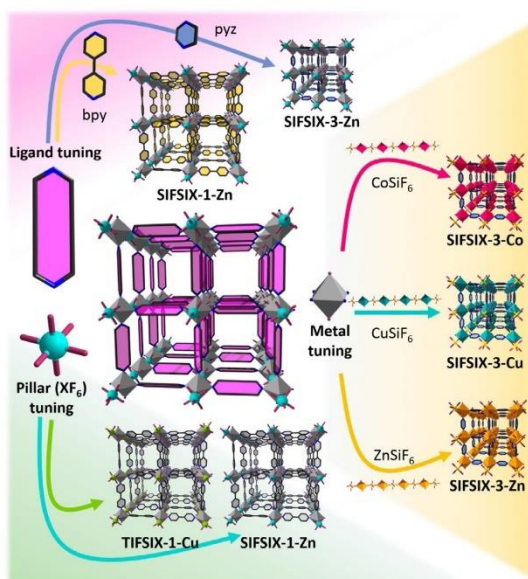


Figure 1. Schematic representation of the different isorecticular *pcu* $M\text{-XF}_6$ -based MOFs synthesised through spray-drying. Note here that this technique allows synthesising this class of MOFs whilst varying the metal ion (Co, Cu, Zn), anionic pillar ($[\text{SiF}_6]^{2-}$, $[\text{Tf}_6]^{2-}$) and ligand (pyrazine, 4,4'-bipyridine).

pillars of the $M\text{-XF}_6$ MOF platform would be ideal candidates for SD synthesis.

We therefore successfully embarked on the SD-based synthesis of several $M\text{-XF}_6$ materials, showing that this method is also compatible for reticular synthesis and metal tuning, ligand elongation and pillar substitution. Importantly, their rapid synthesis (a few minutes versus a few hours up to a few days) does not negatively affect their sorption properties, demonstrating in most cases their ready-to-use character without the need of additional purification steps or time consuming repeated solvent exchange procedures. Moreover, we also demonstrate that SD can be used not only to synthesise porous materials based on coordination bonds but also based on hydrogen bonds.

Results and Discussion

SIFSIX-3-M materials

Synthesis and characterisation

The one-step SD synthesis consisted of the combined atomisation of two methanolic solutions containing 1) $M\text{-SiF}_6$ ($M = \text{Co}, \text{Cu}, \text{Zn}$) and 2) pyz at 85°C , which produced fine powders that were collected with a minimum amount of methanol (MeOH). Collection of these powders in methanol was a crucial protection step as we found that they were air-sensitive (see below). To assess the quality of the as-made SIFSIX-3-M MOFs, their CO_2 sorption properties were compared with those of their

bulk analogues. For this, the SD-synthesised SIFSIX-3-M collected in methanol were directly transferred from the spray drier collector to sorption cells, and dried and evacuated for 12 h at 65°C . Then, their CO_2 uptake at 298 K was measured. Notably, we confirmed that spray-dried SIFSIX-3-M did not require additional solvent exchange or purification steps to exhibit remarkable CO_2 capacities at low pressure and 298 K (Figure 2h, Table 1), with an uptake less than 10% lower than the reported bulk materials.

SD-synthesised SIFSIX-3-M were further characterised by powder X-ray diffraction (PXRD), from which experimental patterns were in excellent agreement with the theoretical diagrams calculated from the corresponding structures (Figure 2g), demonstrating both the high crystallinity and purity of the MOFs.

The morphology of the materials was also investigated by field-emission scanning electron microscopy (FESEM), showing in all cases the occurrence of nanosized SIFSIX-3-M crystals assembled into spherical superstructures or beads; a shape that is typical for MOFs assembled by the SD method. The sizes of these superstructures were $7.9 \pm 4.8 \mu\text{m}$ for SIFSIX-3-Co, $6.9 \pm 3.4 \mu\text{m}$ for SIFSIX-3-Cu and $3.5 \pm 2.7 \mu\text{m}$ for SIFSIX-3-Zn (Figure 2 a–c and Figure S14a in Supporting Information).^[9,11] Moreover, FESEM images confirmed the homogeneity of the materials, as already suggested by the absence of crystalline impurity peaks in the PXRD diagrams.

To finally determine the size of crystals composing the superstructures, they were disassembled by sonication and immediately transferred to a transmission electron microscopy (TEM) grid. TEM images confirmed the formation of nanocrystals with a size of $32 \pm 13 \text{ nm}$ for SIFSIX-3-Co, $80 \pm 12 \text{ nm}$ for SIFSIX-3-Cu and $28 \pm 9 \text{ nm}$ for SIFSIX-3-Zn (Figure 2d–f and Figure S14b).

Stability in different media

The use of methanol to collect the fine powders produced with the SD method is essential to protect and use the as-made SIFSIX-3-M MOFs.^[12] Without this precaution, all nanosized SIFSIX-3-M MOFs suffered a fast degradation and a loss of their CO_2 sorption properties when they were exposed to ambient conditions. In addition, following the optimised washing procedure reported by Nugent et al.,^[7a] we observed that the SD-synthesised SIFSIX-3-Zn was instantaneously solubilised upon addition of *N,N*-dimethylformamide (DMF), leading to a clear solution. Attempts to re-spray this clear solution did not allow the re-assembly of the SIFSIX-3-Zn framework. Instead, colourless single crystals (versus the yellow colour of SIFSIX-3-Zn crystals) appeared in the DMF solution after a period of ca. one month. This unknown structure, which crystallises in the $P\bar{1}$ space group, was solved by single-crystal X-ray diffraction and appeared to be a cationic 1D coordination polymer with formula $\{[\text{Zn}(\text{pyz})_2(\text{DMF})_2(\text{H}_2\text{O})_2]_n[\text{SiF}_6]_n\}$ (1). This structure results from the replacement of all SiF_6 pillars and half of the pyz ligand by DMF and water molecules (Table S1, Figures S15–19). The positive charge of this coordination polymer $[\text{Zn}(\text{pyz})_2(\text{DMF})_2(\text{H}_2\text{O})_2]^{2+}$ is balanced by $[\text{SiF}_6]^{2-}$ anions.

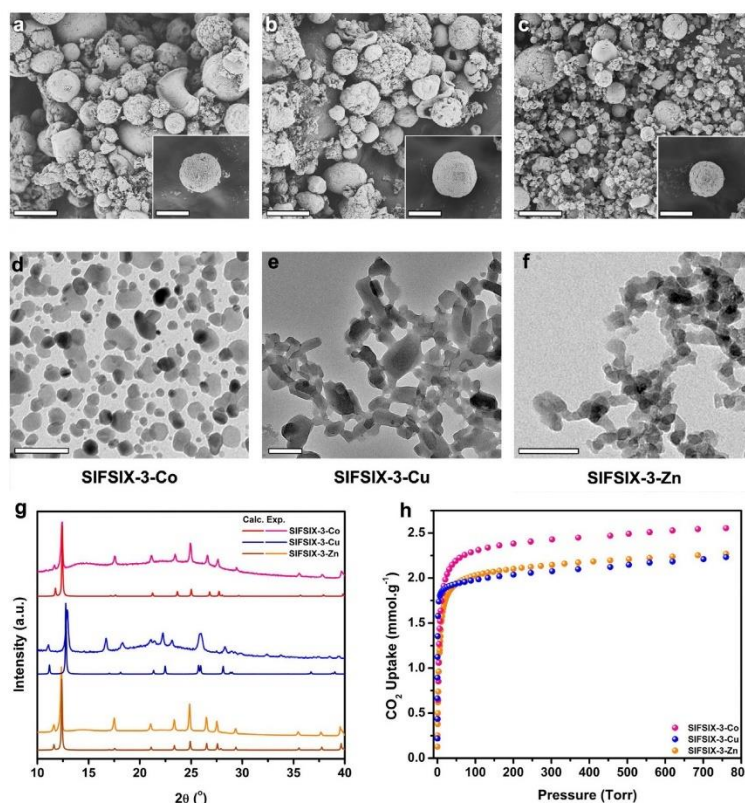


Figure 2. Representative FESEM images of (a) SIFSIX-3-Co, (b) SIFSIX-3-Cu and (c) SIFSIX-3-Zn. TEM images of (d) SIFSIX-3-Co, (e) SIFSIX-3-Cu and (f) SIFSIX-3-Zn. (g) PXRD patterns of the SD-synthesised SIFSIX-3-M. (h) CO₂ sorption isotherms at 298 K for SIFSIX-3-M. Scale bars for FESEM: 15 and 5 μm (insets). Scale bars for TEM: 100 nm (d, f) and 200 nm (e).

MOF	CO ₂ uptake [mmol g ⁻¹]	
	Bulk	Sprayed (% of bulk)
SIFSIX-3-Co	≈ 2.79 ^[7k]	2.56 (92%)
SIFSIX-3-Cu	≈ 2.40 ^[7l]	2.23 (93%)
SIFSIX-3-Zn	≈ 2.46 ^[7a]	2.27 (91%)

It is important to mention here that a similar behaviour was found when immersing SIFSIX-3-Zn in water, also leading to a complete solubilisation of the crystals. The incubation of nanosized SIFSIX-3-Zn in other organic solvents, including acetonitrile, hexane, dichloromethane, chloroform, toluene, tetrahydrofuran and acetone, did not result in the solubilisation of the crystals but instead a fast phase transition into unidentified crystalline powders (Figure S20).

The only tested solvent in which SIFSIX-3-Zn showed certain stability was MeOH. Initial incubation studies using microcrystals instead of nanocrystals, to easily follow the evolution by FESEM, showed that SIFSIX-3-Zn is also etched and finally solubilised in MeOH (Figure S13). However, we found that the

minimum amount of MeOH needed for the complete solubilisation of the nanosized SIFSIX-3-Zn without stirring was around 0.14 mL_{MeOH} per mg_{SIFSIX-3-Zn}. In addition, below this amount of MeOH, SIFSIX-3-Zn remained stable and did not suffer any phase transition, as confirmed by PXRD. It is also worth mentioning that a similar behaviour occurred for the Cu and Co analogues. To this end, altogether these observations allowed us to define MeOH as the best solvent to collect these materials, which were in all cases collected using no more than 0.015 mL_{MeOH} per mg of MOF.

Reticular chemistry: organic ligand and anionic pillar tuning

Synthesis and characterisation of SIFSIX-1-Zn

In line with global efforts of the MOF community to use some network topologies as design platforms to rationally synthesise isorecticular MOFs,^[13] we intended to take advantage of the already reported versatility of the M-XF₆ platform^[6c,e,7a,b,e-g,k] to demonstrate the suitability of the SD method for reticular chemistry. Following the successful synthesis of SIFSIX-3-M (M=Co, Cu and Zn), we achieved the synthesis of an expanded analogue, SIFSIX-1-Zn,^[6e] by replacing the pyz ligand with

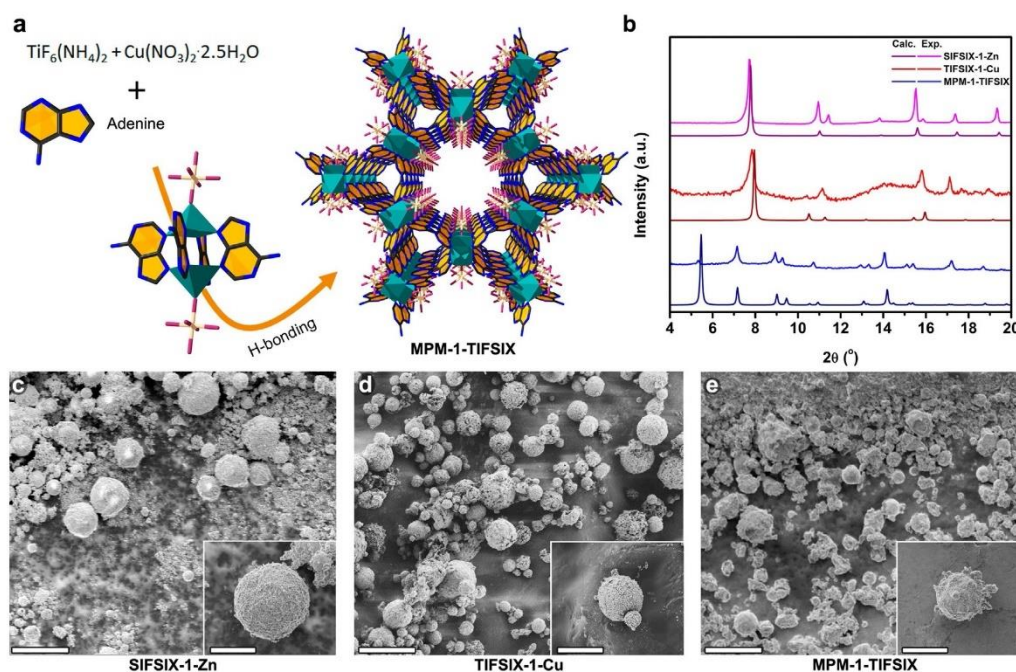


Figure 3. (a) Schematic for the synthesis and structure of **MPM-TIFSIX-1**; (b) comparison of theoretical and experimental PXRD diagrams of **MPM-1-TIFSIX**, **TIFSIX-1-Cu** and **SIFSIX-1-Zn**; FESEM images of (c) **SIFSIX-1-Zn**, (d) **TIFSIX-1-Cu** and (e) **MPM-1-TIFSIX**. Scale bars for FESEM: 20 and 5 μm (insets).

the longer 4,4'-bipyridine (bpy). Here, a methanolic solution of ZnSiF_6 was spray-dried along with a methanolic solution of bpy using a 3-fluid nozzle at 85 °C. The resulting yellow spherical superstructures (size = 7.9 ± 3.6 μm; Figure 3c and Figure S14a in Supporting Information) were collected and washed with MeOH. The material was obtained as a pure phase, as confirmed by PXRD (Figure 3b). It was found to be porous to N_2 at 77 K, exhibiting an apparent BET surface area of $1300 \text{ m}^2 \text{ g}^{-1}$ (Table 2, Figure S21). Again, the nanosized nature of the **SIFSIX-1-Zn** crystals was confirmed by TEM; performed after disassembling the superstructures by sonication. The size of these nanocrystals was 20 ± 5 nm (Figures S14b, S24).

MOF	$A_{\text{BET}} [\text{m}^2 \text{ g}^{-1}]$	$V_{\text{micro}} [\text{cm}^3 \text{ g}^{-1}]$ $P/P_0 = 0.3$	$V_t [\text{cm}^3 \text{ g}^{-1}]$ $P/P_0 = 0.95$	Theo. $V_t [\text{cm}^3 \text{ g}^{-1}]$
SIFSIX-1-Zn	1300	0.53	0.58	0.68
TIFSIX-1-Cu	1650	0.66	0.88	0.70
MPM-1-TIFSIX	805	0.32	0.32	0.39

Synthesis and characterisation of TIFSIX-1-Cu

Recently, Nugent et al.^[70] reported the possibility to not only vary the metal in this type of **pcu**-MOF, but also the anion, by achieving the replacement of the pillaring $[\text{SiF}_6]^{2-}$ anion by

$[\text{TiF}_6]^{2-}$. Bulk **TIFSIX-1-Cu** is commonly synthesised using a layering of methanol and ethylene glycol at room temperature. However, this synthesis could not be reproduced in the spray-drier due to the high boiling point of ethylene glycol (197.3 °C). For this reason, we successfully replaced ethylene glycol by water, adjusting the SD temperature to 150 °C. Thus, an aqueous solution of $\text{Cu}(\text{NO}_3)_2 \cdot 2.5\text{H}_2\text{O}$ and $\text{TiF}_6(\text{NH}_4)_2$ was spray-dried along with a methanolic solution of bpy using a 3-fluid nozzle at 150 °C. The resulting grey/purple spherical superstructures (size = 5.3 ± 3.1 μm; Figure 3d and Figure S14a) were collected with MeOH. Their PXRD pattern was found to be in excellent agreement with the theoretical diagram (Figure 3b). N_2 sorption performed at 77 K revealed an apparent BET surface area of $1650 \text{ m}^2 \text{ g}^{-1}$. This value is very similar to that reported for the bulk material ($1690 \text{ m}^2 \text{ g}^{-1}$)^[70] demonstrating the high quality of the SD-synthesised **TIFSIX-1-Cu** MOF (Table 2, Figure S22). The nanosized nature of the **TIFSIX-1-Cu** crystals (size = 43 ± 9 nm, Figures S14b, S25) was again confirmed by TEM performed after disassembling the superstructures by sonication.

Synthesis and characterisation of supramolecular open material

Finally, due to the apparent ease of synthesis of these **M-XF₆** based MOFs by SD technology, we selected another porous material, **MPM-1-TIFSIX**,^[70] based on the supramolecular assembly of $[\text{Cu}_2(\text{ade})_4(\text{TiF}_6)_2]$ (ade = adenine) paddlewheels (Fig-

ure 3a). It is worth mentioning that, in the present case, the selected material to be synthesised by SD was not a MOF but a supramolecular hydrogen-bonded network. To our knowledge, the aerosol synthesis of such kind of open materials based on weak bonding has not been reported yet.

An aqueous solution of $\text{Cu}(\text{NO}_3)_2 \cdot 2.5\text{H}_2\text{O}$ and $\text{TiF}_6(\text{NH}_4)_2$ was spray-dried along with a solution of adenine in water/acetonitrile mixture using a 2-fluid nozzle (Scheme S3 in Supporting Information) at 150°C . The resulting grey/purple spherical superstructures (size = $6.1 \pm 3.1 \mu\text{m}$; Figure 3e and Figure S14a) were collected with MeOH. Remarkably, the PXRD diagram was found to be in excellent agreement with the theoretical one (Figure 3b). N_2 sorption performed at 77 K after a methanol solvent exchange procedure revealed an apparent BET surface area of $805 \text{ m}^2\text{g}^{-1}$ ($996 \text{ m}^2\text{g}^{-1}$ for bulk),^[7d] demonstrating the porosity of the SD-synthesised **MPM-1-TIFSIX** supramolecular material (Table 2, Figure S3). In this case, TEM experiments performed after disassembling the superstructures by sonication showed **MPM-1-TIFSIX** crystals with a size of $201 \pm 65 \text{ nm}$ (Figures S14b, S26).

Conclusion

We reported here the one-step and continuous synthesis of various M-XF_6 based MOFs using the SD technique. Using this method, these M-XF_6 based MOFs could be synthesised at the nanoscale. There is no doubt that the possibility of obtaining and stabilizing nanosized M-XF_6 based MOFs opens new avenues for the re-exploration of this old-fashioned sub-class of MOFs for emerging applications. In addition, we demonstrated the suitability of the SD method to perform fine structural tuning through ligand size variation (pyz versus bpy), anionic pillar substitution ($[\text{SiF}_6]^{2-}$ versus $[\text{TiF}_6]^{2-}$) and variation of metal ion (Co, Cu and Zn). Importantly, this novel way to synthesise these materials does not jeopardise their sorption properties. This fact together with the short synthesis times and the absence of time consuming purification and solvent exchange procedures demonstrates the ability and competitiveness of SD methods versus conventional ones for the fast production of ready-to-use sorbents. Finally, we demonstrated the first aerosol synthesis of a supramolecular, hydrogen-bonded porous network, **MPM-1-TIFSIX**, which opens new avenues for the synthesis of this class of porous materials using SD.

Experimental Section

Materials

All the materials were synthesised using a Mini Spray Dryer B-290 (BÜCHI Labortechnik). All solvents and reagents were purchased from Sigma-Aldrich, City Chemicals or Scharlab and used as received.

Synthesis of SIFSIX-3-Co

6 mL of a methanolic solution of CoSiF_6 (300 mg, 1.49 mmol) and 6 mL of a methanolic solution of pyz (325 mg, 4.05 mmol) were si-

multaneously spray-dried using a 3-fluid nozzle (Scheme S2 in Supporting Information), a feed rate of 2.4 mL min^{-1} , a flow rate of 414 mL min^{-1} , an inlet N_2 temperature of 85°C and a spray cap with a 0.5 mm hole. The light pink powder of **SIFSIX-3-Co** was recovered with a minimum amount of MeOH (235 mg; 44% yield based on Co). IR: $\tilde{\nu} = 690 \text{ (s)}, 1062 \text{ (s)}, 1124 \text{ (w)}, 1153 \text{ (m)}, 1421 \text{ (s)}, 1628 \text{ (m)}, 1660 \text{ (m)}, 3196 \text{ (br)}, 3403 \text{ (br)}, 3522 \text{ cm}^{-1} \text{ (w)}$ (Figure S1).

Synthesis of SIFSIX-3-Cu

6 mL of a methanolic solution of $\text{CuSiF}_6 \cdot \text{H}_2\text{O}$ (300 mg, 1.34 mmol) and 6 mL of a methanolic solution of pyz (325 mg, 4.05 mmol) were simultaneously spray-dried using a 3-fluid nozzle, a feed rate of 2.4 mL min^{-1} , a flow rate of 414 mL min^{-1} , an inlet N_2 temperature of 85°C and a spray cap with a 0.5 mm hole. The blue powder of **SIFSIX-3-Cu** was recovered with a minimum amount of MeOH (272 mg; 55% yield based on Cu). IR: $\tilde{\nu} = 686 \text{ (s)}, 822 \text{ (s)}, 1078 \text{ (s)}, 1132 \text{ (s)}, 1161 \text{ (s)}, 1429 \text{ (s)}, 1652 \text{ (m)}, 1660 \text{ (m)}, 3147 \text{ (m)}, 3325 \text{ cm}^{-1} \text{ (br)}$ (Figure S2).

Synthesis of SIFSIX-3-Zn

6 mL of a methanolic solution of $\text{ZnSiF}_6 \cdot x\text{H}_2\text{O}$ (300 mg, 1.45 mmol, anhydrous based) and 6 mL of a methanolic solution of pyz (325 mg, 4.05 mmol) were simultaneously spray-dried using a 3-fluid nozzle, a feed rate of 2.4 mL min^{-1} , a flow rate of 414 mL min^{-1} , an inlet N_2 temperature of 85°C and a spray cap with a 0.5 mm hole. The yellow powder of **SIFSIX-3-Zn** was recovered with a minimum amount of MeOH (305 mg; 57% yield based on Zn). IR: $\tilde{\nu} = 686 \text{ (s)}, 822 \text{ (w)}, 1062 \text{ (s)}, 1099 \text{ (w)}, 1128 \text{ (w)}, 1161 \text{ (w)}, 1425 \text{ (s)}, 1635 \text{ (s)}, 1660 \text{ (m)}, 3432 \text{ cm}^{-1} \text{ (br)}$ (Figure S3).

Synthesis of SIFSIX-1-Zn

6 mL of a methanolic solution of $\text{ZnSiF}_6 \cdot x\text{H}_2\text{O}$ (300 mg, 1.45 mmol, anhydrous based) and 6 mL of a methanolic solution of bpy (650 mg, 4.16 mmol) were simultaneously spray-dried using a 3-fluid nozzle, a feed rate of 2.4 mL min^{-1} , a flow rate of 414 mL min^{-1} , an inlet N_2 temperature of 85°C and a spray cap with a 0.5 mm hole. The yellow powder of **SIFSIX-1-Zn** was recovered with a minimum amount of MeOH (302 mg; 40% yield based on Zn). The sample was then washed with 5 mL of MeOH to remove potential contamination with the highly soluble, unreacted precursors. IR: $\tilde{\nu} = 632 \text{ (m)}, 649 \text{ (s)}, 764 \text{ (m)}, 806 \text{ (s)}, 851 \text{ (s)}, 1008 \text{ (m)}, 1062 \text{ (s)}, 1223 \text{ (m)}, 1317 \text{ (w)}, 1413 \text{ (s)}, 1491 \text{ (m)}, 1536 \text{ (m)}, 1611 \text{ (s)}, 1644 \text{ (w)}, 3230 \text{ (w)}, 3345 \text{ cm}^{-1} \text{ (br)}$ (Figure S4).

Synthesis of TIFSIX-1-Cu

6 mL of an aqueous solution of $\text{TiF}_6(\text{NH}_4)_2$ (30 mg, 0.15 mmol) and $\text{Cu}(\text{NO}_3)_2 \cdot 2.5\text{H}_2\text{O}$ (35 mg, 0.15 mmol) and 6 mL of a methanolic solution of bpy (46.8 mg, 0.30 mmol) were simultaneously spray-dried using a 3-fluid nozzle, a feed rate of 2.4 mL min^{-1} , a flow rate of 414 mL min^{-1} , an inlet N_2 temperature of 130°C and a spray cap with a 0.5 mm hole. The blue powder of **TIFSIX-1-Cu** was recovered with a minimum amount of MeOH (64 mg; 79% yield based on Cu). IR: $\tilde{\nu} = 632 \text{ (s)}, 678 \text{ (w)}, 728 \text{ (m)}, 810 \text{ (s)}, 851 \text{ (w)}, 921 \text{ (w)}, 1012 \text{ (s)}, 1066 \text{ (s)}, 1223 \text{ (m)}, 1280 \text{ (s)}, 1326 \text{ (w)}, 1409 \text{ (s)}, 1471 \text{ (m)}, 1491 \text{ (m)}, 1536 \text{ (m)}, 1607 \text{ (s)}, 1644 \text{ (w)}, 3101 \text{ (w)}, 3283 \text{ (w)}, 3357 \text{ cm}^{-1} \text{ (w)}$ (Figure S5).

Synthesis of MPM-1-TIFSIX

12 mL of an aqueous solution of $\text{TiF}_6 \cdot (\text{NH}_4)_2$ (30 mg, 0.15 mmol) and $\text{Cu}(\text{NO}_3)_2 \cdot 2.5\text{H}_2\text{O}$ (35 mg, 0.15 mmol) and 12 mL of a $\text{H}_2\text{O}:\text{CH}_3\text{CN}$ (1:1 vol.) solution of adenine (82 mg, 0.60 mmol) were simultaneously spray-dried using a 2-fluid nozzle and T-shaped system (Scheme S3), a feed rate of 2.4 mL min^{-1} , a flow rate of 414 mL min^{-1} , an inlet N_2 temperature of 150°C and a spray cap with a 0.5 mm hole. The purple/grey powder of MPM-1-TIFSIX was recovered with a minimum amount of MeOH (110 mg; 74% yield based on Zn). Prior to sorption measurements, this powder was immersed in MeOH for 3 days, refreshing the MeOH twice a day. IR: $\tilde{\nu} = 715$ (m), 789 (m), 827 (w), 806 (s), 889 (m), 938 (m), 1037 (w), 1107 (w), 1149 (w), 1231 (s), 1314 (s), 1409 (s), 1607 (s), 1652 (s), 1702 (w), 3089 (w), 3200 (w), 3419 cm^{-1} (w) (Figure S6).

Characterisation

PXRD diagrams were collected on a Panalytical X'pert diffractometer with monochromatic $\text{Cu}_{\text{K}\alpha}$ radiation ($\lambda_{\text{Cu}} = 1.5406 \text{ \AA}$) under a Kapton film. Fourier transform infrared (FTIR) spectra were recorded on a Bruker Tensor 27 FTIR spectrometer equipped with a Golden Gate diamond attenuated total reflection (ATR) cell, in transmittance mode at room temperature. The main IR bands (Figures S1–6) are reported as follow: strong (s), medium (m), weak (w) and broad (br). TGA curves (Figures S7–12) were measured in a PerkinElmer Pyris 1 under O_2 atmosphere and a heating rate of $10^\circ\text{C min}^{-1}$. Volumetric N_2 and CO_2 sorption isotherms were collected at 77 K (N_2) and 298 K (CO_2) using an ASAP 2020 HD (Micromeritics). Temperature was controlled by using a liquid nitrogen bath (77 K) or a Lauda Proline RP 890 chiller (298 K). For N_2 sorption at 77 K, micropore volumes (V_{micro}) were calculated at $P/P_0 = 0.3$, whereas the total pore volumes (V_{t}) were calculated at $P/P_0 = 0.95$. Field-emission scanning electron microscopy (FESEM) images were collected on scanning electron microscopes (FEI Magellan 400 L XHR and Quanta 650 FEG) at an acceleration voltage of 1.0 kV, and using dry powder on carbon as support. Transmission electron microscopy (TEM) images were obtained with a JEOL JEM 1400 at 100 kV. Prior to TEM, all superstructures immersed in MeOH were disassembled by sonication for 10 s in a Fisher Scientific FB15051 sonicator and then directly transferred onto the TEM grids. The average size range of superstructures and crystals has been calculated on 100 crystals/superstructures using the Image J software.

Stability study of SIFSIX-3-Zn

6 mL of a methanolic solution of $\text{ZnSiF}_6 \cdot x\text{H}_2\text{O}$ (300 mg, 1.45 mmol, anhydrous based) was injected into 6 mL of a methanolic solution of pyz (325 mg, 4.05 mmol) at room temperature, without stirring. After 1 h, 1 mL of the solution containing the resulting microcrystals was pipetted from the middle of the vial and mixed with 2 mL of MeOH. Aliquots of the sample were transferred immediately to the microscope to avoid contact with air, and the morphology of the crystals was studied by FESEM after 15 min (Figure S13).

Crystallography

Crystallographic data for **1** were collected at 100 K at XALOC beamline at ALBA synchrotron^[14] ($\lambda = 0.79472 \text{ \AA}$). Data were indexed, integrated and scaled using the XDS program.^[15] Absorption correction was not applied. The structure was solved by direct methods and subsequently refined by correction of F^2 against all reflections, using SHELXS2013^[16] and SHELXL2013^[17] within the WinGX package.^[18] All non-hydrogen atoms were refined with ani-

sotropic thermal parameters by full-matrix least-squares calculations on F^2 using the program SHELXL2013. Hydrogen atoms were inserted at calculated positions and constrained with isotropic thermal parameters.

Acknowledgements

This work was supported by the MINECO-Spain through projects PN MAT2012-30994, 2014-SGR-80, EU FP7 ERC-Co 615954, and European Union's Horizon 2020 research and innovation programme under grant agreement No 685727. V.G. is grateful to the Generalitat de Catalunya for a Beatriu de Pinós fellowship (2014 BP-B 00155) and I.I. thanks the MINECO for a Ramón y Cajal fellowship (RYC-2010-06530). A.Y. and ICN2 acknowledge the support of the Spanish MINECO through the Severo Ochoa Centers of Excellence Program, under Grant SEV-2013-0295.

Conflict of interest

The authors declare no conflict of interest.

Keywords: CO_2 sorption · fluorinated materials · metal-organic frameworks · spray-drying · stability

- [1] R. Monastersky, *Nature* **2009**, *458*, 1091–1094.
- [2] South Pole is the last place on Earth to pass a global warming milestone <http://research.noaa.gov/News/NewsArchive/LatestNews/TabId/684/ArtMID/1768/ArticleID/11760/South-Pole-is-the-last-place-on-Earth-to-pass-a-global-warming-milestone.aspx> (accessed June 28th, 2016).
- [3] Up-to-date weekly average CO_2 at Mauna Loa, <http://www.esrl.noaa.gov/gmd/ccgg/trends/weekly.html> (accessed October 4th, 2016).
- [4] a) K. Sumida, D. L. Rogow, J. A. Mason, T. M. McDonald, E. D. Bloch, Z. R. Herm, T.-H. Bae, J. R. Long, *Chem. Rev.* **2012**, *112*, 724–781; b) Y. Belmabkhout, V. Guillerm, M. Eddaoudi, *Chem. Eng. J.* **2016**, *296*, 386–397.
- [5] a) H. C. Zhou, J. R. Long, O. M. Yaghi, *Chem. Rev.* **2012**, *112*, 673–1268; b) J. R. Long, O. M. Yaghi, *Chem. Soc. Rev.* **2009**, *38*, 1213; c) J. R. Long, O. M. Yaghi, *Chem. Soc. Rev.* **2014**, *43*, 6288; d) R. Dawson, A. I. Cooper, D. J. Adams, *Prog. Polym. Sci.* **2012**, *37*, 530–563.
- [6] a) K. Uemura, A. Maeda, T. K. Maji, P. Kanoo, H. Kita, *Eur. J. Inorg. Chem.* **2009**, *2009*, 2329–2337; b) D. N. Dybtsev, H. Chun, K. Kim, *Angew. Chem. Int. Ed.* **2004**, *43*, 5033–5036; *Angew. Chem.* **2004**, *116*, 5143–5146; c) S.-I. Noro, S. Kitagawa, M. Kondo, K. Seki, *Angew. Chem. Int. Ed.* **2000**, *39*, 2081–2084; *Angew. Chem.* **2000**, *112*, 2161–2164; d) M. J. Zaworotko, *Angew. Chem. Int. Ed.* **2000**, *39*, 3052–3054; *Angew. Chem.* **2000**, *112*, 3180–3182; e) S. Subramanian, M. J. Zaworotko, *Angew. Chem. Int. Ed. Engl.* **1995**, *34*, 2127–2129; *Angew. Chem.* **1995**, *107*, 2295–2297; f) S.-I. Noro, R. Kitaura, M. Kondo, S. Kitagawa, T. Ishii, H. Matsuzaka, M. Yamashita, *J. Am. Chem. Soc.* **2002**, *124*, 2568–2583; g) M.-J. Lin, A. Jouaiti, N. Kyritsakas, M. W. Hosseini, *CrystEngComm* **2009**, *11*, 189–191.
- [7] a) P. Nugent, Y. Belmabkhout, S. D. Burd, A. J. Cairns, R. Luebke, K. Forrest, T. Pham, S. Ma, B. Space, E. Wojtas, M. Eddaoudi, M. J. Zaworotko, *Nature* **2013**, *495*, 80–84; b) O. Shekhat, Y. Belmabkhout, Z. Chen, V. Guillerm, A. Cairns, K. Adil, M. Eddaoudi, *Nat. Commun.* **2014**, *5*, 4228; c) P. Kanoo, S. K. Reddy, G. Kumari, R. Haldar, C. Narayana, S. Balasubramanian, T. K. Maji, *Chem. Commun.* **2012**, *48*, 8487–8489; d) P. S. Nugent, V. L. Rhodus, T. Pham, K. Forrest, E. Wojtas, B. Space, M. J. Zaworotko, *J. Am. Chem. Soc.* **2013**, *135*, 10950–10953; e) O. Shekhat, Y. Belmabkhout, K. Adil, P. M. Bhatt, A. J. Cairns, M. Eddaoudi, *Chem. Commun.* **2015**, *51*, 13595–13598; f) P. Nugent, V. Rhodus, T. Pham, B. Tudor, K. Forrest, E. Wojtas, B. Space, M. Zaworotko, *Chem. Commun.* **2013**, *49*, 1606–1608; g) S. D. Burd, S. Ma, J. A. Perman, B. J. Sikora,

- R. Q. Snurr, P. K. Thallapally, J. Tian, Ł. Wojtas, M. J. Zaworotko, *J. Am. Chem. Soc.* **2012**, *134*, 3663–3666; h) X. Cui, K. Chen, H. Xing, Q. Yang, R. Krishna, Z. Bao, H. Wu, W. Zhou, X. Dong, Y. Han, B. Li, Q. Ren, M. J. Zaworotko, B. Chen, *Science* **2016**, *353*, 141–144; i) A. Cadiau, K. Adil, P. M. Bhatt, Y. Belmabkhout, M. Eddaoudi, *Science* **2016**, *353*, 137–140; j) J. L. Manson, J. A. Schlueter, K. E. Garrett, P. A. Goddard, T. Lancaster, J. Möller, S. J. Blundell, A. J. Steele, I. Franke, F. L. Pratt, J. Singleton, J. Bendix, S. H. Lapidus, M. Uhlarz, O. Ayala-Valenzuela, R. McDonald, M. Gurak, C. Baines, *Chem. Commun.* **2016**, *52*, 12653–12656; k) S. K. Elsaidi, M. H. Mohamed, H. T. Schaefer, A. Kumar, M. Lusi, T. Pham, K. A. Forrest, B. Space, W. Xu, G. J. Halder, J. Liu, M. J. Zaworotko, P. K. Thallapally, *Chem. Commun.* **2015**, *51*, 15530–15533.
- [8] a) P. Silva, S. M. F. Vilela, J. P. C. Tome, F. A. Almeida Paz, *Chem. Soc. Rev.* **2015**, *44*, 6774–6803; b) A. U. Czaja, N. Trukhan, U. Müller, *Chem. Soc. Rev.* **2009**, *38*, 1284–1293; c) U. Mueller, M. Schubert, F. Teich, H. Puetter, K. Schierle-Arndt, J. Pastre, *J. Mater. Chem.* **2006**, *16*, 626–636; d) M. Gaab, N. Trukhan, S. Maurer, R. Gummaraju, U. Müller, *Microporous Mesoporous Mater.* **2012**, *157*, 131–136; e) D. Crawford, J. Casaban, R. Haydon, N. Giri, T. McNally, S. L. James, *Chem. Sci.* **2015**, *6*, 1645–1649; f) M. Rubio-Martinez, M. P. Batten, A. Polyzos, K.-C. Carey, J. I. Mardel, K.-S. Lim, M. R. Hill, *Sci. Rep.* **2014**, *4*, 5443; g) M. Rubio-Martinez, T. D. Hadley, M. P. Batten, K. Constanti-Carey, T. Barton, D. Marley, A. Mönch, K.-S. Lim, M. R. Hill, *ChemSusChem* **2016**, *9*, 938–941; h) P. A. Bayliss, I. A. Ibarra, E. Perez, S. Yang, C. C. Tang, M. Poliakoff, M. Schroder, *Green Chem.* **2014**, *16*, 3796–3802; i) M. Faustini, J. Kim, G.-Y. Jeong, J. Y. Kim, H. R. Moon, W.-S. Ahn, D.-P. Kim, *J. Am. Chem. Soc.* **2013**, *135*, 14619–14626; j) P. W. Dunne, E. Lester, R. I. Walton, *React. Chem. Eng.* **2016**, *1*, 352–360; k) L. Garzón-Tovar, A. Carné-Sánchez, C. Carbonell, I. Imaz, D. Maspoch, *J. Mater. Chem. A* **2015**, *3*, 20819–20826; l) L. Garzón-Tovar, M. Cano-Sarabia, A. Carné-Sánchez, C. Carbonell, I. Imaz, D. Maspoch, *React. Chem. Eng.* **2016**, *1*, 533–539.
- [9] a) Z. Wang, D. Ananias, A. Carné-Sánchez, C. D. S. Brites, I. Imaz, D. Maspoch, J. Rocha, L. D. Carlos, *Adv. Funct. Mater.* **2015**, *25*, 2824–2830; b) A. Carné-Sánchez, K. C. Stylianou, C. Carbonell, M. Naderi, I. Imaz, D. Maspoch, *Adv. Mater.* **2015**, *27*, 869–873; c) A. Carné-Sánchez, I. Imaz, M. Cano-Sarabia, D. Maspoch, *Nat. Chem.* **2013**, *5*, 203–211.
- [10] a) D. C. Cantu, B. P. McGrail, V.-A. Glezakou, *Chem. Mater.* **2014**, *26*, 6401–6409; b) O. Shekhah, H. Wang, D. Zacher, R. A. Fischer, C. Woll, *Angew. Chem. Int. Ed.* **2009**, *48*, 5038–5041; *Angew. Chem.* **2009**, *121*, 5138–5142; c) S. Surblé, F. Millange, C. Serre, G. Férey, R. I. Walton, *Chem. Commun.* **2006**, 1518–1520; d) V. Guillemin, S. Gross, C. Serre, T. Devic, M. Bauer, G. Férey, *Chem. Commun.* **2010**, *46*, 767–769; e) D. Alezi, Y. Belmabkhout, M. Suyetin, P. M. Bhatt, Ł. J. Weseliński, V. Solovyeva, K. Adil, I. Spanopoulos, P. N. Trikalitis, A.-H. Emwas, M. Eddaoudi, *J. Am. Chem. Soc.* **2015**, *137*, 13308–13318.
- [11] a) A. Garcia Marquez, P. Horcajada, D. Grosso, G. Férey, C. Serre, C. Sanchez, C. Boissière, *Chem. Commun.* **2013**, *49*, 3848–3850; b) A. Carné-Sánchez, I. Imaz, K. C. Stylianou, D. Maspoch, *Chem. Eur. J.* **2014**, *20*, 5192–5201.
- [12] J. A. Mason, T. M. McDonald, T.-H. Bae, J. E. Bachman, K. Sumida, J. J. Dutton, S. S. Kaye, J. R. Long, *J. Am. Chem. Soc.* **2015**, *137*, 4787–4803.
- [13] a) V. Guillemin, D. Kim, J. F. Eubank, R. Luebke, X. Liu, K. Adil, M. S. Lah, M. Eddaoudi, *Chem. Soc. Rev.* **2014**, *43*, 6141–6172; b) M. Eddaoudi, J. Kim, N. Rosi, D. Vodak, J. Wachter, M. O’Keeffe, O. M. Yaghi, *Science* **2002**, *295*, 469–472; c) O. M. Yaghi, M. O’Keeffe, N. W. Ockwig, H. K. Chae, M. Eddaoudi, J. Kim, *Nature* **2003**, *423*, 705–714; d) H. Furukawa, K. E. Cordova, M. O’Keeffe, O. M. Yaghi, *Science* **2013**, *341*, 1230444; e) V. Guillemin, Ł. J. Weseliński, J. Y. Belmabkhout, A. J. Cairns, V. D’Elia, Ł. Wojtas, K. Adil, M. Eddaoudi, *Nat. Chem.* **2014**, *6*, 673–680.
- [14] J. Juanhuix, F. Gil-Ortiz, G. Cuni, C. Colldelram, J. Nicolas, J. Lidon, E. Boter, C. Ruget, S. Ferrer, J. Benach, *J. Synchrotron Radiat.* **2014**, *21*, 679–689.
- [15] W. Kabsch, *Acta Crystallogr. Sect. D* **2010**, *66*, 125–132.
- [16] G. M. Sheldrick, Z. Dauter, K. S. Wilson, H. Hope, L. C. Sieker, *Acta Crystallogr. Sect. D* **1993**, *49*, 18–23.
- [17] G. M. Sheldrick, *Acta Crystallogr. Sect. C* **2015**, *71*, 3–8.
- [18] L. Farrugia, *J. Appl. Crystallogr.* **2012**, *45*, 849–854.

Manuscript received: November 24, 2016

Accepted Article published: March 30, 2017

Final Article published: April 25, 2017

Sequential Deconstruction–Reconstruction of Metal–Organic Frameworks: An Alternative Strategy for Synthesizing (Multi)-Layered ZIF Composites

Civan Avci,[†] Amiralı Yazdı,^{†,‡} Màrius Tarrés,[‡] Elise Bernoud,[‡] Neus G. Bastús,^{†,§} Victor Puntès,^{†,§} Inhar Imaz,^{†,§} Xavi Ribas,^{‡,§} and Daniel Maspoch^{*,†,§}

[†]Catalan Institute of Nanoscience and Nanotechnology (ICN2), CSIC, and The Barcelona Institute of Science and Technology, Campus UAB, Bellaterra, Barcelona 08193, Spain

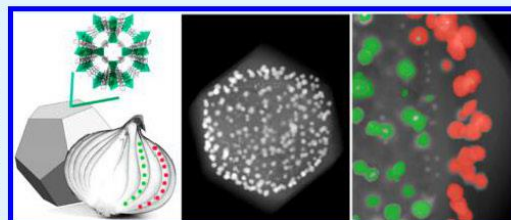
[‡]Institut de Química Computacional i Catàlisi (IQCC) and Departament de Química, Universitat de Girona, Campus Montilivi, Girona E-17071, Catalonia, Spain

[§]ICREA, Pg. Lluís Companys 23, Barcelona 08010, Spain

Supporting Information

ABSTRACT: Here, we report the synthesis of (multi)-layered zeolitic imidazolate framework (ZIF-8/-67) composite particles via a sequential deconstruction–reconstruction process. We show that this process can be applied to construct ZIF-8-on-ZIF-67 composite particles whose cores are the initially etched particles. In addition, we demonstrate that introduction of functional inorganic nanoparticles (INPs) onto the crystal surface of etched particles does not disrupt ZIF particle reconstruction, opening new avenues for designing (multi)-layered ZIF-on-INP-on-ZIF composite particles comprising more than one class of inorganic nanoparticles. In these latter composites, the location of the inorganic nanoparticles inside each single metal–organic framework particle as well as of their separation at the nanoscale (20 nm) is controlled. Preliminary results show that (multi)-layered ZIF-on-INP-on-ZIF composite particles comprising a good sequence of inorganic nanoparticles can potentially catalyze cascade reactions.

KEYWORDS: metal–organic frameworks, inorganic nanoparticles, ZIF composites, etching, crystal growth, cascade catalysis



INTRODUCTION

A major obstacle to the practical application of diverse nanomaterials is the lack of methods to control their morphology.^{1,2} To date, several top-down (e.g., etching, lithography, etc.)^{3–5} and bottom-up (e.g., use of surfactants, controlled self-assembly, etc.)^{6–8} approaches have been employed to design nanomaterials with specific shapes. However, most advanced nanomaterials are not produced and shaped in a single step but rather consecutively, via top-down and bottom-up strategies. A well-known example is the production of integrated circuits,⁹ whereby multiple steps of material deposition (bottom-up) are followed by consecutive photolithographic processes (top-down) to reach complex patterns of heterogeneous composition. In the field of inorganic nanoparticles (INPs), a common approach is to combine oxidative etching (top-down) with growth methods (bottom-up), which yields nanoparticles with unprecedented shapes.^{10–13}

Recent efforts to control the growth of metal–organic framework (MOF) particles have aimed at discovering new shapes¹⁴ and at making more complex, multicomponent (composite) particles, built by growing one MOF on top of

another (known as MOF-on-MOF systems)^{15,16} and by combining MOFs with other functional materials, such as INPs^{17–19} and biosystems.^{20–22} Among the many reported MOFs, the most studied case by far is that of the zeolitic imidazolate frameworks ZIF-8 and ZIF-67, which are isostructural porous materials ($S_{\text{BET}} \sim 1400\text{--}1700\text{ m}^2/\text{g}$) made of Zn(II) and Co(II) ions, respectively. Each ZIF is very interesting because one can epitaxially grow on top of the other one (bottom-up) to afford either ZIF-8-on-ZIF-67 or ZIF-67-on-ZIF-8 particles.^{23–26} Also, ZIF-8/ZIF-67 particles can be etched (top-down) into novel shapes^{27,28} or synthesized as hollow or yolk-shelled particles.^{29–34} Furthermore, both of these ZIFs can grow on the surface of INPs and biosystems, meaning that a rich variety of core–shell^{35–44} and layered composites^{17,23,45} could be designed.

With these advances, both MOF-on-MOF and etching approaches are now being combined, either sequentially (in said order) or simultaneously, to afford new ZIF-8/ZIF-67

Received: March 29, 2018

Accepted: June 22, 2018

Published: June 22, 2018

particles. For instance, Li et al. and Muhler et al. reported formation of hollow Zn/Co ZIF particles in which ZIF-8-on-ZIF-67 particles were built and then the ZIF-67 core was etched due to its lower stability in MeOH compared to ZIF-8 under mild solvothermal conditions.^{46,47} Similarly, Tsung et al. have shown that preformed ZIF-8 particles could be simultaneously regrown and etched to create hollow ZIF-8 particles.³¹ And very recently, Liu et al. have applied regrowth processes followed by etching to build multishelled hollow particles of the well-known MIL-101.²⁹

Herein, we report a novel strategy to construct ZIF-on-ZIF and (multi)-layered ZIF-on-INP-on-ZIF particles. Unlike the aforementioned combination (bottom-up/top-down) methods, our method begins with controlled etching followed by MOF-on-MOF growth. Recently, we have demonstrated that colloidal ZIF-8 and ZIF-67 particles can be anisotropically etched into well-defined, unprecedented morphologies. With this deconstructive method, truncated rhombic dodecahedral (tRD) and rhombic dodecahedral (RD) particles can be transformed into uniform cubic (C), hollow (H), or tetrahedral (T) particles (Figure S1). We show that these etched ZIF-8/-67 particles can be reversibly reconstructed to their initial shapes. This reconstruction entails growing ZIF-8 on the etched particles. Therefore, the sequential deconstruction–reconstruction process can be used to form ZIF-8-on-ZIF-67 particles whose cores are the initially etched particles. In addition, we demonstrate that the inclusion of functional INPs on the crystal surface of etched particles does not disrupt particle reconstruction. This observation opens the possibility of using this sequential process to design (multi)-layered ZIF-on-INP-on-ZIF composites formed by more than one class of INPs. In these onionlike composites, the sequence of the INPs can be controlled from outside to inside the ZIF crystal, paving the way for using them for innovative cascade catalytic reactions.

EXPERIMENTAL SECTION

Materials. All materials were purchased from Sigma-Aldrich with no further modification.

Synthesis of tRD_{ZIF-67}, RD_{ZIF-67}, and tRD_{ZIF-8} Particles. A solution of 0.6 g of Co(OAc)₂·4H₂O in 5 mL of deionized (DI) water was added into a solution of 2.24 g of 2-methylimidazole (2-MiM) in 5 mL of deionized (DI) water, and the resulting mixture was homogenized by stirring for a few seconds. Then, the mixture was let at room temperature for 10 min to form tRD_{ZIF-67} particles. RD_{ZIF-67} particles were prepared using the same procedure as for the truncated ones, except that the mixture was let for 5 h at room temperature. In both cases, purple crystals were collected and washed several times with methanol. Finally, the powder was dried under vacuum for 5 h at room temperature. In the case of tRD_{ZIF-8} particles, a solution of 0.3 g of Zn(OAc)₂·2H₂O in 5 mL of DI water was added into a solution of 1.12 g of 2-MiM in 5 mL of DI water and the resulting mixture was homogenized by stirring for a few seconds. Then, the mixture was let at room temperature for 5 h to form tRD_{ZIF-8} particles.

General Route for Etching ZIF-67 Particles. The general method starts with the preparation of a colloidal ZIF-67 solution by ultrasonication of 25 mg of tRD or RD ZIF-67 particles in 2.5 mL of DI water for 15 min. In parallel, 40 mg of xylenol orange (XO) was dissolved in 2.5 mL of DI water and the pH of this etchant solution was adjusted by adding HCl or NaOH. Note here that the etching solution in this process is acidified/basified XO, which protonates the 2-MiM linkers, breaks the coordination bonds, and sequesters the liberated Co(II) ions. The colloidal solution was then injected into the etchant solution, and the resulting mixture was stirred at 300 rpm for an optimized time (*t*). The final solid was collected by centrifugation and washed several times using methanol. The specific

conditions for each etching process were C_{ZIF-67}: pH = 8.0 and *t* = 3 h and T_{ZIF-67}: pH = 3.5 and *t* = 3 h. Note here that, only for T_{ZIF-67}, a second etching step was needed to obtain a uniform sample. This second etching step consisted on washing the primarily etched crystals with water, redispersing them in 1 mL of DI water, and incubating them with 1 mL of XO etchant solution at pH = 5.80 for 30 min.

General Route for Growing ZIF-8-on-ZIF-67 Particles. The general method started with the preparation of a colloidal ZIF-67 solution by ultrasonication of 5 mg of core ZIF-67 particles in 5 mL of methanol for 15 min. 2-MiM (2.5 mL) and Zn(NO₃)₂·6H₂O (2.5 mL) with varying concentrations (*C*) were added to the colloidal solution, and the resulting mixture was let at room temperature for a time *t*. Finally, the regrown particles were collected by centrifugation, followed by washing steps with methanol. To make RD_{ZIF-8}-on-ZIF-67 crystals with C_{ZIF-67} or T_{ZIF-67} core: *C* = 25 mM, *t* = 1 day and with H_{ZIF-67} core: *C* = 25 mM, *t* = 4 days. To make tRD_{ZIF-8}-on-ZIF-67 crystals with C_{ZIF-67} or T_{ZIF-67} core: *C* = 10 mM, *t* = 1 day and with H_{ZIF-67} intermediate: *C* = 25 mM, *t* = 1 day.

Synthesis of Au Nanoparticles (~9 nm Diameter). Au NPs were produced following a previously reported protocol.¹⁸ In detail, a solution of 2.2 mM sodium citrate in DI water (150 mL) was heated with a heating mantle in a 250 mL three-necked round-bottomed flask for 15 min under vigorous stirring. A condenser was utilized to prevent the evaporation of the solvent. After boiling had commenced, 1 mL of HAuCl₄ (25 mM) was injected. The color of the solution changed from yellow to bluish gray and then to soft pink in 10 min. Under these conditions, the resulting particles (9 ± 2 nm, ~3 × 10¹² NPs/mL) were coated with negatively charged citrate ions and hence they were well suspended in H₂O. After the Au nanoparticle solution was cooled to room temperature, a solution of 0.5 g of poly(vinylpyrrolidone) (PVP, MW = 40 000) in water (20 mL) was added dropwise to the Au nanoparticle solution under continuous stirring, and the mixture was further stirred at room temperature for 24 h. Then, 600 mL of acetone was added to this mixture and left overnight. The supernatant was removed, and the resulting nanoparticles were washed three times with methanol, and finally dispersed in methanol at a concentration of 0.6 mg/mL.

Synthesis of Au Nanoparticles (~22 nm Diameter). A solution of 2.2 mM sodium citrate in DI water (150 mL) was heated with a heating mantle in a 250 mL three-necked round-bottomed flask for 15 min under vigorous stirring. A condenser was utilized to prevent the evaporation of the solvent. After boiling had commenced, 1 mL of HAuCl₄ (25 mM) was injected. The color of the solution changed from yellow to bluish gray and then to soft pink in 10 min. Then, the reaction was cooled until the temperature of the solution reached 90 °C; after that, 1 mL of a HAuCl₄ solution (25 mM) was injected to the solution and stirred for 30 min. This process was repeated one more time. Under these conditions, the resulting particles (22 ± 2 nm, ~1.2 × 10¹² NPs/mL) were coated with negatively charged citrate ions and hence they were well suspended in H₂O. After the Au nanoparticle solution was cooled to room temperature, a solution of 0.5 g of PVP in water (20 mL) was added dropwise to the Au nanoparticle solution under continuous stirring, and the mixture was further stirred at room temperature for 24 h. Then, 600 mL of acetone was added to this mixture and left overnight. The supernatant was removed, and the resulting nanoparticles were washed three times with methanol, and finally dispersed in methanol at a concentration of 1.4 mg/mL.⁴⁸

Synthesis of Au Nanoparticles (~4 nm Diameter). A solution of 2.2 mM sodium citrate in DI water (300 mL) was heated up to 70 °C under vigorous stirring. Then, 0.2 mL of tannic acid (2.5 mM) and 2 mL of potassium carbonate (K₂CO₃, 150 mM) were added to the heated solution. Afterward, 2 mL of HAuCl₄ (25 mM) was injected and the color of the solution changed from yellow to bluish gray to reddish orange in 10 min. The solution was stirred at the same temperature for 2 h. Under these conditions, the resulting nanoparticles (3.6 ± 0.4 nm, 0.2 mg/mL) were coated with negatively charged citrate ions and hence they were well suspended in H₂O. The same coating producer as for Au nanoparticles (~9 nm diameter) was used to functionalize these nanoparticles with PVP.⁴⁹

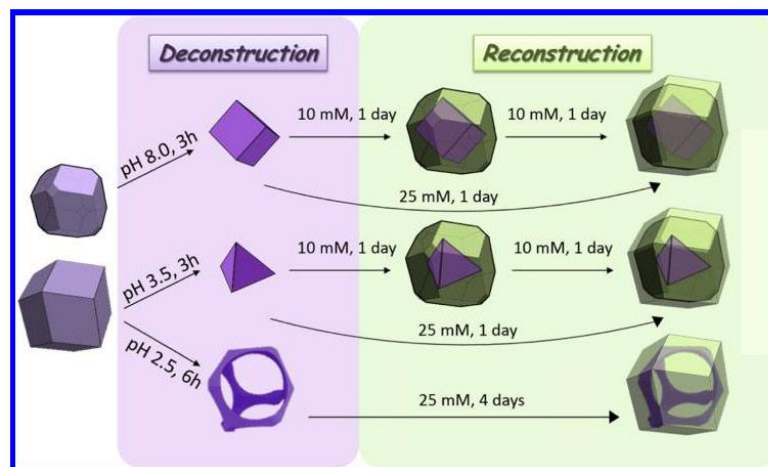


Figure 1. Schematic illustration of the synthetic conditions used to construct the different ZIF-8-on-ZIF-67 particles according to the sequential deconstruction–reconstruction strategy.

Synthesis of Cubic Pd Nanoparticles (~18 nm Diameter).

KBr (547 mg), PVP (100 mg, MW = 55 000), Na_2PdCl_4 (51 mg), and L-ascorbic acid (55 mg) were added to 10 mL of DI water and heated to 80 °C under reflux and vigorous stirring for 3 h. After the nanoparticle solution was cooled to room temperature, the nanoparticles were washed twice with a mixture of acetone and water and one time with methanol and finally dispersed in methanol at a concentration of 0.5 mg/mL (size = 18 ± 2 nm).⁶

Synthesis of Icosahedral Pd Nanoparticles (~13 nm Diameter). In a standard procedure for the synthesis of Pd icosahedra, 160 mg of PVP and 20 μL of HCL (3 M) were introduced into 4 mL of diethylene glycol (DEG) hosted in a 20 mL vial. This mixture was preheated in an oil bath at 105 °C for 20 min under magnetic stirring. Subsequently, 2 mL of DEG solution containing 31 mg of Na_2PdCl_4 was added using a pipette. After the reaction had proceeded for 1 h, it was quenched by immersing the vial in an ice/water bath. Finally, the product was collected by centrifugation, washed once with acetone and twice with water to remove DEG and excess of PVP, and finally dispersed in methanol at a concentration of 0.6 mg/mL (size = 13 ± 4 nm).⁵⁰

Synthesis of Cu/Pd Nanoparticles (~10 nm Diameter). In a typical process, 10 mg of Na_2PdCl_4 , 36 mg of CuSO_4 , and 240 mg of sodium citrate were added to a mixture of 40 mL of DI water and 20 mL of ethylene glycol. This mixture was then heated in an oil bath up to 160 °C in a 100 mL round-bottomed flask under vigorous stirring for 6 h. A condenser was utilized to prevent the evaporation of the solvent. After the nanoparticle solution was cooled to room temperature, a solution of 0.7 g of PVP (MW = 55 000) in water (10 mL) was added dropwise to the nanoparticle solution under continuous stirring and the mixture was further stirred at room temperature for 24 h. Then, 200 mL of acetone was added to this mixture and left overnight. The supernatant was removed, and the resulting nanoparticles were washed twice with water and twice with methanol, and finally dispersed in methanol at a concentration of 1.8 mg/mL (size = 10 ± 3 nm, Cu/Pd = 1:2).

Synthesis of Au (9 nm)-on-ZIF-67 Composites. $\text{C}/\text{T}/\text{H}_{\text{ZIF-67}}$ (10 mg) was dispersed in 5 mL of ethanol in a sonication bath for 10 min and then 10 mL of Au nanoparticle solution was added dropwise to the dispersion while stirring. The resulting composites were collected by centrifugation, washed twice with ethanol, and dried at 60 °C overnight.

Synthesis of $\text{tRD}_{\text{ZIF-8}}$ -on-Au (9 nm)-on-ZIF-67 Composites. The same general route for growing $\text{tRD}_{\text{ZIF-8}}$ -on- $\text{C}_{\text{ZIF-67}}$ was applied.

The only difference is that we used Au (9 nm)-on- $\text{C}_{\text{ZIF-67}}$ cores in various shapes instead of only ZIF-67 cores.

Synthesis of $\text{RD}_{\text{ZIF-8}}$ -on-INPs-on- $\text{tRD}_{\text{ZIF-8}}$ -on-Au (9 nm)-on- $\text{C}_{\text{ZIF-67}}$ Layered Composites. $\text{tRD}_{\text{ZIF-8}}$ -on-Au (9 nm)-on- $\text{C}_{\text{ZIF-67}}$ crystals (10 mg) were dispersed in 5 mL of ethanol in a sonication bath for 10 min. Then, desired amount of the corresponding INP (22 nm in diameter Au NPs, 13 nm in diameter icosahedral Pd NPs, or 18 nm in size cubic Pd NPs) solution was added dropwise to the dispersion while stirring. The resulting composites were collected by centrifugation, washed twice with ethanol, and dried at 60 °C overnight. The different INP-on- $\text{tRD}_{\text{ZIF-8}}$ -on-Au (9 nm)-on- $\text{C}_{\text{ZIF-67}}$ composite crystals were finally subjected to a ZIF-8 growing using $\text{C} = 10$ mM and $\text{f} = 1$ day.

Synthesis of INP-on- $\text{tRD}_{\text{ZIF-8}}$ Composites. The same general route for growing Au (9 nm)-on- $\text{C}_{\text{ZIF-67}}$ was applied. $\text{tRD}_{\text{ZIF-8}}$ (10 mg) particles were dispersed in 5 mL of methanol in a sonication bath for 10 min. Then, 10 mL of Au (3 nm) nanoparticle solution, 1 mL of Cu/Pd (10 nm) nanoparticle solution, or a mixture of both nanoparticle solutions were added dropwise to this dispersion under continuous stirring. The different Au-on- $\text{tRD}_{\text{ZIF-8}}$, Cu/Pd-on- $\text{tRD}_{\text{ZIF-8}}$, and Au/Cu/Pd-on- $\text{tRD}_{\text{ZIF-8}}$ composites were collected by centrifugation, washed twice with ethanol, and dried at 60 °C overnight.

Synthesis of INP-on- $\text{tRD}_{\text{ZIF-8}}$ -on-INP-on- $\text{tRD}_{\text{ZIF-8}}$ Layered Composites. A similar methodology used for growing $\text{RD}_{\text{ZIF-8}}$ -on-INPs-on- $\text{tRD}_{\text{ZIF-8}}$ -on-Au (9 nm)-on- $\text{C}_{\text{ZIF-67}}$ layered composites was applied. INP-on- $\text{tRD}_{\text{ZIF-8}}$ (10 mg) particles were dispersed in 10 mL of methanol in a sonication bath for 10 min. Then, 5 mL of 25 mM 2-MiM and 5 mL of 25 mM $\text{Zn}(\text{NO}_3)_2 \cdot 6\text{H}_2\text{O}$ in methanol were sequentially added to this dispersion in this order and left at room temperature without stirring for 10 min. The resulting particles were collected by centrifugation, washed twice with methanol, and dried at 60 °C overnight. Then, 10 mg of these particles were dispersed in 5 mL of methanol in a sonication bath for 10 min. Afterward, desired amount of the corresponding INP (Au (3 nm) or Cu/Pd (10 nm)) solution was added dropwise to the dispersion under continuous stirring. The final particles were collected by centrifugation, washed once with methanol, and dried at 60 °C overnight.

General Route for the Catalytic Reactions. A mixture of 1-(prop-2-yn-1-yloxy)naphthalene (1) (2.32 mg, 12.7 μmol), K_2CO_3 (3.52 mg, 25.5 μmol), iodobenzene (PhI) (1.42 μL , 12.7 μmol), xantphos (0.37 mg, 0.63 μmol), mesitylene as internal standard (0.35 μL , 5.1 μmol), and the desired ZIF-8-based catalyst (5 mol %) were mixed in 0.6 mL of dry toluene in a 2 mL sealed vial. The dispersion was sonicated for 15 min and stirred for 6 days at 110 °C. Afterward,

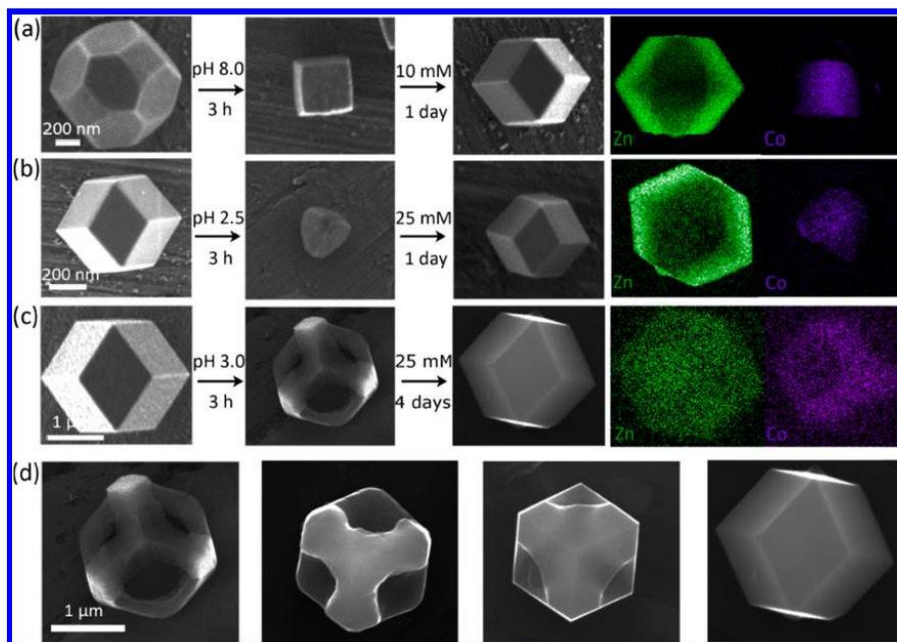


Figure 2. (a–c) FE-SEM images of single particles showing the formation of $\text{RD}_{\text{ZIF-8-on-C-ZIF-67}}$ (a), $\text{RD}_{\text{ZIF-8-on-T-ZIF-67}}$ (b), and $\text{RD}_{\text{ZIF-8-on-H-ZIF-67}}$ (c) particles built by the deconstruction–reconstruction strategy. Right-hand panel: the corresponding elemental mapping (energy-dispersive X-ray spectrometry, EDXS) results, showing the distribution of Zn (green) and Co (violet). (d) FE-SEM images showing the evolution of the formation of $\text{RD}_{\text{ZIF-8-on-H-ZIF-67}}$.

the raw solution was filtered through a silica pad and 4 mL of ethyl acetate were passed to elute all of the generated products. The obtained components were analyzed and quantified by means of gas chromatography and ^1H NMR. Compounds 1–4 were synthesized and characterized according to the literature.^{51–55}

Characterization. Powder X-ray diffraction (PXRD) patterns were collected on an X'Pert PRO MPDP analytical diffractometer (Panalytical) at 45 kV, 40 mA using Cu $K\alpha$ radiation ($\lambda = 1.5419 \text{ \AA}$). Nitrogen adsorption and desorption measurements were done at 77 K using an Autosorb-IQ-AG analyzer (Quantachrome Instruments). Field-emission scanning electron microscopy (FE-SEM) images were collected on a FEI Magellan 400L scanning electron microscope at an acceleration voltage of 1.0–2.0 kV, using aluminum as support. High-angle annular dark-field scanning transmission electron microscopy (HAADF-STEM) images were obtained with a FEI Tecnai G2 F20 at 200 kV. Metal contents of all composites were determined by inductively coupled plasma optical emission spectroscopy (ICP-OES). These measurements were performed using an ICP-OES PerkinElmer, model Optima 4300DV by previous digestion of the composites in a mixture of HNO_3 and HCl (1:2) at 220 °C. Gas chromatography product analyses were performed on an Agilent 7820A gas chromatograph equipped with a HP-5 capillary column (30 m \times 0.32 mm \times 0.25 μm). The injection was carried out on a split/splitless automatic injector Agilent G4513A, in split mode with ratio 100:1 with an injected volume of 1 μL . The detection was conducted by a flame ionization detector (Agilent 7820A GC-System). ^1H NMR data concerning product identity were collected with a Bruker 400 Avance (Serveis Tècnics de Recerca, University of Girona) spectrometer in the corresponding deuterated solvent (CDCl_3) and calibrated relative to the residual protons of the solvent. 1,3,5-Trimethoxybenzene (mesitylene) was used as internal standard.

RESULTS AND DISCUSSION

Figure 1 depicts the different ZIF-8-on-ZIF-67 particles generated by sequential deconstruction–reconstruction. This process starts with anisotropic etching of the ZIF-67 particles to C, H, and T particles under our previously reported synthetic conditions.²⁷ The resulting etched particles are then dispersed in methanol (MeOH) and mixed with a solution of 2-methylimidazole (2-MiM) in MeOH at an optimized concentration. Afterward, a solution of $\text{Zn}(\text{NO}_3)_2 \cdot 6\text{H}_2\text{O}$ in MeOH at the same concentration is added, and the resulting mixture is left at room temperature for a certain time. Note that the required precursor concentration and the reaction time vary by the initial morphology of the etched core particle and that, in all cases, we could optimize them to selectively generate tRD or RD particles. For instance, when the core was a cubic or tetrahedral ZIF-67 particle, $\text{tRD}_{\text{ZIF-8-on-C-ZIF-67}}$ and $\text{tRD}_{\text{ZIF-8-on-T-ZIF-67}}$ particles were formed at a concentration of 10 mM and a reaction time of 1 day. In contrast, $\text{RD}_{\text{ZIF-8-on-C-ZIF-67}}$ and $\text{RD}_{\text{ZIF-8-on-T-ZIF-67}}$ particles were synthesized by increasing the concentration up to 25 mM and maintaining the reaction time at 1 day (for full synthetic procedures, see Experimental Section).

For the hollow microboxes, $\text{RD}_{\text{ZIF-8-on-H-ZIF-67}}$ particles were formed at a concentration of 25 mM and a reaction time of 4 days. With this core, controlled growth of an external $\text{tRD}_{\text{ZIF-8}}$ layer was not possible, since in etched hollow microboxes all six (100) vertices are already fully grown. However, the RD shape was fully recovered. Indeed, we found that these particles grew mainly inside of the hollow core, thus fully reversing the etching process (Figure 2d).

Comparison of field-emission scanning electron microscopy (FE-SEM) images of the etched particles and the resulting ZIF-8-on-ZIF-67 particles confirmed their reconstruction into homogeneous tRD or RD particles (Figures 2 and S1). The internal composition of single particles was investigated by elemental mapping with energy-dispersive X-ray spectrometry (EDXS), which revealed a distribution of Co atoms following the shape of the initial etched ZIF-67 particles and a distribution of Zn atoms corresponding to the newly reconstructed layers (Figure 2). Moreover, powder X-ray diffraction (PXRD) patterns and Brunauer–Emmett–Teller (BET) surface areas ($RD_{ZIF-8-on-C_{ZIF-67}}$, $S_{BET} = 1417 \text{ m}^2/\text{g}$; $RD_{ZIF-8-on-T_{ZIF-67}}$, $S_{BET} = 1422 \text{ m}^2/\text{g}$; and $RD_{ZIF-8-on-H_{ZIF-67}}$, $S_{BET} = 1324 \text{ m}^2/\text{g}$) confirmed that these ZIF-on-ZIF systems are pure ZIF-8/ZIF-67 (Figures S3 and S4). Also note here that all $RD_{ZIF-8-on-(C/T)_{ZIF-67}}$ particles could be generated from the $tRD_{ZIF-8-on-(C/T)_{ZIF-67}}$ particles under the conditions described in Figure 1.

Altogether, these experiments showed that, even for the hollow microboxes, all etched cores can be reconstructed to its original shape by controlled regrowing. The fact that all the final shapes are similarly $\{110\}$ dominant is the consequence of the difference in the growing kinetics in the $\langle 100 \rangle$, $\langle 110 \rangle$, and $\langle 111 \rangle$ directions, from which $\langle 110 \rangle$ is the slowest.

Having demonstrated that stepwise reconstruction of our etched particles from C/T to tRD to RD was possible, we envisioned using our strategy to make layered ZIF-8-on-INP-on-ZIF-67 composites by simply attaching the INPs onto the crystal surfaces of the etched ZIF-67 particles before their reconstruction. To this end, we began by investigating attachment of Au NPs ($\sim 9 \text{ nm}$ diameter) to the crystal surface of C particles of ZIF-67. The formed Au NPs were previously coated with poly(vinylpyrrolidone) (PVP; see Supporting Information) and then quantitatively attached to the ZIF-67 particles by simply adding them dropwise to a colloidal solution of ZIF-67 particles in MeOH (5 mg/mL) under vigorous stirring. After 1 min, Au (9 nm)-on- C_{ZIF-67} composites and a transparent supernatant were separated by centrifugation. Remarkably, the transparency of the supernatant indicated that it was deprived of Au NPs and therefore the Au NPs had attached to the ZIF-67 particles massively. Indeed, FE-SEM images of the Au (9 nm)-on- C_{ZIF-67} composites revealed homogeneous attachment of the Au NPs to the crystal surface of ZIF-67 and showed neither any evidence of significant Au–Au aggregation, nor presence of isolated Au NPs in the background (Figure 3a,b).

We then attempted to grow a ZIF-8 layer on top of the Au (9 nm)-on- C_{ZIF-67} composites, seeking to control the reconstruction into either tRD or RD shapes. Thus, we reproduced the same growing conditions as for C_{ZIF-67} except that we used a dispersion of Au-on- C_{ZIF-67} in MeOH (5 mg/mL). Figure 3c,d shows that, when a solution of 2-MiM/ $Zn(NO_3)_2 \cdot 6H_2O$ was used at concentrations of 10 or 25 mM, $tRD_{ZIF-8-on-Au(9\text{ nm})-on-C_{ZIF-67}}$ or $RD_{ZIF-8-on-Au(9\text{ nm})-on-C_{ZIF-67}}$ composites, respectively, were formed. Remarkably, we could apply the same sequential process for the T and H particles, enabling us to generate the corresponding $RD_{ZIF-8-on-Au(9\text{ nm})-on-T_{ZIF-67}}$ and $RD_{ZIF-8-on-Au(9\text{ nm})-on-H_{ZIF-67}}$ particles (Figure 4). The homogeneity of the Au NP distribution observed in Figures 3 and 4 witnesses the ordered formation of the growing ZIF-8 layer in the experimental conditions.

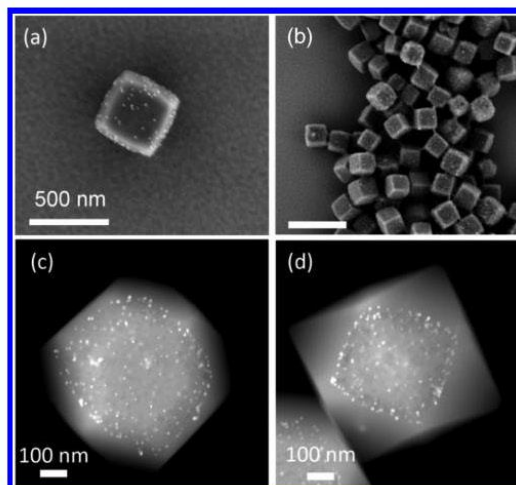


Figure 3. (a, b) FE-SEM images showing an individual (a) and a general view (b) of Au (9 nm)-on- C_{ZIF-67} composites. (c, d) HAADF-STEM images of single $tRD_{ZIF-8-on-Au(9\text{ nm})-on-C_{ZIF-67}}$ (c) and $RD_{ZIF-8-on-Au(9\text{ nm})-on-C_{ZIF-67}}$ (d) composites.

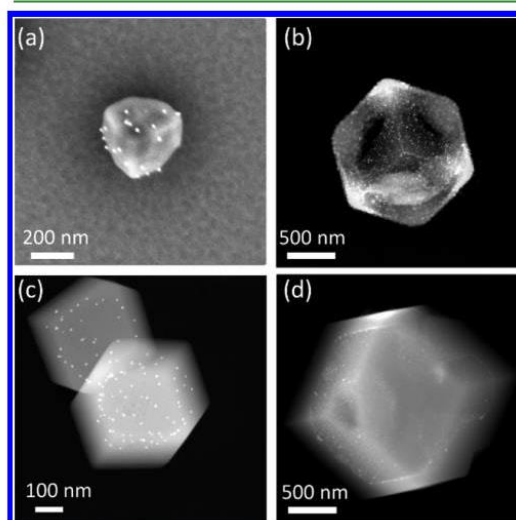


Figure 4. (a) FE-SEM image showing an individual Au-on- T_{ZIF-67} composite. (b) HAADF-STEM image of a single Au-on- H_{ZIF-67} composite. (c, d) HAADF-STEM images of single $RD_{ZIF-8-on-Au-on-T_{ZIF-67}}$ (c) and $RD_{ZIF-8-on-Au-on-H_{ZIF-67}}$ (d) composites.

Having shown that the layer of Au NPs does not preclude ZIF reconstruction and that reconstruction could be done stepwise, we next sought to use our strategy to construct onionlike composites made of (multi)-layered INPs (Figure 5a). To do this, we divided the $tRD_{ZIF-8-on-Au(9\text{ nm})-on-C_{ZIF-67}}$ particles into three portions, to each of which we attached either PVP-coated Au NPs ($\sim 22 \text{ nm}$ in diameter), icosahedral Pd NPs ($\sim 13 \text{ nm}$ in diameter) or cubic Pd NPs ($\sim 18 \text{ nm}$ in side length), using the same protocol. Then, similarly to the first reconstruction process, we deposited a

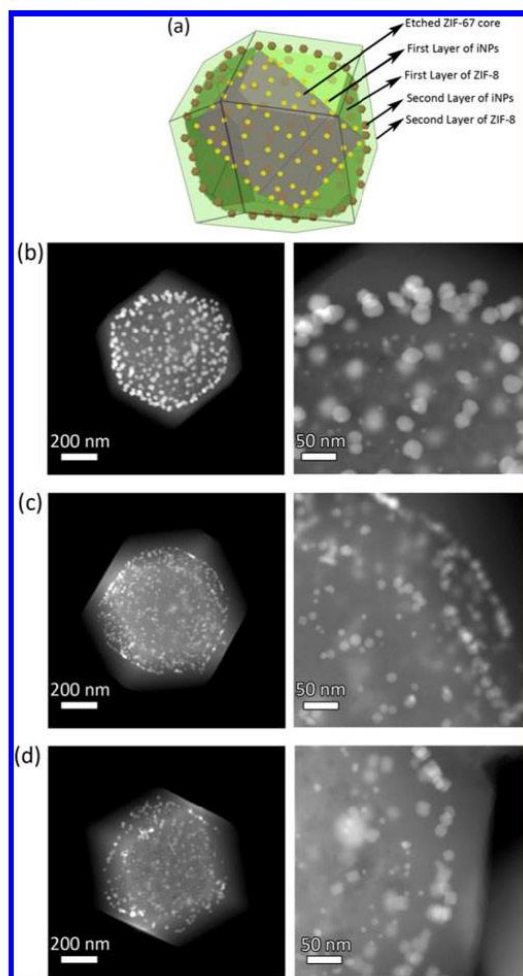


Figure 5. (a) Schematic illustration of the ZIF-based composites composed of two different layers of INPs. (b–d) HAADF-STEM images of single $\text{RD}_{\text{ZIF-8}}\text{-on-Au}$ (22 nm)- $\text{on-tRD}_{\text{ZIF-8}}\text{-on-Au}$ (9 nm)- $\text{on-C}_{\text{ZIF-67}}$ (b), $\text{RD}_{\text{ZIF-8}}\text{-on-Pd}$ (icosahedral)- $\text{on-tRD}_{\text{ZIF-8}}\text{-on-Au}$ (9 nm)- $\text{on-C}_{\text{ZIF-67}}$ (c), and $\text{RD}_{\text{ZIF-8}}\text{-on-Pd}$ (cubic)- $\text{on-tRD}_{\text{ZIF-8}}\text{-on-Au}$ (9 nm)- $\text{on-C}_{\text{ZIF-67}}$ (d) composites.

second ZIF-8 layer using a precursor concentration of 10 mM and a reaction time of 1 day. Figures S5b–d and S5 show high-angle annular dark-field scanning transmission electron microscopy (HAADF-STEM) images of three resulting multicomposites, revealing RD as the final shape and two different layers of INPs, that is, an internal layer of Au NPs (9 nm) and an external layer of either Au NPs (22 nm), icosahedral Pd NPs (13 nm) or cubic Pd NPs (18 nm). These (multi)-layered composites were found to retain the crystallinity and porosity of the starting ZIF particles (Figures S6 and S7). Interestingly, the two different layers of INPs inside a single ZIF particle could be separated by a distance of 40–50 nm (Figure S5b–d, right column).

MOF particles composed of separated layers of INPs should be useful for heterogeneous cascade catalysis because the involved reactions can be chronologically catalyzed in a stepwise manner. As a proof-of-concept, we studied a cascade reaction comprising a first Sonogashira coupling from 1-(prop-2-yn-1-yloxy)naphthalene (**1**) to 1-((3-phenylprop-2-yn-1-yl)oxy)naphthalene (**2**) catalyzed by Cu/Pd NPs, followed by a second cyclization reaction from **2** to 4-phenyl-2H-benzo[*h*]chromene (**3**) catalyzed by Au NPs (Figure 6a). We

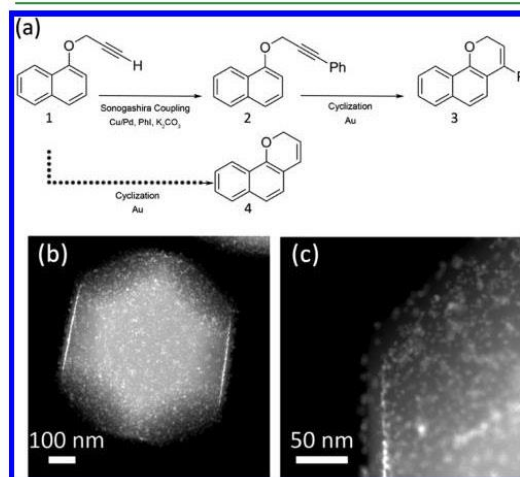


Figure 6. (a) Schematic illustration of the cascade reaction. (b, c) HAADF-STEM images of $\text{Cu/Pd-on-tRD}_{\text{ZIF-8}}\text{-on-Au-on-tRD}_{\text{ZIF-8}}$ composite.

selected this reaction because the cyclization of **1** to 2H-benzo[*h*]chromene (**4**) can occur either under thermal conditions⁵⁶ or can be catalyzed by Au NPs, thus highlighting the importance of the INP that starts catalyzing the reaction involving **1**.

Accordingly, we synthesized a composite composed of an internal layer of Au NPs (~4 nm in diameter) and an external layer of Cu/Pd NPs (~10 nm in diameter, Figure 6b). In this composite, both core and layer separating the INPs was ZIF-8 because it is more stable than ZIF-67. The thickness of the ZIF-8 layer was as small as 20 nm to facilitate the diffusion of the large reagents that occurs mainly through the framework and/or layer defects (Figure 6c).⁵⁷ The catalytic cascade reactions were then conducted by mixing **1**, K_2CO_3 , iodobenzene (PhI), and xantphos in toluene with a toluene dispersion of $\text{Cu/Pd-on-tRD}_{\text{ZIF-8}}\text{-on-Au-on-tRD}_{\text{ZIF-8}}$ (Au: 2.2% w/w; Cu: 0.6% w/w; Pd: 1.3% w/w; metal content was estimated by analyzing the digested composite by ICP-OES) and reacted at 110 °C for 6 days under continuous stirring. As control experiments, we also reproduced the same reaction using $\text{tRD}_{\text{ZIF-8}}$ (without NPs), $\text{Au-on-tRD}_{\text{ZIF-8}}$ (Au: 2.1% w/w), $\text{Cu/Pd-on-tRD}_{\text{ZIF-8}}$ (Cu: 0.6% w/w; Pd: 1.2% w/w), $\text{Au-on-tRD}_{\text{ZIF-8}}\text{-on-Cu/Pd-on-tRD}_{\text{ZIF-8}}$ (Au: 2.2% w/w; Cu: 0.5% w/w; Pd: 1.0% w/w), and $\text{Au/Cu/Pd-on-tRD}_{\text{ZIF-8}}$ (Au: 2.1% w/w; Cu: 0.5% w/w; Pd: 1.2% w/w) as catalysts (Table 1).

In the case of ZIF-8 and the composite containing only Au NPs, $\text{Au-on-tRD}_{\text{ZIF-8}}$, they produced the nondesired **4** (yield: 21 and 31%, respectively, see Figure 6a). The 21% of **4**

Table 1. Summary of the Catalytic Reactions

entry	catalyst	1 (%)	2 (%)	3 (%)	4 (%)
1 ^a	ZIF-8	58			21
2 ^a	Au-on-tRD _{ZIF-8}	40			31
3 ^{a,b,c}	Au-on-tRD _{ZIF-8} (reaction from 2 to 3)		64	22	
4	Cu/Pd-on-tRD _{ZIF-8}	20	35		8
5	Cu/Pd-on-tRD _{ZIF-8} -on-Au-on-tRD _{ZIF-8}		53	11	1
6	Au-on-tRD _{ZIF-8} -on-Cu/Pd-on-tRD _{ZIF-8}	45			18
7	Au/Cu/Pd-on-tRD _{ZIF-8}		28	4	2
9 ^a	no ZIF-8	53			18
10 ^b	ZIF-8		71	8	
11 ^b	no ZIF-8		71	11	

^aWithout PhI and xantphos. ^b2 as starting material. ^c3 days.

produced using only ZIF-8 was exclusively due to the thermal conditions of the reaction, as seen from blanks in Table 1 (entries 1 and 9). Note also here that a higher yield of 4 (65%) was obtained when Au-on-tRD_{ZIF-8} was used without K₂CO₃. This yield increase demonstrates that K₂CO₃, which is necessary for the Sonogashira coupling, is detrimental for the cyclization reaction. For the composite containing only Cu/Pd NPs, Cu/Pd-on-tRD_{ZIF-8}, a mixture of 2 (yield: 35%) and 4 (yield: 8%) was synthesized. For the (multi)-layered composite with the incorrect sequence of INPs (external: Au NPs; internal: Cu/Pd NPs), it also produced 4 (yield: 18%) and not 2 or 3, proving that the cyclization of 1 mainly takes place as it first encounters Au NPs and not Cu/Pd NPs, which were embedded further in the ZIF. For the composite that contains a mixture of both types of NPs on the external surface, Au/Cu/Pd-on-tRD_{ZIF-8}, 2 was mainly produced (yield: 28%). In this reaction, small proportions of 3 (yield: 4%) resulting from the cascade reaction and 4 (yield: 2%) were also formed. For the composite with the good sequence, Cu/Pd-on-tRD_{ZIF-8}-on-Au-on-tRD_{ZIF-8}, we mainly obtained 2 (yield: 53%), a higher proportion of 3 (yield: 11%), and a small proportion of 4 (1%). The increase in the formation of 3 agrees with the occurrence of the cascade reaction, which is first catalyzed with Cu/Pd NPs and then with Au NPs. In addition, the yield of 3 also agrees with the expected value taking into account the independent performance of both reactions involved in the cascade process (Figure 6a). Indeed, as seen before, reaction of 1 in the presence of Cu/Pd-on-tRD_{ZIF-8} gave 2 (yield: 35%), whereas the reaction of 2 in the presence of Au-on-tRD_{ZIF-8} gave 3 (yield: 22%). These values result in an expected yield for the cascade reaction of 8%. Nevertheless, the fact that a higher yield of 3 could be obtained using Cu/Pd-on-tRD_{ZIF-8}-on-Au-on-tRD_{ZIF-8} in comparison to the other binary Au-on-tRD_{ZIF-8}-on-Cu/Pd-on-tRD_{ZIF-8} and Au/Cu/Pd-on-tRD_{ZIF-8} composites is a first proof-of-concept that (multi)-layered MOF composites with a suitable sequence of INPs can potentially catalyze cascade reactions.

CONCLUSIONS

In conclusion, we have reported that ZIF-8/ZIF-67 particles that have been etched can be fully reconstructed and that this reversibility can be used as an alternative strategy to synthesize novel ZIF-on-ZIF and layered ZIF-on-INP-on-ZIF composites. The first step of our approach comprises anisotropic etching of ZIF-8/ZIF-67 particles, which yields unprecedented C, T, and H morphologies. Second, exposing these etched particles to a ZIF precursor solution enables their reversible construction.

Here, precursor concentration and regrowth time were critical variables for optimizing the final shape (tRD or RD) of the reconstructed particles. Moreover, we have demonstrated that even hollow microboxes can be recovered to a final RD shape by filling the inner space of the box with ZIF-8. Remarkably, the reconstruction step may also be accompanied with a step for attaching PVP-capped INPs onto the ZIF particle surface. This attachment, coupled with the ZIF-on-ZIF growth, affords layered ZIF-on-INP-on-ZIF composites. Furthermore, this latter process can be repeated to construct (multi)-layered composites composed of several types of INPs. In these composites, the different INPs are well separated by a nanometric layer of ZIF-8 that can be as small as 20 nm. These composites offer potential for diverse practical domains, such as catalysis, among other applications. Preliminary results obtained for a model cascade reaction paves the way to an improved design of new catalytic protocols for cascade reactions.

ASSOCIATED CONTENT

Supporting Information

The Supporting Information is available free of charge on the ACS Publications website at DOI: 10.1021/acsami.8b05098.

Additional FE-SEM and HAADF-STEM images, PXRD, and sorption isotherms (PDF)

AUTHOR INFORMATION

Corresponding Author

*E-mail: daniel.maspoch@icn2.cat.

ORCID

Amirali Yazdi: 0000-0001-9420-8504

Neus G. Bastús: 0000-0002-3144-7986

Inhar Imaz: 0000-0002-0278-1141

Xavi Ribas: 0000-0002-2850-4409

Daniel Maspoch: 0000-0003-1325-9161

Notes

The authors declare no competing financial interest.

ACKNOWLEDGMENTS

This work was supported by the EU FP7 ERC-Co 615954, the Spanish MINECO (projects PN MAT2015-65354-C2-1-R, MAT2015-70725-R, and CTQ2016-77989-P), and the Catalan AGAUR (projects 2014 SGR 80, 2014 SGR 612 and 2014 SGR 862). It was also funded by the CERCA Program/Generalitat de Catalunya. N.G.B. acknowledges financial support by MINECO through the Ramon y Cajal program (RYC-2012-10991). ICN2 acknowledges the support of the Spanish MINECO through the Severo Ochoa Centers of Excellence Program under Grant SEV-2013-0295. X.R. is also grateful for ICREA-Acadèmia awards. We thank STR UdG for technical support.

REFERENCES

- Lee, S. Y.; Gradon, L.; Janeczko, S.; Iskandar, F.; Okuyama, K. Formation of Highly Ordered Nanostructures by Drying Micrometer Colloidal Droplets. *ACS Nano* **2010**, *4*, 4717–4724.
- Meyer, R. A.; Green, J. J. Shaping the future of nanomedicine: anisotropy in polymeric nanoparticle design. *Wiley Interdiscip. Rev.: Nanomed. Nanobiotechnol.* **2016**, *8*, 191–207.
- Zeng, J.; Zhang, Q.; Chen, J.; Xia, Y. A comparison study of the catalytic properties of Au-based nanocages, nanoboxes, and nanoparticles. *Nano Lett.* **2010**, *10*, 30–35.

- (4) Chen, J.; Wiley, B.; McLellan, J.; Xiong, Y.; Li, Z.-Y.; Xia, Y. Optical Properties of Pd–Ag and Pt–Ag Nanoboxes Synthesized via Galvanic Replacement Reactions. *Nano Lett.* **2005**, *5*, 2058–2062.
- (5) Merkel, T. J.; Herlihy, K. P.; Nunes, J.; Orgel, R. M.; Rolland, J. P.; DeSimone, J. M. Scalable, Shape-specific, Top-down Fabrication Methods for the Synthesis of Engineered Colloidal Particles. *Langmuir* **2010**, *26*, 13086–13096.
- (6) Lim, B.; Jiang, M.; Tao, J.; Camargo, P. H. C.; Zhu, Y.; Xia, Y. Shape-Controlled Synthesis of Pd Nanocrystals in Aqueous Solutions. *Adv. Funct. Mater.* **2009**, *19*, 189–200.
- (7) Moon, S. Y.; Kusunose, T.; Sekino, T. CTAB-Assisted Synthesis of Size- and Shape-Controlled Gold Nanoparticles in SDS Aqueous Solution. *Mater. Lett.* **2009**, *63*, 2038–2040.
- (8) Gómez-Graña, S.; Goris, B.; Altantzis, T.; Fernández-López, C.; Carbó-Argibay, E.; Guerrero-Martínez, A.; Almora-Barrios, N.; López, N.; Pastoriza-Santos, I.; Pérez-Juste, J.; Bals, S.; Van Tendeloo, G.; Liz-Marzán, L. M. Au@Ag Nanoparticles: Halides Stabilize {100} Facets. *J. Phys. Chem. Lett.* **2013**, *4*, 2209–2216.
- (9) Chen, C.; Hirdes, D.; Folch, A. Gray-scale photolithography using microfluidic photomasks. *Proc. Natl. Acad. Sci. U.S.A.* **2003**, *100*, 1499–1504.
- (10) Liu, M.; Zheng, Y.; Zhang, L.; Guo, L.; Xia, Y. Transformation of Pd Nanocubes into Octahedra with Controlled Sizes by Maneuvering the Rates of Etching and Regrowth. *J. Am. Chem. Soc.* **2013**, *135*, 11752–11755.
- (11) Wang, Z.; Wang, H.; Zhang, Z.; Yang, G.; He, T.; Yin, Y.; Jin, M. Synthesis of Pd Nanoframes by Excavating Solid Nanocrystals for Enhanced Catalytic Properties. *ACS Nano* **2017**, *11*, 163–170.
- (12) Du, J.-H.; Sheng, T.; Xiao, C.; Tian, N.; Xiao, J.; Xie, A.-Y.; Liu, S.; Zhou, Z.-Y.; Sun, S.-G. Shape Transformation of {hk0}-Faceted Pt Nanocrystals from a Tetrahedron into a Truncated Ditetragonal Prism. *Chem. Commun.* **2017**, *53*, 3236–3238.
- (13) Lee, J. H.; Gibson, K. J.; Chen, G.; Weizmann, Y. Bipyramid-Templated Synthesis of Monodisperse Anisotropic Gold Nanocrystals. *Nat. Commun.* **2015**, *6*, No. 7571.
- (14) Choi, S.; Kim, T.; Ji, H.; Lee, H. J.; Oh, M. Isotropic and Anisotropic Growth of Metal–Organic Framework (MOF) on MOF: Logical Inference on MOF Structure Based on Growth Behavior and Morphological Feature. *J. Am. Chem. Soc.* **2016**, *138*, 14434–14440.
- (15) Furukawa, S.; Hirai, K.; Takashima, Y.; Nakagawa, K.; Kondo, M.; Tsuruoka, T.; Sakata, O.; Kitagawa, S. A Block PCP Crystal: Anisotropic Hybridization of Porous Coordination Polymers by Face-selective Epitaxial Growth. *Chem. Commun.* **2009**, 5097–5099.
- (16) Koh, K.; Wong-Foy, A. G.; Matzger, A. J. MOF@MOF: Microporous Core–Shell Architectures. *Chem. Commun.* **2009**, 6162–6164.
- (17) Zhao, M.; Yuan, K.; Wang, Y.; Li, G.; Guo, J.; Gu, L.; Hu, W.; Zhao, H.; Tang, Z. Metal–Organic Frameworks as Selectivity Regulators for Hydrogenation Reactions. *Nature* **2016**, *539*, 76–80.
- (18) Falcaro, P.; Ricco, R.; Yazdi, A.; Imaz, I.; Furukawa, S.; Maspocho, D.; Ameloot, R.; Evans, J. D.; Doonan, C. J. Application of Metal and Metal Oxide Nanoparticles@MOFs. *Coord. Chem. Rev.* **2016**, *307*, 237–254.
- (19) Kim, C. R.; Uemura, T.; Kitagawa, S. Inorganic Nanoparticles in Porous Coordination Polymers. *Chem. Soc. Rev.* **2016**, *45*, 3828–3845.
- (20) Cai, W.; Chu, C.-C.; Liu, G.; Wang, Y.-X. J. Metal–Organic Framework-Based Nanomedicine Platforms for Drug Delivery and Molecular Imaging. *Small* **2015**, *11*, 4806–4822.
- (21) Doonan, C.; Ricco, R.; Liang, K.; Bradshaw, D.; Falcaro, P. Metal–Organic Frameworks at the Biointerface: Synthetic Strategies and Applications. *Acc. Chem. Res.* **2017**, *50*, 1423–1432.
- (22) Horcajada, P.; Chalati, T.; Serre, C.; Gillet, B.; Sebrie, C.; Baati, T.; Eubank, J. F.; Heurtaux, D.; Clayette, P.; Kreuz, C.; Chang, J.-S.; Hwang, Y. K.; Marsaud, V.; Bories, P.-N.; Cynober, L.; Gil, S.; Férey, G.; Couvreur, P.; Gref, R. Porous Metal–Organic Framework Nanoscale Carriers as a Potential Platform for Drug Delivery and Imaging. *Nat. Mater.* **2010**, *9*, 172–178.
- (23) Li, Z.; Zeng, H. C. Surface and Bulk Integrations of Single-Layered Au or Ag Nanoparticles onto Designated Crystal Planes {110} or {100} of ZIF-8. *Chem. Mater.* **2013**, *25*, 1761–1768.
- (24) Hu, Z.; Zhang, Z.; Li, Z.; Dou, M.; Wang, F. One-Step Conversion from Core–Shell Metal–Organic Framework Materials to Cobalt and Nitrogen Codoped Carbon Nanopolyhedra with Hierarchically Porous Structure for Highly Efficient Oxygen Reduction. *ACS Appl. Mater. Interfaces* **2017**, *9*, 16109–16116.
- (25) Zhang, J.; Zhang, T.; Xiao, K.; Cheng, S.; Qian, G.; Wang, Y.; Feng, Y. Novel and Facile Strategy for Controllable Synthesis of Multilayered Core–Shell Zeolitic Imidazolate Frameworks. *Cryst. Growth Des.* **2016**, *16*, 6494–6498.
- (26) Tang, J.; Salunkhe, R. R.; Liu, J.; Torad, N. L.; Imura, M.; Furukawa, S.; Yamauchi, Y. Thermal Conversion of Core–Shell Metal–Organic Frameworks: a New Method for Selectively Functionalized Nanoporous Hybrid Carbon. *J. Am. Chem. Soc.* **2015**, *137*, 1572–1580.
- (27) Avci, C.; Ariñez-Soriano, J.; Carné-Sánchez, A.; Guillerm, V.; Carbonell, C.; Imaz, I.; Maspocho, D. Post-synthetic Anisotropic Wet-Chemical Etching of Colloidal Sodalite ZIF Crystals. *Angew. Chem., Int. Ed.* **2015**, *54*, 14417–14421.
- (28) Pang, S. H.; Han, C.; Sholl, D. S.; Jones, C. W.; Lively, R. P. Facet-Specific Stability of ZIF-8 in the Presence of Acid Gases Dissolved in Aqueous Solutions. *Chem. Mater.* **2016**, *28*, 6960–6967.
- (29) Liu, W.; Huang, J.; Yang, Q.; Wang, S.; Sun, X.; Zhang, W.; Liu, J.; Huo, F. Multi-shelled Hollow Metal–Organic Frameworks. *Angew. Chem., Int. Ed.* **2017**, *56*, 5512–5516.
- (30) Hu, M.; Ju, Y.; Liang, K.; Suma, T.; Cui, J.; Caruso, F. Void Engineering in Metal–Organic Frameworks via Synergistic Etching and Surface Functionalization. *Adv. Funct. Mater.* **2016**, *26*, 5827–5834.
- (31) Chou, L.-Y.; Hu, P.; Zhuang, J.; Morabito, J. V.; Ng, K. C.; Kao, Y.-C.; Wang, S.-C.; Shieh, F.-K.; Kuo, C.-H.; Tsung, C.-K. Formation of Hollow and Mesoporous Structures in Single-Crystalline Microcrystals of Metal–Organic Frameworks via Double-solvent Mediated Overgrowth. *Nanoscale* **2015**, *7*, 19408–19412.
- (32) Chen, H.; Shen, K.; Chen, J.; Chen, X.; Li, Y. Hollow-ZIF-Templated Formation of a ZnO@C–N–Co Core–Shell Nanostructure for Highly Efficient Pollutant Photodegradation. *J. Mater. Chem. A* **2017**, *5*, 9937–9945.
- (33) Jiang, Z.; Li, Z.; Qin, Z.; Sun, H.; Jiao, X.; Chen, D. LDH Nanocages Synthesized with MOF Templates and their High Performance as Supercapacitors. *Nanoscale* **2013**, *5*, 11770–11775.
- (34) Zhang, P.; Guan, B. Y.; Yu, L.; Lou, X. W. D. Formation of Double-Shelled Zinc–Cobalt Sulfide Dodecahedral Cages from Bimetallic Zeolitic Imidazolate Frameworks for Hybrid Supercapacitors. *Angew. Chem., Int. Ed.* **2017**, *56*, 7141–7145.
- (35) Li, S.; Dharmawardana, M.; Welch, R. P.; Ren, Y.; Thompson, C. M.; Smaldone, R. A.; Gassensmith, J. J. Template-Directed Synthesis of Porous and Protective Core–Shell Bionanoparticles. *Angew. Chem., Int. Ed.* **2016**, *55*, 10691–10696.
- (36) Lu, G.; Li, S.; Guo, Z.; Farha, O. K.; Hauser, B. G.; Qi, X.; Wang, Y.; Wang, X.; Han, S.; Liu, X.; DuChene, J. S.; Zhang, H.; Zhang, Q.; Chen, X.; Ma, J.; Loo, S. C.; Wei, W. D.; Yang, Y.; Hupp, J. T.; Huo, F. Imparting Functionality to a Metal–Organic Framework Material by Controlled Nanoparticle Encapsulation. *Nat. Chem.* **2012**, *4*, 310–316.
- (37) Yazdi, A.; Mercoci, F.; Bastus, N. G.; Imaz, I.; Puentes, V.; Maspocho, D. The Influence of the MOF Shell Thickness on the Catalytic Performance of Composites made of Inorganic (Hollow) Nanoparticles Encapsulated into MOFs. *Catal. Sci. Technol.* **2016**, *6*, 8388–8391.
- (38) Liang, K.; Ricco, R.; Doherty, C. M.; Styles, M. J.; Bell, S.; Kirby, N.; Mudie, S.; Haylock, D.; Hill, A. J.; Doonan, C. J.; Falcaro, P. Biomimetic Mineralization of Metal–Organic Frameworks as Protective Coatings for Biomacromolecules. *Nat. Commun.* **2015**, *6*, No. 7240.
- (39) Jiang, H.-L.; Liu, B.; Akita, T.; Haruta, M.; Sakurai, H.; Xu, Q. Au@ZIF-8: CO Oxidation over Gold Nanoparticles Deposited to

Metal-Organic Framework. *J. Am. Chem. Soc.* **2009**, *131*, 11302–11303.

(40) Schejn, A.; Mazet, T.; Falk, V.; Balan, L.; Aranda, L.; Medjahdib, G.; Schneider, R. Fe₃O₄@ZIF-8: Magnetically Recoverable Catalysts by Loading Fe₃O₄ Nanoparticles Inside a Zinc Imidazolate Framework. *Dalton Trans.* **2015**, *44*, 10136–10140.

(41) Yang, Q.; Xu, Q.; Yu, S.-H.; Jiang, H.-L. Pd Nanocubes@ZIF-8: Integration of Plasmon-Driven Photothermal Conversion with a Metal–Organic Framework for Efficient and Selective Catalysis. *Angew. Chem., Int. Ed.* **2016**, *55*, 3685–3689.

(42) Huang, Y.; Zhang, Y.; Chen, X.; Wu, D.; Yia, Z.; Cao, R. Bimetallic Alloy Nanocrystals Encapsulated in ZIF-8 for Synergistic Catalysis of Ethylene Oxidative Degradation. *Chem. Commun.* **2014**, *50*, 10115–10117.

(43) Jiang, H.-L.; Akita, T.; Ishida, T.; Haruta, M.; Xu, Q. Synergistic Catalysis of Au@Ag Core–Shell Nanoparticles Stabilized on Metal–Organic Framework. *J. Am. Chem. Soc.* **2011**, *133*, 1304–1306.

(44) Li, P.-Z.; Aranishi, K.; Xu, Q. ZIF-8 Immobilized Nickel Nanoparticles: Highly Effective Catalysts for Hydrogen Generation from Hydrolysis of Ammonia Borane. *Chem. Commun.* **2012**, *48*, 3173–3175.

(45) Chen, L.; Zhan, W.; Fang, H.; Cao, Z.; Yuan, C.; Xie, Z.; Kuang, Q.; Zheng, L. Selective Catalytic Performances of Noble Metal Nanoparticle@MOF Composites: The Concomitant Effect of Aperture Size and Structural Flexibility of MOF Matrices. *Chem. - Eur. J.* **2017**, *23*, 11397–11403.

(46) Rösler, C.; Aijaz, A.; Turner, S.; Filippousi, M.; Shahabi, A.; Xia, W.; Van Tendeloo, G.; Muhler, M.; Fischer, R. A. Hollow Zn/Co Zeolitic Imidazolate Framework (ZIF) and Yolk-Shell Metal@Zn/Co ZIF Nanostructures. *Chem. - Eur. J.* **2016**, *22*, 3304–3311.

(47) Yang, J.; Zhang, F.; Lu, H.; Hong, X.; Jiang, H.; Wu, Y.; Li, Y. Hollow Zn/Co ZIF Particles Derived from Core–Shell ZIF-67@ZIF-8 as Selective Catalyst for the Semi-Hydrogenation of Acetylene. *Angew. Chem., Int. Ed.* **2015**, *54*, 10889–10893.

(48) Bastús, N. G.; Comenge, J.; Puentes, V. Kinetically Controlled Seeded Growth Synthesis of Citrate-Stabilized Gold Nanoparticles of up to 200 nm: Size Focusing versus Ostwald Ripening. *Langmuir* **2011**, *27*, 11098–11105.

(49) Piella, J.; Bastús, N. G.; Puentes, V. Size-Controlled Synthesis of Sub-10-nanometer Citrate-Stabilized Gold Nanoparticles and Related Optical Properties. *Chem. Mater.* **2016**, *28*, 1066–1075.

(50) Huang, H.; Wang, Y.; Ruditskiy, A.; Peng, H.-C.; Zhao, X.; Zhang, L.; Liu, J.; Ye, Z.; Xia, Y. Polyol Syntheses of Palladium Decahedra and Icosahedra as Pure Samples by Maneuvering the Reaction Kinetics with Additives. *ACS Nano* **2014**, *8*, 7041–7050.

(51) Mézailles, N.; Ricard, L.; Gagosz, F. Phosphine Gold(I) Bis-(trifluoromethanesulfonyl)imidate Complexes as New Highly Efficient and Air-Stable Catalysts for the Cycloisomerization of Enynes. *Org. Lett.* **2005**, *7*, 4133–4136.

(52) Worlikar, S. A.; Kesharwani, T.; Yao, T.; Larock, R. C. Synthesis of 3,4-Disubstituted 2H-Benzopyrans through C–C Bond Formation via Electrophilic Cyclization. *J. Org. Chem.* **2007**, *72*, 1347–1353.

(53) Efe, C.; Lykakis, I. N.; Stratakis, M. Gold Nanoparticles Supported on TiO₂ Catalyze the Cycloisomerisation/Oxidative Dimerisation of Aryl Propargyl Ethers. *Chem. Commun.* **2011**, *47*, 803–805.

(54) Lykakis, I. N.; Efe, C.; Gryparis, C.; Stratakis, M. Ph₃PAuNTf₂ as a Superior Catalyst for the Selective Synthesis of 2H-Chromenes: Application to the Concise Synthesis of Benzopyran Natural Products. *Eur. J. Org. Chem.* **2011**, 2334–2338.

(55) Arcadi, A.; Blesi, F.; Cacchi, S.; Fabrizi, G.; Goggiani, A.; Marinelli, F. Gold versus Silver Catalyzed Intramolecular Hydroarylation Reactions of [(3-arylprop-2-ynyl)oxy]benzene Derivatives. *Org. Biomol. Chem.* **2012**, *10*, 9700–9708.

(56) Lutz, R. P. Catalysis of the Cope and Claisen rearrangements. *Chem. Rev.* **1984**, *84*, 205–247.

(57) Wu, X.; Yang, C.; Ge, J. Green Synthesis of Enzyme/metal-organic framework Composites with High Stability in Protein Denaturing Solvents. *Bioresour. Bioprocess.* **2017**, *4*, 24.